ENERGY
www.csiro.au

The Lesueur: Deposition, Rocks, Facies, Properties

Project 7-0115-0240 Final report

February 2018

Report compiled by: Claudio Delle Piane[1]

Contributions from: Julien Bourdet[1], Jeremie Dautriat[1], Lionel Esteban[1], Shane Kager[1], Maxim Lebedev[2], Bruce Maney[1], Nazanin Nourifard[2], Ali Rezagholilou[2], Mohammad Sarmadivaleh[2], Joel Sarout[1], Christopher Skea[2], Alexey Yurikov[2]

[1] CSIRO ENERGY

[2] Curtin University

CSIRO Report: EP181193

Citation

Delle Piane, C., Bourdet, J., Dautriat, J., Esteban, L., Kager, S., Lebedev, M., Maney, B., Nourifard, N., Rezagholilou, A., Sarmadivaleh, M., Sarout, J., Skea, C., Yurikov, A. 2018. The Lesueur: Deposition, Rocks, Facies, Properties ANLEC Project 7-0115-0240 Final report. CSIRO Report Number EP133710

Copyright

© Commonwealth Scientific and Industrial Research Organisation 2016. To the extent permitted by law, all rights are reserved and no part of this publication covered by copyright may be reproduced or copied in any form or by any means except with the written permission of CSIRO.

Important disclaimer

CSIRO advises that the information contained in this publication comprises general statements based on scientific research. The reader is advised and needs to be aware that such information may be incomplete or unable to be used in any specific situation. No reliance or actions must therefore be made on that information without seeking prior expert professional, scientific and technical advice. To the extent permitted by law, CSIRO (including its employees and consultants) excludes all liability to any person for any consequences, including but not limited to all losses, damages, costs, expenses and any other compensation, arising directly or indirectly from using this publication (in part or in whole) and any information or material contained in it.

CSIRO is committed to providing web accessible content wherever possible. If you are having difficulties with accessing this document please contact enquiries@csiro.au.

Contents

Acknowledgments 7

Executive summary 8

Preliminary notes 10

Section 1: Introduction and scope of the project 11

References section 1 18

Section 2: Diagenesis, fluid inclusions and fault analysis 19

Summary 20

2A: Diagenesis and fluid inclusion 21

2B: Fault analysis 36

Conclusions 49

References section 2 50

Appendix 2A: Fluid inclusions results 53

Section 3: Petrophysical core plug characterization 60

Summary 61

3A: Porosity, permeability and Nuclear Magnetic Resonance 62

3B: Brine permeability 71

3C: Permeability anisotropy 82

Section 3 Discussion and conclusions 94

References section 3 97

Appendix 3A 100

Appendix 3B 102

Section 4: Geomechanical-acoustic core plug characterisation 104

Summary 105

4A: Triaxial testing of Yalgorup samples 106

4B: Ultrasonic monitoring of dry and brine saturated Wonnerup samples 116

4C: Broadband elastic moduli measurements to determine the frequency dependence of the elastic moduli 124

4D: Calibration of stress induced anisotropy changes during fluid substitution 143

Appendix 4A: Ultrasonic frequency measurements: tabulated results 155

Appendix 4B: Low frequency measurements: tabulated results 167

References section 4 177
Section 5: Evaluation of SC-CO_2 containment capacity of shale: Testing recommendations and results on the Yalgorup 178
Scope and objectives 179
SC-CO_2 containment capacity of shales: How? 179
Indirect estimation of P_{cap} 180
Direct laboratory evaluation 181
Discussion 182
Recommended evaluation method 183
Recommendations and conclusions 188
References section 5 189
Section 6: Image analysis evaluation of Harvey 1 rock cuttings for wellbore instability 190
Introduction 191
Particle Descriptions 191
Initial evaluations 198
Particle size analysis 199
Conclusions and recommendations 200
References section 6 202
Appendix 5A: Image analysis results 204
Section 7: Summary and recommendations 218

Acknowledgments

The authors would like to acknowledge contributions to the South West Hub Flagship project by the Western Australian Department of Mines and Petroleum (including the Geological Survey of Western Australia), the Western Australian Royalty for Regions Program and the Commonwealth Department Industry and Science The author wish to also acknowledge financial assistance provided through Australian National Low Emissions Coal Research and Development (ANLEC R&D). ANLEC R&D is supported by Australian Coal Association Low Emissions Technology Limited and the Australian Government through the Clean Energy Initiative. The researchers acknowledge the contribution made by National Geosequestration Laboratory (NGL) to the progress of this research work. Some of the analysis and measurements performed in this work were carried out using the state-of-the-art laboratory facility housed within the NGL.

Gratitude goes to Julien Strand and Laurent Langhi for numerous discussions on faults and for providing some of the figures used in section 2. David N. Dewhurst, Tess Dance and Karsten Michael are thanked for internal review of the report. We also would like to acknowledge the technical assistance of Derek Winchester, David Nguyen and Leigh Kiewiet for sample preparation and laboratory operations.

We thank three anonymous reviewers for their supportive comments and suggestions.

Executive summary

The South West Hub project has entered a stage aimed at reducing uncertainties related to the distribution of properties of the potential subsurface reservoir represented by the Triassic Lesueur Sandstone. The drilling program completed on boreholes Harvey 2, Harvey 3 and Harvey 4 in 2015 provided new data and core material for laboratory characterization of the Lesueur Sandstone in the South West Hub area to complement the work done on Harvey 1. In this context, this project was delineated to provide new hard data and interpretation to shed light and reduce uncertainty on the following aspects of the subsurface characterization identified as priorities by the South West Hub Project Sub-surface Uncertainty Management Plan (UMP) compiled by the Department of Mines, Industry Regulation and Safety in 2017:

- Injectivity potential: what are the depositional, diagenetic and structural controls affecting the reservoir quality of the targeted units?
- Current and past nature of the formation fluids and reservoir compartmentalization: are there indications of faults acting as conduits or barriers in the geological record?
- Seismic constraints: can the reservoir and seal units be identified by their seismic characteristics?
- Geomechanical properties of the storage reservoir and overlying units: what are their failure parameters will they be mechanically stable during CO_2 injection?
- Containment potential of the palaeosols identified in the Yalgorup Member of the Lesueur Sandstone is there sufficient contrast in hydraulic properties between the reservoir and overlying units to ensure CO_2 containment?

Addressing these questions required a highly multi-disciplinary approach based on a combination of core analysis, micro analytical techniques and innovative laboratory testing focused on the core material extracted from the boreholes mentioned above.
Results collected in samples from Harvey 2, Harvey 3 and Harvey 4 indicate that:

- The lithofacies scheme used for Harvey 1 is broadly applicable to the other boreholes in the south West Hub area indicating a uniformity in the sedimentological characteristics of the Lesueur Sandstone in the subsurface;
- The upper section (100 - 220 m) of the Wonnerup Member intersected by the three new boreholes is dominated by quartzo-feldspathic sandstones showing good reservoir quality and permeability
- Petrographic analysis of samples from the new boreholes and a review of those from boreholes intersecting deeper sections of the Wonnerup indicate a significant effect of diagenesis on reservoir quality. Porosity and permeability reduce with increasing depth (and temperature) via diagenetic precipitation of pore occluding clay minerals and deposition of quartz overgrowth. Porosity and permeability drastically deteriorate above an estimated temperature of approximately 120 °C due to an increase in chemical compaction;
- Sub-seismic scale faults are identified within the three new boreholes and described for the first time based on core observation and microstructural analysis. It is inferred that these structures could act as local baffles to subsurface fluid flow and potentially could reduce injectivity in the targeted reservoir. Based on geometrical relationships an estimate density of these structure is provided that can be implemented in geological reservoir models;
- Geochemical analysis of fluid inclusions indicate a consistent range of palaeo-salinities in the different boreholes and give no indication of compartmentalization across different borehole locations. These salinities compensate partly for the lack of reliable data on the current formation water salinity in the subsurface of the South West Hub and provide a realistic range to be used in reservoir models to constrain CO_2 solubility in the Lesueur Sandstone aquifer;

- Temperatures recorded in fluid inclusions provide information on the burial history of the sediments in the South West Hub area which can be reconciled with a local uplift of approximately 1.5 km. This data set is particularly valuable to understand the geological history of the Perth Basin considering the paucity of conventional geothermal constraints like vitrinite reflectance in the area;
- Laboratory tests conducted under pressure and temperature conditions replicating those found at depth and a realistic pore water chemistry show that permeability to brine is systematically lower than the Klinkenberg corrected gas permeability measured on the same samples. Therefore, the former should be used for populating the flow properties of the reservoir in dynamic reservoir models;
- A novel experimental set up was used to estimate directional permeability on single core plugs at in situ conditions. The permeability of samples from the Lesueur Sandstone is moderately anisotropic as estimated by ratios of vertical to horizontal permeability ranging between 0.88 and 0.41; the estimated values are consistent with other fluvial sandstone reported in the literature and can be added to realistically model fluid movement in the South West Hub area;
- The elastic properties of the Lesueur Sandstone estimated from laboratory experiments are sensitive to fluid saturation state, and the experimental results can be well predicted via the use of Gassmann fluid substitution theory supporting its use for CO_2 saturation monitoring via seismic methods;
- The geomechanical properties of the Lesueur Sandstone have been experimentally evaluated and show that the potential reservoir (i.e. the Wonnerup Member of the Lesueur Sandstone) follows a dilational Mohr Coulomb behaviour characterised by a friction coefficient of 0.71 ± 0.13 and cohesion of 10.93 ± 6.06 MPa. On the other hand, the experimental data collected on the clay rich samples of Yalgorup Member are best described by a compactant yield envelope suggesting that the mechanical response of the formation is sensitive to its lithological characteristics and different constitutive behaviours should be used to appropriately model different facies.

Overall the project results should be used in an updated static and dynamic model of the South West Hub that captures the geological and petrophysical characteristics of formations of interest for the project. Some of the information generated within this project is also feeding into workflows developed for concurrent ANLEC supported activities related to the South West Hub.

Preliminary notes

The report is organised in chapters describing the analytical approach and results of each work unit. Each chapter was prepared to be self-standing. Formation names and formation tops are taken from the post-drilling documents circulated by the GSWA. Depth of samples used in this report is based on the indications provided on the casing of the retrieved cores. Details of the researchers' contributions to the work presented in this report are as follows:

Part	Title	Contributors
Section 1	Introduction and scope of the project	Claudio Delle Piane
Section 2	2A. Diagenesis and fluid inclusion	Julien Bourdet, Claudio Delle Piane
	2B. Faults analysis	Claudio Delle Piane
Section 3	3A. Porosity, permeability and Nuclear Magnetic Resonance	Lionel Esteban
	3B. Brine Permeability	Alexey Yurikov, Maxim Lebedev, Claudio Delle Piane
	3C. Permeability anisotropy	Jeremie Dautriat, Shane Kager
Section 4	4A. Triaxial testing of Yalgorup samples	Claudio Delle Piane
	4B. Ultrasonic monitoring of dry and brine saturated Wonnerup samples	Jeremie Dautriat, Shane Kager
	4C. Broadband elastic moduli measurements to determine the frequency dependence of the elastic moduli and calibrate seismic	Alexey Yurikov, Maxim Lebedev
	4D. Calibration of stress induced changes in anisotropy during fluid substitution.	Nazanin Nourifard, Maxim Lebedev
Section 5 (CSIRO in kind contribution)	A feasibility study for the development of a protocol to experimentally measure the Supercritical CO_2 breakthrough pressure in clay rich formations	Joel Sarout, Bruce Maney, Jeremie Dautriat
Section 6 (Curtin University in kind contribution)	Evaluation of Harvey 1 rock cuttings for wellbore instability Issues Using Image Analysis	Ali Rezagholilou, Christopher Skea, Mohammad Sarmadivaleh
Section 7	Summary, conclusions and recommendations	Claudio Delle Piane

Section 1: Introduction and scope of the project

The International Energy Agency (IEA) assesses the role that low carbon technological options can play in transforming the current energy market and associated greenhouse gas emissions. The 2012 edition of the IEA's Energy Technology Perspectives identifies the technology options that ensure an 80 % chance of limiting long-term global temperature increase to 2 °C showing that carbon capture and storage
(CCS) is an essential part of any lowest-cost mitigation scenario and probably the only technology currently available that would allow industrial sectors to meet deep emissions reduction goals (Johansson et al., 2012). CCS is accomplished by injecting CO_2 into a porous rock formation below the Earth's surface. So far, three types of geological formations have been considered for the storage of CO_2: depleted oil and gas reservoirs, un-minable coal beds and deep saline formations. A number of studies demonstrated that globally the largest CO_2 storage potential lies in deep saline formations (e.g. Gale, 2017).
Demonstration scale CCS projects are rising in numbers around the world and the South West Hub in Western Australian is one of the Flagship Australian projects under development. Within this project Phase 1 of the data acquisition program included a 2D seismic survey (2011) and the drilling of Harvey 1 (2012). Subsequently, under Phase 2 of the data acquisition program, new data has been acquired through drilling of new boreholes Harvey 2, 3 and 4 and further seismic investigations. The current technical uncertainties of the project identified by the South West Hub project Sub-surface Uncertainty Management Plan (UMP) are related to the characterization and modelling of i) Injectivity and ii) containment of the subsurface. In particular, the UMP document highlights that prioritised technical work is required to better define:

- Sedimentary facies;
- Porosity-permeability relationships;
- Porosity depth trend;
- Reservoir diagenesis;
- Lateral heterogeneity of permeability;
- Presence of faults and fractures
- Fault compartmentalisation;
- Fluid and rock compressibility;
- Formation salinity
- The minimum CO_2 capillary entry pressure (seal capacity).

The scope of this project is to provide data to address these topics in the South West Hub area and inform the stage gate decisions on the continuation of the project. In particular, the South West Hub is investigating the extent that residual trapping of migrating CO_2 may contribute to overall containment. The resulting information from this work will be of benefit both for the commercialisation and wider deployment of CCS technology as well as for gaining public confidence around geosequestration projects.
This report presents the results of thin section petrography; fluid inclusion micro-thermometry analysis and laboratory based measurements of porosity, permeability, geomechanical and elastic properties on samples from Harvey 2, Harvey 3 and Harvey 4 drilled in the South West Hub area of the Perth Basin. A brief overview of the Perth Basin geology and the characteristics of the potential target formation (i.e. the Triassic Lesueur Sandstone) is given below.

Geological framework

The north to north-northwest trending Perth Basin (PB) extends about 1300 km along the south-western margin of Australia and contains a thick succession of mainly continental clastic rocks deposited since the Permian. The PB is part of the East Gondwana rift system and its structural features derive from strike-slip movements associated with the separation of India and Australia which culminated with early Cretaceous break-up and seafloor spreading (Playford et al., 1976; Harris, 1994). Previous authors (Mory and Iasky, 1996;

Crostella and Backhouse, 2000), subdivided the Basin into northern (north of latitude 31°S), central (part lying between latitudes 31° and 33°S), and southern (south of latitude 33°S) parts. The central and southern parts of the basin are further subdivided into five structural units: the offshore Vlaming Sub-basin, the partly onshore and partly offshore Mandurah Terrace, the onshore Beermullah and Bunbury Troughs, and the onshore Vasse Shelf. Of interest here is the southern part of the Basin, particularly the area in proximity of the Harvey Ridge, a structural high marked by the presence of the left-lateral Harvey Transfer Zone recognizable on magnetic and gravity data, both offshore and onshore (Figure 1).

The sedimentary succession of the PB ranges in age from Permian to Holocene; here we focused on the Triassic Lesueur Sandstone, a fluvial to shallow marine siliciclastic unit currently being evaluated as a possible reservoir for geosequestration of CO_2 in the South West Hub. Formation tops of the boreholes of interest for the South West Hub area are reported in Table 1. Importantly for the project, the study area has a unique structure compared to the rest of Southern Perth Basin, wherein, the major potable water aquifer hosted within the Yarragadee Formation has been eroded possibly as a result of local uplift. It should be noted that the burial history of the central Perth Basin is currently not well understood and the data in its support are limited to unpublished vitrinite reflectance studies.

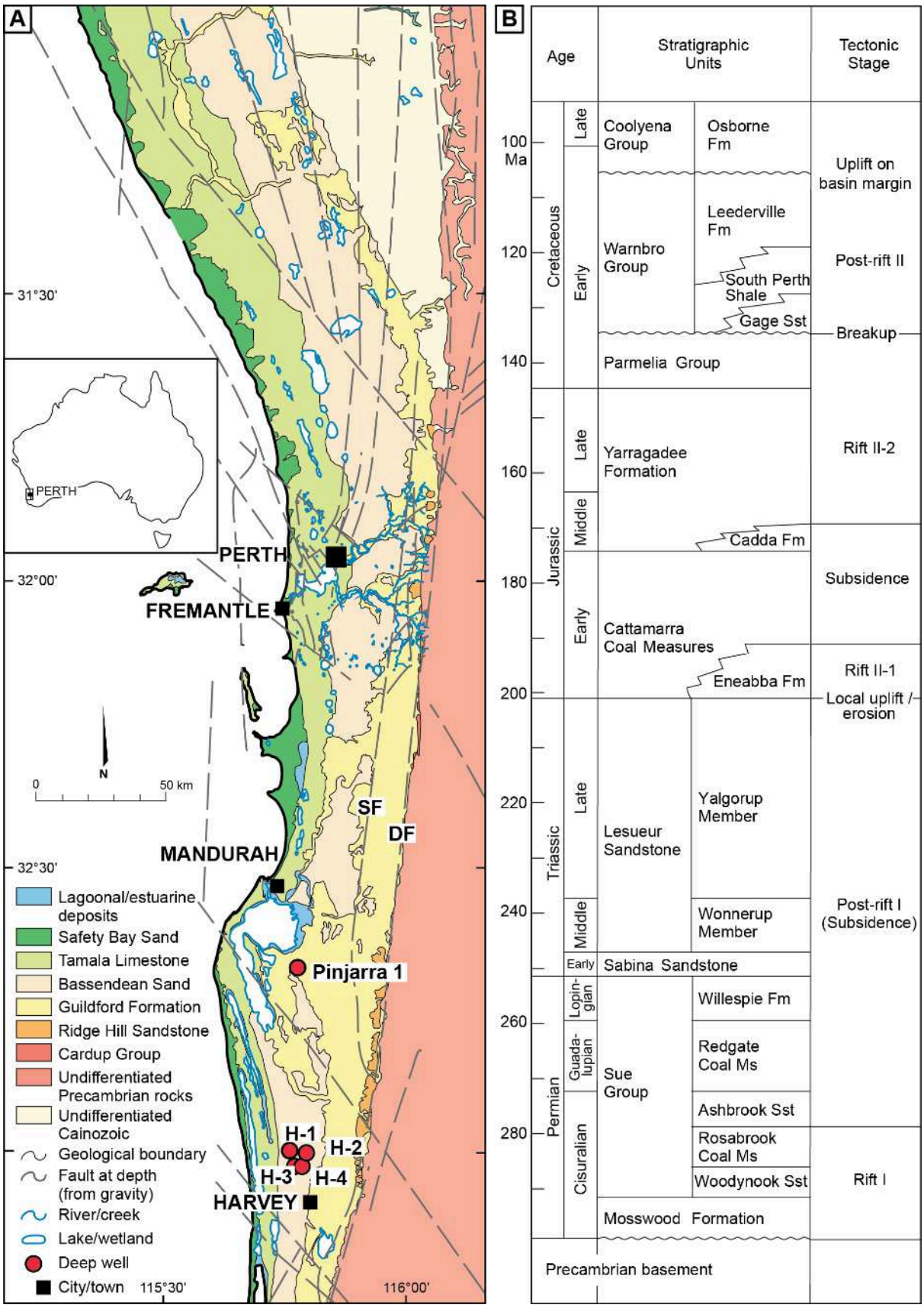


Figure 1 A) Geological map of the Perth Basin with location of the studied boreholes Pinjarra-1 and Harvey 1, 2, 3 and 4 (H-1, H-2, H-3 and H-4). B) Generalized stratigraphy of the Perth Basin. Modified after Olierook et al. (2014). Note that the geological map only shows surface sediments (mostly Quaternary) while the stratigraphic column shows the deeper part of the sedimentary package of Permian and Cretaceous age.

	Age	Harvey 1	Harvey 2	Harvey 3	Harvey 4
Location E		385502.04	392052.65	387392.34	389946.08
Location N		6348947.56	6347141.74	6343895.95	6343842.51
Ground level datum (m)		19.1	15.4	20.2	15.9
		Depth below ground level (m)			
Eneabba	E. Jurass.	250	135	245	165
Lesueur	L.-M. Triass.	704	419	741	1020
Yalgorup	L. Triass.	704	419	741	1020
Wonnerup	M. Triass.	1380	1245	1418	1579
Sabina	E. Triass.	2895			
	Total depth	2945	1350	1550	1802

Table 1 Stratigraphic boundaries of the boreholes of interest for the South West Hub area. The formations encountered were dated by palynology and formation boundaries ware delineated by breaks on the wireline logs.

Previous studies have described the Lesueur Sandstone in terms of its sedimentological characteristics and depositional environment based on core material recovered from Harvey 1 and Pinjarra 1 and defined a common lithofacies scheme for the two boreholes (Timms et al., 2012; Delle Piane et al., 2013; Olierook et al., 2014; Timms et al. 2015). This includes a number of facies attributed to deposition in a braided, fluvial-dominated environment (Figure 2); the characteristics of the nine facies are reported in Table 2. In general, it was observed that the Upper Member (Yalgorup) of the Lesueur Sandstone contains mixed sandstone/siltstone/claystone characterised by highly variable porosity and permeability; the dominant lithology is typically assigned to the palaeosols facies (D) with interbedded, very coarse-grained and poorly-sorted moderate-energy channel barforms (facies B). The Lower Member (Wonnerup) of the Lesueur Sandstone consists mostly of interbedded coarse, very coarse to gravelly sandstone, typically related to high-energy channel fill (facies Ai-Aiii) with relatively high porosity and permeability. Cross-bedding in lithofacies Aii is defined by changes in grain size rather than changes in mineralogy. Despite the geographical distance and distinct structural position with respect to the Harvey Ridge, the lithofacies distribution in the Wonnerup is very similar in Pinjarra-1 and Harvey 1 (Figure 2).

X-ray diffraction and petrography analyses show that facies Ai–C contain primarily quartz, K-feldspar, with minor clays, framework carbonates and rare opaque minerals, micas, organic carbon and heavy minerals. K-feldspar grains are often skeletal with kaolinite infill. Facies D - G are clay-dominated and also contain 30% - 40% quartz, feldspar and albite (Olierook et al., 2014; Timms et al. 2015). Clay minerals significantly occlude the primary porosity in all lithofacies. The same facies were also observed in cores from Harvey 2, Harvey 3 and Harvey 4, consistent with the interpretation of a fluvial depositional setting. Moreover, a review of the available mineralogy data estimated via quantitative X-ray Diffraction (XRD) analysis shows that there is reasonable consistency in mineralogy between samples from the different boreholes, especially within the Wonnerup Member of the Lesueur Sandstone which appears to be mainly consisting of quartz (75.63 ± 9.38 wt %), K-feldspar (7.53 ± 5.5 wt %) and kaolinite (7.86 ± 5.86 wt %).

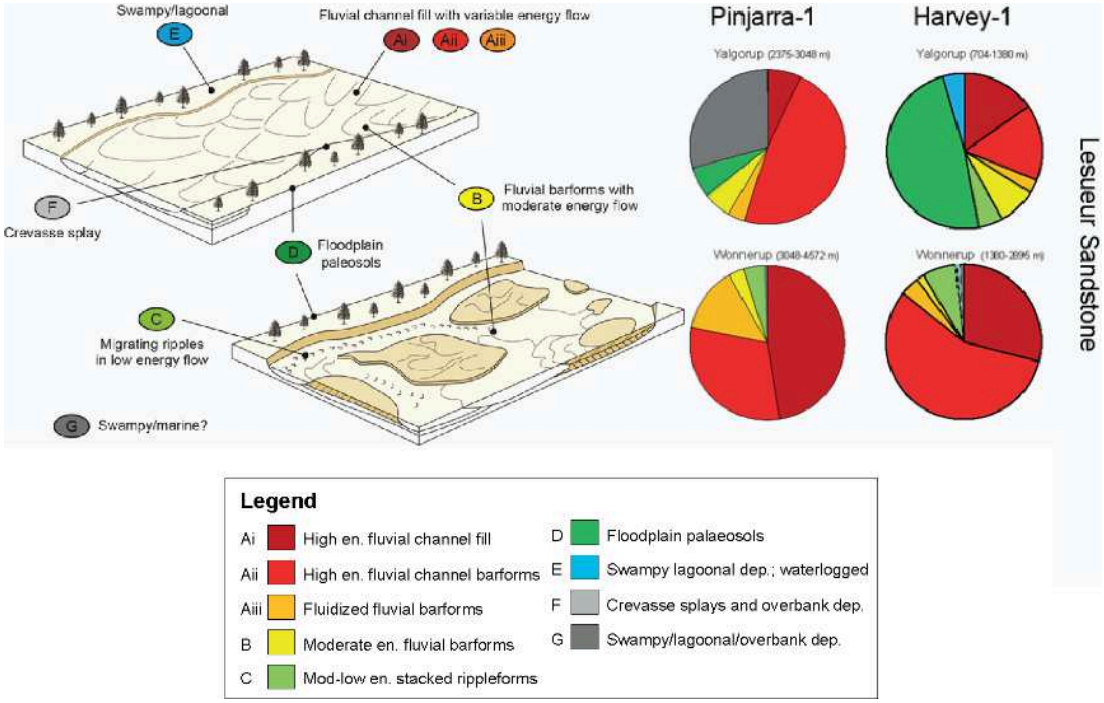


Figure 2 Block diagrams to illustrate the sedimentary depositional environment and architecture of lithofacies Ai-G. After Miall (1996). Right: comparison of facies distribution within the cored sections of the Lesueur Sandstone encountered in Pinjarra 1 and Harvey 1.

Facies	Lithology	Grain size	Sorting	Sedimentary structures	Depositional environment
Ai	Sand/gravel	Very coarse–gravelly	Poor	Cross-bedded	High energy channel fill
Aii	Sandstone	Medium – very coarse	Poor	Cross-bedded	High energy barforms
Aiii	Sandstone	Coarse – very coarse	Medium	Massive	Fluidized barforms
B	Sandstone	Medium	Medium	Massive with flaser	Medium energy barforms
C	Sandstone	Fine – medium	Medium	X-lamination with flaser	Medium – low energy rippleforms
D	Clay/silt/sand	Silt – medium	Poor	Fractures, slickensides	Floodplain paleosols
E	Clay/silt/sand	Clay – very fine	Medium–well	Bioturbations, slumps, dewatering	Swampy deposit; waterlogged
F	Silt/sand	Silt – very fine	Medium–well	Trough cross-lamination	Crevasse splays
G	Clay/silt/sand	Clay – very fine	Well	Thin lamination	Swampy/overbank deposit

Table 2 Summary of facies recognised in the cored sections of the Lesueur Sandstone and their characteristics. For comprehensive descriptions see Timms et al., 2012; Delle Piane et al., 2013; Olierook et al., 2014 and Timms et al., 2015.

Overall, the observed cores conform to the lithofacies scheme proposed for Harvey 1 and Pinjarra 1 consistent with the interpretation of a fluvial depositional setting and a dominance of high energy facies in the Wonnerup Member of the Lesueur Sandstone. Correlations between variations in porosity/permeability, lithofacies and depth have been established from samples extracted from Harvey 1 (Delle Piane et al. 2013a; Olierook et al. 2014). At a given depth, high-energy channel fills and barforms (facies Ai–Aiii) have the highest porosity and permeability; moderate- to low-energy barforms, migrating rippleforms and palaeosols (facies B–D) have intermediate porosity and permeability; and swampy/overbank deposits and crevasse splays have the lowest porosity and permeability (facies E–G) (Figure 3).

Expanding the dataset to include samples from Harvey 4 and Pinjarra 1 confirms the strong lithofacies control on petrophysical properties: at any given porosity high energy facies show significantly higher permeability than moderate to low energy facies (Figure 3).

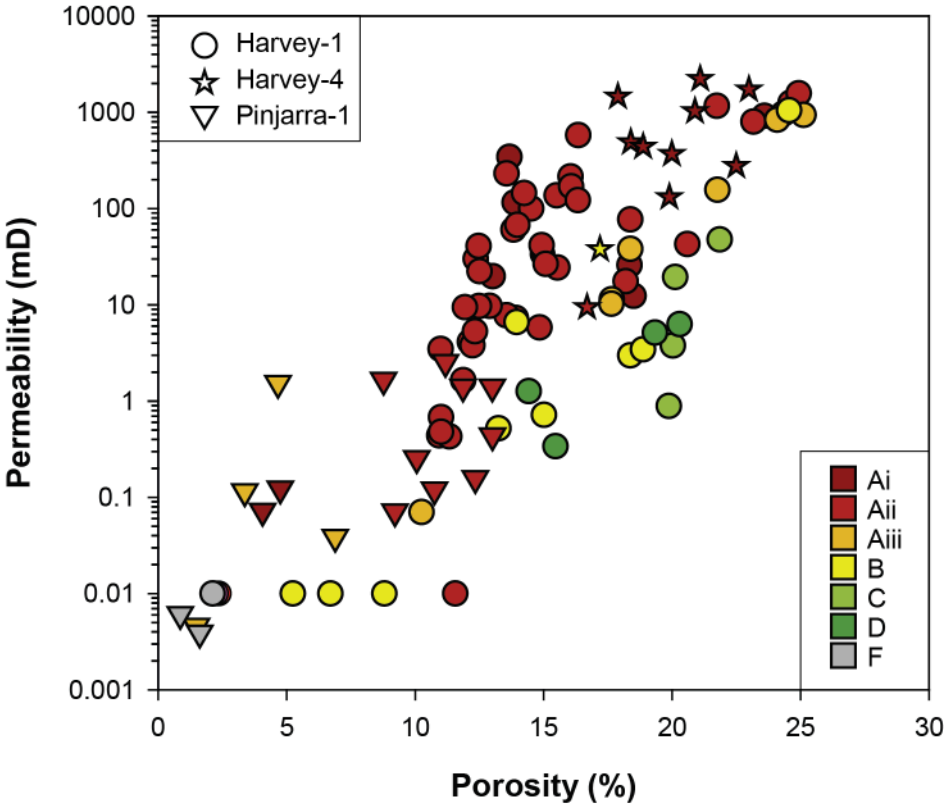


Figure 3 Facies control on porosity and permeability, determined from helium-injection core plugs from Harvey 1; Harvey 4 and Pinjarra 1. Porosity versus permeability plot colour coded by facies type.

Data points from the three boreholes sorted by facies are summarised in Figure 4 showing an inverse depth dependency of porosity and permeability, with higher values at shallow depth decreasing towards the greater depths. These trends can be attributed to the combined effects of mechanical and chemical compaction (i.e. diagenesis) becoming more evident at deeper conditions in the basin (as detailed in Section 2 of the report).

The following sections of the report detail the technical work and frame and outcomes of the project within the list of topics identified by the DMIRS UMP outlined above.

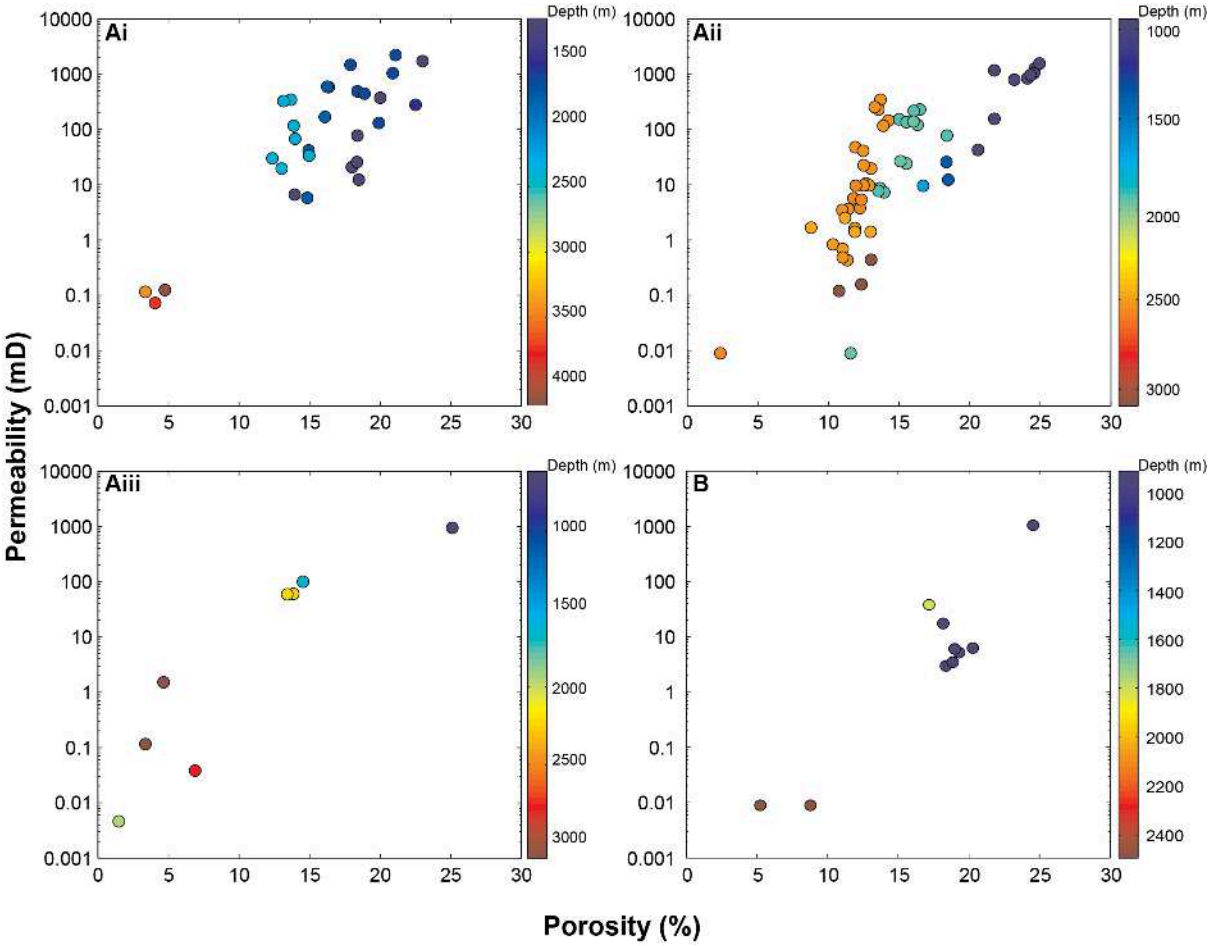


Figure 4 Facies and depth control on porosity and permeability, determined from helium-injection core plugs from Harvey 1, Harvey 4 and Pinjarra 1. Porosity versus permeability plots colour coded by depth in meters.

References section 1

Crostella, A. and Backhouse, J., 2000. Geology and petroleum exploration of the central and southern Perth Basin, Western Australia (No. 57). Perth, WA: Geological Survey of Western Australia.

Delle Piane, C., Olierook, H.K., Timms, N.E., Saeedi, A., Esteban, L., Rezaee, R., Mikhaltsevitch, V., Iglauer, S. and Lebedev, M., 2013. Facies-based rock properties distribution along the Harvey 1 stratigraphic well. Australian National Low Emissions Coal Research & Development CSIRO Report Number EP133710. Available at: http://anlecrd.com.au/projects/facies-based-rock-properties-distribution-along-the-Harvey-1-stratigraphic-well/

Gale, J., 2017. CO_2 Storage in Deep Geological Formations: The Concept. In Geological Storage of CO_2 in Deep Saline Formations (pp. 1-14). Springer Netherlands.

Harris, L.B., 1994. Structural and tectonic synthesis for the Perth Basin, Western Australia. Journal of Petroleum Geology, 17 (1994), pp. 129-156

Johansson, T.B., Patwardhan, A.P., Nakićenović, N. and Gomez-Echeverri, L. eds., 2012. Global energy assessment: toward a sustainable future. Cambridge University Press.

Miall, A.D., 1996. The Geology of Fluvial Deposits: Sedimentary Facies, Basin Analysis. Petroleum Geology. Springer-Verlag, New York, p.582.

Mory, A.J., Iasky, R.P., 1996. Stratigraphy and Structure of the onshore Northern Perth Basin, Western Australia. 46, Geological Survey of Western Australia, Perth.

Olierook, H.K., Delle Piane, C., Timms, N.E., Esteban, L., Rezaee, R., Mory, A.J. and Hancock, L., 2014. Facies-based rock properties characterization for CO_2 sequestration: GSWA Harvey 1 well, Western Australia. Marine and Petroleum Geology, 50, pp.83-102.

Playford, P.E., Cockbain, A.E., Low, G.H., 1976. Geology of the Perth Basin, Western Australia, Bulletin 124. Geological Survey of Western Australia, Perth.

Timms, N.E., Corbel, S., Olierook, H., Wilkes, P.G., Delle Piane, C., Sheldon, H.A., Alix, R., Horowitz, F.G., Wilson, M.E.J., Evans, K.A. and Griffiths, C., 2012. Perth Basin Assessment Program project 2: geomodel. Western Australian Geothermal Centre of Excellence, Perth, Australia.

Timms, N.E., Olierook, H.K., Wilson, M.E., Delle Piane, C., Hamilton, P.J., Cope, P. and Stütenbecker, L., 2015. Sedimentary facies analysis, mineralogy and diagenesis of the Mesozoic aquifers of the central Perth Basin, Western Australia. Marine and Petroleum Geology, 60, pp.54-78.

Section 2: Diagenesis, fluid inclusions and fault analysis

Summary

The potential CO_2 capacity and injectivity of a geological reservoir depend on textural and compositional characteristics determined by depositional and diagenetic processes. In particular, the prediction of the available pore space at depth requires detailed knowledge of mineralogy, depositional and diagenetic textures their control the petrophysical character of the reservoir, and how they vary spatially. Here, we summarize the reservoir characteristics of the Lesueur Sandstone based on microstructural analysis of samples from the four Harvey boreholes drilled in the South West Hub Area. Diagenetic processes that have been significant in modifying the reservoir include feldspar dissolution, formation of pore occluding kaolinite, precipitation of multiple generations of quartz overgrowth, chemical compaction. This work demonstrates that overall reservoir quality in the relatively homogeneous, sandstone-dominated Wonnerup Member of the Lesueur Sandstone deteriorates with increasing depth (and temperature) due to diverse diagenetic modifications. This is important for estimations of capacity potential and reactivity to CO_2.

Furthermore, we estimated palaeo-formation water salinity and diagenetic quartz cementation temperatures based on the analysis of fluid inclusions obtaining a range of salinities for the formation brine in the Wonnerup that compensates the lack of reliable in situ chemical analysis. These data are important to provide constraints for dynamic model scenario as the solubility of CO_2 in water is controlled by the salinity of the formation water, and the interfacial tension between free CO_2 and brine has a strong positive correlation with brine concentration. The measured cementation temperature data are critical to inform the burial history of the basin, currently based on few sparse measurements of vitrinite reflectance.

Finally, this section describes subseismic scale faults (cataclastic deformation bands) in the cores retrieved from the new boreholes affecting the Lesueur Sandstone and discusses their potential impact on injectivity and subsurface fluid flow. Importantly, due to their thin nature, these structures may be “invisible” on conventional seismic profiles. Nevertheless their abundance can be estimated based on published geometrical relationships so their presence can be captured in dynamic reservoir models.

2A: Diagenesis and fluid inclusion

Julien Bourdet[1] and Claudio Delle Piane[1]

[1]CSIRO Energy

Diagenesis in the South West Hub Area and effects on reservoir quality

From the time the sediments are deposited, their properties change continuously during burial via the combined effects of mechanical compaction and chemical processes leading to dissolution and precipitation of mineral phases. Diagenesis is concerned with these chemical and mineralogical changes occurring after sediment deposition. Understanding diagenetic processes and their spatial distribution has important implications for practical aspects of reservoir management. Mechanical and chemical compaction lower porosity and permeability and affect other physical properties that are measurable via wireline logging (i.e. elastic properties). Mechanical compaction, involving grain rotation, sliding, crushing and ductile deformation, is a significant cause of porosity reduction during the early stages of burial, but chemical compaction generally becomes more important at depths greater than about 1.5 km (Bjørlykke, 2015). Deep reservoir quality in sandstones is the cumulative product of depositional, shallow diagenetic, and deep- burial diagenetic processes. Lithologic attributes created at each stage strongly influence subsequent pore-system evolution (Ajdukiewicz et al., 2010). Decades of observations collected by the oil and gas industry worldwide indicate that as a general rule, sandstone porosity decreases with increasing depth as shown by well logging data and by laboratory measurements on core samples. In general, three major diagenetic processes are contributing to the general loss of pore volume during burial; mechanical compaction, chemical compaction and cementation. Moreover, it has been demonstrated that only a few percent of diagenetic cement strongly affect the elastic properties of sands resulting in a drastic difference between the seismic response of slightly cemented and friable reservoirs (e.g. Avseth et al., 2000).

Quartzo-feldspathic sandstones like those constituting the Lesueur Sandstone can change their properties by chemical reactions both at shallow depth and during deep burial (e.g. Bjørlykke, 2015). Close to the surface, humid climates can lead to the dissolution of detrital minerals like feldspar and precipitation of kaolinite clay according to the following reaction:

K-feldspar + H_20 = kaolinite + silica

$2KAlSi_3O_8 + 2H^+ + H_2O = Al_2Si_2O_5(OH)_4 + 4SiO_2 + 2K^+$

This is a typical weathering reaction that requires an open flux of water so that silica and potassium can be removed as solutes in the flowing pore fluids, allowing the reaction to continue. Precipitation of kaolinite can only occur when the K^+/H^+ ratio and silica concentration in the pore water are below certain values (Figure 5). Such low K^+/H^+ ratios are normally are only found in fresh or brackish water. This implies that fluvial sands will be subjected to feldspar dissolution and precipitation of kaolinite in all but very dry climates and is expected to be more intense at shallow levels (Bjørlykke, 2015). In a closed system, beyond the reach of meteoric water influx, the composition of the pore water will gradually approach equilibrium with respect to the non-reacted feldspar grains present in the sandstone.

Accompanying feldspar dissolution and kaolinite precipitation is also the release of silica into solution; this is then precipitated as quartz overgrowths. Significant amounts of quartz cement tend to occur during burial diagenesis at temperatures above 60 °C, and is controlled by the kinetics of quartz precipitation. This is a function of temperature and the silica concentration as well as the available surface area (Walderhaug, 1996).

A metastable kaolin + K-feldspar + quartz assemblage frequently persists to temperatures of about 120°C, above which kaolinite reacts with residual K-feldspar or other sources of potassium to produce illite and silica (Bjørlykke et al., 1989; Bjorkum et al., 1993; Lanson et al., 2002) according to the following reaction:

K-feldspar + kaolinite = illite + silica + H_20

$KAlSi_3O_8 + Al_2Si_2O_5(OH)_4 = KAl_3Si_3O_{10}(OH)_2 + 2SiO_2 + H_20$

Without a source of potassium, kaolinite remains stable at higher temperatures (Jahren and Aagaard, 1992).

Another source of silica leading to quartz cementation is intergranular pressure solution, i.e. dissolution of grain material at point contacts and transport of solute by diffusion to the adjacent pore space where it re-precipitates as diagenetic cement. Pressure solution, also referred to as chemical compaction, contributes significantly to porosity reduction and it is thought to be prevalent at burial conditions of at least 2.5 km (Bjørlykke, 2015). Mica and clay laminae seem to enhance dissolution, and clay laminae often develop into

stylolites (Bjørkum, 1996; Renard et al., 1997). The net result is the reduction of porosity and bulk volume due to closer packing of grains and cementation. At the microscale pressure solution is manifested by interpenetrating grain contacts where quartz grains have dissolved into each other (Figure 6). Insoluble material between the two grains consists of clay, organic matter, oxides and sulphides.

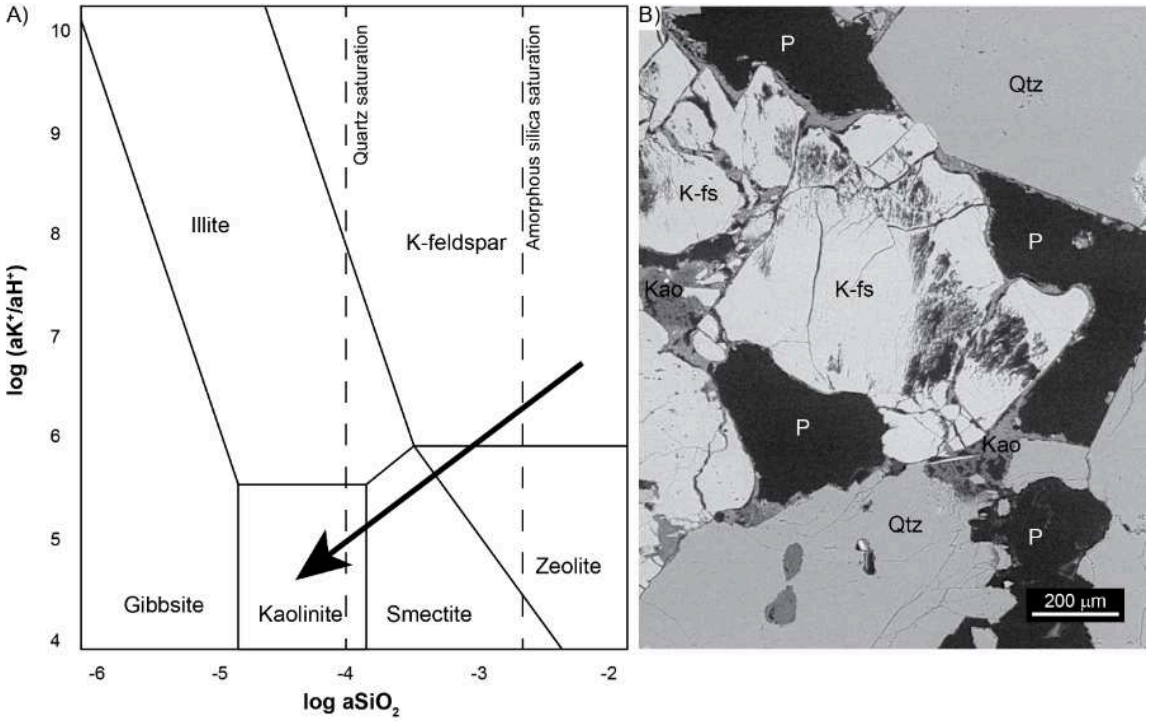


Figure 5 A) Phase diagram for the system log(aK^+/aH^+)– log $aSiO_2$ (where 'a' indicates chemical activity of species) illustrating how changing isothermal water geochemistry can lead to diagenetic reactions. (after Worden and Burley 2003). B) SEM image of a Wonnerup sample from Harvey 3 (1347.7 m) illustrating typical diagenetic features at the microscale: partially dissolved detrital K-feldspar (K-fs) grains with authigenic pore filling and pore bridging kaolinite (Kao). Also visible are pores (P) and detrital quartz grains (Qtz).

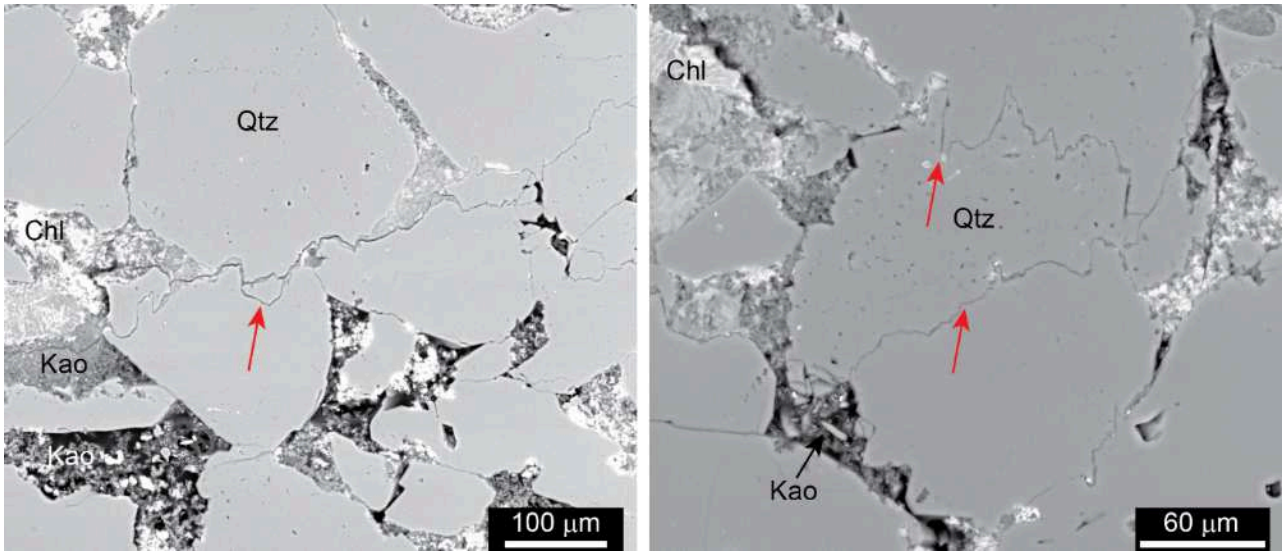


Figure 6 SEM images of inter-granular (left) and intra-granular (right) pressure solution surfaces indicated by the red arrows. Qtz = quartz; Kao = kaolinite; Chl = chlorite. Sample from the Wonnerup Member of the Lesueur Sandstone from Harvey 1, depth of 1940.58 m.

Microstructural observations collected via scanning electron microscopy (SEM) indicate that the main diagenetic process in the shallow part of the Wonnerup intersected by Harvey 2, 3 and 4 is the dissolution of detrital K-feldspar grains leading to the precipitation of pore occluding kaolinite and quartz overgrowth (Figure 7). The latter can be identified via cathodoluminescence (CL) imaging as a dark rind that form on detrital quartz grains, the grey level contrast is due to different concentration of trace elements between detrital and authigenic quartz (e.g. Boggs and Krinsley, 2006) (Figure 7). As discussed above, development of kaolinite in these rocks is consistent with via near surface diagenetic dissolution of feldspars by the action of free flowing groundwater having low K^+/H^+ ratio and silica concentration. This process is more prevalent in permeable lithofacies, such as channel sand deposits (Worden and Burley, 2003).

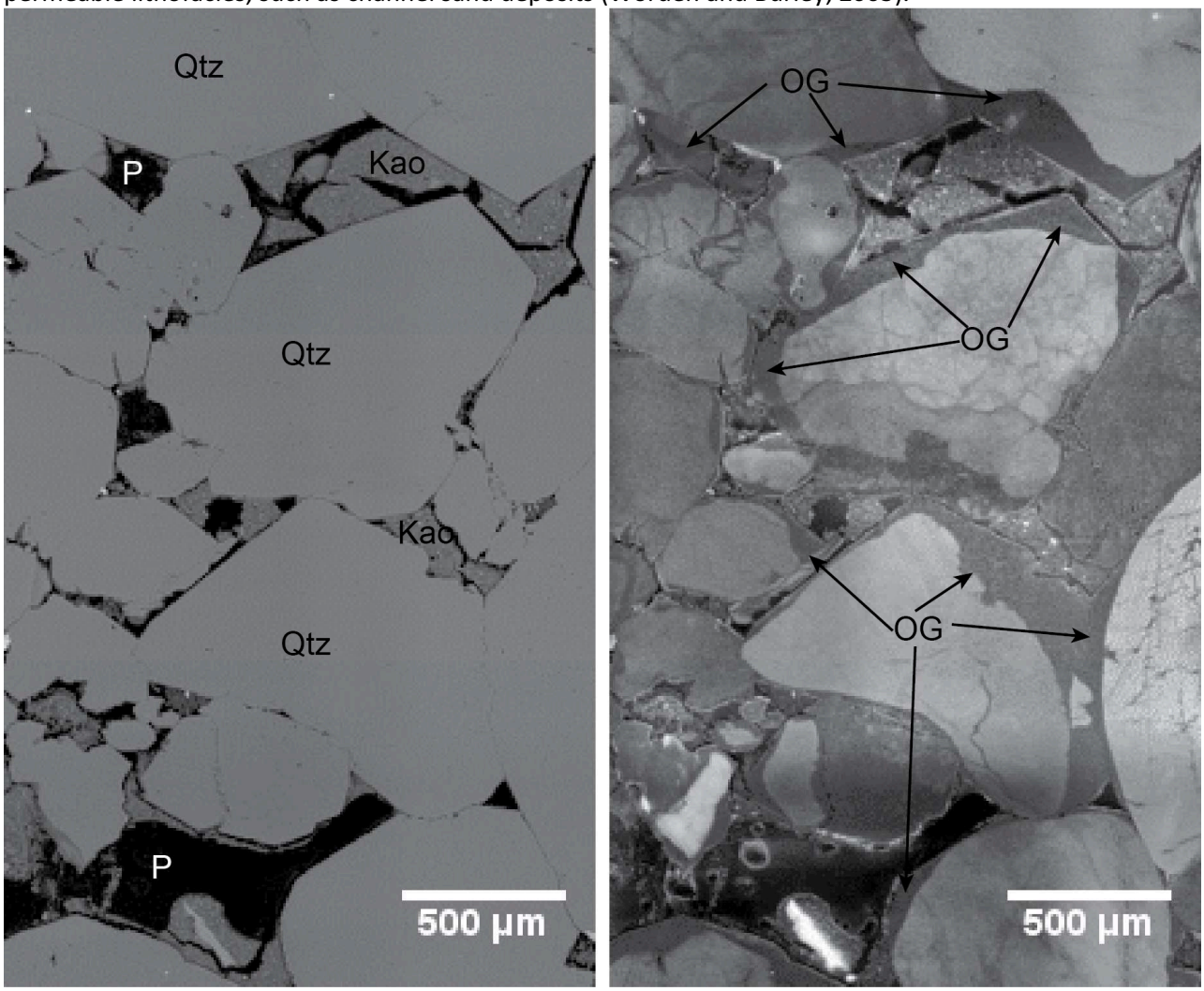


Figure 7 Left: SEM image: Qtz = quartz; Kao = kaolinite; P = pore. Right: Cathodoluminescence image of the same area as in (A), note the dark rim of quartz cement overgrowth (OG) around detrital quartz grains. Images are from a sample collected at 1473.1 m of depth from Harvey 3.

Diagenetic kaolinite aggregates occasionally enclose discrete lamellae of chlorite which interpreted as a coeval, authigenic phase (Figure 8).

Quartz overgrowth and dissolution of detrital K-feldspar grains have been documented in samples from the Lesueur Sandstone from all boreholes analysed so far. The estimated abundance of quartz cement in the analysed sample is shown as a function of depth in Figure 9. The figure also plots values obtained on North Sea sandstones at their maximum burial depth using an approach comparable to the one used in this study (Fisher et al. 2000). Importantly, the figure shows that the Wonnerup samples in the SW-Hub area display an anomalously high content of quartz cement for their current depth; generally quartz cement abundance in the order of 10 % is expected to represent conditions of temperature of at least 80 °C or burial depths of

around 2.5-3 km (e.g. Worden and Morad, 2000). This discrepancy could be explained by taking into account an exhumation of the SW-Hub area of 1.5-2 km: an estimate consistent with previous evaluations based on sonic transit time-depth trends analysed across the Basin (Olierook and Timms, 2015). Pressure solution features are also visible in samples recovered from depth of approximately 1800 m and deeper (see Figure 6 for example) and become pervasive in the deepest parts of the Wonnerup samples in Harvey 1 (depth of approximately 2500 m) and Pinjarra-1 (depth of approximately 4300m).

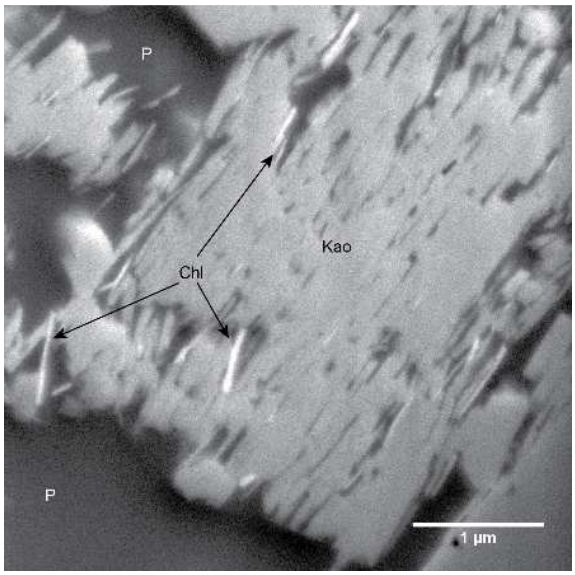


Figure 8 SEM image of a diagenetic kaolinite aggregate with discrete chlorite flakes. Kao = kaolinite; Chl = chlorite; P = pores. Sample from Harvey 3, depth-1473.7m.

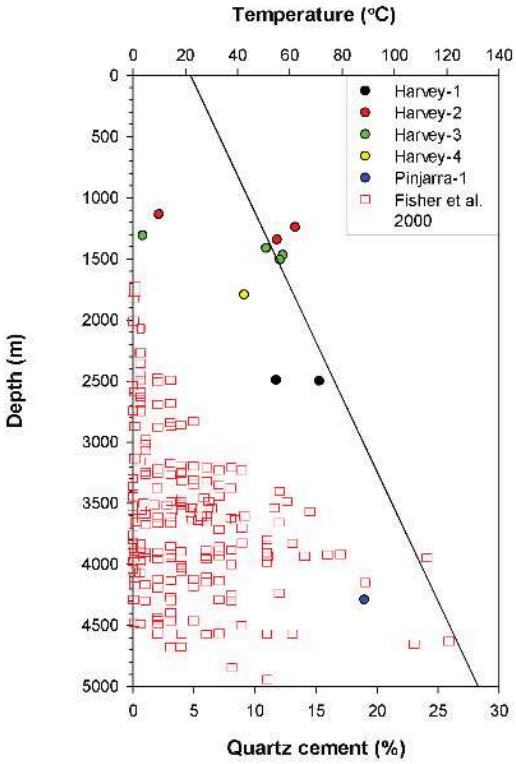


Figure 9 Trends of quartz cement as a function of depth as established from point counting analysis. Red squares are a compilation of data from North Sea sandstones (Fisher et al. 2000). The black line represents a geothermal gradient of 22 °C/km representative of the South West Hub area (based on borehole temperature measurements from well completion reports).

In samples recovered from depths greater than 2400 m, the pore occluding kaolinite starts to be replaced by illite and more extensive chlorite. The deepest available samples from Pinjarra-1 (depth 4295.2 m) show that almost all observable clay aggregates are transformed into illite and chlorite and display extensive chemical cementation via precipitation of quartz overgrowths and pressure solution (Figure 10). Primary porosity in these deep samples is almost completely lost (Figure 11).

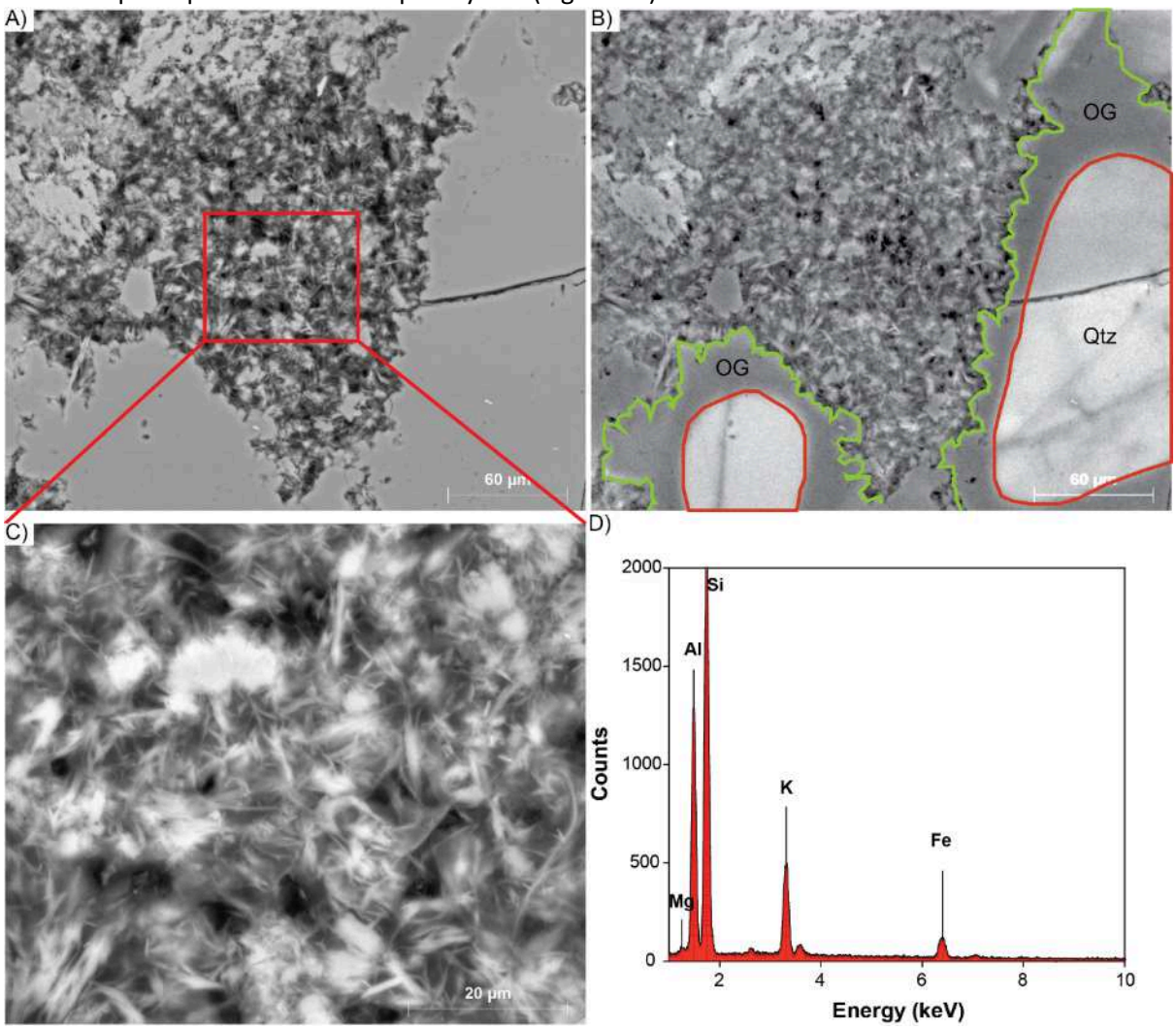


Figure 10 SEM images of pore occluding clay aggregates in the deep part of the Wonnerup Member of the Lesueur Sandstone. A) SEM image in back-scattered electron mode of a pore occluding clay aggregate surrounded by framework grains of quartz (dark grey) and K-feldspar (light grey, upper left). B) SEM image in cathodoluminescence mode of the same area shown in (A) highlighting the presence of diagenetic quartz overgrowths (OG) surrounding detrital quartz grains (Qtz). C) Detail of the clay aggregate showing the co-existence of vermicular chlorite aggregates (bright area in the image) and filamentous illite. D) Energy dispersive spectroscopy (EDS) spectrum of the area shown in (C) showing elemental composition of the clay aggregate consistent with co-existing illite and chlorite. Sample from Pinjarra-1, depth 4295.2 m.

Additional diagenetic events of minor volumetric proportion identified in samples from Lesueur Sandstone are precipitation of sparse calcite, titanium oxides and detrital clay/labile grain dissolution to form secondary porosity (Olierook et al., 2014a; Timms et al. 2015; Conciadori et al. 2015).

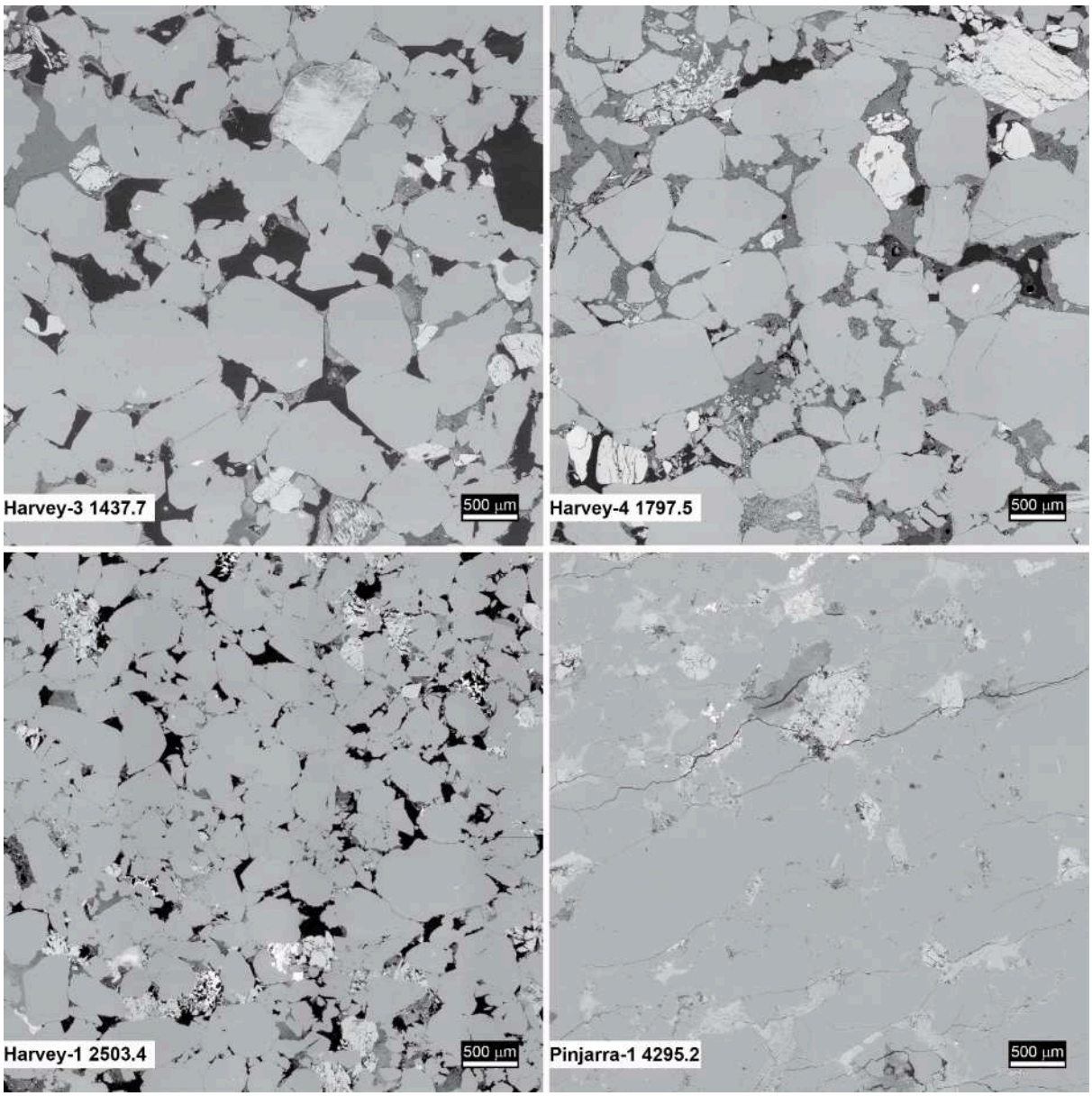


Figure 11 SEM images of samples of the Wonnerup Member of the Lesueur Sandstone from different boreholes at different depth. Note how the porosity (in black in all images) and individual pore size decrease with increasing depth.

Fluid inclusions

Diagenetic fluid inclusions trapped in cements (quartz, feldspar, carbonates) or in diagenetic fractures through grains or minerals enclose palaeo-fluids and can be observed using an optical microscope. Their chemical composition such as salinity and gas content are fingerprints of the palaeo-formation water and of the physical conditions at entrapment. Fluid inclusion chambers have fixed volumes and therefore their densities are constant, identical to the density of the ambient pore fluid at trapping. The microthermometry technique consists of observing fluid phases and measuring the temperatures of phase transitions (freezing, melting, homogenising) in fluid inclusions. The phase arrangements within a fluid inclusion changes with temperature and, crossing a phase boundary, an observable phase transition takes place and the temperature can be recorded. In this work, the homogenisation temperature (T_h) corresponds to the disappearance of a contraction bubble in the liquid water upon heating. During heating from room temperature, the bubble decreases in size and disappears completely at T_h. Considering the initial entrapment of water as a homogeneous liquid phase, this temperature also corresponds to the minimum temperature of trapping. The pressures within the inclusions change with changing temperature, following an isochore (or iso-density curve) (Figure 12). The path between homogenisation conditions and the trapping conditions consists of the isochore line and is calculated using the composition and temperature data.

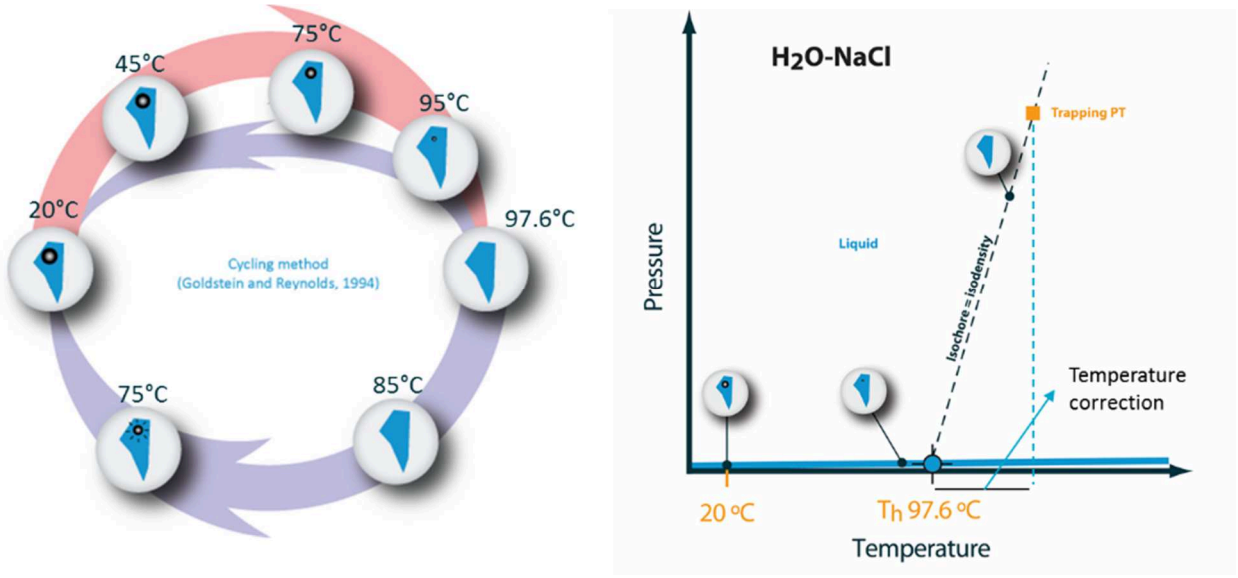


Figure 12 Cycling method for measuring $T_{m\ ice}$ and deriving salinity and homogenisation temperature of water inclusions.

Upon cooling from the T_h to laboratory conditions, a bubble will usually nucleate at several degrees to some tens of degrees below the T_h. This metastable behaviour is well described by Roedder (1984) as due to the ability of water to stretch. There is a critical size of the bubble to nucleate and the absence of the bubble is compensated by the stretching ability of water, creating negative pressure within the inclusion (Figure 13).

When water inclusions are formed at shallow depths, the densities of the trapped fluids are high and the T_h of the water inclusions are low. At room temperature, those inclusions often present a metastable behaviour, they can be observed as only filled by super-stretched liquid water, and typically have no contraction bubble (Figure 14). A bubble may sometimes nucleate by cooling the inclusion. In the absence of a bubble, T_h cannot be recorded. In order to be able to derive a T_h from those inclusions, we used ultrashort laser pulses (Krüger et al., 2007) to stimulate bubble nucleation in the metastable liquid, a precondition for subsequent measurements of the liquid-vapour homogenisation temperature.

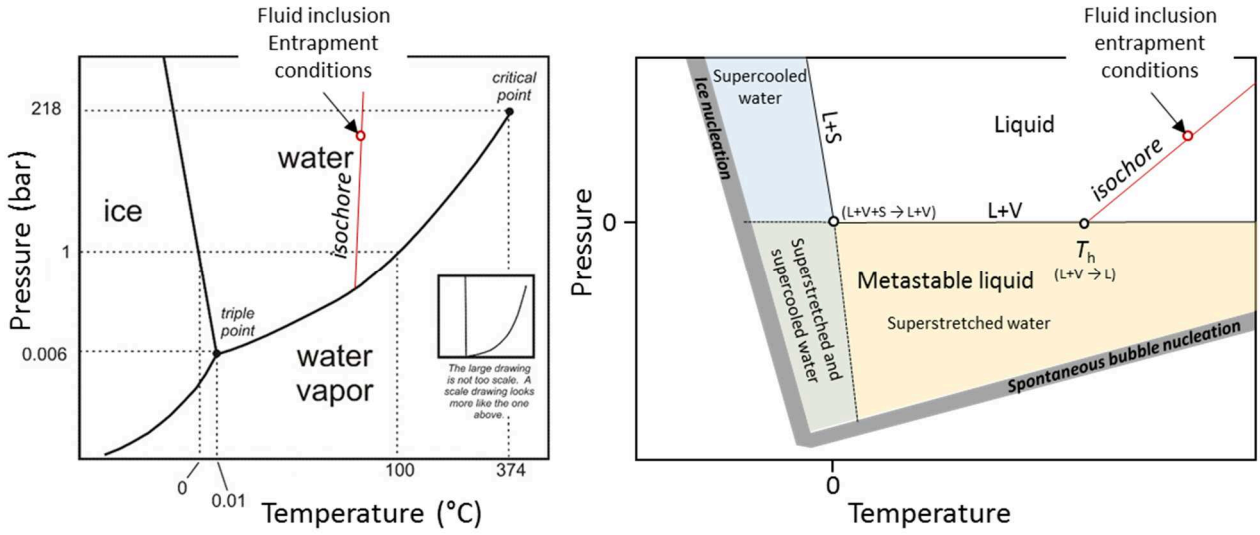


Figure 13 Left: phase diagram of H_2O in pressure-temperature (PT) space. Right: phase diagram of H_2O showing the existence of metastablility state of liquid water (modified from Qiu et al., 2016): (i) the superstretched water domain limited by the spontaneous bubble nucleation and the bubble point curve (liquid-vapour equilibrium); (ii) the supercooled water domain and the ice nucleation. The dotted lines represent the liquid-vapour and liquid-ice equilibrium curves extended into the supercooled and superstretched regions respectively. Liquid–vapour homogenisation (L + V → L), final ice melting (L + V + S → L + V).

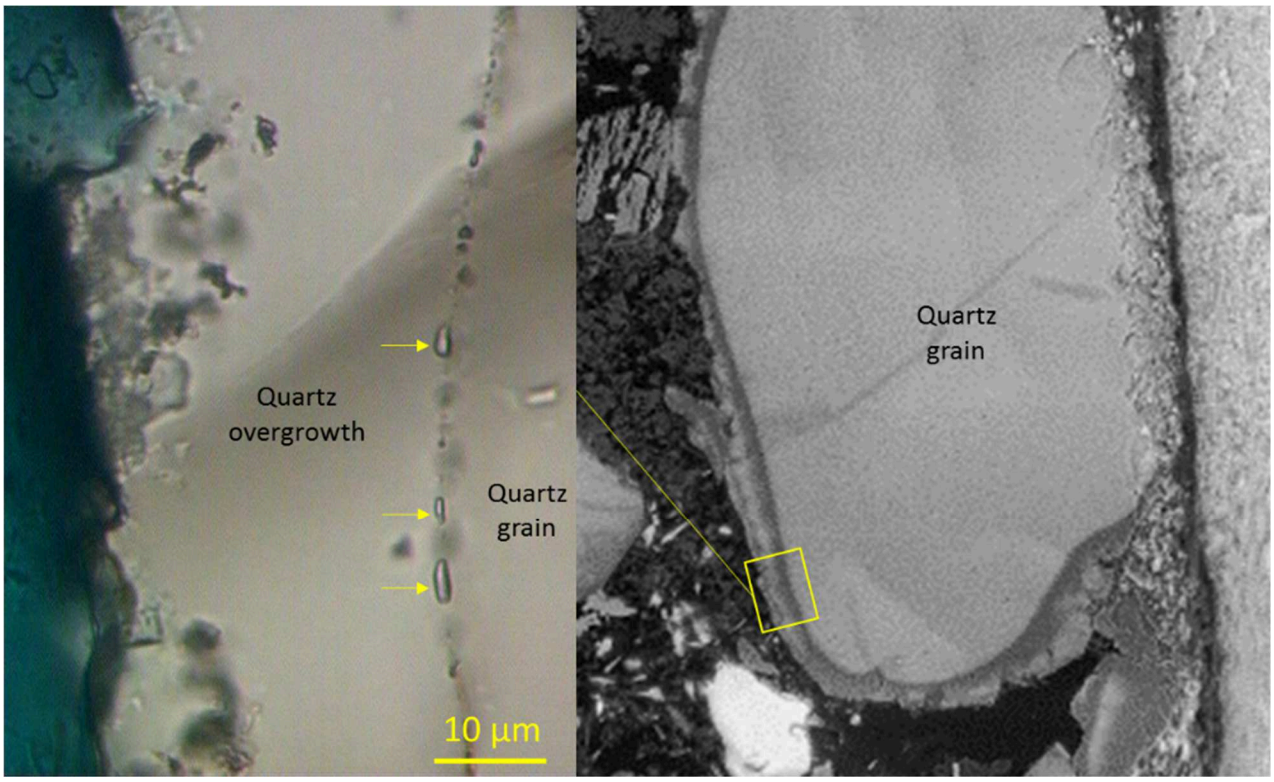


Figure 14 Transmitted light (left) and SEM-cathodoluminescence (right) images showing monophasic water inclusions at the quartz-overgrowth boundary from Harvey 2 at 1347.5 mRT.

Salinities

Due to the metastability issue of the water inclusions, the microthermometry technique for deriving salinity was not providing results. Salinity of water inclusions were measured using Raman spectroscopy (Georgiev et al, 1984; Mernagh & Wilde; 1989; Dubessy et al, 2002; Baumgartner & Bakker, 2009; Sun et al, 2010). Raman spectroscopy offers an alternative and non-destructive method to quantify the salinity of metastable water inclusions that do not provide reliable $T_{m\ ice}$ using microthermometric method. In quartz, the mineral changes the polarization state of the incident laser and of the Raman light (Dubessy et al, 2002; Baumgartner & Bakker, 2009; Sun et al., 2010) and to compensate for this the quartz host mineral must be optimally aligned relative to the polarization state of the laser (Dubessy et al, 2002; Baumgartner & Bakker). On every spectrum, a derivative function was fitted between 3360 and 3460 cm^{-1} to calculate the position (in cm^{-1}) of the maximum Raman spectral intensity (ω_{max}). A first order function was also fitted between 3248 and 3280 cm^{-1} to calculate the intensity value at 3260 cm^{-1} and to derive a ratio (I_{3260}/I_{max}) of the Raman signal intensity at 3260 cm^{-1} compared to the maximum Raman intensity (Figure 15). More details on the calibration are given in Bourdet and Kempton (2014).

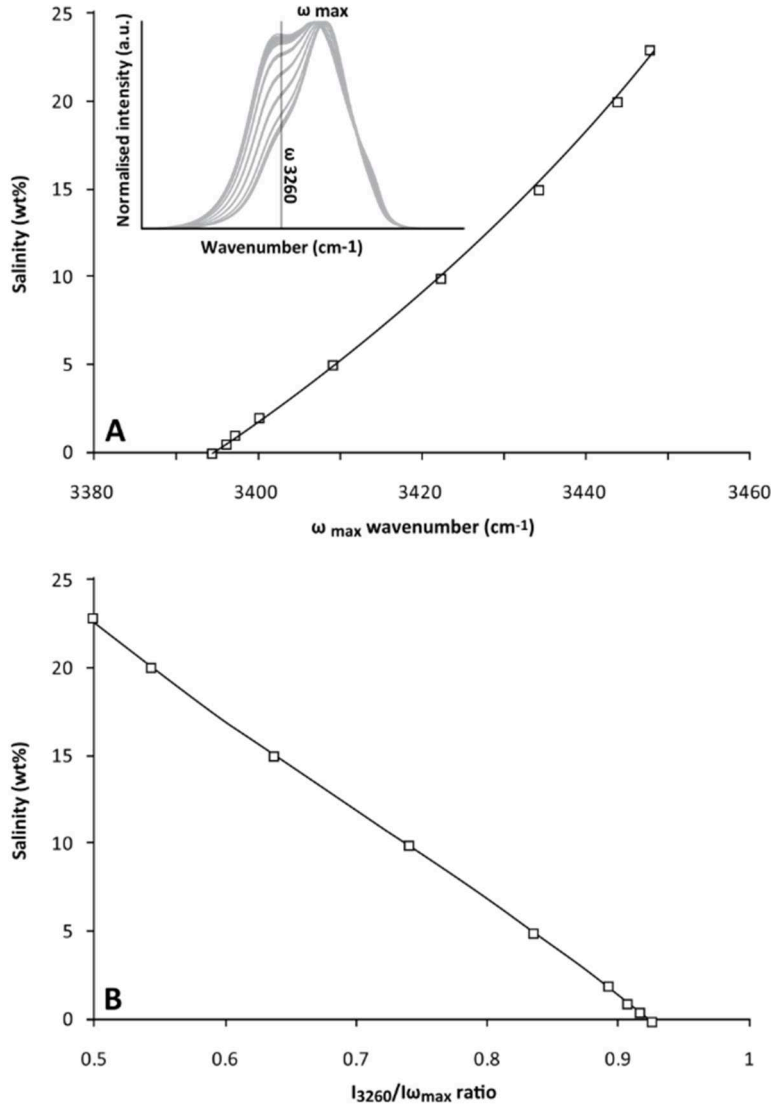


Figure 15 Calibration of saline solutions: (top) wavenumber at the maximum Raman band intensity of water versus the known salinity of the solutions. (bottom) Ratios of the intensity at 3260 cm^{-1} to the maximum Raman band intensity of the solutions (I_{3260}/I_{max}) versus the corresponding salinity.

Sample preparation and equipment

For fluid inclusion analysis, the samples were prepared as double polished 100 µm thick sections glued on a petrographic glass slide using acetone-dissolvable superglue. While still glued on the glass slides, the rock wafers were cut in 5 mm squares using a diamond saw fitted to a Dremel drill. Separation of the double polished sections from the glass was performed by a three hours acetone bath. Each wafer square surface was then carefully cleaned using methanol and optical tissues.

The microthermometry technique is performed using a standard transmitted light petrographic microscope with Linkam MDS600 heating-freezing stage and T95 controller connected to a LNP95 cooling system. The stage was calibrated using final ice melting temperatures of H_2O-NaCl synthetic inclusions in quartz of known salinities at 100 ppm and 30,000 ppm. The precision and accuracy on temperature measurements is ± 0.1°C.

The Raman spectrometer at CSIRO is a Horiba LabRam HR Evolution using a 532 nm single frequency 100 mW diode laser, providing 12 mW at the focus point through a 100X objective. Grating settings were 600 groves/mm for salinity measurements and 1800 groves/mm for gas detection. The signal was collected using a 1024x256 pixels Peltier cooled CCD Synapse detector, sensitive in the 300-1050 nm range.

An amplified femtosecond laser system (Coherent) at University of Bern (Switzerland) was used to stimulate vapour bubble nucleation in the metastable liquid state of the inclusions by means of single ultrashort laser pulses. For a detailed description of the setup we refer to Krüger et al. (2007).

Results

Fluid inclusions were observed in quartz cements showing a liquid water phase containing a small bubble (diphasic L-V) or only a monophasic liquid (L). Fluid inclusions were observed in quartz overgrowths, at the quartz-overgrowths boundary (QOB), within the quartz overgrowth (WQO) or in fractures transecting the overgrowth (FTQO). The quartz grains in sample 1313 m do not present quartz cement overgrowth and only quartz cement in fracture through the grains were observed. The fluid inclusions in this fracture-fill cement are at the quartz grain-fracture boundary (QFB) or within the fracture cement (WFC).

Generally, the salinity values were ranging from below 5000 ppm to 70,000 ppm. The histogram of salinity values (Figure 16) shows two modes:

- between 15,000 and 25,000 ppm;
- between 30,000 and 40,000 ppm.

Values above 35,000 ppm were mostly found in samples in the Yalgorup (at 1313 m in Harvey 3A) or at the interface between the Yalgorup and the top of the Wonnerup (1417.9 m at Harvey 3A and 1245.15 m at Harvey 2). Fluid inclusions in samples from within the Wonnerup generally have salinities below 35,000 ppm.

Overall, the T_h values of the fluid inclusions are between 43.7 and 115°C, with most values below 80°C. Within the 43.5 to 80°C range, shallower samples have lower T_h and deeper samples have higher T_h.
When plotting the salinity against the T_h of the water inclusions, there is a broad trend from high salinities and low temperatures to low salinities and higher temperatures. Three graphs in Figure 17 differentiate three petrographic locations: i) quartz-overgrowth boundary (QOB); ii) within quartz overgrowth (WQO); and iii) along fracture transecting quartz overgrowth (FTQO). These petrographic locations provide some degree of relative time sequence from older to younger QOB<WQO<FTQO. However cements cannot be interpreted as growing on every grain at the same rate, and therefore timing can only be assessed when comparing inclusions in a same grain. When comparing fluid inclusions trapped at those three locations, a shift to lower salinity can be observed. Inclusions with T_h higher than 80°C are mainly found in Harvey 2 and Harvey 3 samples and do not seem to present a strong trend with salinities.

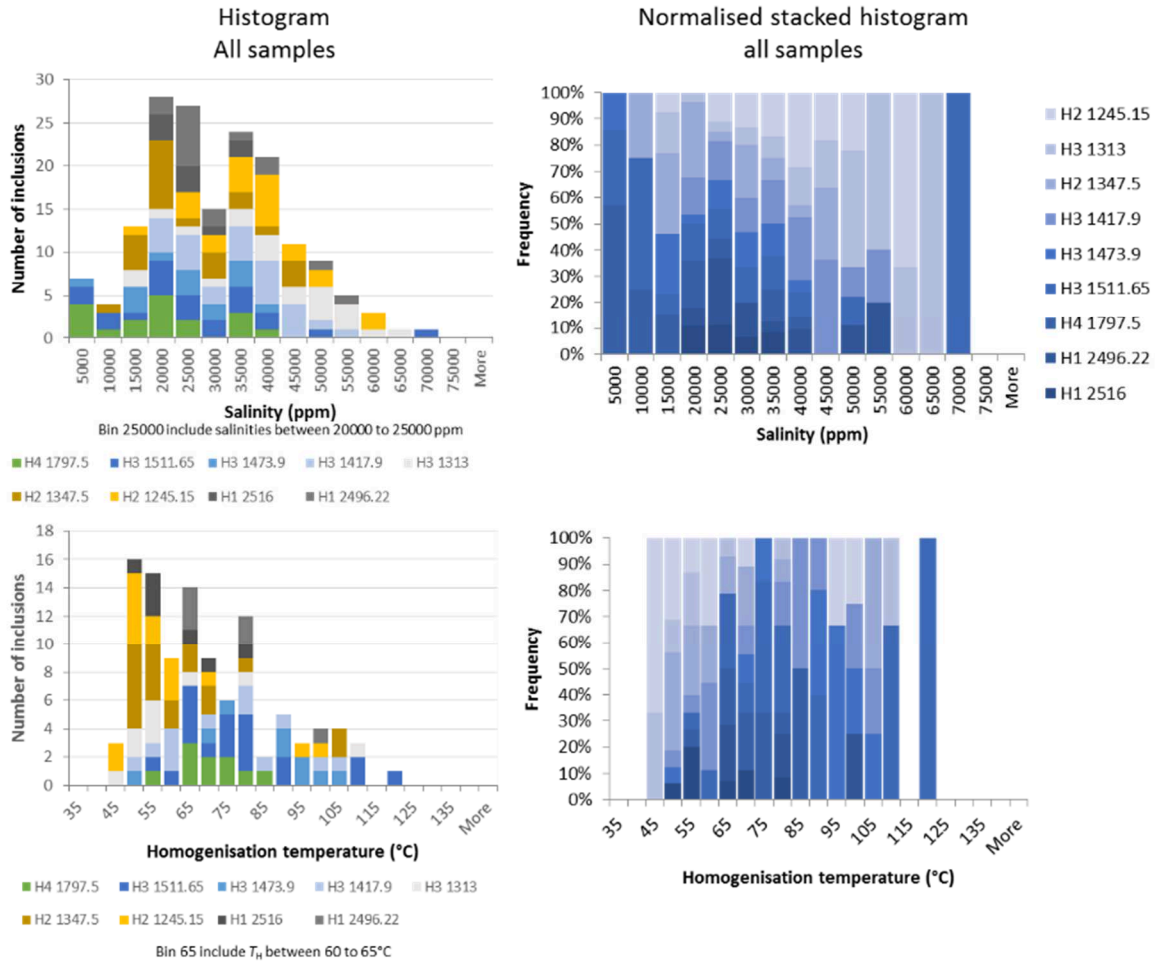


Figure 16 Fluid inclusion salinity and temperature histograms from the quartz cements.

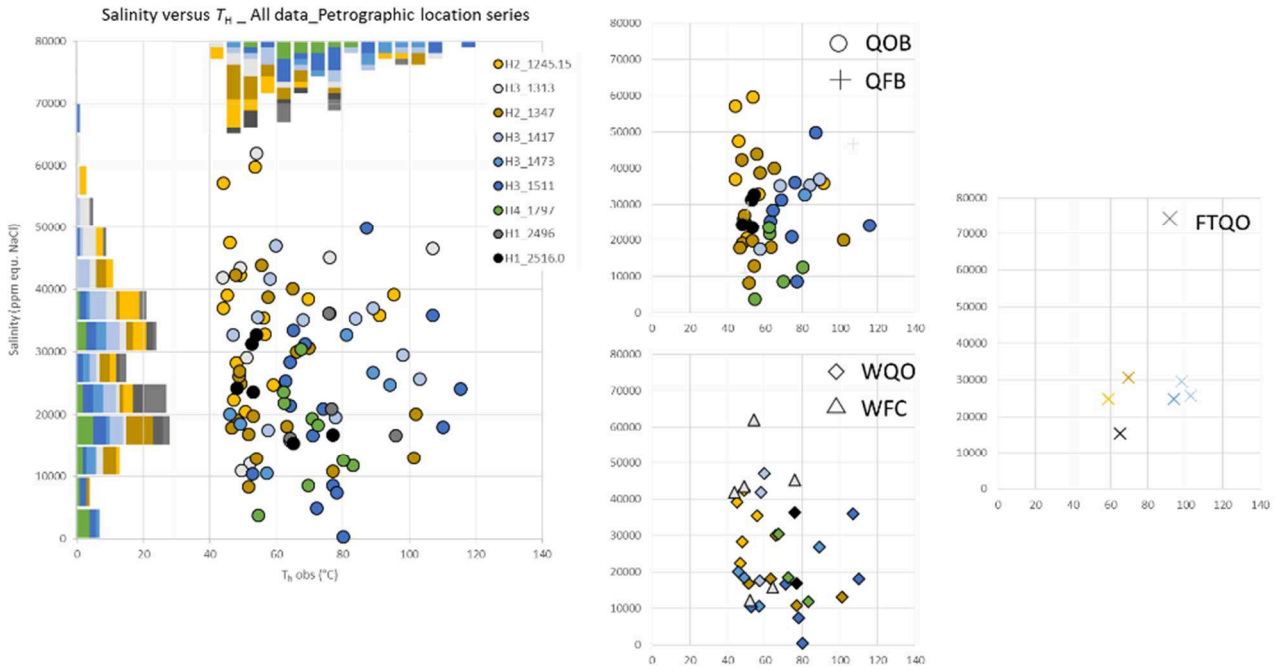


Figure 16 Fluid inclusion salinity versus temperature plots differentiating the petrographic location of the fluid inclusions. QOB: quartz-overgrowth boundary; WQO: within quartz overgrowth; FTQO: along fracture transecting quartz overgrowth; QFB: quartz grain-fracture cement boundary; WFC: Within Fracture cement.

The T_h values are shown as a function of depth in Figure 18, it should be considered that T_h correspond to minimum trapping temperatures and the values need to be corrected to estimate the true trapping temperature. Raman spectroscopy indicated that no dissolved gas such as CH_4, CO_2 or H_2S could be detected in the vapour phase of the water inclusions. Consequently, we calculated the isochores of the water inclusions for the system H_2O-NaCl (Zhang and Frantz, 1987) and, considering the local geothermal gradient based on current *PT* data, we estimate the following temperature corrections:

- For a T_h of 50°C, the temperature correction is 9°C, the true trapping temperature is 59°C;
- For a T_h of 80°C, the temperature correction is about 20°C, the true trapping temperature is 100°C.

As shown in Figure 16 and Figure 18, for a specific current depth the recorded T_h show wide range and the estimated trapping temperatures are lower, equal or higher than the estimated current conditions, based on the assumed geothermal gradient. For each borehole, temperatures and derived pressures conditions can be compatible with early quartz cementation, current day cementation and deeper burial cementation. The samples from Harvey 1 are located at about 1100 m below the top of the Wonnerup Mbr. It can be considered as a good proxy for the deep cementation that took place in the Wonnerup sandstone package. The samples show fluid inclusions T_h at around 60°C, compatible with current day cementation and their salinities are about 16,000 ppm. Fluid inclusions with lower T_h can be interpreted as shallower entrapment, considering a constant geothermal gradient. Those fluid inclusions relate with an early cementation process that took place at around 50 °C and pressure of around 150 bar or a depth equivalent of 1500 m. The salinities of those water inclusions are between 24,000 to 32,000 ppm. Deeper burial conditions relative to the current depth can be interpreted from the fluid inclusions with T_h around 80 °C corresponding to an equivalent pressure of 370 bar or an additional 1200 m compared to the current depth. The salinities of those inclusions range from 17,000 to 32,000 ppm.
In the Harvey 4 sample from 1797.5 mRT, 180 m below the top of the Wonnerup, most of the T_h range from 60°C and 72°C compatible with pressure between 2500 and 3400 m equivalent to an additional 700 to 1600 m of burial. The salinities of those inclusion range from 8,500 to 31,000 ppm with most values around 20,000 ppm. Some inclusions had T_h values exceeding 80°C, associated with salinities of about 12,000ppm. The fluid inclusion with the lowest T_h at 55°C either formed before the deeper burial as an early quartz or after, close to current day conditions. Its salinities is below 5,000 ppm.
The T_h histogram of the samples from Harvey 3 is multimodal. Considering first the deepest sample from Harvey 3 at 1511.65 mRT, about 100 m below the top of the Wonnerup, the fluid inclusions with the lowest T_h at 52.8°C is compatible with current day entrapment. Its salinity is about 10,000 ppm. A significant number of inclusions present T_h values in the range 60-65°C which is compatible with deeper burial of about 1200 m. Their salinities are ranging from 21,000 to 33,000 ppm. A significant number of inclusions present T_h in the range 70-80°C with low salinities (<20,000 ppm).
At Harvey 2 most of the T_h range from 40°C and 60°C compatible with current day temperatures. The salinity range of these inclusions is very wide.
The fluid inclusion data indicate that the sediments of the Lesueur Sandstone in the South West Hub area have been exposed to significantly higher temperatures than they currently are. Some of the temperatures are compatible with burial to maximum depths approximately 1-2 km deeper than the current ones. Such a scenario would increase the current temperatures at depth by around 44 °C assuming the current geothermal gradient in the area (22 °C/km). Some inclusions have their T_h in the range 85-115°C range that would correspond to true trapping temperatures of above 105°C. Considering a temperature of trapping controlled by burial alone, these T_h would require an even deeper additional burial than the 1-2 km. However, an alternative interpretation is that those high temperature inclusions, especially seen at Harvey 2 and Harvey 3, are generated by the mobilisation of deeper fluids during fault movements.

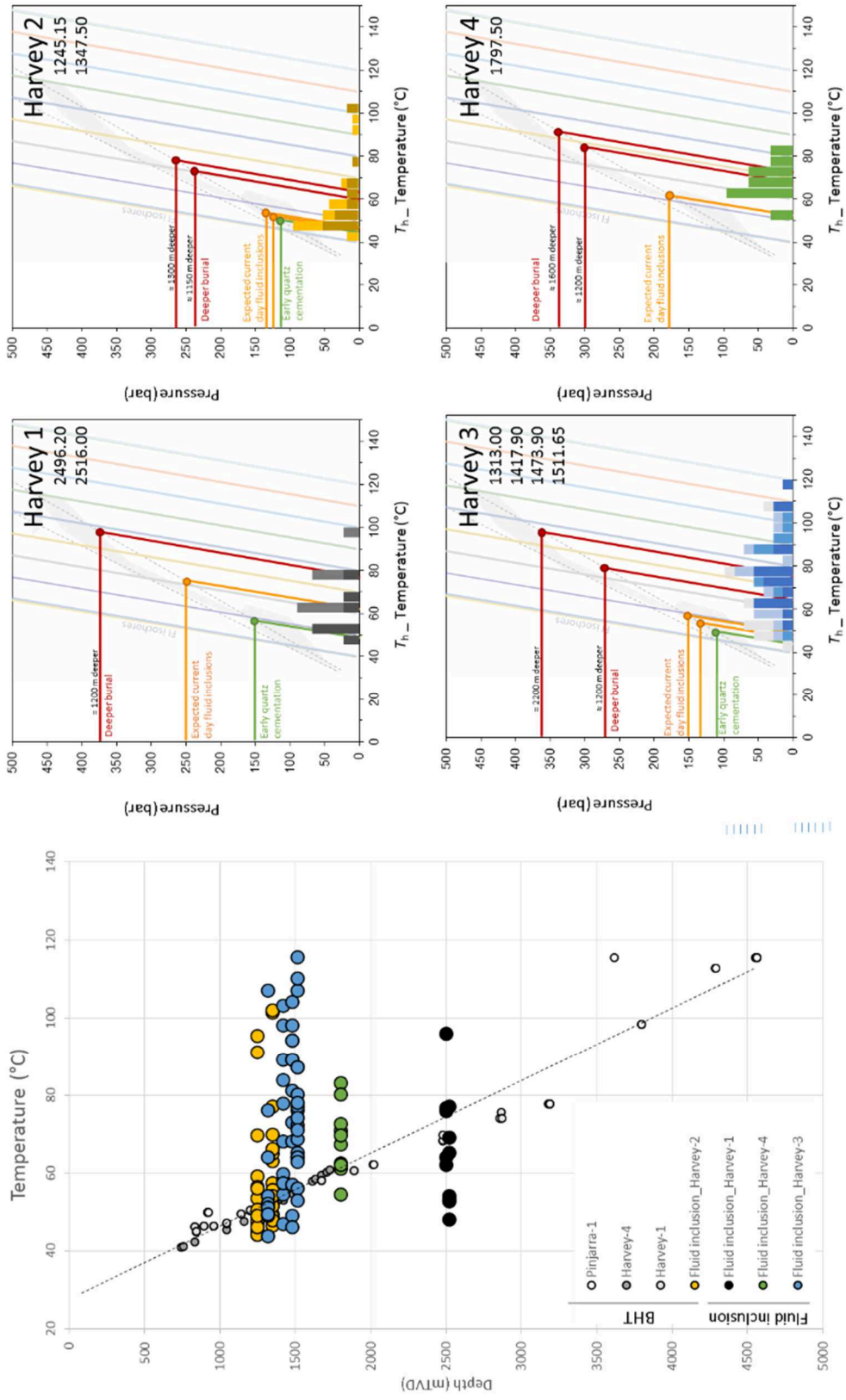


Figure 18 Left: range of T_h values measured via microthermometry analysis of aqueous fluid inclusions in samples from the Harvey boreholes drilled in the South West Hub area. Black lines represent the current local geothermal gradient based on pressure and temperature data measred in different boreholes. Right: Pressure-temperature diagrams presenting the T_h histograms of the water inclusions trapped in quartz cements from the Harvey 1, 3 and 4 samples, theoritical isochores for H_2O-NaCl water inclusions and the local geothermal gradient.

Conclusions

Samples from Harvey 2, 3 and 4 have been used to characterise their microstructure, quantify diagenetic cement phases and infer the diagenetic and burial history of the Triassic sediments in the South West Hub subsurface. Results indicate that the target storage formation of the South West Hub shows a clear pattern of diagenetic alteration involving i) dissolution of detrital K-feldspar and concomitant precipitation of kaolinite in the primary porosity; ii) precipitation of quartz overgrowth on the rims of detrital quartz grains. Quartz overgrowth and pore-filling kaolinite may reduce the permeability by cementing pore throats between neighbouring quartz grains and filling large primary pores with a micro porous kaolinite aggregates with significantly higher tortuosity for the pore fluid. At a high burial temperature (> 120°C) kaolinite illitization progresses in the presence of K-feldspar, and results in further quartz cement precipitation and reduction in permeability (Bjørlykke, 1984; Bjørlykke, 1998). Further densification by pressure solution/chemical compaction is also a major cause of reservoir quality reduction. Quartz cement is the most important pore reducing diagenetic phase in the Wonnerup Member of the Lesueur Sandstone with modal abundance of up to 13% by area, i.e. anomalously high given the relatively shallow depth of the analysed samples (approximately 1.5 km). Quartz cement is comparatively much less abundant in samples from the Yalgorup Member of the Lesueur. Salinities of palaeo-formation fluids trapped in fluid inclusions indicate a consistent range of values between 5000 and 45000 ppm for all samples analysed in the four Harvey boreholes. The spectroscopy method used for deriving those salinities has an error of 5000 ppm that reduces with improving quality of the Raman spectrum. Thus, the range of salinity measured is interpreted to represent a paleo-fluid record rather than to be artificially created by the error of the method. It appears in the fluid inclusion salinity data that high saline brines are absent from the geological record of fluids trapped in quartz cement. The salinities are broadly consistent with connate water from fluvial and marine environments. The data also suggests that in the Wonnerup Member, salinities decrease with depths (e.g. the normalised salinity histogram in Figure 17) and over time (e.g. comparing QOB and WQO data in Figure 17). We can attribute this to the release of fresh water during diagenetic mineralogical changes, such as transformation of smectite to illite or the kaolinite illitisation that are stimulated by increasing temperature. These salinity values can be used to better constrain the values inverted from wireline logs collected in the area (Varma et al. 2009 and Delle Piane et al 2013) and also serve as a comparison to better understand the level of contamination of the water samples collected in Harvey 3 and Harvey 4. With only one sample in the Yalgorup Mbr, there is limited data to conclude on the possible compartmentalisation between the Yalgorup and the Wonnerup Mbrs. Homogenisation temperatures from fluid inclusions together with the anomalously high amount of quartz cement could be interpreted as evidence of an exhumation of the South West Hub area with a magnitude in the order of 1.5-2 km consistent with that estimated from sonic transit time-depth trends across the Perth Basin (Olierook and Timms, 2015). It is inferred that such a scenario could significantly influence the preservation of porosity and permeability at depth in the Lesueur Sandstone. Indeed microstructural investigations confirm that the deepest samples from Harvey 1 and Pinjarra 1 have witnessed a more intense diagenetic alteration than the shallower ones as indicated by a higher amount of quartz overgrowth and the presence of illite substituting kaolinite as a pore occluding clay. Laboratory measurements of porosity and permeability also concur in showing significantly reduced reservoir quality as a function of depth (see also results presented as part of the ongoing ANLEC supported project 7-1215-0263 “Influence of heterogeneity and diagenesis on injectivity and containment in the Wonnerup Member”).

In summary, the target storage formation of the South West Hub shows a clear pattern of diagenetic alteration leading to a reduction of pore space. Microstructural observations indicate that this diagenetic pattern is repeated in samples from the available core material from the 4 Harvey boreholes. We interpret this as evidence that the Wonnerup Member of the Lesueur Sandstone underwent a similar degree of alteration at the 4 borehole locations before these were affected by faulting and tectonic movement. It is further observed that severe reservoir quality degradation by extensive pressure solution and kaolinite illitization is only observed in the deepest sections of the Wonnerup, although the observation of such sections is limited to Harvey 1 and Pinjarra 1.

2B: Fault analysis

Claudio Delle Piane[1]

[1]CSIRO Energy

Introduction

Despite the significant implications of fault zones for hydrocarbon and geothermal exploration, groundwater management and CO_2 storage, the available literature on their structure, deformation mechanisms, and effects on permeability in the Perth Basin is extremely scarce (Olierook et al., 2014b). Due to the lack of outcrops, knowledge of fault distribution, geometry and timing is based on geophysical methods. However, resolution of faulting in the onshore central and southern Perth Basin is hampered by the poor-quality of the available seismic data and scarce stratigraphic constraints. As a consequence, only major faults are resolved, with poor constraints on their activity, re-activation potential and importance for basin compartmentalisation (Iasky et al. 1991; Iasky 1993). Fault patterns are intricate as a result of the Permo-Cretaceous rifting of Greater India and Australia that led to a transtensional rift setting with a complex history of faulting and syn-sedimentary fault block movement which eventually made up the Perth Basin (Harris, 1994; Song and Cawood, 2000).

The South West Hub area

In the context of the South West Hub Area, a geological and structural framework was constructed by Langhi et al. (2013) for the geometries of major faults and stratigraphic units, based on the interpretation of the available seismic data. From the structural point of view, the South West Hub area is located at the southern end of the Mandurah Terrace, east of the off-shore Vlaming Sub-basin (Figure 19A). At a regional scale, the area is bounded by the N–S trending Darling fault to the east and by the Badaminna fault and Harvey Ridge to the west and southwest, respectively. The analysis of Langhi et al. (2013) indicates that the fault population is characterised by a series of mainly WNW-, NW- and NNW-trending small faults (F2, F4, F5, F6, F11–F15) bounded by two larger faults (the N–S to NNW-trending F1 and NW to NNW trending F10) (Figure 19B). Harvey 1 is located between the F5 and F9 faults, both ENE dipping. Harvey 2 well is located to the west of the surface expression of the W dipping F10 fault (i.e. one of the two larger faults in the area). Harvey 3 and Harvey 4 are located in the southern part of the South West Hub area covered by seismic and are in close proximity (< 1 km) to numerous faults (Figure 19B).

Fault borehole intersections

The available seismic data indicate that Harvey 2 and Harvey 4 intersected faults at depth. Both CSIRO's and Odin Reservoir Consultants' interpretations place the intersection of the F10 fault and Harvey 2 at an estimated depth ranging between 350 – 800 m. Best estimates indicate potentially up to 900 m of normal displacement along this major NNW-SSE striking structure (Figure 20A). Interpretation of seismic profiles indicate that Harvey 4 also intersected normal faults at depths corresponding to the Eneabba Formation and the Yalgorup Member of the Lesueur Sandstone (Figure 20B and 20C). It should be noted that these are relatively minor faults with sizes close to the spatial resolution of the available seismic data, consequently there are discrepancies between CSIRO's and ODIN's interpretation of their geometries around Harvey 4.

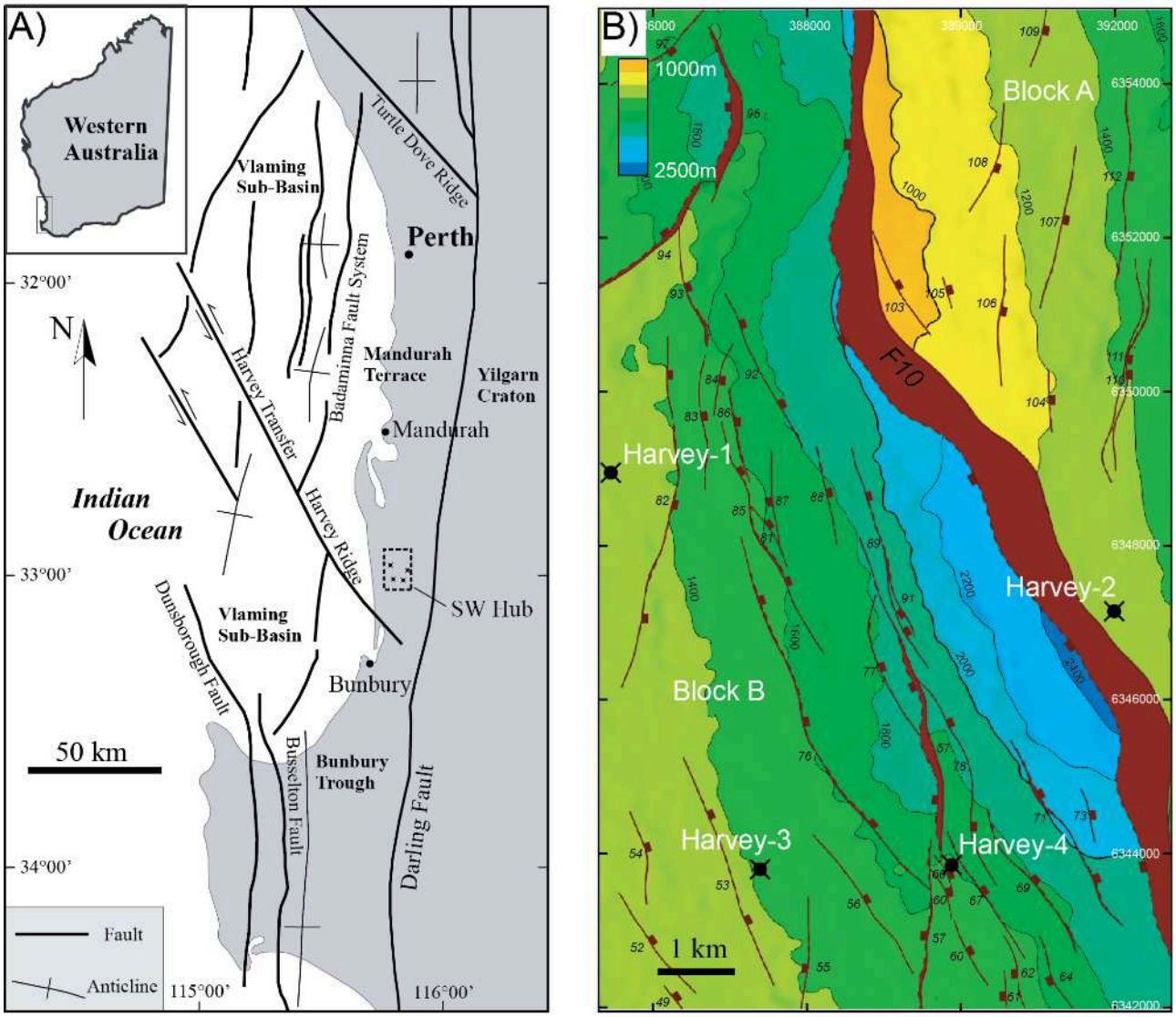


Figure 19 (A) Regional geological map showing the location and structural outline of the South Perth Basin and location of the South West Hub (SW Hub), after Langhi et al. (2013). (B) Structural map of the SW Hub area showing fault traces and dip directions for the area in the dashed line box in (A). Image is a representation of the Top Wonnerup reflector as interpreted from seismic. Fault traces are shown as red segments, dip angle is marked next to each fault trace (after Pevzner et al. 2015).

The well completion report from Harvey 2 also mentions the intersection of faults or fault zones: in particular a fault was identified in the retrieved core by the on-site geologist at 508 m, additionally an unstable zone at depth of 615.1m was interpreted as due to intersection with a potential fault zone that had to be stabilised by pumping 180 litres of cement (Russell and Pollock, 2015). Harvey 2 was fully cored and several examinations of the retrieved material allowed the identification of fault related structures. The Detailed Lithological Log provided by ROCKWATER Pty Ltd Consultant Hydrogeologists to the Department of Mines and Petroleum mentions a number of small faults occurring at various depths and lithologies in Harvey 2: namely, small faults are identified at 507.70, 674.5, 877.6 and 1333.75 m of depth in sandstones; a complex fault zone with displaced bedding in conglomerate was observed at depth 772.95 – 773.70 m and a shear zone with slickensides in a well consolidated mudstone at 808.8 – 811.35 m.

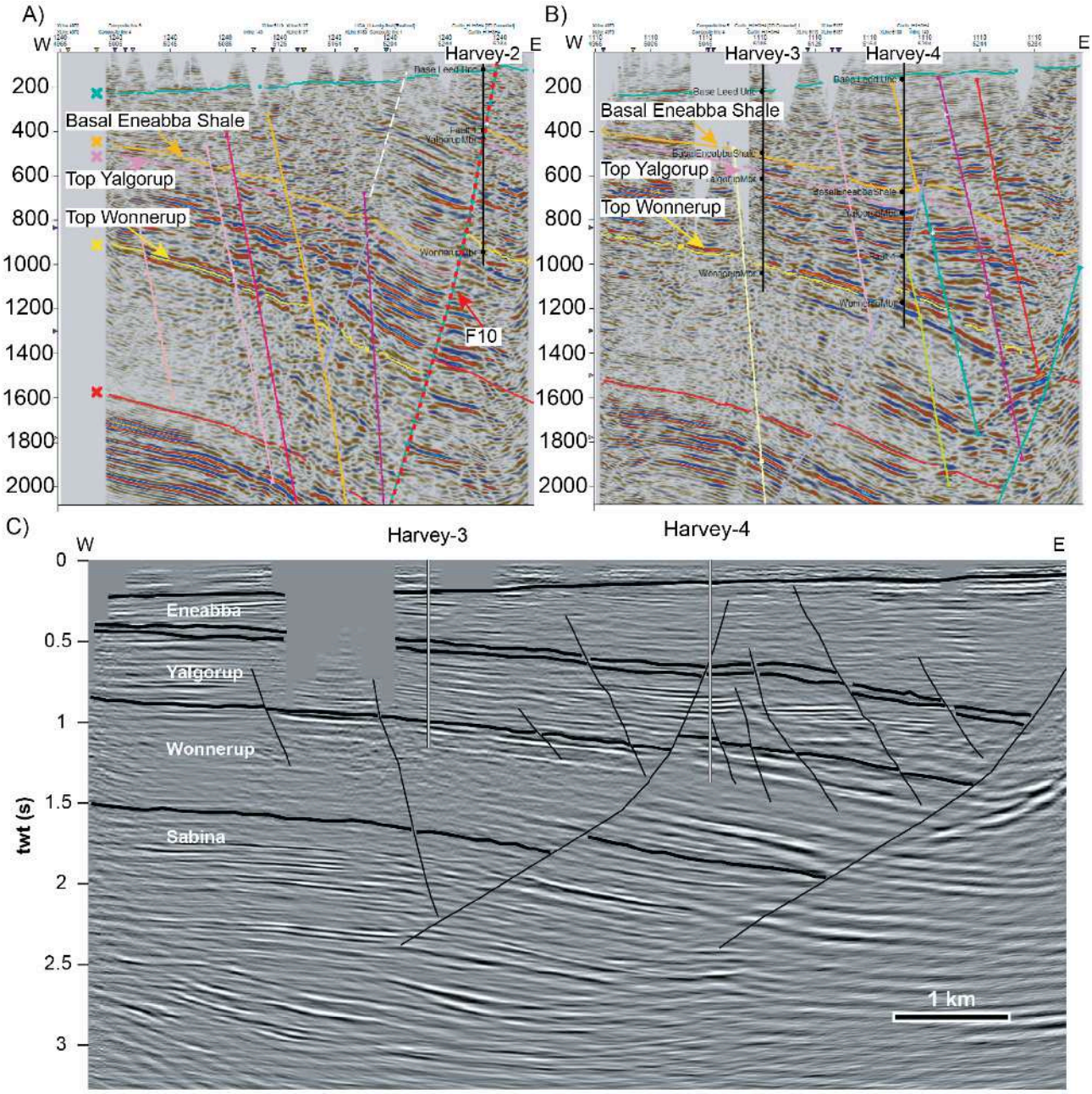


Figure 20 E-W seismic profiles in the South West Hub area higlighing interpreted faults and their intersections with boreholes. A) Seismic profile showing intersection between the F10 fault and Harvey 2 at depth of approximately 430 m. B) Seismic profile showing intersections between Harvey 4 and an E dipping fault and a W dipping fault at depths of approximately 400 and 1000 m, respectively. Interpretation of A and B is from ODIN Reservoir Consultants. C) Cross line showing intersection between Harvey 4 and a W-dipping fault just above the top of the Basal Eneabba Shale, and an E-dipping fault in the Yalgorup. Line 1111 from 3D Curtin PSTM processing, courtesy of Laurent Langhi.

Additional fault related features recognised on cores from Harvey 2 include: slickensides on minor fault planes in well compacted mudstone (Figure 21A); incohesive breccia zones (Figure 21B); and cataclastic bands in sandstones (Figure 21C). Furthermore, the entire cored section of Harvey 2 was scanned using the HyLogger technology by the Geological Survey of Western Australia (GSWA) to retrieve hyperspectral data for mineralogical analysis. The results presented to the South West Hub research community indicated an anomalous high water content and relatively high a-spectral response between 421 and 857 m that was tentatively explained as the due to the intersection with the F10 fault (Hancock and Sando, 2015). This depth

interval roughly corresponds to one in which the fault related structures described above are identified on cores.

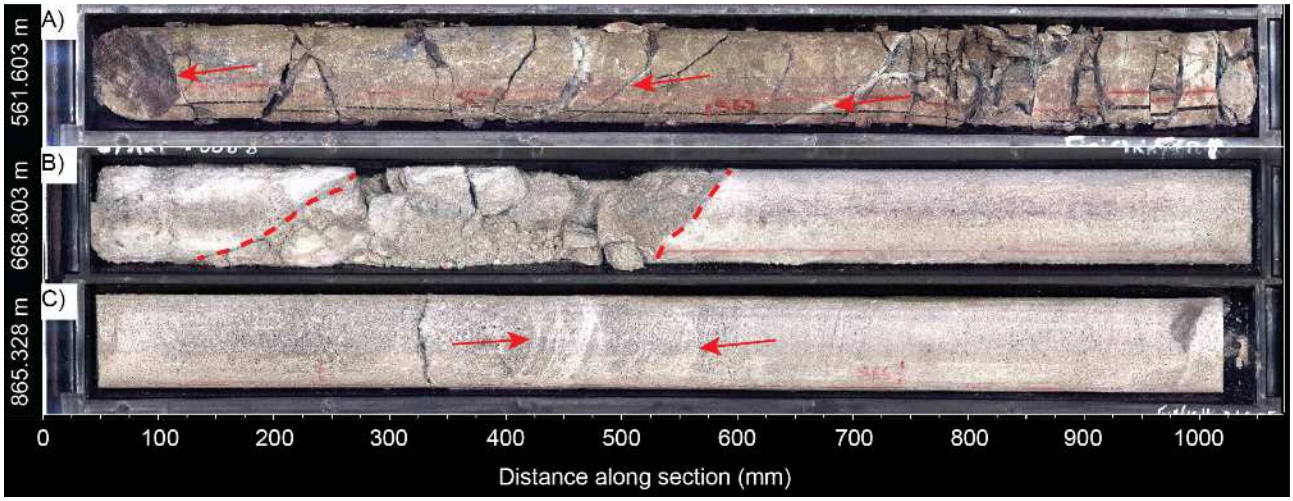


Figure 21 Examples of structures observed in cores affected by the F10 fault in Harvey 2, all cores are within the Yalgorup Member of the Lesueur Sandstone. A) Red arrows indicate minor fault surfaces with slickensides in a well consolidated mudstone interval. B) Approximately 40 cm thick incohesive breccia (bound by red dashed lines) in a sandstone interval. C) Approximately 15 cm thick cluster of cataclastic deformation bands (bound by the two opposing red arrows) in a lithified sandstone.

In summary, the F10 fault is observed in cores as a thick zone of diffuse deformation rather than a well-defined, discrete slip surface. When corrected for its dip, the fault zone is constituted of variably damaged material with a cumulative width of approximately 70 m. While individual structures in this zone are below seismic resolution, their collective thickness defines the seismically visible trace of the interpreted F10 fault. Additional observations on the structure of the F10 fault are being collected as part of ANLEC project 7-1215-0261 “Potential for preferential flow through faults and fractures”.

Sub-seismic structures in the South West Hub area

A conventional conceptual model for fault zone structure envisages the presence of a “core zone” accommodating most of the displacement along one or more slip surfaces, surrounded by a distributed “damage zone” characterised by fractures and subsidiary faults (e.g. Faulkner et al., 2010). Damage zones are considered as relict ‘process zones’ – where deformation occurs ahead of the advancing fault tip and accommodate considerably less strain than the principal displacement surfaces (Kim et al., 2004). The development of different structures within damage zones is influenced by the environmental conditions at the time of deformation and the mechanical properties of the host rock. Characterization of structures within damage zones can give information about i) fault propagation and growth and ii) structural modification of fluid flow properties in porous reservoirs (e.g. Kim et al., 2004; Odling et al., 2004; Johansen et al., 2005; Olierook et al., 2014b).

Here we studied samples from boreholes drilled in the South West Hub Area, focussing on the cores extracted from Harvey 2, 3 and 4. In particular, we identified cataclastic structures typically ascribed to the damage zones of faults occurring in porous sandstones. The studied rocks are affected by single or clustered mm- to cm-thick deformation bands (DBs). Deformation bands are common structures in deformed porous rocks (siliciclastics and carbonates) in which pores collapse and sand grains fracture, they have been described as small, roughly planar fault-like features that appear as thin bands with lengths ranging from a few centimetres to a few tens of meters (Aydin, 1978; Aydin and Johnson, 1978). DBs are generally thicker and show smaller offsets than slip surfaces of comparable length. Also, whereas cohesion is lost or reduced across fractures, most deformation bands maintain or even increase cohesion with respect to the host rock.

Furthermore, deformation bands often exhibit a reduction in porosity and permeability, whereas both slip surfaces and tension fractures are typically associated with dilation and permeability increase. Deformation bands may play an important role in determining the flow behaviour of faulted reservoirs and aquifers in situations where sandstone is faulted against sandstone potentially leading to compartmentalization and fault sealing (e.g. Pittman 1981; Hardmann & Booth 1991). As stated by Fossen et al. (2007): "Petroleum geologists and hydrogeologists (should) look for DBs in cores from clastic reservoirs and aquifers because of their potential role as barriers or baffles to fluid flow and because they commonly indicate proximity to a larger offset fault".

Several deformation bands have been identified within the Lesueur Sandstone in cores from the South West Hub area (Figure 22). DBs are identified as high relief, near planar features oriented at small angle to the core axis cutting through sedimentary bedding. Each band is about 3 - 10 mm thick (Figure 22B and 22C) and accommodates a small offset on the order of a few mm generally with normal kinematic (Figure 22D).

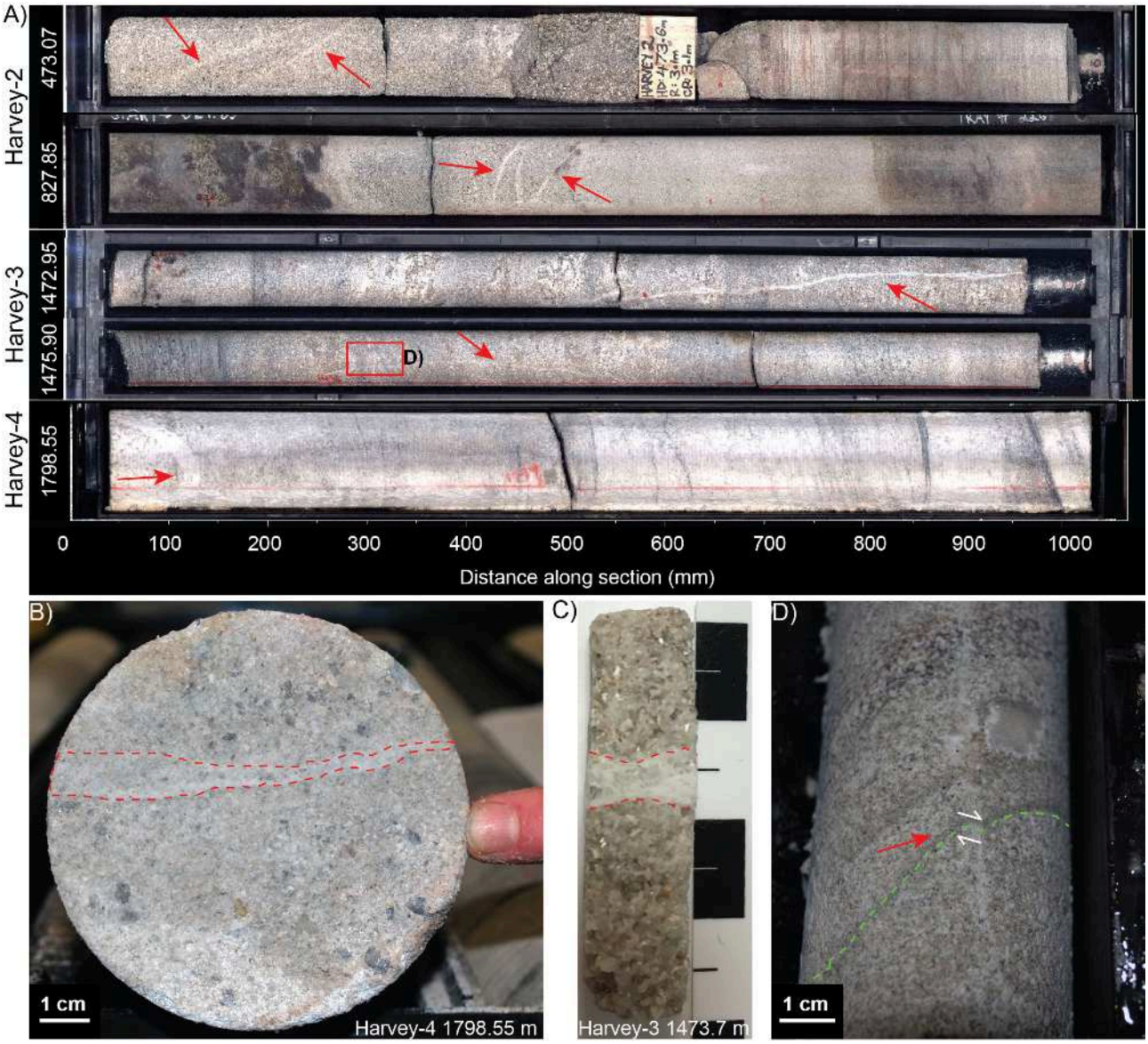


Figure 22 A) Deformation bands identified in cores from Harvey 2, 3 and 4 highlighted by red arrows. B) DB visible within the dashed lines. C) Offcut of a sample used for thin section preparation. D) DB crossing through and slightly offsetting a sedimentary bed (green dashed line), the point of intersection is indicated by the red arrow.

Samples from selected cores were used for thin section preparation and microstructural analysis (Table 3) conducted using optical and electron microscopy. The analysis aimed at i) assessing the microstructural features of DBs and identify kinematic indicators; ii) estimating DB thickness; iii) assessing the relative timing

between diagenetic quartz cementation and formation of DBs; and iv) evaluating the contrast in petrophysical properties between host rocks and DBs.

Borehole	Depth (m)	Band thickness (mm)
Harvey 2	856.3	8 ± 1.7
	865.7	8.3 ± 1.5
Harvey 3a	1470.86	5.3 ± 2.5
	1473.7	3 ± 1
	1476.3	2.7 ± 0.6
	1476.45	2.7 ± 2.1
	1470.96	2 ± 1
Harvey 4	1798.3	20.3 ± 2.9
	1798.6	9 ± 1.73
	1798.55	8 ± 2.7

Table 3 List of samples with deformation bands used for microstructural analysis and their estimated thickness.

Results

The thickness of the bands ranges between 3 - 20 mm (Table 3), displacement is difficult to quantify as the analysed samples seldom show clear markers. The porosity loss in the analysed DBs is usually very pronounced as is the grain size reduction with respect to the undeformed host rock (Figure 23A, 23B and 23C). Together with grain crushing and pore collapse, shear deformation is also visible in the cataclastic zone as evidenced by numerous spectacular kinematic indicators such as offset K-feldspar grains (see inset in Figure 23B). The studied structures can be classified as shear enhanced compaction bands (see classification by Fossen et al., 2007) owing to the co-existence of compaction and shear deformation in all the analysed samples. This classification has implications in terms of deformation mechanisms as well as porosity and permeability reduction due to the amount of cataclasis involved. Cataclasis typically generates a mechanically strong (ultra) cataclastic layer of rock through microscale deformation mechanisms such as pore collapse, grain crushing, frictional grain sliding and rotation. The intense grain crushing indicates deformation under high effective stress conditions. The fact that fragments of quartz overgrowths are sheared in the cataclastic zones of the studied DBs (Figure 23D), implies that their formation postdates the precipitation of diagenetic quartz cement and that the DBs formed at an advanced stage of burial and are possibly linked to the development of the major structural features in the Basin associated with the break up.

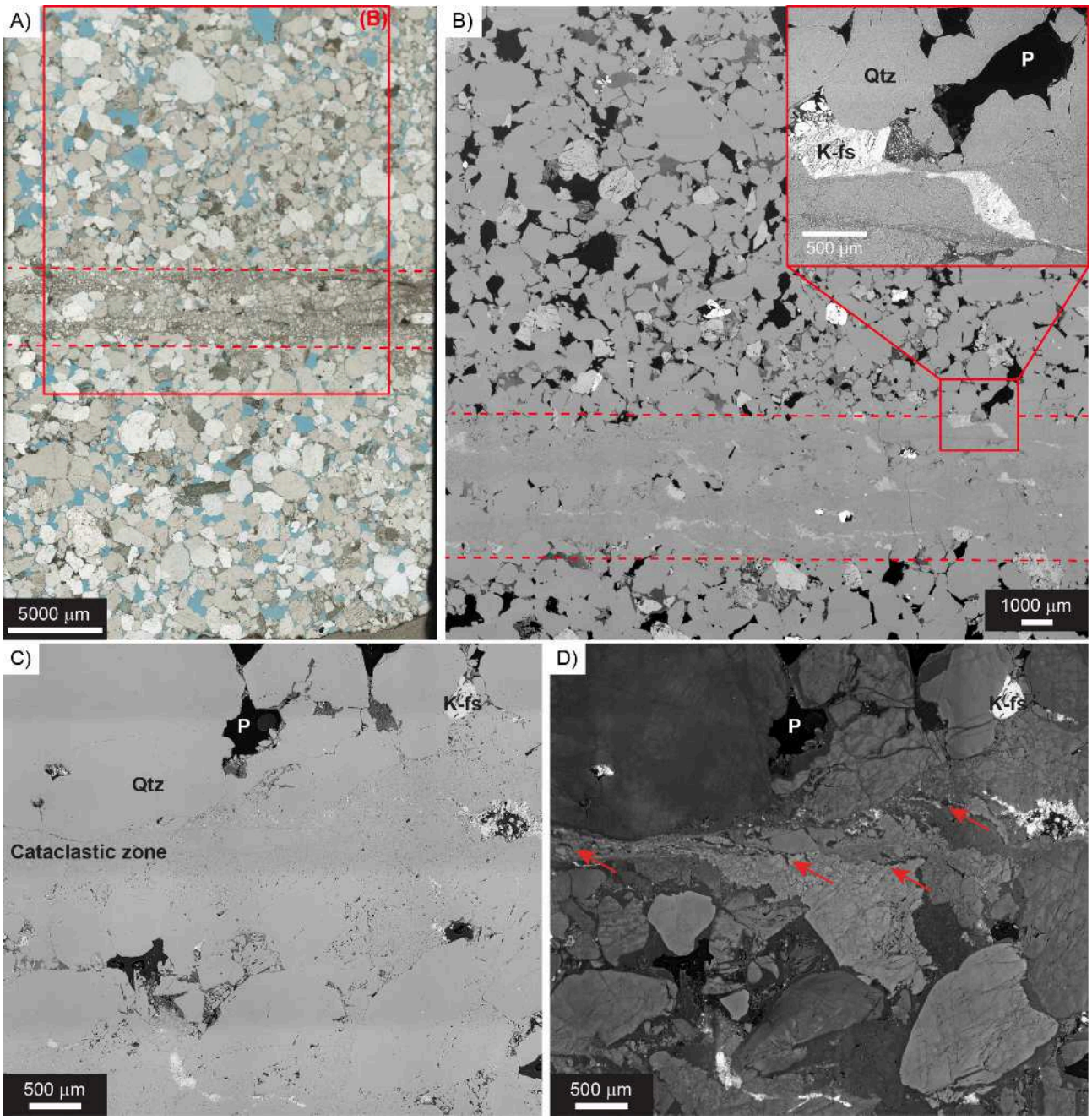


Figure 23 Microstructural characteristics of deformation bands in the South West Hub area. A) Plane polarised transmitted light image of a blue resin impregnated sample. Porosity appears in blue, deformation bands is delimited by the red dashed lines, note the intense grain size and porosity reduction within the deformation band with respect to the surrounding host rock, sample from Harvey 3 (1347.7 m). B) SEM image of the red box in (A), dashed lines bound the deformation band. Pores are black, mineral grains are shown in different levels of grey as clay, quartz, K-feldspar, Ti-oxides (from dark to light). Inset shows a fractured and offset K-feldspar grain indicating shear kinematic along the band. Note the intense grain size and porosity reduction within the deformation band with respect to the surrounding host rock. C) SEM image of deformation band showing strongly comminuted quartz and feldspar grains in a thin cataclastic zone of strongly reduced porosity and pore size (porosity is in black). D) Cathodoluminescence image of the same area shown in C) showing shearing of the grains and entrapment of diagenetic quartz overgrowths, visible as dark, elongated fragments aligned along the transport direction (red arrows).

Effects of DBs on fluid flow

Analysis of outcrop analogues indicates that compaction and reduction in porosity typical of shear enhanced compaction bands lead to a contrast in porosity, pore connectivity and consequently permeability, with the host rock the latter can amount to up to several orders of magnitude (Ballas et al. 2015). The internal porosity and permeability structure of deformation bands is difficult to assess experimentally due to their thin nature hindering the preparation of suitable samples for laboratory testing. While an in-depth characterization is beyond the scope of this project, an attempt was made to visually estimate porosity and pore size in a deformation band and host rock sample from Harvey 3. A portion of the rock containing a 3 mm thick deformation band and the surrounding host rock was cut into a polished petrographic thin section and imaged using SEM in backscattered electron mode where contrast in grey levels in the resulting images originates from contrasts in the atomic numbers of the materials analysed. Thus porosity appears as black while the various mineral phases appear in different shades of grey, with lighter and darker shades representing heavier and lighter phases, respectively. Image analysis was then used to transform the SEM images into binary format by using an appropriate threshold; the binary image shows porosity in black and mineral phases in white. Total porosity is calculated as the area % of the image occupied by the pore space, while pore size is estimated as the average value of the analysed pore population and expressed as equivalent circular diameter, i.e. the diameter of a circle having the same area as the pore. The results of this approach are shown in Figure 24 showing the original SEM and binary images of the host rock and deformation band side by side.

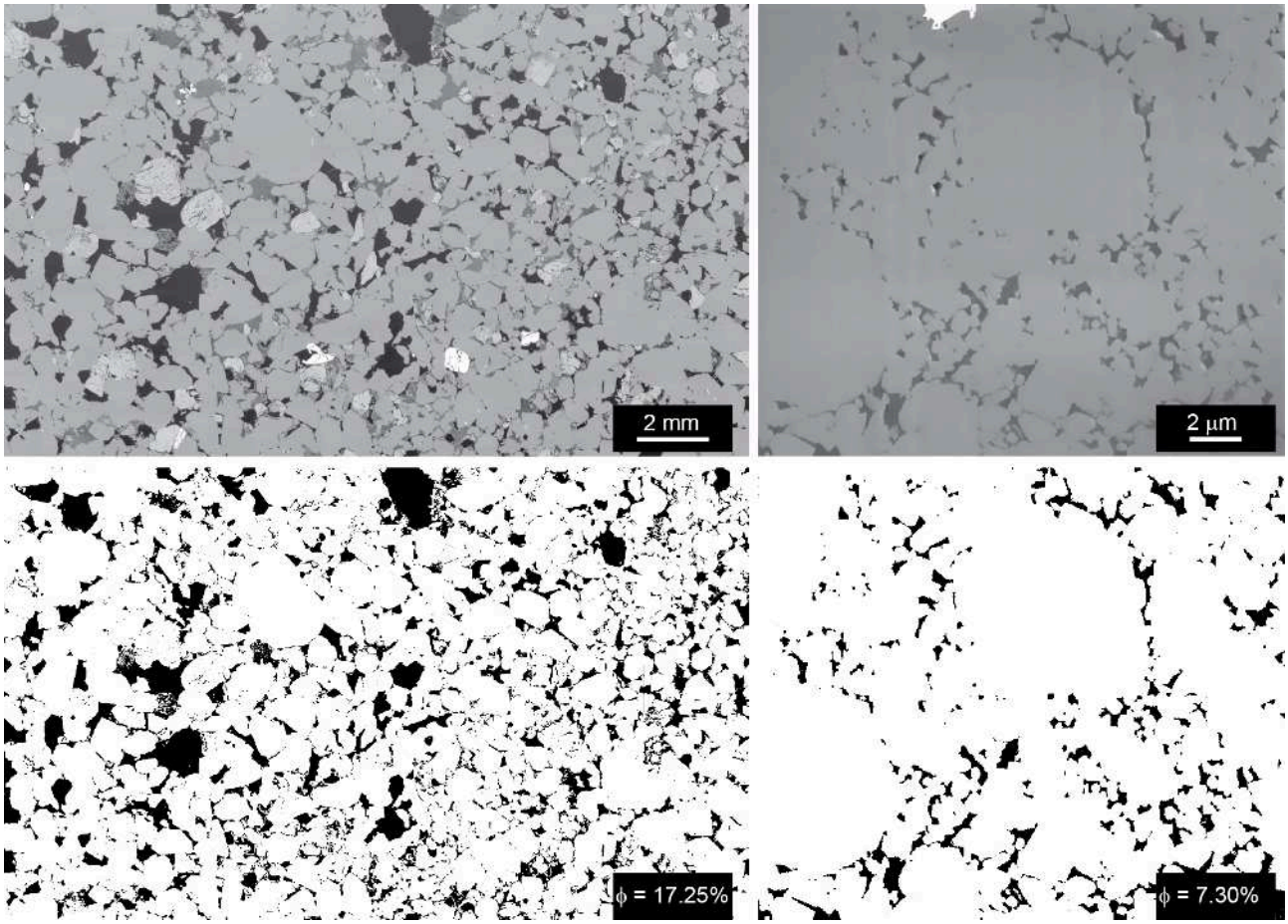


Figure 24 SEM images used to quantify porosity and average pore size in the host rock (left) and deformation band (right). Top row shows the original SEM images, note the difference in scale between the two visualizations. Bottom row shows the resulting binary images with pores in black and mineral phases in white. Sample from Harvey 3, depth 1473.7 m.

2D image analysis returns a porosity of 17.25 % and 7.30 % for the host rock and deformation band, respectively. Importantly, the average pore size diameter is quantified as 114.45 microns host rock and 0.37 microns for the deformation band based on populations of 3504 and 356 pores, respectively. This severe reduction of porosity and pore size distribution is likely to affect fluid movement in-situ in proximity of the deformation bands. A qualitative assessment of the effect of DBs on fluid movement can be inferred by visualising the intruded blue dyed resin in the blocks used for thin section preparation: systematically, DBs act as barriers to the intrusion of the resin (Figure 25).

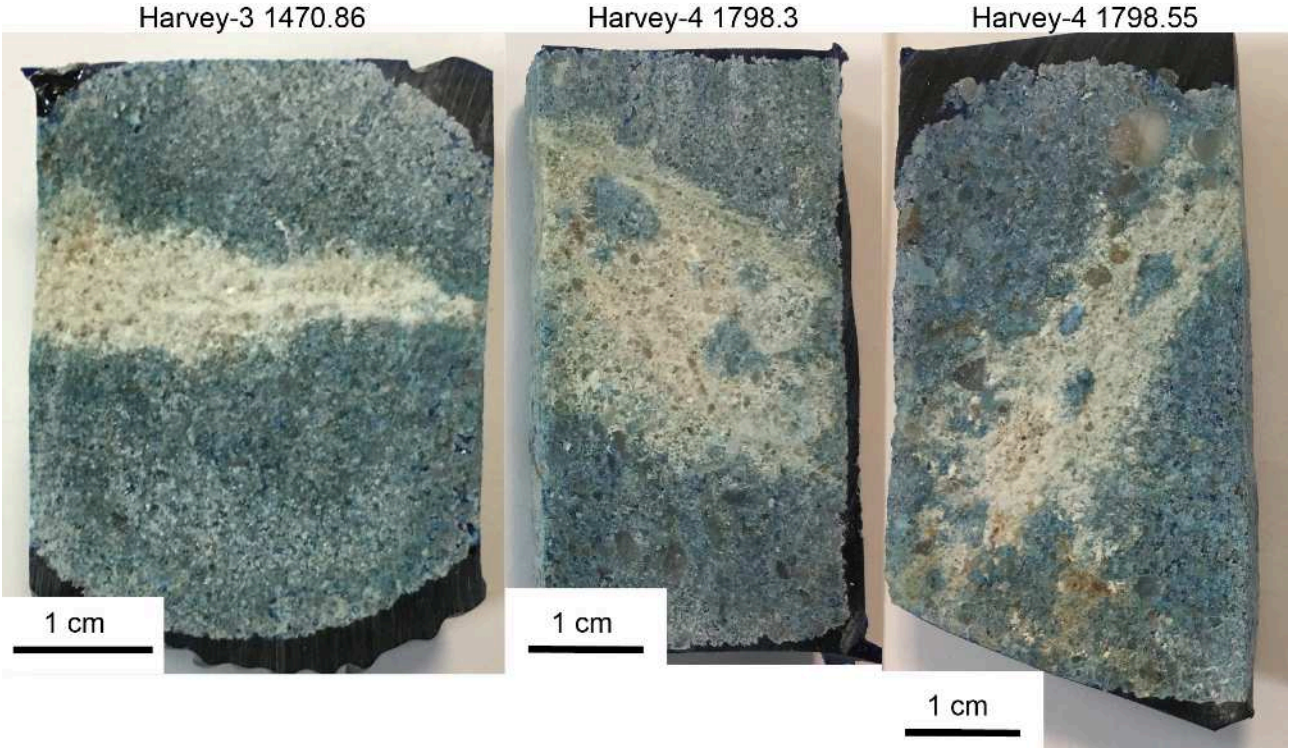


Figure 25 Photographs of blocks used for thin section preparation. The porous rock fragments are impregnated with low viscosity blue dyed resin before cutting. It can be seen that resin did not permeate the whole sample volume due to the presence of cataclastic deformation bands.

Having established the presence DBs in cores from the Harvey boreholes and their potential effects of on fluid flow in the subsurface, it is of interest to estimate their likely extent and density so that this information could be fed into an updated geological model of the South West Hub Area to make a first order prediction on the occurrence and influence of these sub-seismic scale features in proximity of the available boreholes. In the following we use the estimated thickness and displacement of the observed DB to estimate the length and linear density per km based on scaling relationships reported in the literature.

Displacement of DBs (*D*) can be estimated from their thickness (*T*) based on the relationship proposed by Soliva et al. (2013) for deformation bands with normal kinematic as:

$$\boldsymbol{D = 0.75 \cdot T^{0.69}} \qquad \textbf{Equation 1}$$

Based on the thickness values reported in Table 3, the estimated displacement ranges between 1.2 and 6 mm in agreement with the limited observable D measured on cores in the order of 3 mm (see for example Figure 23B). These values can further be used to estimate the length (*L*) of individual DBs using the following scaling relationship from Schultz et al. (2008):

$$D = 0.001 \cdot L^{0.5}$$ Equation 2

The expected length distribution ranges between 1.5 and 36 m. Finally, as commonly done in reservoir modeling of oil fields throughout the world (Childs et al., 1990; Gauthier and Lake, 1993), DBs frequency is estimated from the power-law correlation between displacement (*D*) and fault frequency (*N*) expressed as number of DBs per km

$$N = aD^{-x}$$ Equation 3

The variable *a* is a constant and the exponent *x* is often referred to as the fractal dimension and has value of 0.67436 (e.g. Fossen et al., 2000). Based on the values reported above a density between 31 and 93 DB/km is expected in the proximity of the boreholes in the South West Hub area. Such densities are commonly observed in exhumed reservoir analogs where deformation bands commonly occur in arrays comprising many (10–100 s) sub-parallel and closely-spaced (<70 mm) bands (Figure 26A) and their frequency generally decreases with distance from a major fault (Figure 26B).

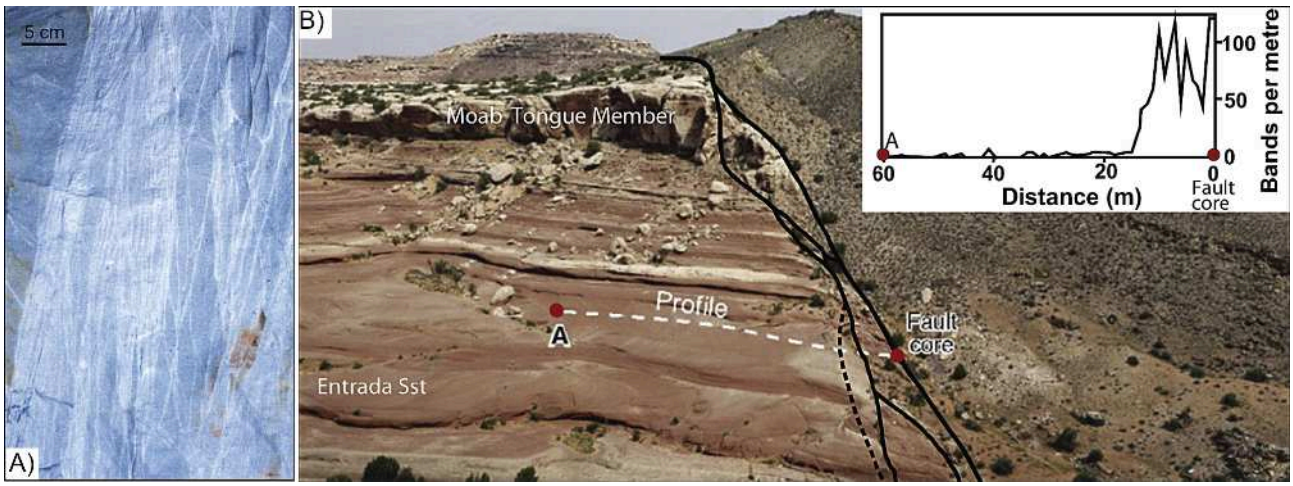


Figure 26 Photographs of deformation bands in outcrop cross sections. A) Sub-parallel deformation bands within a fault zone with a total throw of ~5.5 m from coastal cliffs of Mount Messenger Formation, Tongaporutu, Taranaki Basin, New Zealand. B) Moab Fault zone, Utah, and inset graph showing abundance of deformation bands across the profile going from point A to the fault core fault zone (from Nicol et al., 2013).

It is recommended that these new data on the geometry and predicted density of subseismic scale faults is implemented in an updated version of the geological model of the South West Hub. Examples from the open literature provide clues to capture the effects of these structure on the large scale flow behaviour of a modelled reservoir. Zuluaga et al. (2016) showed that field based geometric relationships can be used to upscale deformation bands to capture flow effects by running simulations with variable scenarios of permeability contrast between host rock and deformation bands. Importantly, the simulations highlighted that deformation band arrays have capabilities of redirecting flow regardless of amount of permeability contrast between them and the host rock. Further, Radhua et al. (2016) examined the potential impact of zones of deformation bands on CO_2 transport in reservoir rock, their numerical modeling results suggest that zones of deformation bands strongly compartmentalize reservoir pressures largely blocking lateral, cross-fault flow of supercritical CO_2.

Finally, we note that image logs collected in Harvey 1 and Harvey 4 identified some structures at high angle to the sedimentary bedding as healed fractures due to their thin geometry, lack of visible offset and electrically resistive nature. Based on the absence of healed fractures in cores, we argue that these structures could alternatively be interpreted as deformation bands. In particular, the image logs (Circumferential Borehole Imaging Log: CBIL and Simultaneous Acoustic and Resistivity Imager: STAR) interpretation of Harvey

1 from Lena Thrane (Baker Hughes) pointed out that most of the identified structures occur in a depth interval ranging between 1375 and 1625 m with dominant strike N-S to NNW-SSE and dips towards E and W. Clusters of these structures in intervals of 6 m are shown in Figures 27 and 28.

Analysis of the image log (X-tended Range Micro Imager: XRMI) collected in Harvey 4 from Odin Reservoir Consultants also identified structural features interpreted as healed fractures in the sandstone rich Wonnerup Member of the Lesueur Sandstone (Figure 29). Their strike is dominantly NW – SE and NNW – SSE with dips towards SW and NE, again we propose that these structures could be interpreted as deformation bands. Their orientation inferred from the image logs in Harvey 1 and Harvey 4 is similar to that of seismically resolved faults in the area, further supporting the interpretation as subsidiary structure of major faults. Their identification in all the Harvey boreholes suggests this to be a common deformation feature in Lesueur Sandstone that should be considered in the new geological model.

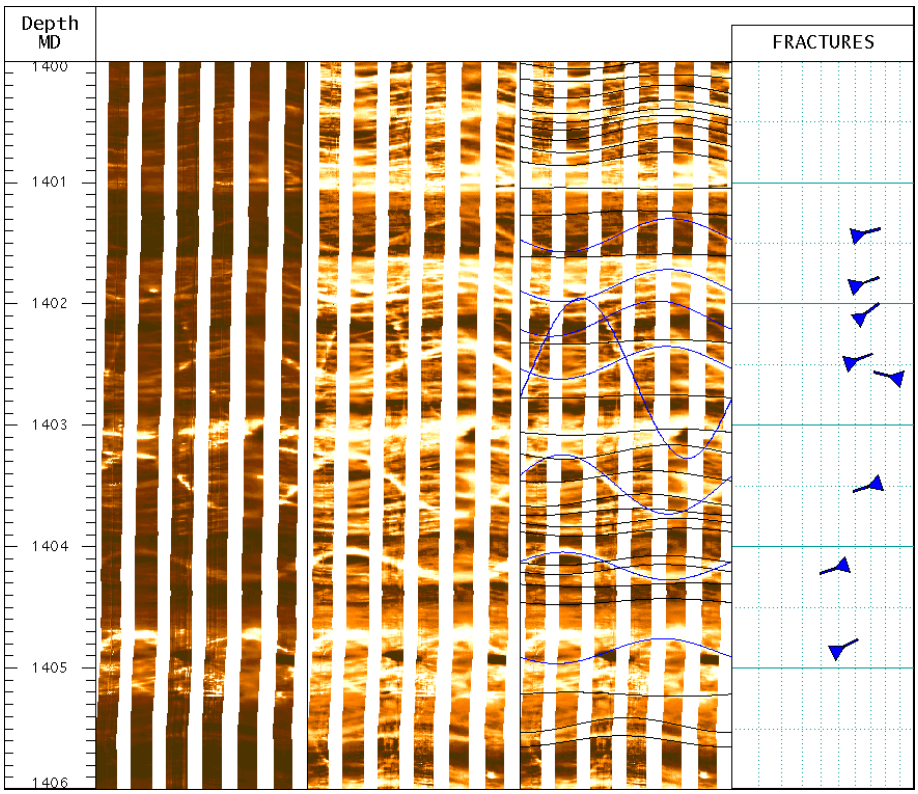


Figure 27 Harvey 1 image log: 6 m section 1400-1406 m. Left: CBIL, centre: static range Star log, right dynamic range Star Log. Sedimentary bedding shown as black sine waves. Resistive features (blue sine waves) could be interpreted as healed fractures (original interpretation from Baker Hughes) or deformation bands.

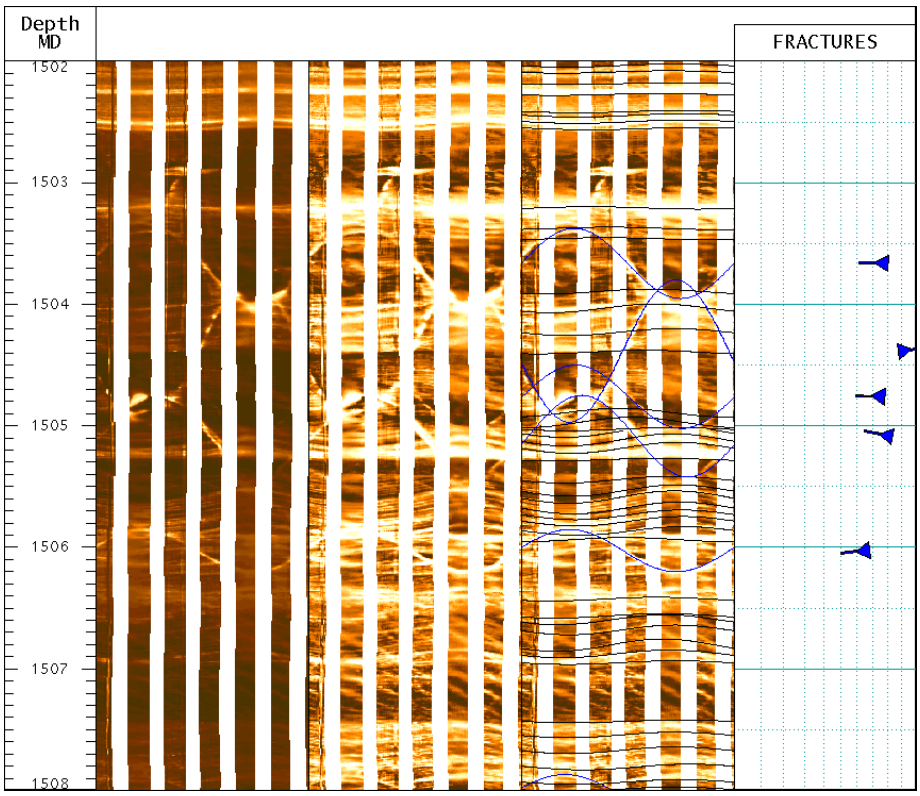


Figure 28 Harvey 1 image log: 6 m section 1502-1508 m. Left: CBIL, centre: static range Star log, right dynamic range Star Log. Sedimentary bedding shown as black sine waves. Resistive features (blue sine waves) could be interpreted as healed fractures (original interpretation from Baker Hughes) or deformation bands.

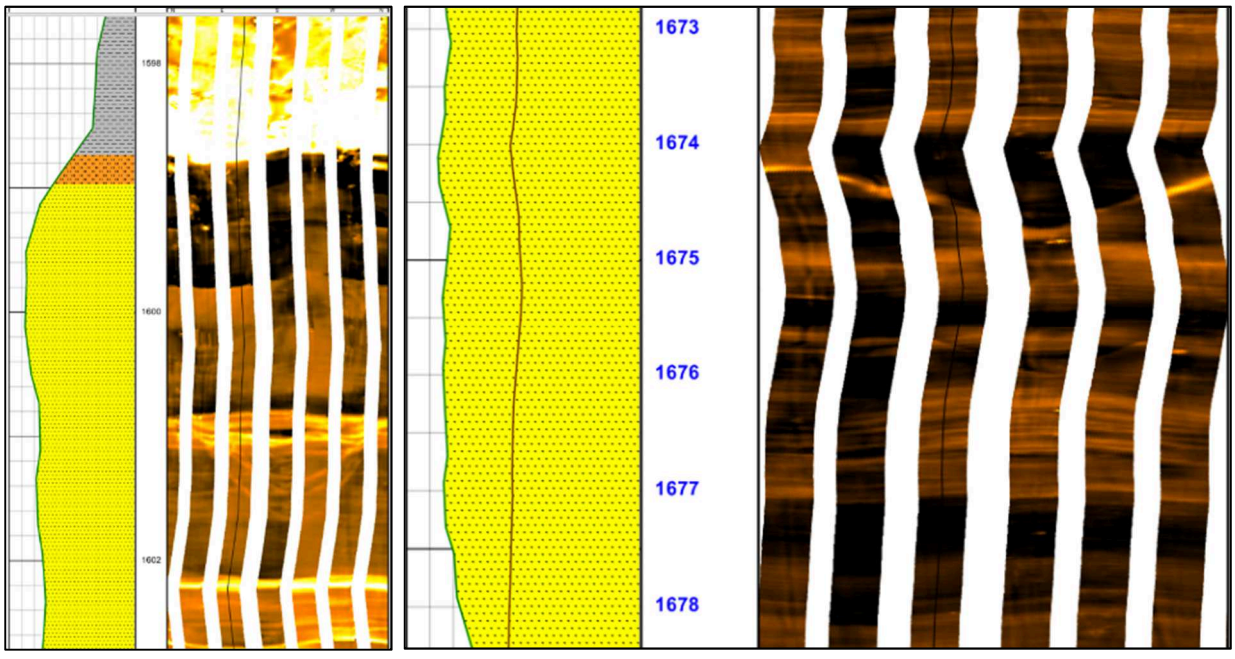


Figure 29 Harvey 4 XRMI log. Left 5.1 m section 1597.6-1602.7 m. Right 5 m section 1673-1678 m showing resistive features (light, thin sine waves) that could be interpreted as healed fractures (original interpretation from Odin Reservoir consultants) or deformation bands.

Conclusions

This study presented the first description of fault related structures based on core observations in the Southern Perth Basin. The intersection between the F10 fault and Harvey 2 affects a large portion of the recovered cores (400-500 m) resulting in a thick diffuse zone of damage identified thanks to the presence of incohesive breccia zones, small slip surfaces and compactive features. This thick zone also corresponds to an anomalous high water content interval as identified by hyperspectral logging and a sector of fluid loss during drilling indicating a potentially important effect on subsurface fluid circulation.

Further, the analysis of cores from the boreholes drilled in the South West Hub Area revealed the presence of previously unrecognised structural features in the form of deformation bands. These cataclastic structures are characteristic of damage zones surrounding mature faults in porous sandstones and occur at a sub-seismic scale resulting in a dramatic porosity and pore size reduction with respect to the host rock which likely impacts on the local fluid flow. Deformation bands are identified in both the members of the Lesueur Sandstone even at relatively shallow levels (< 1km, see Table 3). Based on the observed geometry a minimum (31/km) and maximum (93/km) expected density is estimated that can be used in the next generation of geo-models of the South West Hub. Importantly their presence in the cores is a potential indicator of proximity to larger faults.

References section 2

Ajdukiewicz, J.M. and Lander, R.H., 2010. Sandstone reservoir quality prediction: The state of the art. AAPG bulletin, 94(8), pp.1083-1091.

Avseth, P., Dvorkin, J., Mavko, G. and Rykkje, J., 2000. Rock physics diagnostic of North Sea sands: Link between microstructure and seismic properties. Geophysical Research Letters, 27(17), pp.2761-2764.

Aydin, A., 1978. Small faults formed as deformation bands in sandstone. In Rock Friction and Earthquake Prediction (pp. 913-930). Part of the Contributions to Current Research in Geophysics (CCRG) book series (CCRG, volume 6). Birkhäuser Basel.

Aydin, A. and Johnson, A.M., 1978. Development of faults as zones of deformation bands and as slip surfaces in sandstone. Pure and Applied Geophysics 116(4), pp.931-942.

Ballas, G., Fossen, H. and Soliva, R., 2015. Factors controlling permeability of cataclastic deformation bands and faults in porous sandstone reservoirs. Journal of Structural Geology 76, pp.1-21.

Baumgartner, M. and Bakker, R.J., 2009. Raman spectroscopy of pure H2O and NaCl-H2O containing synthetic fluid inclusions in quartz—a study of polarization effects. Mineralogy and Petrology, 95(1-2), pp.1-15.

Bodnar, R.J., 1993. Revised equation and table for determing the freezing point depression of H2O-NaCl solutions. Geochimica et Cosmochimica Acta. 57, 683-684.

Boggs, S.J. and Krinsley, D. 2006 Applications of Cathodoluminescence Imaging to the Study of Sedimentary Rocks. 165 pp. Cambridge University Press. ISBN 9780 521 85878 6.

Bjørkum, P.A., 1996, How important is pressure in causing dissolution of quartz in sandstones?: Journal of Sedimentary Research, v. 66, p. 147-154.

Bjorkum, P.A., Walderhaug, O. and Aase, N.E., 1993. A model for the effect of illitization on porosity and quartz cementation of sandstones. Journal of Sedimentary Research, 63(6).

Bjorlykke, K., 1984. Formation of secondary porosity: How important is it? Clastic diagenesis, pp.277-286.

Bjørlykke, K., 1998. Clay mineral diagenesis in sedimentary basins—a key to the prediction of rock properties. Examples from the North Sea Basin. Clay minerals, 33(1), pp.15-34.

Bjørlykke, K., 2015. Petroleum Geoscience. Springer Berlin Heidelberg.

Bjørlykke, K., Ramm, M. and Saigal, G.C., 1989. Sandstone diagenesis and porosity modification during basin evolution. Geologische Rundschau, 78(1), pp.243-268.

Bourdet J., Kempton, R., 2014. Novel Approach to Measuring Irreducible Water Salinity in Gas Reservoirs. Offshore Technology Conference Asia, Kuala Lumpur, Malaysia, 25–28 March.

Childs, C., Walsh, J.J. and Watterson, J., 1990. A method for estimation of the density of fault displacements below the limits of seismic resolution in reservoir formations. In North Sea Oil and Gas Reservoirs—II (pp. 309-318). Springer Netherlands.

Conciadori, M.; Bourdet, J.; Delle Piane, C. Diagenesis and palaeo-fluid circulation in the Lesueur Sandstone, Perth Basin. 2015. CSIRO report: EP149172. https://doi.org/10.5072/83/5849a35f05f0e

Crostella, A. and Backhouse, J., 2000. Geology and petroleum exploration of the central and southern Perth Basin, Western Australia (No. 57). Perth, WA: Geological Survey of Western Australia.

Delle Piane, C., Olierook, H.K., Timms, N.E., Saeedi, A., Esteban, L., Rezaee, R., Mikhaltsevitch, V., Iglauer, S. and Lebedev, M., 2013. Facies-based rock properties distribution along the Harvey 1 stratigraphic well. Australian National Low Emissions Coal Research & Development CSIRO Report Number EP133710. Available at: http://anlecrd.com.au/projects/facies-based-rock-properties-distribution-along-the-Harvey-1-stratigraphic-well/

Driesner, T., Heinrich, C.A., 2007. The system H2O–NaCl. Part I: Correlation formulae for phase relations in temperature–pressure–composition space from 0 to 1000°C, 0 to 5000bar, and 0 to 1 , Geochimica et Cosmochimica Acta, Volume 71, Issue 20, 2007, Pages 4880-4901.

Dubessy, J., Lhomme, T., Boiron, M.C. and Rull, F., 2002. Determination of chlorinity in aqueous fluids using Raman spectroscopy of the stretching band of water at room temperature: application to fluid inclusions. Applied spectroscopy, 56(1), pp.99-106.

Faulkner, D. R., Jackson, C. A. L., Lunn, R. J., Schlische, R. W., Shipton, Z. K., Wibberley, C. A. J., & Withjack, M. O., 2010. A review of recent developments concerning the structure, mechanics and fluid flow properties of fault zones. Journal of Structural Geology 32(11), 1557-1575.

Fossen, H. and Hesthammer, J., 2000. Possible absence of small faults in the Gullfaks Field, northern North Sea: implications for downscaling of faults in some porous sandstones. Journal of Structural Geology, 22(7), pp.851-863.

Fossen, H., Schultz, R.A., Shipton, Z.K. and Mair, K., 2007. Deformation bands in sandstone: a review. Journal of the Geological Society 164(4), 755-769.

Fossen, H., Soliva, R., Ballas, G., Trzaskos, B., Cavalcante, C. and Schultz, R.A., 2017. A review of deformation bands in reservoir sandstones: geometries, mechanisms and distribution. From: Ashton, M., Dee, S. J. & Wennberg, O. P. (eds) Subseismic-Scale Reservoir Deformation. Geological Society, London, Special Publications, 459.

Gauthier, B.D.M. and Lake, S.D., 1993. Probabilistic modeling of faults below the limit of seismic resolution in Pelican Field, North Sea, offshore United Kingdom. AAPG Bulletin, 77(5), pp.761-777.

Georgiev, G.M., Kalkanjiev, T.K., Petrov, V.P. and Nickolov, Z., 1984. Determination of salts in water solutions by a skewing parameter of the water Raman band. Applied spectroscopy, 38(4), pp.593-595.

Goldstein, R. H., Reynolds, and T. J., 1994. Systematics of fluid inclusions in diagenetic minerals: SEPM Short Course Notes 31. 213.

Hancock, L. and Sando, K., 2015. Harvey 2 Fault 10 HyLogging data. Additional interpretation from GSWA. Powerpoint slide pack distributed to the South West Hub researchers.

Hardman, R.F.P. and Booth, J.E., 1991. The significance of normal faults in the exploration and production of North Sea hydrocarbons. Geological Society, London, Special Publications 56(1), pp.1-13.

Harris, L.B., 1994. Structural and tectonic synthesis for the Perth Basin, Western Australia. Journal of Petroleum Geology, 17(2), pp.129-156.

Iasky R. P., Young R. A. & Middleton M. F., 1991. Structural study of the southern Perth Basin by geophysical methods. Exploration Geophysics, 22, 199–206.

Iasky R. P., 1993. A structural study of the southern Perth Basin, Western Australia. Geological Survey of Western Australia, No. 31, 56 p.

Jahren, J.S. and Aagaard, P., 1992. Diagenetic illite-chlorite assemblages in arenites. I. Chemical evolution. Clays and Clay Minerals, 40, pp.540-540.

Johansen, T.E.S., Fossen, H. and Kluge, R., 2005. The impact of syn-faulting porosity reduction on damage zone architecture in porous sandstone: an outcrop example from the Moab Fault, Utah. Journal of Structural Geology 27(8), 1469-1485.

Keller, W.D., 1978. Classification of kaolins exemplified by their textures in scan electron micrographs. Clays and Clay Minerals, 26(1), pp.1-20.

Kim, Y.S., Peacock, D.C. and Sanderson, D.J., 2004. Fault damage zones. Journal of structural geology 26(3), pp.503-517.

Krüger, Y., Stoller, P., Rička, J. and Frenz, M., 2007. Femtosecond lasers in fluid-inclusion analysis: overcoming metastable phase states. European Journal of Mineralogy, 19(5), pp.693-706.

Langhi, L., Ciftci, B., Strand, J., 2013. Fault seal first-order analysis–SW Hub. CSIRO report EP13879, pp. 50 http://www.anlecrd.com.au/announcements/media-release-research-project-drills-down-for-results.

Lanson, B., Beaufort, D., Berger, G., Bauer, A., Cassagnabere, A. and Meunier, A., 2002. Authigenic kaolin and illitic minerals during burial diagenesis of sandstones: a review. Clay minerals, 37(1), pp.1-22.

Mernagh, T.P. and Wilde, A.R., 1989. The use of the laser Raman microprobe for the determination of salinity in fluid inclusions. Geochimica et Cosmochimica Acta, 53(4), pp.765-771.

Miall, A.D., 1996. The Geology of Fluvial Deposits: Sedimentary Facies, Basin Analysis, and Petroleum Geology. Springer, New York (1996).

Mory, A.J. and Iasky, R.P., 1996. Stratigraphy and structure of the onshore northern Perth Basin, Western Australia (Vol. 46). Geological Survey of Western Australia.

Nicol, A., Childs, C., Walsh, J.J. and Schafer, K.W., 2013. A geometric model for the formation of deformation band clusters. Journal of Structural Geology, 55, pp.21-33.

Odling, N.E., Harris, S.D. and Knipe, R.J., 2004. Permeability scaling properties of fault damage zones in siliclastic rocks. Journal of Structural Geology 26(9), 1727-1747.

Olierook, H.K., Delle Piane, C., Timms, N.E., Esteban, L., Rezaee, R., Mory, A.J. and Hancock, L., 2014a. Facies-based rock properties characterization for CO 2 sequestration: GSWA Harvey 1 well, Western Australia. Marine and Petroleum Geology, 50, pp.83-102.

Olierook, H.K., Timms, N.E. and Hamilton, P.J., 2014b. Mechanisms for permeability modification in the damage zone of a normal fault, northern Perth Basin, Western Australia. Marine and Petroleum Geology, 50, pp.130-147.

Pevzner, R., Langhi, L., Shragge, J., Ziramov, S., Strand, J., Potter, T., Tertyshnikov, K., Bona, A., Urosevic, M., 2015, Advanced Processing and Analysis of South West Hub 3D Seismic Data. ANLEC R&D Project 7-0314-0231, 137p.

Playford, P.E., Low, G.H. and Cockbain, A.E., 1976. Geology of the Perth Basin, Western Australia. Geological Survey of Western Australia.

Pittman, E.D., 1981. Effect of fault-related granulation on porosity and permeability of quartz sandstones, Simpson Group (Ordovician) Oklahoma. AAPG Bulletin 65, 2381–2387.

Qiu, C., Krüger Y., Wilke, M., Marti, D., Rička J., Frenz M., 2016. Exploration of the phase diagram of liquid water in the low-temperature metastable region using synthetic fluid inclusions. Physical Chemistry Chemical Physics, 18, 28227-28241.

Raduha, S., Butler, D., Mozley, P.S., Person, M., Evans, J., Heath, J.E., Dewers, T.A., Stauffer, P.H., Gable, C.W. and Kelkar, S., 2016. Potential seal bypass and caprock storage produced by deformation-band-to-opening-mode-fracture transition at the reservoir/caprock interface. Geofluids, 16(4), pp.752-768.

Renard R., Ortoleva P., and Gratier J. P., 1997, Pressure solution in sandstones: Influence of clays and dependence on temperature and stress: Tectonophysics, 280, 257–266,

Roedder, E., 1984. Fluid inclusions. Reviews in Mineralogy, Mineralogical Society of America. Vol.12.

Russell R and Pollock M, November 2015. Harvey-2 Well Completion Report, South West Hub Carbon Capture and Storage Project. DDH1 Drilling Report to Department of Mines and Petroleum Western Australia, unpublished.

Schultz, R.A., Soliva, R., Fossen, H., Okubo, C.H. and Reeves, D.M., 2008. Dependence of displacement–length scaling relations for fractures and deformation bands on the volumetric changes across them. Journal of Structural Geology, 30(11), 1405-1411.

Soliva, R., Schultz, R.A., Ballas, G., Taboada, A., Wibberley, C., Saillet, E. and Benedicto, A., 2013. A model of strain localization in porous sandstone as a function of tectonic setting, burial and material properties; new insight from Provence (southern France). Journal of Structural Geology, 49, 50-63.

Song T. & Cawood P. A., 2000. Structural styles in the Perth Basin associated with the Mesozoic break-up of Greater India and Australia. Tectonophysics, 317, 55–72.

Sun, Q., Zhao, L., Li, N. and Liu, J., 2010. Raman spectroscopic study for the determination of Cl− concentration (molarity scale) in aqueous solutions: Application to fluid inclusions. Chemical Geology, 272(1), pp.55-61.

Timms, N.E., Corbel, S., Olierook, H., Wilkes, P., Delle Piane, C., Sheldon, H., Alix, R., Horowitz, F., Wilson, M., Evans, K.A. and Stütenbecker, L., 2012. Project 2: Geomodel. WA Geothermal Centre of Excellence/CSIRO.

Timms, N.E., Olierook, H.K., Wilson, M.E., Delle Piane, C., Hamilton, P.J., Cope, P. and Stütenbecker, L., 2015. Sedimentary facies analysis, mineralogy and diagenesis of the Mesozoic aquifers of the central Perth Basin, Western Australia. Marine and Petroleum Geology, 60, pp.54-78.

Varma, S., Undershultz, J., Dance, T., Langford, R., Esterle, J., Dodds, K., Vand Gent, D., 2009. Regional study on potential CO2 geosequestration in the Collie Basin and the Southern Perth Basin of Western Australia. Marine and Petroleum Geology. 26, 1255-1273.

Walderhaug, O., 1996. Kinetic modeling of quartz cementation and porosity loss in deeply buried sandstone reservoirs. AAPG bulletin, 80(5), pp.731-745.

Worden, R.H. and Burley, S.D., 2003. Sandstone diagenesis: the evolution of sand to stone. Sandstone Diagenesis: Recent and Ancient, 4, pp.3-44.

Worden, R.H. and Morad, S., 2000. Quartz cementation in oil field sandstones: a review of the key controversies. Quartz cementation in sandstones. International Association of Sedimentologists Special publication, 29, pp.1-20.

Zuluaga, L.F., Rotevatn, A., Keilegavlen, E. and Fossen, H., 2016. The effect of deformation bands on simulated fluid flow within fault-propagation fold trap types: Lessons from the San Rafael monocline, Utah. AAPG Bulletin, 100(10), pp.1523-1540.

Appendix 2A: Fluid inclusions results

List of analysed fluid inclusions and corresponding results: Th = homogenisation temperature; salinity expressed as NaCl equivalent. The T_h dataset is limited to two-phase inclusions provide, numerous 1-phase are listed below that could not be used for T_h determination due to metastable behaviour of water at shallow depth. Key for location: FTQG: Fracture in quartz grain; QOB = quartz overgrowth boundary; WQO = within quartz overgrowth; FTQO = fracture transecting quartz overgrowth.

Borehole	Depth (m)	Location	Th (°C)	Salinity (ppm)
Harvey 1	2496.22	FTQG		24774
Harvey 1	2496.22	FTQG		33550
Harvey 1	2496.22	QOB		26521
Harvey 1	2496.22	WQO		53804
Harvey 1	2496.22	WQO		21135
Harvey 1	2496.22	QOB		45128
Harvey 1	2496.22	FTQO		21828
Harvey 1	2496.22	WQO		35465
Harvey 1	2496.22	QOB		24391
Harvey 1	2496.22	FTQG		29587
Harvey 1	2496.22	FTQG		23092
Harvey 1	2496.22	FTQO		24589
Harvey 1	2496.22	FTQG	64	16267
Harvey 1	2496.22	FTQG	95.8	16728
Harvey 1	2496.22	FTQG	76.5	20968
Harvey 1	2496.22	QOB	62	
Harvey 1	2496.22	WQO	75.8	36280
Harvey 1	2496.22	QOB	64	
Harvey 1	2516	QOB		16374
Harvey 1	2516	QOB	69	
Harvey 1	2516	FTQO	65	15459
Harvey 1	2516	QOB		28480
Harvey 1	2516	QOB	48	24271
Harvey 1	2516	QOB		21120
Harvey 1	2516	QOB	54	32782
Harvey 1	2516	QOB	53	23609
Harvey 1	2516	QOB	52.6	31314
Harvey 1	2516	WQO	77	16835

Borehole	Depth (m)	Location	Th (°C)	Salinity (ppm)
Harvey 2	1347.5	WQO	77	10850
Harvey 2	1347.5	WQO		17863
Harvey 2	1347.5	QOB		18929
Harvey 2	1347.5	QOB-WQO	63	18130
Harvey 2	1347.5	FTQG		11186
Harvey 2	1347.5	QOB	48	19139
Harvey 2	1347.5	WQO	101.2	13065
Harvey 2	1347.5	QOB	46.5	17890
Harvey 2	1347.5	WQO		15255
Harvey 2	1347.5	QOB	49.3	25007
Harvey 2	1347.5	QOB	48.6	26143
Harvey 2	1347.5	QOB	57.4	38846
Harvey 2	1347.5	QOB	48.8	26972
Harvey 2	1347.5	QOB	101.8	20109
Harvey 2	1347.5	QOB	53	19848
Harvey 2	1347.5	QOB	55.5	43951
Harvey 2	1347.5	QOB	51.5	8337
Harvey 2	1347.5	QOB	47.7	42370
Harvey 2	1347.5	WQO	51.5	16847
Harvey 2	1347.5	FTQO	69.7	30733
Harvey 2	1347.5	QOB	64.9	40130
Harvey 2	1347.5	QOB	54	12952
Harvey 2	1347.5	WQO	66	30115

Borehole	Depth (m)	Location	Th (°C)	Salinity (ppm)
Harvey 2	1245.15	WQO	45.1	39165
Harvey 2	1245.15	WQO	47	22439
Harvey 2	1245.15	QOB		33908
Harvey 2	1245.15	Fracture	69.6	38479
Harvey 2	1245.15	Fracture	95.3	39193
Harvey 2	1245.15	QOB	44	57245
Harvey 2	1245.15	QOB	53.5	59822
Harvey 2	1245.15	FTQO		42300
Harvey 2	1245.15	WQO	47.8	28307
Harvey 2	1245.15	FTQO		34350
Harvey 2	1245.15	QOB	50.5	20541
Harvey 2	1245.15	QOB	44	37014
Harvey 2	1245.15	FTQO	59	24756
Harvey 2	1245.15	QOB	46	47566
Harvey 2	1245.15	QOB	91	35927
Harvey 2	1245.15	QOB	56.4	32940
Harvey 2	1245.15	WQO	56	35500
Harvey 2	1245.15	WQO	49	42338
Harvey 2	1245.15	WQO		47622
Harvey 2	1245.15	QOB		13686
Harvey 2	1245.15	QOB		29701
Harvey 2	1245.15	QOB		30650

Borehole	Depth (m)	Location	Th (°C)	Salinity (ppm)
Harvey 3	1313	WFC	49	43525
Harvey 3	1313	WFC	76	45194
Harvey 3	1313	WFC		54306
Harvey 3	1313	QFC		36292
Harvey 3	1313	WFC	54	62039
Harvey 3	1313	WFC	52	12141
Harvey 3	1313	WFC	64	15811
Harvey 3	1313	WFC	43.7	41925
Harvey 3	1313	QFB	51	29176
Harvey 3	1313	QFB	49.4	10981
Harvey 3	1313	WFC		50596
Harvey 3	1313	QFB		22766
Harvey 3	1313	WFC		45938
Harvey 3	1313	WFC		50907
Harvey 3	1313	QFB		35631
Harvey 3	1313	QFB		57379
Harvey 3	1313	QFB		30759
Harvey 3	1313	QFB	107	46640
Harvey 3	1313	QFB		48461
Harvey 3	1313	QFB		34674
Harvey 3	1313	QFB		36705

Borehole	Depth (m)	Location	Th (°C)	Salinity (ppm)
Harvey 3	1417.9	FWQO	76	
Harvey 3	1417.9	WQO		36990
Harvey 3	1417.9	QFB	46.8	32788
Harvey 3	1417.9	WFC	54.3	35607
Harvey 3	1417.9	QFB		33030
Harvey 3	1417.9	QOB-WQO		53617
Harvey 3	1417.9	WQO		43514
Harvey 3	1417.9	FTQo	103	25693
Harvey 3	1417.9	FTQo	98	29623
Harvey 3	1417.9	WFC		33367
Harvey 3	1417.9	QFB	77.7	19541
Harvey 3	1417.9	WQO	58	41790
Harvey 3	1417.9	WQO	59.7	46991
Harvey 3	1417.9	QOB-WQO	57.4	17506
Harvey 3	1417.9	WFC		16177
Harvey 3	1417.9	WFC		24404
Harvey 3	1417.9	QOB		21977
Harvey 3	1417.9	FTQo		41811
Harvey 3	1417.9	FTQo		15908
Harvey 3	1417.9	QOB	83.7	35386
Harvey 3	1417.9	QOB	89	37014
Harvey 3	1417.9	WQo		22942
Harvey 3	1417.9	WFC		41993
Harvey 3	1417.9	QOB		33706
Harvey 3	1417.9	QOB		20324
Harvey 3	1417.9	QOB		35234

Borehole	Depth (m)	Location	Th (°C)	Salinity (ppm)
Harvey 3	1511.65	QOB	76	36180
Harvey 3	1511.65	QOB	55.9	
Harvey 3	1511.65		65	33488
Harvey 3	1511.65	QOB	115.4	24126
Harvey 3	1511.65		64	21414
Harvey 3	1511.65		72	4927
Harvey 3	1511.65	WQO	52.8	10450
Harvey 3	1511.65	WQO	80	400
Harvey 3	1511.65	QOB	77	8529
Harvey 3	1511.65	QOB	87	49926
Harvey 3	1511.65	QOB	87	
Harvey 3	1511.65	QOB2	64	28420
Harvey 3	1511.65	WQO1	78	7442
Harvey 3	1511.65	QOB1		16536
Harvey 3	1511.65	QOB	74	20978
Harvey 3	1511.65	WQO	107	35923
Harvey 3	1511.65	QOB	62.7	25436
Harvey 3	1511.65	WQO	110	18011
Harvey 3	1511.65	QOB	68.5	31383
Harvey 3	1511.65	QOB		33093
Harvey 3	1511.65	WQO		15226
Harvey 3	1511.65	WQO		67769
Harvey 3	1511.65	WQO	70.9	16642

Borehole	Depth (m)	Location	Th (°C)	Salinity (ppm)
Harvey 4	1797.5	QOB		3281
Harvey 4	1797.5	QOB		894
Harvey 4	1797.5		70.7	19388
Harvey 4	1797.5	QOB	62.3	21925
Harvey 4	1797.5	QOB		17260
Harvey 4	1797.5			31795
Harvey 4	1797.5	WQO	67.3	30500
Harvey 4	1797.5	WQO	61	
Harvey 4	1797.5	WQO	83	11775
Harvey 4	1797.5	QOB		32676
Harvey 4	1797.5	QOB	62	23668
Harvey 4	1797.5	WQO		19652
Harvey 4	1797.5	WQO		16628
Harvey 4	1797.5	WQO	72.5	18396
Harvey 4	1797.5	QOB	80	12600
Harvey 4	1797.5	FTQG		36215
Harvey 4	1797.5	QOB	69.5	8573
Harvey 4	1797.5	WQO		3619
Harvey 4	1797.5	QOB	54.4	3826

Section 3: Petrophysical core plug characterization

Summary

This section of the project is dedicated to the experimental characterisation of core plugs extracted from the new boreholes drilled in the South West Hub area with the aim of providing data to be used for i) comparison with petrophysical properties determined from the interpretation of the wireline logs and ii) populating updated geological models of the subsurface. To this end, a comprehensive series of non-destructive core analysis has been performed on a number of samples. Following and expanding the workflow developed in ANLEC project 199 for the Harvey 1 samples, measurements included:

- X-ray computer tomography (CT): to assess sample quality and create 3D visualization of mm scale heterogeneity (medical CT);
- Porosity and permeability to gas as a function of overburden stress;
- Nuclear Magnetic Resonance (NMR) relaxation time measurements to quantify pore water distribution and mobility within the plugs;
- Permeability to brine;
- Brine Permeability anisotropy.

These petrophysical measurements complement those collected as part of the routine core and special analysis program commissioned by the Department of Mines, Industry Regulation and Safety (DMIRS) and provide additional means of comparing laboratory and wireline log derived porosity and permeability measurements.

The results of the experimental program show that:

- There is excellent correlation between gas and NMR porosity;
- There is significant discrepancy between gas permeability and brine permeability
- Low to moderate permeability anisotropy is measured in samples from the shallow part of the Wonnerup.

Moreover it is shown that samples from the Wonnerup Member of the Lesueur Sandstone (i.e. the potential injection target) share similar depth trends and these become even more apparent when scaled by the depth of the Wonnerup to Yalgorup transition, i.e. the only correlatable stratigraphic horizon within the Lesueur Sandstone in the region of interest

The permeability anisotropy values estimated from laboratory measurements on plugs from the shallow parts of the Wonnerup are in good agreement with those estimated based on small scale fluid flow simulations (conducted as part of project 7-1215-0263) and fit within the range reported in the literature for fluvial sandstone.

3A: Porosity, permeability and Nuclear Magnetic Resonance

Lionel Esteban[1]

[1]CSIRO Energy

Introduction and objectives

A series of non-destructive core analyses were performed on core plugs to improve the characterisation of rock material extracted from the South West Hub boreholes. The workflow included:

- X-ray CT scans: to assess sample quality and heterogeneity;
- Porosity and permeability to gas as a function of overburden stress;
- Nuclear Magnetic Resonance (NMR) relaxation time measurements to identify pore water distribution and mobility, and calibrate log measurements.

The X-ray CT data was presented in a previous milestone report (P 7-0240 Milestone3a) and will not be repeated here. Below we give a brief introduction to the experimental methods and present the results obtained in this work package.

Methods

Gas porosity and permeability

An automated AP 608 nitrogen Permeameter-Porosimeter (Coretest Inc.) was used to measure gas porosity and permeability following the procedure illustrated elsewhere (Delle Piane et al., 2013a and 2013b). For this study, porosity and permeability measurements were conducted on each plug at confining pressure values 3.4, 5.5, 6.9 and 10.3 MPa and constant pore pressure of 1.7 MPa. Three measurements were collected at each pressure to assess the statistical error of the measurements. A power law was fitted to the experimental results to derive the pressure sensitivity of porosity and permeability that was used to extrapolate the results to room conditions for comparison with independent porosity-permeability measurements. Permeability units are expressed hereafter in mD (millidarcy) and 1 mD = 1.01×10^{-15} m^2.

Nuclear magnetic resonance

Nuclear magnetic resonance (NMR) relaxation time measurements can provide critical information about the physico-chemical properties of fluids in porous materials from both wireline logging and laboratory tools (Gruenwald and Knight, 2011; Walbrecker et al., 2011). Applications of NMR in petroleum well logging over the past several decades have demonstrated robust links between measured relaxation times and important formation properties, including pore size distribution and permeability (Clennell et al., 2006; Coates et al,. 1991; Josh et al., 2012). During NMR measurement, proton nuclei are first aligned according to the direction of an applied magnetic field B_0, and then perturbed from their equilibrium state by a pulse characterized by the proton resonance frequency. In an NMR test the magnetization and transverse relaxation time (T_2) of hydrogen nuclei contained in the pore fluid is measured. Different pore sizes in fluid saturated rocks will produce characteristic T_2 distributions as the amplitude of transverse magnetization is proportional to the number of hydrogen nuclei. As a consequence the observed T_2 distribution of a saturated core sample represents the pore size distribution of the rock.

Low field NMR measurements have been collected on plugs from Harvey 2, Harvey 3 and Harvey 4 using a Maran-Ultra spectrometer at 2 MHz (Oxford Instruments Ltd.) to quantify their water content, pore size distribution and estimate permeability. Before NMR measurements, the dry samples were brine saturated under vacuum for 24-48 hours; brine was then injected under a hydrostatic pressure of approximately 14 MPa (2000 PSI) using a ISCO Teledyne syringe pump. The difference in mass between the dry and brine saturated core plugs was used to calculate porosity and compared to the helium gas porosity (extrapolated to room conditions) to check for full saturation. Once saturated the samples were wrapped in cling film to avoid water evaporation, and tested in the NMR spectrometer using the Carr–Purcell–Meiboom–Gill (CPMG) pulse sequence following the same protocol used in previous studies (Delle Piane et al., 2013; Saeedi et al., 2016a). This spin-echo method returns the pore size distribution of the analysed samples based on measured

distribution of transverse magnetic relaxation time (T_2). The experimental protocol ensures a resolution of pore body size >10 nm; pore diameters (in μm) are calculated assuming spherical pore shape from the following equation:

$$\frac{1}{T_2} = \rho_2 \left(\frac{S_{pore}}{V_{pore}}\right) \cong D = 6\rho_2 T_2 \qquad \text{Equation 4}$$

where ρ_2 is the surface relaxivity of quartz (23μm/s); S and V are the surface and volume of pores, respectively and D is the pore diameter.

Finally, permeability is estimated from the T_2 distribution spectrum using a permeability model based on a combination of empirical and theoretical relationships. Permeability was calculated using the free fluid model of Coates based on the Bulk Volume of Immovable fluid (BVI) and the Free Fluid Index (FFI) representing the volumes of immobile (clay bound water and capillary bound water; or strongly and weakly bound water) and movable water respectively (Timur, 1968; Coates et al., 1991; Coates et al., 1998):

$$k_{Coates} = \left[\left(\frac{\emptyset}{C}\right)^2 \times \left(\frac{FFI}{BVI}\right)\right]^2 \qquad \text{Equation 5}$$

Where ø is the total porosity (%), and C is a constant with value 10 (Jorand, 2011). This equation implies the knowledge of the T_2 cut-off separating the capillary and clay-bound water (BVI), residing in small pores and clay layers, from the movable water (FFI) residing in large pores and susceptible to flow during well production. A commonly used T_2 cut-off for sandstone reservoirs is 33 ms (Coates et al., 1998; Hurlimann et al., 2003; Daigle and Dugan, 2009) though it can be severely affected by lithology variations, fluid chemistry, pore geometry, and occurrence of paramagnetic and/or ferromagnetic minerals (smectite and magnetite for instance).

Results

Gas porosity and permeability

Experimentally measured gas porosity and permeability as a function of effective pressure are shown in Figure 30 and Figure 31, respectively and listed Appendix 3A where the extrapolated gas porosity and permeability based on the power law fit of the data are also presented. Results of the petrophysical characterisation tests are illustrated in Figure 32 plotting porosity and permeability to gas as a function of depth in comparison with the data collection acquired by DMIRS. The gas permeability values illustrated below are corrected to account for the Klinkenberg effect and therefore correspond to equivalent liquid permeability. Klinkenberg (1941) illustrated that the permeability of a porous medium to gas is higher than that to water due to “slip flow” between gas molecules and solid walls. This phenomenon occurs when pore radius approaches the mean free path of the gas molecule and the frequency of collisions between gas molecules and the solid walls induces an additional flux due to gas flow at the wall surface, effectively enhancing the flow rate. The Klinkenberg correction is quite important for low-permeability rocks and less important or unimportant for high-permeability rocks.

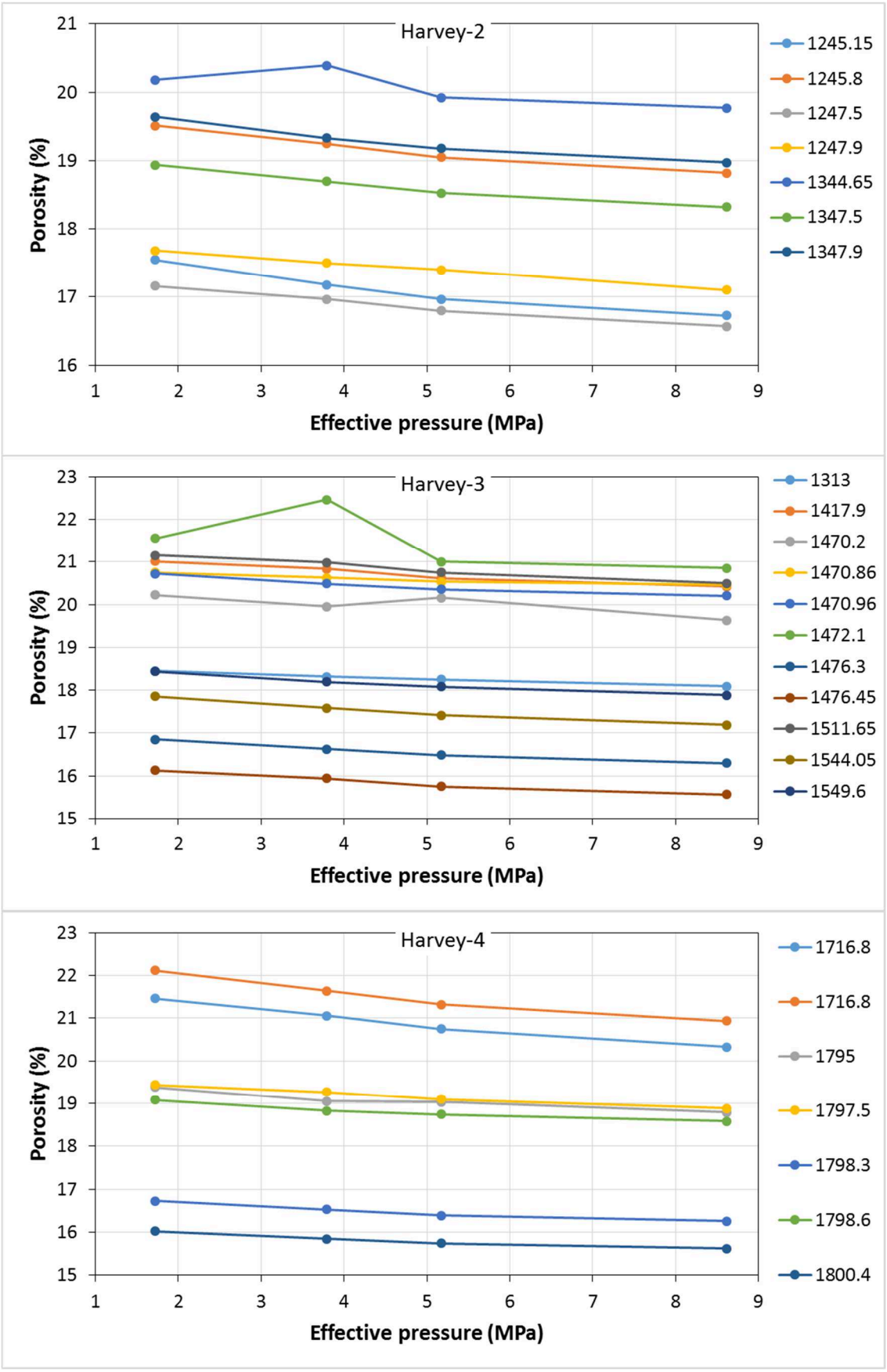


Figure 30 Gas porosity as a function of effective pressure in samples from Harvey 2, Harvey 3 and Harvey 4.

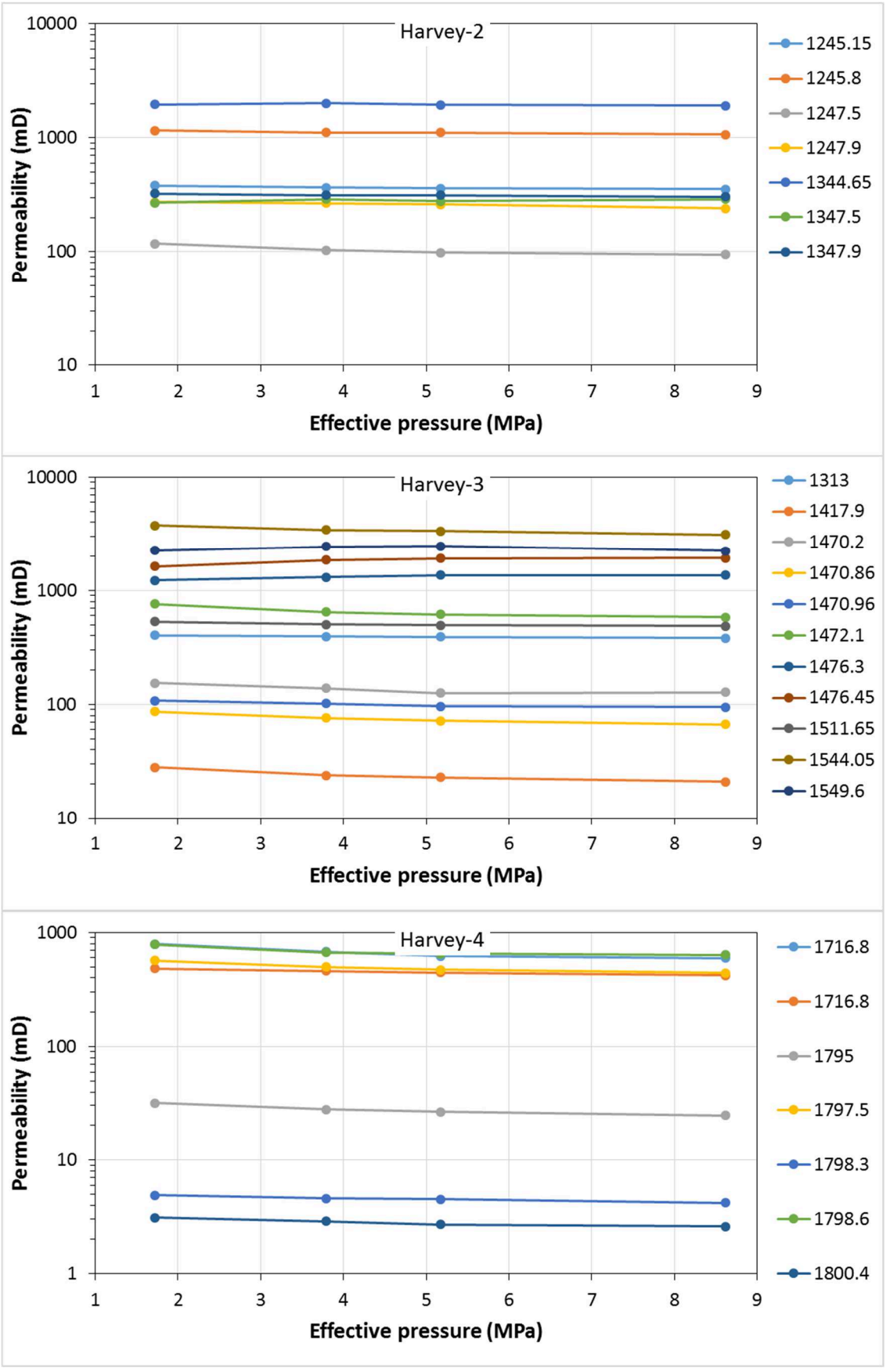


Figure 31 Klinkenberg corrected gas permeability as a function of effective pressure in samples from Harvey 2, Harvey 3 and Harvey 4.

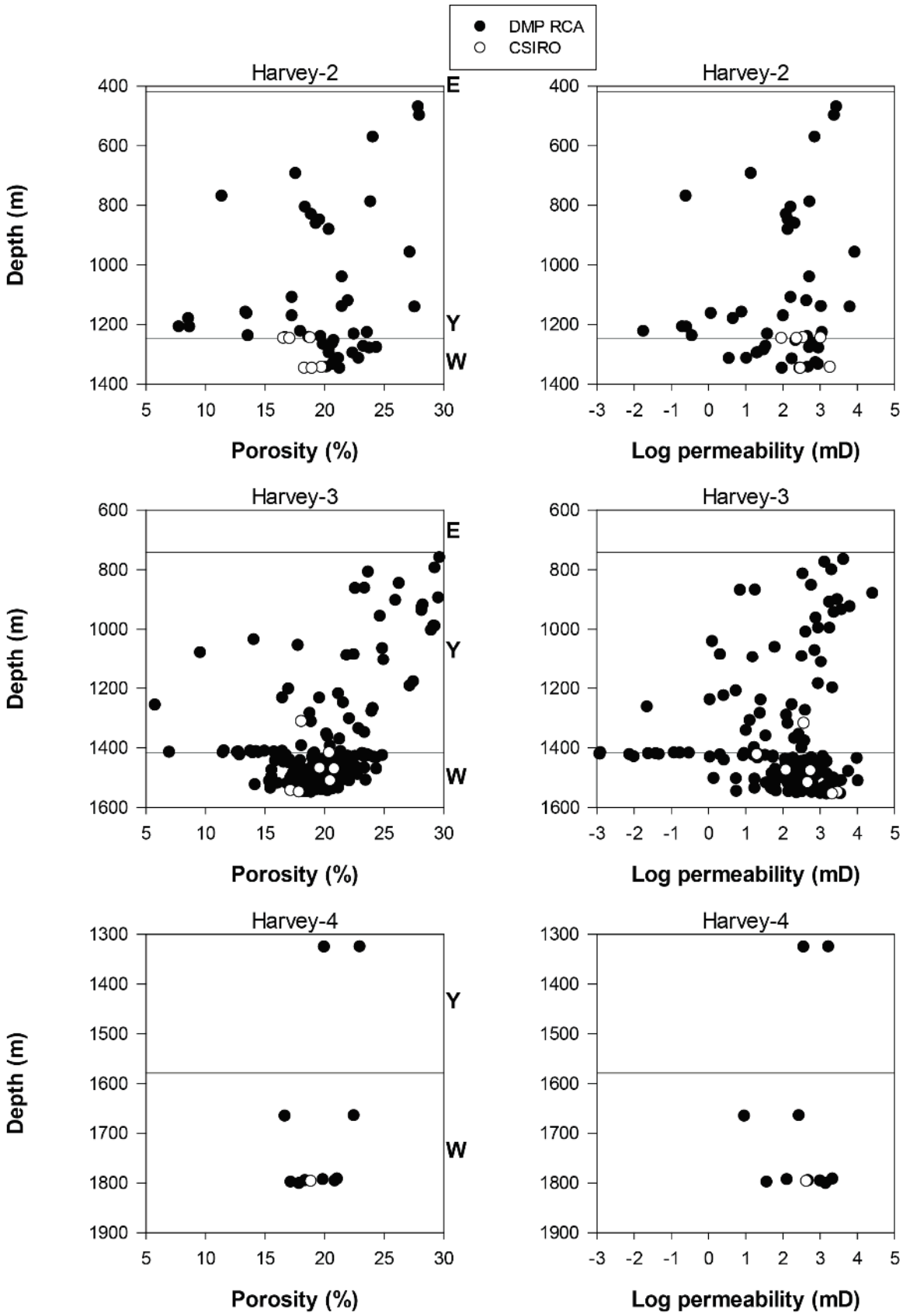


Figure 32 Comparison of gas porosity and permeability values measured on core plugs by DMIRS and CSIRO. Horizontal lines mark the boundaries between the Eneabba Formation (E), the Yalgorup (Y) and Wonnerup (W) Members of the Lesueur Sandstone. Values in the plot were measured under an effective pressure of 8.6 MPa (1250 PSI).

Overall, there is good agreement between the two data sets for all boreholes investigated. Moreover, there is very good agreement between porosity measured via gas permeametry and the NMR computed values measured on brine saturated samples (Figure 33 and Appendix 3B). This should give confidence in the wireline log NMR based porosity estimation in the South West Hub area.

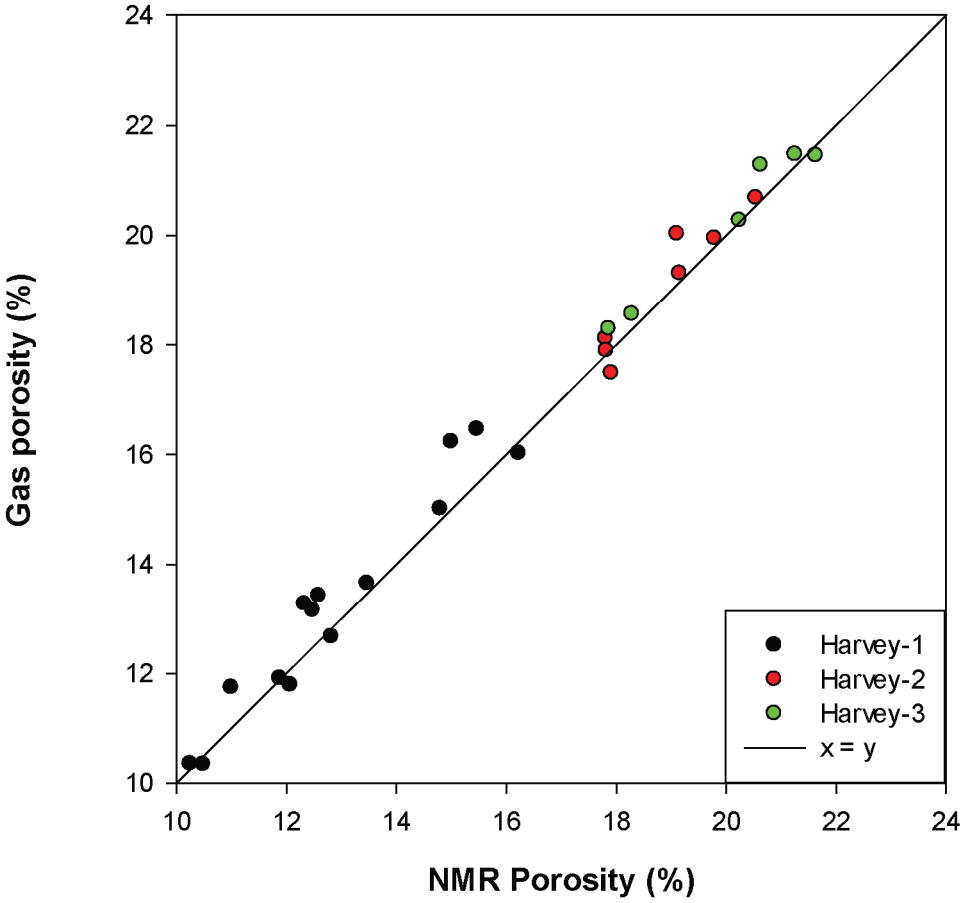


Figure 33 comparison between laboratory measurements of gas and NMR porosity from the core plugs analysed in this study.

NMR

NMR T_2 transversal relaxation time distribution collected on the brine saturated samples are illustrated in Figure 34. T_2 distributions provide significant information on the pore structure and interactions between pore fluids and grain surfaces. In the Harvey 2 samples, the T_2 distribution displays a bi-modal behaviour with:

- A short component with a peak centred between 0.2 and 2 ms;
- A dominant, long component with peak centred between 40 and 200 ms

The short component seems to be more prevalent in the samples belonging to the Yalgorup Member of the Lesueur Sandstone (Figure 34a) possibly due to a higher content of clay minerals within the sands of this Member of the Lesueur Sandstone. The Wonnerup samples show that water in the pore space is mostly movable (i.e. free water above the T_2 cut-off time).

T2 distribution in the Harvey 3 samples seems more complex (Figure 34b) and is characterised by:

- A short component characterised by peak position similar to that observed in the Harvey 2 samples;
- A long component comprising multiple broad peaks centred between 30 and 400 ms

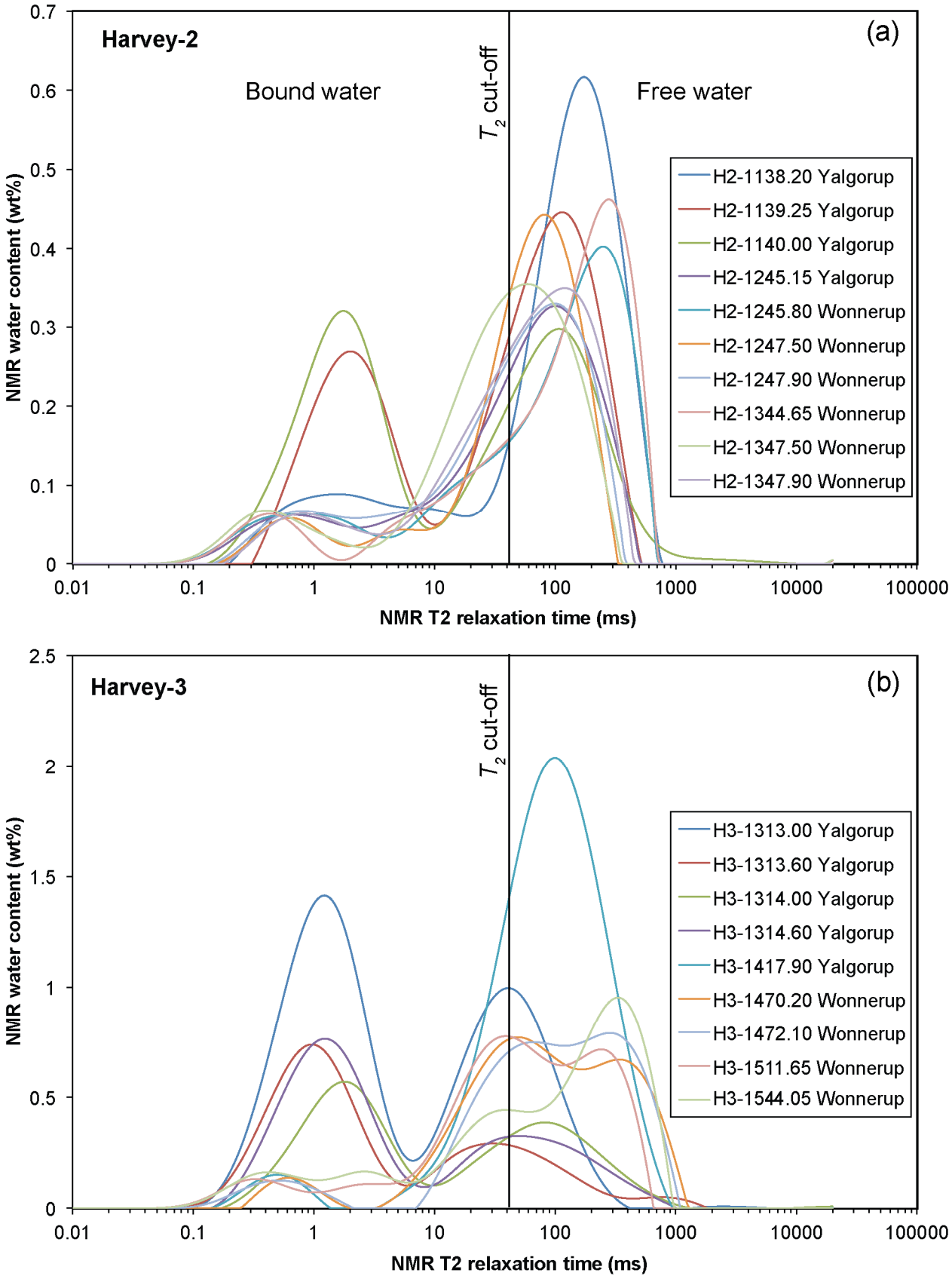


Figure 34 Porosity distribution as a function of the relaxation time T_2 for samples from Harvey 2 (a) and Harvey 3 (b).

While NMR measurements do not provide a direct permeability value, an estimate can be calculated from the T_2 distribution spectrum using a permeability model based on a combination of empirical and theoretical

relationships. The permeability was deduced herein by following the free fluid model of Coates, a variation of the Timur equation, in which the irreducible water saturation (Swirr) has been replaced by the Bulk Volume of Immovable fluid (BVI) and the Free Fluid Index (FFI) representing the volumes of immobile (clay bound water and capillary bound water; or strongly and weakly bound water) and movable water respectively (Timur, 1968; Coates et al., 1991; Coates et al., 1998) modelled permeability (k_{Coates}) is calculated according to equation 5.

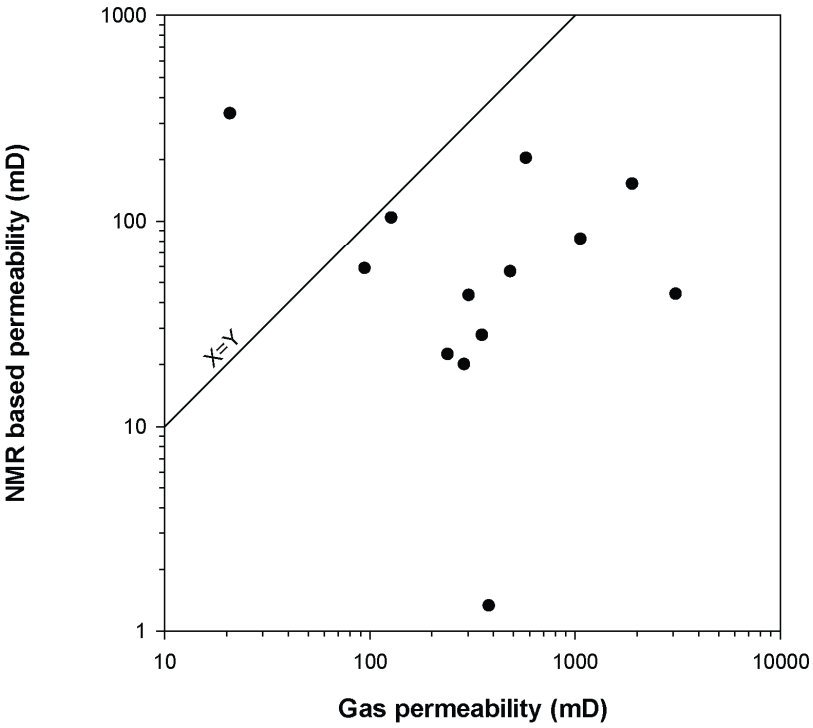


Figure 35 comparison between measured gas permeability and NMR predicted permeability using Coates model described in the main text.

A comparison between Klinkenberg corrected gas permeability and k_{Coates} is presented in Figure 35 and there is an obvious disagreement between the two methods of permeability estimation. It has been previously shown that brine permeability measured on samples from Harvey 1 is significantly lower (approximately 1 order of magnitude) than the Klinkenberg corrected gas permeability measured on the same plug (Delle Piane et al. 2013). We postulate that a similar discrepancy is possibly affecting the values of permeability collected on Harvey 2, 3 and 4 and this could explain the difference between NMR predicted permeability and lab measurements. To verify this hypothesis, a series of brine permeability measurements on the new plugs is presented and discussed in the sections below.

3B: Brine permeability

Alexey Yurikov[2], Maxim Lebedev[2] and Claudio Delle Piane[1]

[1]CSIRO Energy

[2]Curtin University

Methodology

Two experimental core test procedures, in two different laboratories, were conducted as a way of independently assessing the difference between gas and brine permeability measured on the same plugs. The first set of experiments were conducted in the National Geosequestration Laboratory (NGL) at conditions of effective pressure replicating those used during gas permeability measurements. The second set of tests were conducted in the Rock Physics Laboratory at Curtin University at conditions replicating the in-situ temperature and stresses.

In both cases the synthetic formation brine was the same as that used in ANLEC project 7-0314-0233 (Saeedi et al. 2016b) and was prepared in the lab using distilled water and highly soluble salts and analytical reagents grade chemicals including $CaCl_2$, $MgSO_4.7H_2O$, KBr, NaCl, $NaHCO_3$, $SrCl_2$ and $CuSO_4.5H_2O$ amounting to a concentration of total dissolved solids of 31426 mg/L. The formulation was intended to generate a brine that has a more balanced and representative chemistry than a simple synthetic brine that only includes NaCl, and was chosen in the absence of a suitable formation fluid sample from the Lesueur Sandstone (see Saeedi et al. 2016b for further details).

NGL protocol

Experiments were conducted using a triaxial testing machine with transducers in place to measure confining and pore pressures, up- and downstream fluid volumes, axial load and sample deformation. The sample assembly included:

- A cylindrical plug with 38 mm of diameter mounted between top and base platens surrounded by an impermeable flexible membrane isolating the specimen from the confining hydraulic oil;
- Two steel loading platens with provision for pore pressure measurements placed at both ends of the specimen;
- Two diametrically opposed linear variable differential transformers (LVDT) clamped on the top and bottom platens to measure axial displacements; a flexible metal cantilevers to measure radial strain at mid-height of the rock sample;
- A load cell placed underneath the bottom platen.

For each plug, the experimental protocol consisted of the following steps:

- Samples are brine saturated under vacuum for at least 24 hours;
- Samples are installed in the triaxial apparatus;
- Brine is injected from the bottom of the sample and bled through the top;
- Sample assembly is heated to approximately 50 °C;
- Confining pressure and pore pressure are increased at a rate of 0.5 MPa/min to conditions replicating those used for gas permeability measurements (confining pressure = 7.13 MPa; pore pressure = 1.7 MPa);
- After sample equilibration, steady state brine permeability is measured.

Permeability measurements were conducted by applying a small pore pressure differential (approximately 0.25 MPa) between the top and bottom ends of the samples while monitoring the injection and production rates of the upstream and downstream pumps, respectively. Once a steady flow was achieved, the specimen's permeability was calculated using Darcy's law:

$$k = \frac{\eta Q L}{A \Delta P_P}$$ Equation 6

where Q is the pump's steady-state injection rate in $m^3 \times s^{-1}$; k is permeability in m^2; η is the brine dynamic viscosity corrected for the applied temperature and fluid pressure following Kestin et al. (1981); ΔP_P is the difference in fluid pressure across the specimen in Pa; A is the cross-sectional area of the cylindrical specimen in m^2, and L is its length in m.

During permeability measurements upstream and downstream fluid volumes are monitored, in a valid test it is expected that the two readings are matching within experimental uncertainty (i.e. as much fluid comes out of the sample as it has been pumped in). In the analysed dataset, the difference between the injected and produced fluid volumes is within < 1%, with one exception where it was as high as 3 % (Sample 2498 from Harvey 3, depth of 1511.65 m).

Curtin University protocol

Brine permeability was measured at room temperature under a confining pressure of 10 MPa and pore pressure of 5 MPa by pumping brine through the sample at varying flowrates. The permeability is derived using Darcy's law as expressed in equation 6.

Results

2497 (Harvey 3 1313 m)

Figure 36 shows differential pressure across the sample during permeability measurement as well as injected and produced fluid volume as a function of time. The derived brine permeability is 145.99 mD (1.44×10^{-13} m^2) and the difference between injected and produced fluids amounts to 0.64%.

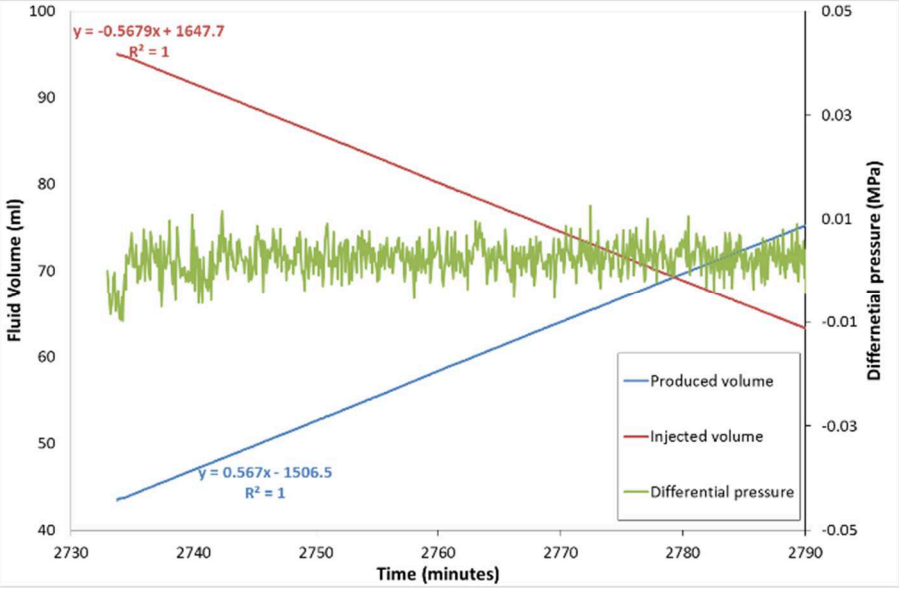


Figure 36 Injected and produced brine volumes and differential pressure as function of time during permeability measurement of sample 2497.

2503 (Harvey 3 1470.2 m)

Figure 37 shows differential pressure across the sample during permeability measurement as well as injected and produced fluid volume as a function of time. The derived brine permeability is 117.77 mD (1.16×10^{-13} m^2) and the difference between injected and produced fluids amounts to 0.06%.

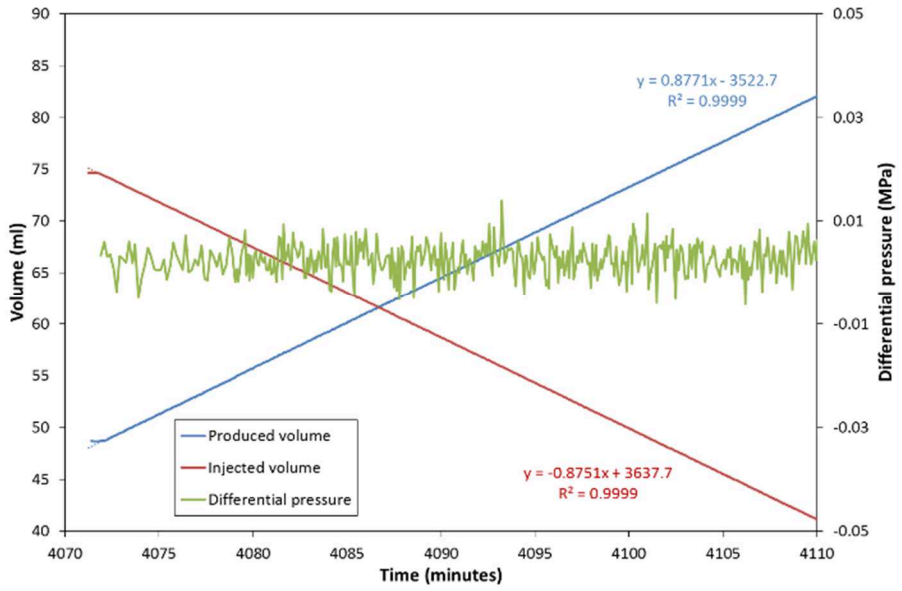


Figure 37 Injected and produced brine volumes and differential pressure as function of time during permeability measurement of sample 2503.

2498 (Harvey 3 1511.65 m)

Figure 38 shows differential pressure across the sample during permeability measurement as well as injected and produced fluid volume as a function of time. The derived brine permeability is 44.89 mD (4.43×10^{-14} m^2) and the difference between injected and produced fluids amounts to 2.64%.

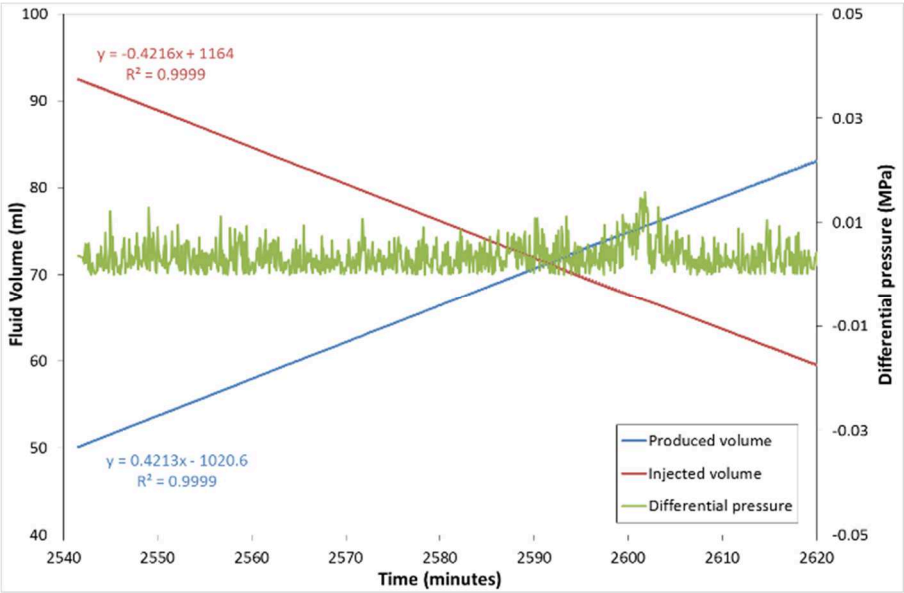


Figure 38 Injected and produced brine volumes and differential pressure as function of time during permeability measurement of sample 2498.

2499 (Harvey 2 1245.15m)

Figure 39 shows differential pressure across the sample during permeability measurement as well as injected and produced fluid volume as a function of time. The derived brine permeability is 19.25 mD (1.9×10^{-14} m^2) and the difference between injected and produced fluids amounts to 0.84%.

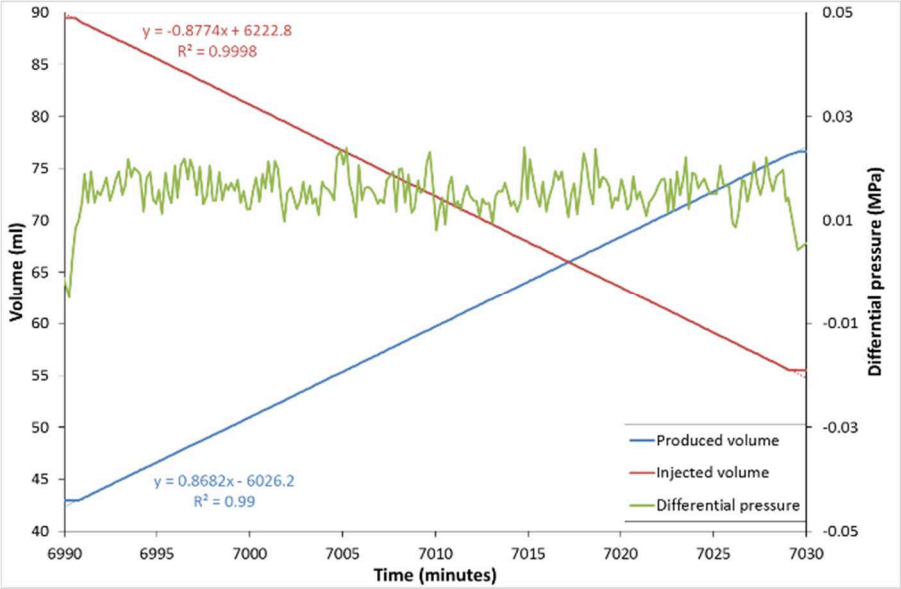


Figure 39 Injected and produced brine volumes and differential pressure as function of time during permeability measurement of sample 2499.

2500 (Harvey 2 1247.5 m)

Figure 40 shows differential pressure across the sample during permeability measurement as well as injected and produced fluid volume as a function of time. The derived brine permeability is 22.97 mD (2.27×10^{-14} m^2) and the difference between injected and produced fluids amounts to 0.92%.

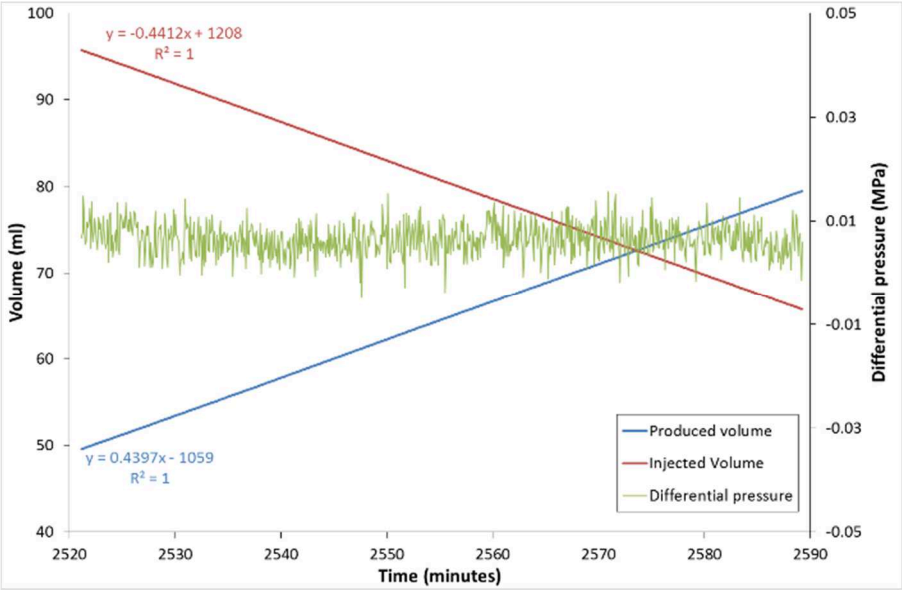


Figure 40 Injected and produced brine volumes and differential pressure as function of time during permeability measurement of sample 2500.

2501 (Harvey 2 1344.65 m)

Figure 41 shows differential pressure across the sample during the permeability measurement as well as injected and produced fluid volume as a function of time. The derived brine permeability is 22.29 mD (2.20×10^{-14} m^2) and the difference between injected and produced fluids amounts to 0.40%.

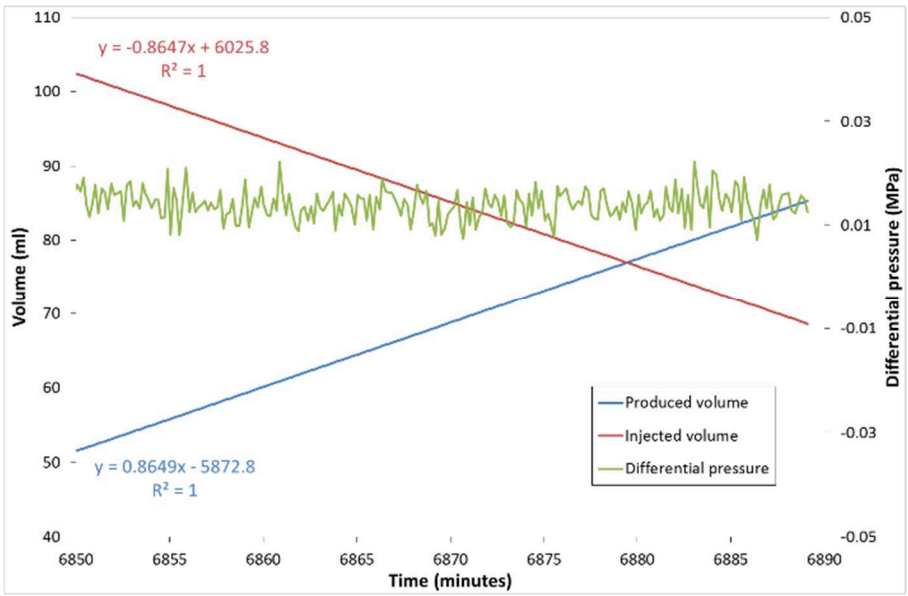


Figure 41 Injected and produced brine volumes and differential pressure as function of time during permeability measurement of sample 2501.

2502 (Harvey 2 1347.5 m)

Figure 42 shows differential pressure across the sample during permeability measurement as well as injected and produced fluid volume as a function of time. The derived brine permeability is 14.24 mD (1.41×10^{-14} m^2) and the difference between injected and produced fluids amounts to 0.64%.

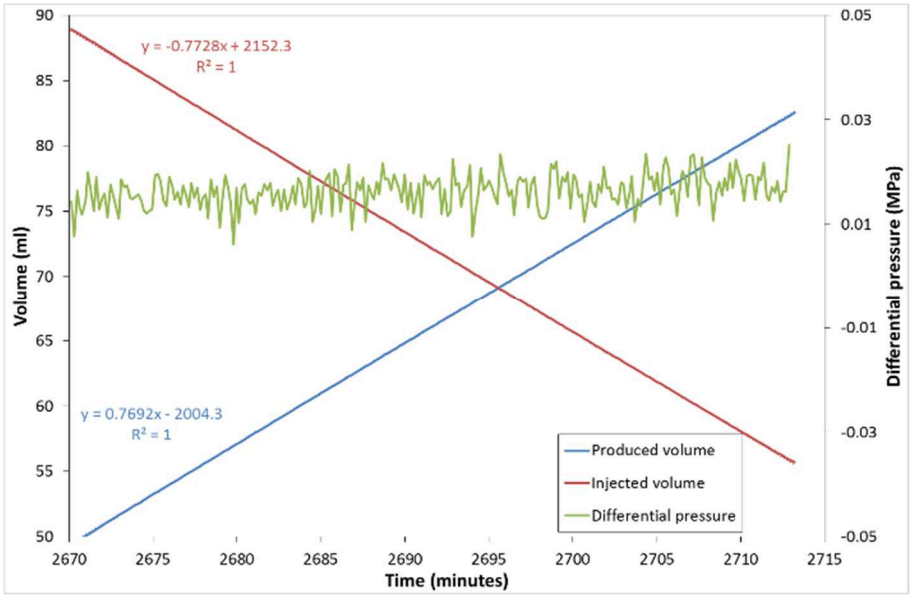


Figure 42 Injected and produced brine volumes and differential pressure as function of time during permeability measurement of sample 2502.

Sample H4-1 (1797.1)

Figure 43 shows differential pressure across the sample and permeability measured while injecting brine at different flowrates. Measurements conducted under pore pressure of 5 MPa and confining pressure of 10 MPa. Derived average permeability of the sample is 33.41 mD.

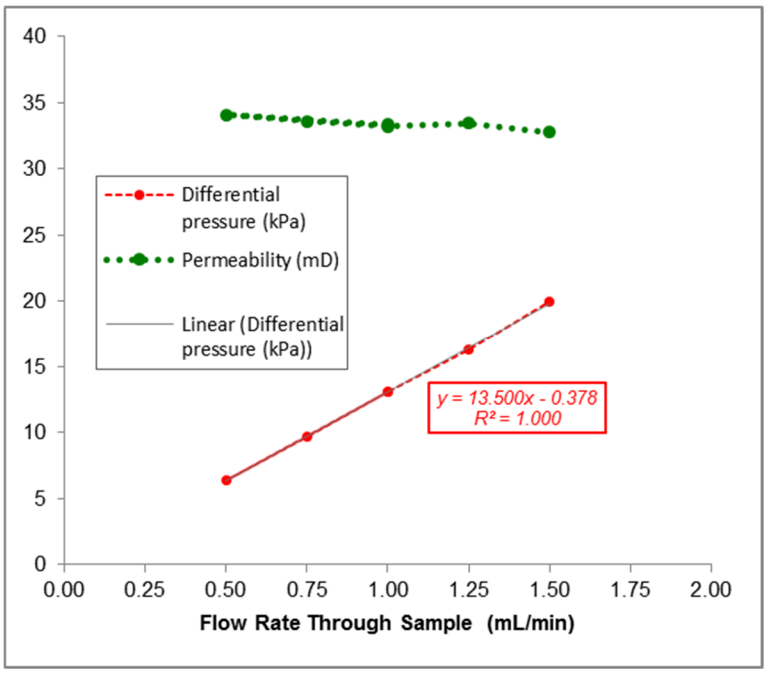


Figure 43 Permeability and differential pressure across the sample dependency on flowrate measured at room temperature and pore pressure of 5MPa.

Sample H4 1797.5

Damage of the sample during saturation stage led to the failure of conducting permeability measurements. During the subsequent part of the tests where the sample was flooded by brine the rubber jacket inside the Hoek cell was damaged and the hydraulic oil intruded the sample. The oil cleaning procedure led to the fracturing of the sample (Figure 44) and it was therefore discarded.

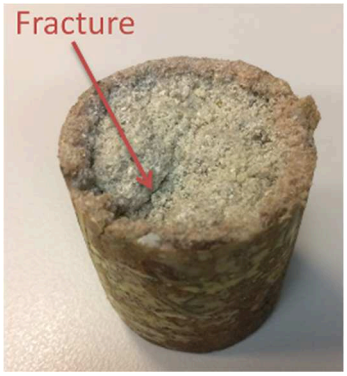


Figure 44 Ruptured Harvey 4 sample after flooding with brine and oil.

Sample H4 (1800.4)

Figure 45 shows differential pressure across the sample and permeability measured while injecting brine at different flowrates. Measurements conducted under pore pressure of 6 MPa and confining pressure of 12 MPa. Derived average permeability of the sample is 0.88 mD.

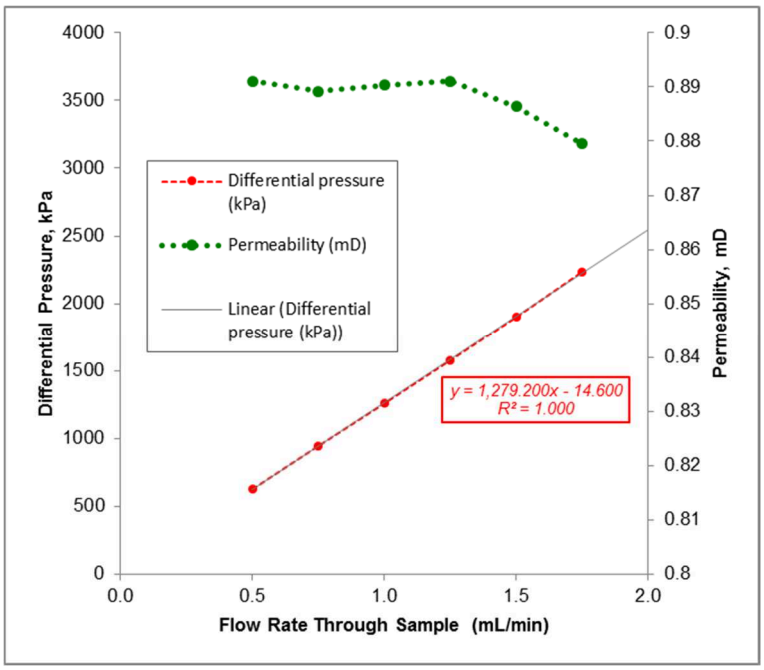


Figure 45 Permeability and differential pressure across the sample dependency on flowrate measured at room temperature and pore pressure of 6 MPa.

Sample H4 (1796.8)

Figure 46 shows differential pressure across the sample and permeability measured while injecting brine at different flowrates. Measurements conducted under pore pressure of 6 MPa and confining pressure of 12 MPa. Flowrate is increased from 1 mL/min to 4 mL/min at increments of 0.5 mL/min and then decreased to 1 mL/min. Derived average permeability of the sample is 810 mD.

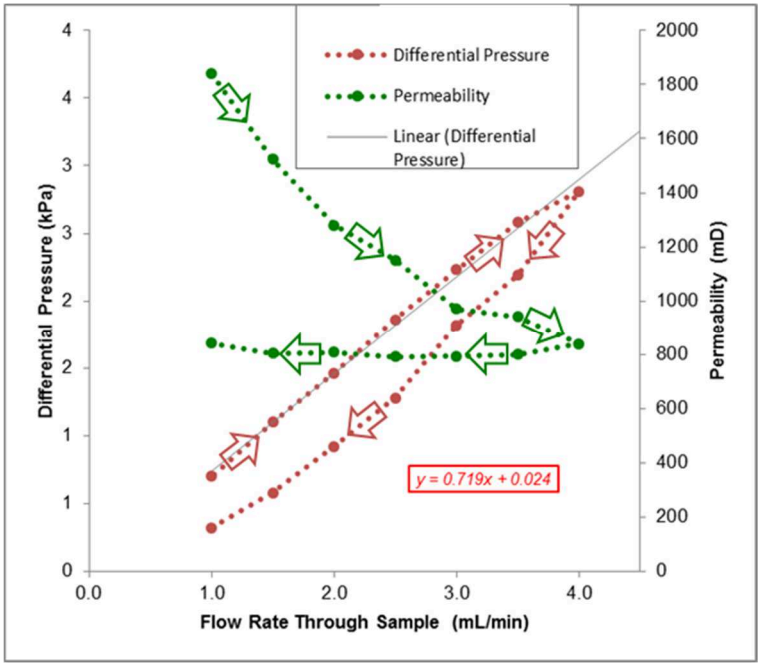


Figure 46 Permeability and differential pressure across the sample dependency on flowrate measured at room temperature and pore pressure of 6 MPa.

Sample H4 1795

Figure 47 shows differential pressure across the sample and permeability measured while injecting brine at different flowrates. Measurements conducted under pore pressure of 6 MPa and confining pressure of 12 MPa. Flowrate is increased from 0.25 mL/min to 2.00 mL/min at increments of 0.25 mL/min and then decreased to 0.25 mL/min. Derived average permeability of the sample is 5.49 mD.

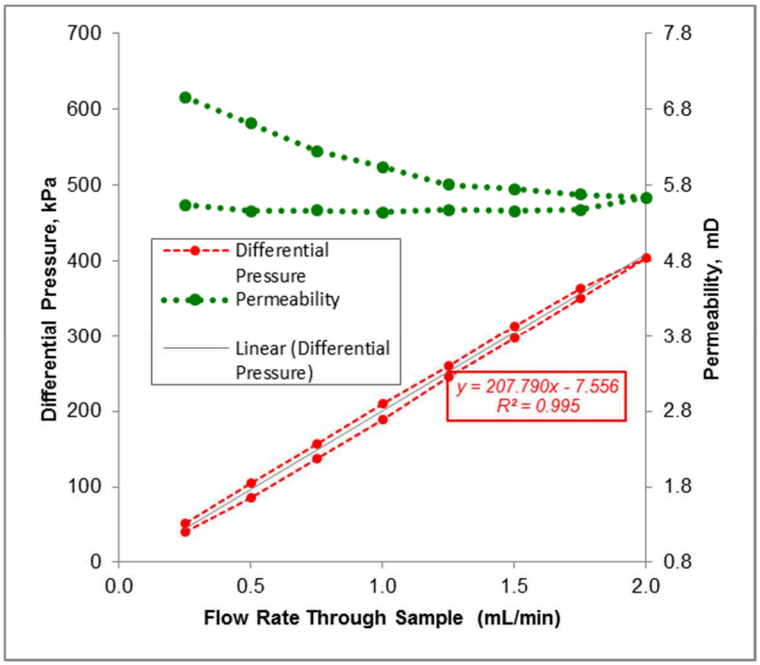


Figure 47 Permeability and differential pressure across the sample dependency on flowrate measured at room temperature and pore pressure of 6 MPa.

Sample H3 (1549.6)

Figure 48 shows differential pressure across the sample and permeability measured while injecting brine at different flowrates. Measurements conducted under pore pressure of 6 MPa and confining pressure of 12 MPa. Flowrate is increased from 0.5 mL/min to 3.00 mL/min at increments of 0.5 mL/min and then decreased to 0.5 mL/min. Derived average permeability is 470 mD.

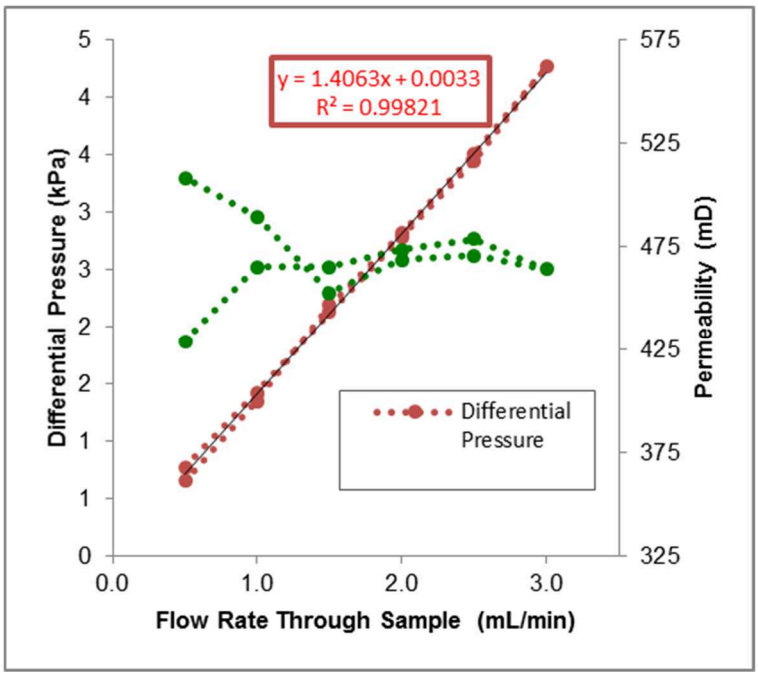


Figure 48 Permeability and differential pressure across the sample dependency on flowrate measured at room temperature and pore pressure of 6 MPa

Table 4 summarises the experimental measurements of porosity and permeability (gas and brine) illustrated above.

Borehole	Depth (m)	Sample ID	k brine (mD)	k gas (mD)	Porosity from gas (%)	Protocol
Harvey 3	1313	2497	145.99	391	18.3	NGL
Harvey 3	1470.2	2503	117.77	126	20.2	NGL
Harvey 3	1511.65	2498	44.89	495	20.7	NGL
Harvey 2	1245.15	2499	19.34	362	17.0	NGL
Harvey 2	1247.5	2500	22.97	99	16.8	NGL
Harvey 2	1344.65	2501	22.29	1941	19.9	NGL
Harvey 2	1347.5	2502	14.24	279	18.5	NGL
Harvey 3	1549.6	H3-26	470	2263	18.4	Curtin
Harvey 4	1795	H4-3	5.49	25.2	18.92	Curtin
Harvey 4	1796.8		820	651	18.74	Curtin
Harvey 4	1797.1	2313	33.41	689	20.2	Curtin
Harvey 4	1797.5	H4-2	N/A	570	19.4	Curtin
Harvey 4	1800.4	H4-4	0.88	2.7	15.74	Curtin

Table 4 Results of the brine permeability tests and comparison with the gas permeability measurements conducted on the same plugs.

3C: Permeability anisotropy

Jeremie Dautriat[1] and Shane Kager[1]

[1]CSIRO Energy

Introduction

This chapter contributes aims to provide new data of brine permeability anisotropy and its dependency with pressure to assess injectivity potential of the Lesueur formation. Anisotropy of permeability is of fundamental importance for CO_2 injectivity, plume migration and containment. Delle Piane et al. (2013) showed that strong fluctuation of petrophysical properties, such as porosity (28% of variation retrieved from density log data) and permeability (up to 6 orders of magnitude retrieved from NMR log data), are mainly controlled by the lithofacies (heterogeneity and layering) for Wonnerup and Yalgorup members in Harvey 1. Accounting for the layered nature of the sediments, Delle Piane et al. (2013) studied the permeability of a pair of 15 plugs cored parallel and normal to the bedding planes. The permeability across bedding ranges between 0.01 and 3mD while along bedding permeability ranges between 38-580mD (Delle Piane et al., 2013). The authors concluded that the anisotropy of gas permeability measured within the Wonnerup sandstones is likely a result of the cross bedded nature of the sandstone, associated with significant grain size variation between beds. The authors also emphasized that the effect of bedding can be enhanced by compaction at depth acting mainly normal to the sedimentary planes. Finally, it has been shown that a strong discrepancy exists between gas and brine permeability in the Harvey 1 samples.

Assuming that permeability is defined by a symmetric tensor of second rank (Bernabe, 1992), the use of a pair of companion samples is the most common approach to derive anisotropy permeability and its pressure dependency (Gray et al., 1963; Zoback and Byerlee, 1975; Zhu and Wong, 1997; Gehne and Benson, 2017). However, the interpretation of the permeability anisotropy might be affected by sample to sample heterogeneity. Ideally, the pressure dependency of this parameter should be retrieved from a single cylindrical sample, using a triaxial cell (Dautriat et al., 2009), or a single cubic sample, using a true triaxial cell (Schutjens and De Ruig, 1997). This project is the opportunity to further investigate the brine permeability anisotropy of the Yalgorup and Wonnerup formations through the development of a non-routine experimental equipment. The new apparatus introduced in this chapter is located in CSIRO Geomechanics and Geophysics Laboratory and allows the measurement of directional permeability of a single core plug combined with acoustic measurements under in-situ conditions (of temperature, confining and fluid pressure.

Experimental set-up adapted to directional permeability measurements

Autonomous triaxial cell

The triaxial cell used in this study is an Autonomous Triaxial Cell (ATC) that has been modified to measure the permeability of a single sample along and orthogonal to its symmetry axis. A schematic of the rig is presented in Figure 49. The confining pressure and axial stress are controlled by two independent pumps (maximum pressure 50MPa at the time of the project). A pore pump is used to generate fluid flows through the rock sample with a maximum pore pressure of 30MPa. This pump can be programmed to perform stepwise flow rates at a constant pore pressure. A backpressure device maintains the pore pressure constant at the outlet of the pore system during the permeability measurements. Two differential pressure sensors, with measurement range of 0-250 mbars and 0-1200 mbars, are available to record the induced pressure gradient. Since the dynamic viscosity of the used fluid is temperature dependent, all the pore lines and the cell are placed inside an oven.

The cylindrical sample is placed into a rubber sleeve to isolate it from the confining oil and apply internal pore pressure and flows. The axial and radial deformations are measured respectively by 2 internal parallel LVDT sensors (of resolution 1 µm) and an internal radial extensometer (of resolution 2 µm) fastened on the core sleeve. The LVDT sensors monitor the displacement between the top and bottom platens. The axial strain εa is deduced from the shortening of the sample. The radial extensometer fastened on inserts moulded

in the elastomer core sleeve, provides one orthogonal measurements of the radial strains εr. Bulk or volumetric strain is calculated from the axial and radial strains by the relation εv = εa + 2εr.

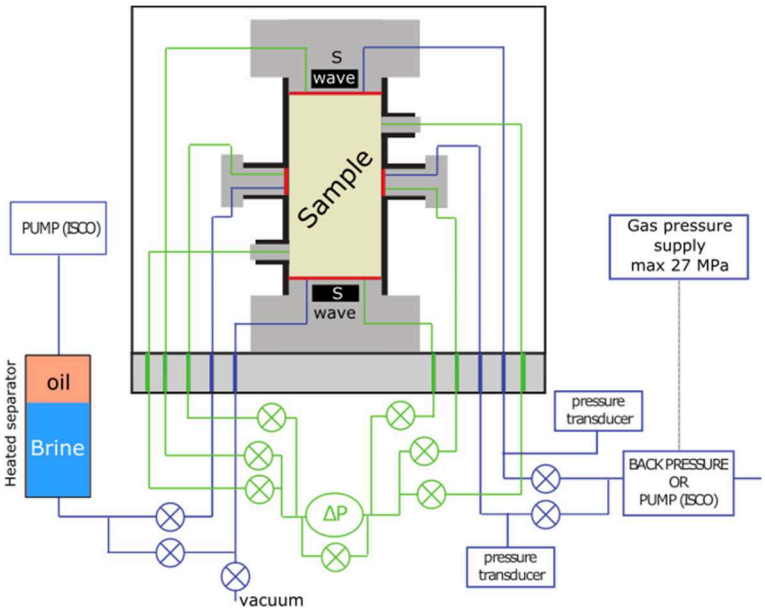


Figure 49 Schematics of the modified Autonomous Triaxial Cell dedicated to directional permeability measurements. The blue pore lines correspond to the flow line, while the green ones represent the pressure ones. Flow paths and pressure points are selected by opening the corresponding valves.

Permeability measurements and calculations

Conventional cells like those used for the measurements presented in module 2B above allow the measurement of permeability only in the longitudinal direction. The innovative feature of the modified ATC lies on the core sleeve which is equipped with radial flow ports, hence allowing measurements of permeability along two orthogonal directions. In addition, the core sleeve equipment also allows an additional measurement of axial permeability through pressure sampling lateral ports. Note that regardless of the investigated permeability direction, the measurements are done by applying successive constant flow rates through the sample while recording associated differential pressure between two selected pressure ports. A minimum of 4 independent flow rates, ideally 5, are applied until steady state pressure response takes place.

Axial permeability measurements

As shown in Figure 50, classical permeability measurement is obtained by applying a constant flow between the top and bottom platens while measuring associated pressure drop between two pressure ports located in each platen. We refer to this measurement as axial permeability along the full length of the sample, k_{ax_FL}, and is derived using Darcy's law:

$$\frac{Q}{A} = \frac{k_{ax_FL}}{\mu}\frac{\Delta P_p}{L} \qquad \text{Equation 7}$$

With Q, the applied flow rate, ΔPp, the induced differential pressure, μ, the dynamic viscosity of the fluid, A, the sample surface area and L, the sample length.

Alternatively, a second measurement of vertical permeability is obtained by recording the differential pressure induced by an axial flow, using two fluid pressure samplers in contact with the sample lateral surface

(see Figure 50). These pressure ports are located at a distance *d* = 24 mm apart and roughly 7.5 mm far from the sample ends. We refer to this measurement as intermediate, k_{ax_int}, and is derived as:

$$\frac{Q}{A} = \frac{k_{ax_int}}{\mu} \frac{\Delta P_p}{d} \qquad \text{Equation 8}$$

This lateral pressure-sampling configuration avoids the inherent end-effects acting in the vicinity of the interfaces between the sample and the pistons (Korsnes et al., 2006; Dautriat et al., 2009; 2011).

Radial permeability measurements

The core sleeve is also equipped with specially designed radial flow ports in contact with the sample's lateral surface for permeability measurements in one radial direction referred to k_{rad}. As shown in Figure 50, an injector port is facing a receptor port along the sample diameter to allow fluid flow and differential pressure sampling. To compute the permeability in the vertical direction, Darcy's law is modified to take into account the deviation from cylindrical to ellipsoidal shape of the flow lines by the introduction of a geometrical factor G (Bai et al., 2002):

$$\frac{Q}{A_r} = G \frac{k_{rad}}{\mu} \frac{\Delta P_p}{D} \qquad \text{Equation 9}$$

with A_r the surface area of the radial ports, and *D* the diameter of the sample. The Geometrical Factor has been determined based on the calibration measurements reported below.

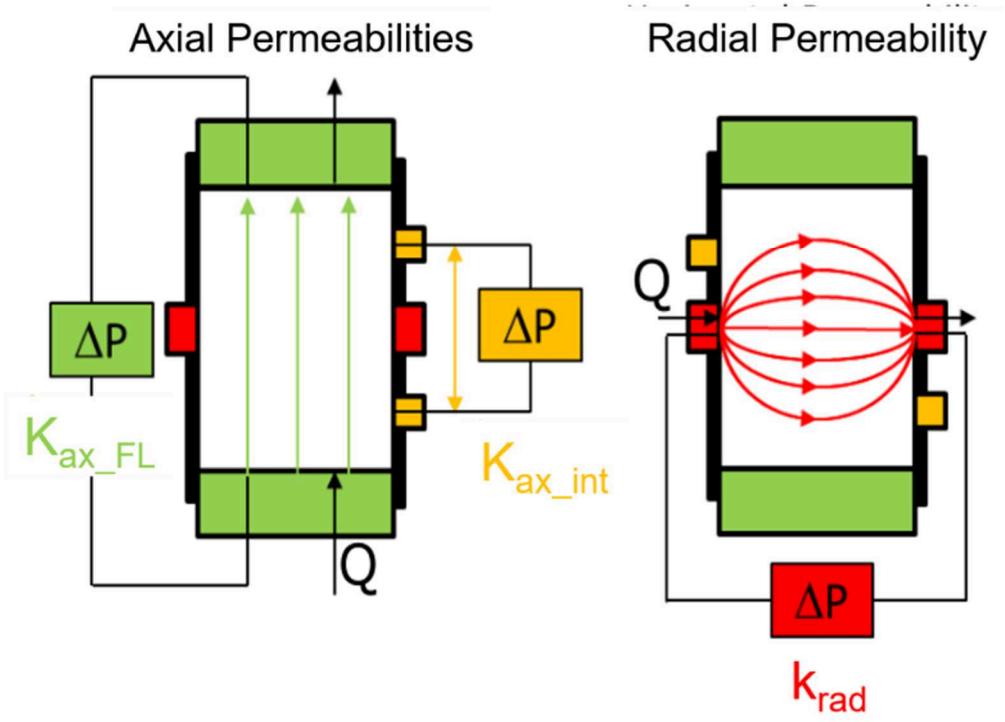


Figure 50 Schematics of flow lines and differential pressure measurement location for Vertical and Horizontal Permeability configurations.

Experimental protocol

The experimental protocol is reported in Figure 51. The studied samples are initially dried for a minimum of 48h prior to be mounted in the rig. An initial confining pressure of 0.7 MPa is applied using a buffer bottle of compressed air, this allows to ensure a slight pre-constrain on the sample while heating. The whole system is then closed and the temperature increase up to the requested in-situ conditions. Once the temperature is

reached, i.e. after one night, the confining pressure is controlled by a stepping motor pump. The sample is first subjected to a hydrostatic pressure increase up to 47 MPa at 0.5 MPa/min and decrease down to 5 MPa at the same rate. During the whole cycle of confining pressure loading/unloading, S-waves (and precursory P-waves) are recorded approximatively every minute (results presented in Section 4B). The pore line system is then connected to a vacuum pump and vacuum is applied for at least 2 hours. The sample is saturated with a synthetized formation brine using the pore pump at a constant 3 MPa pore pressure. Once the injected volume is equilibrated, gas pressure of 3MPa is applied on the membrane of the Back-Pressure Regulator. To evacuate potential residual gas trapped in the pore system, the sample is flushed at low flow rate, at least one pore volume is injected at 1 ml/min, in the vertical and horizontal direction successively. First permeability measurements are performed at 2MPa effective pressure, k_{ax_FL}, k_{ax_int} and k_{rad} successively. Each measurement is achieve by applying successive increment of flow rate, corresponding to 20, 40, 60, 80 and 100% of a maximum rate set to cover the full measurement range of the differential pressure transducers. Depending on the permeability path investigated and the considered sample properties, this maximum value ranges typically between 2 and 30 ml/min. Each increment is maintained constant until a steady state value of the differential pressure is reached, commonly between 5 and 20 minutes. Once the 3 measurements are performed the confining pressure is increased up to 13 MPa at 0.5 MPa/min, i.e. an effective pressure of 10 MPa, and ultrasonic measurement are taken. The permeabilities are measured at 10 MPa effective pressure. The sample will be stepwise loaded by increment of 10 MPa up to the limit of the cell (50 MPa) and permeabilities will be taken at each stage. Finally, confining pressure is decreased and pore pressure is increased to reach the in-situ conditions at which permeabilities are measured.

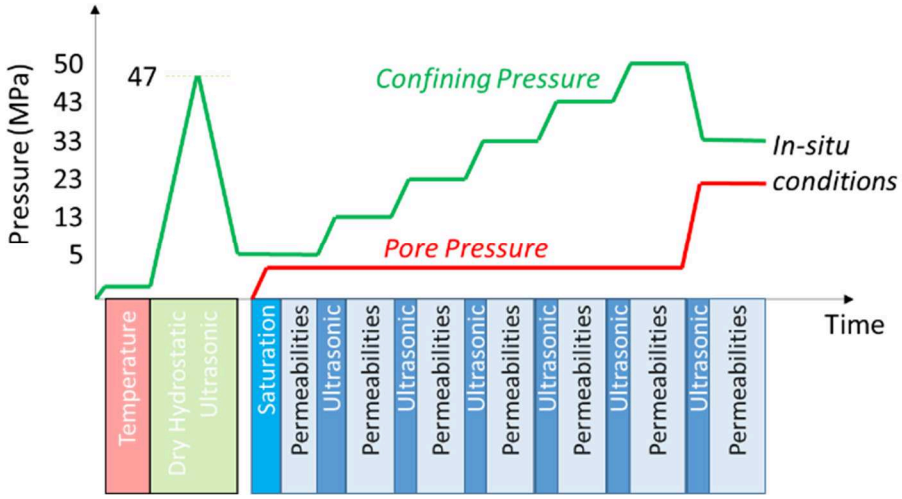


Figure 51 Experimental protocol: Loading path and associated measurements performed at each stage.

Calibration

A preliminary test has been performed to determine the geometrical factor to correct the radial permeability measurements. For this purpose, the Donnybrook Sandstone has been selected from the CSIRO rock collection. This sandstone presents a homogeneous structure with no apparent layering or bedding planes. From previous studies, it is known that permeability is isotropic (based on gas permeability measured on two independent samples cored orthogonal to each other). The mean gas permeability of this sandstone is of 40 mD. As shown by Dautriat et al. (2009), the geometrical factor is highly dependent on the geometry of the lateral injector and the sample dimensions. A sample of 50.2 mm in length and 38.4 mm in diameter has been prepared to be representative of the Harvey 2 and Harvey 3 sample dimensions. Following the same protocol described above, 3 sets of permeability measurements have been taken at a constant pore pressure of 3 MPa and at successive confining pressures of 5, 10 and 15 MPa. The temperature was set at 50 ˚C and the sample

was saturated with the same formation brine used for the experiment described in section 3C. Figure 52 presents the response of the differential pressure induced by successive increases of the flow rates for the 3 permeability measurements at 2 MPa effective pressure. The mean differential pressure value is then plotted against each increment of flow rate to derive the slope $\Delta P/Q$, which is directly used to calculate the permeability. The values of the directional permeabilities of the Donnybrook sandstone are reported in Table 5. Regardless of the measurement direction, the permeability decreases with the increasing effective pressure. In addition, the difference between both axial permeability measurements is within the measurement uncertainty. Similarly to the homogenous Bentheimer and Fontainebleau sandstones (Dautriat et al., 2009), the full length permeability is more sensitive to the confining pressure increase than the intermediate one. Finally, assuming that the sample is homogeneous and its permeability isotropic, the ratio between k_{ax_FL} and k_{rad} provides a direct estimate of the Geometrical Factor. The calculated G value is 0.23 and is not dependent on the pressure applied to the sample, which is to be expected for a hydrostatic loading of an homogeneous sample.

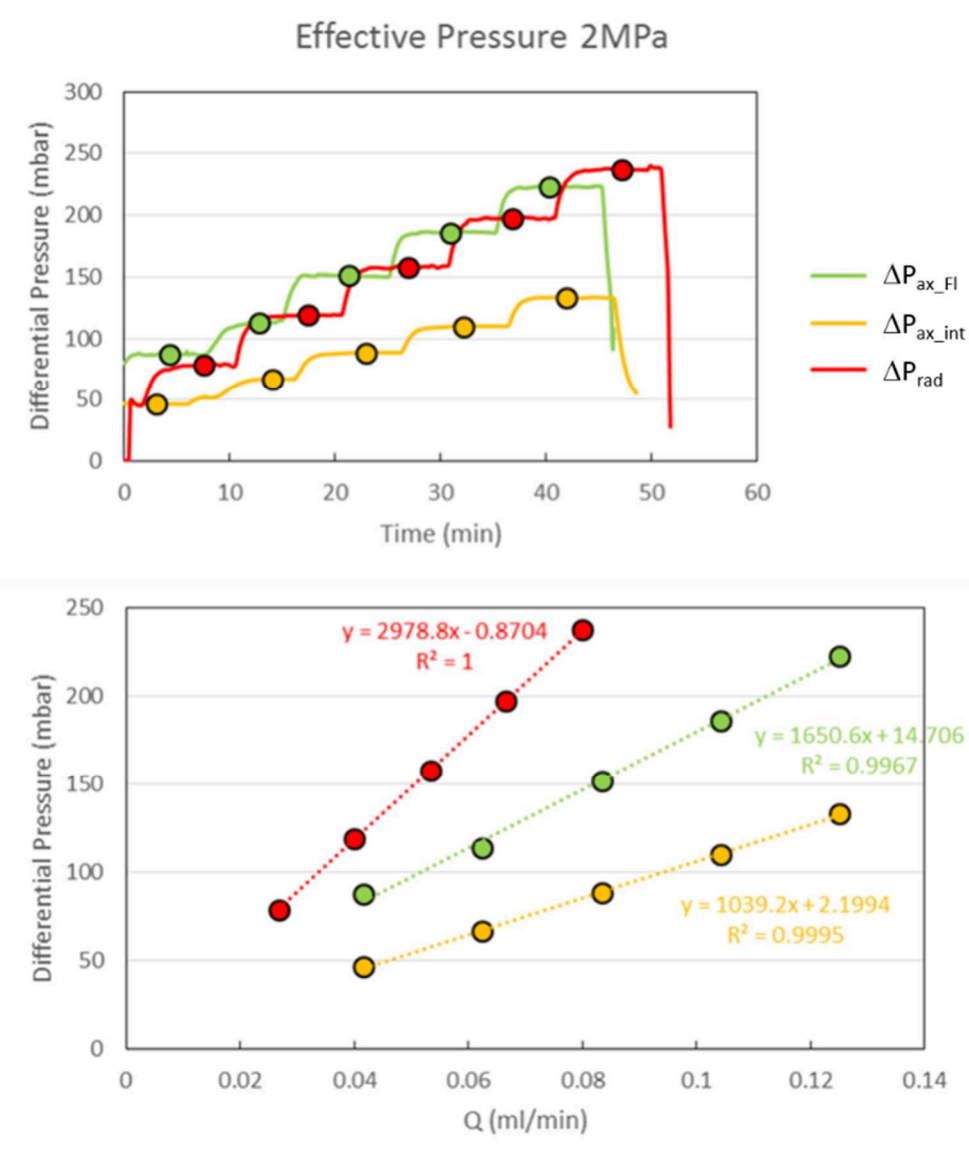


Figure 52 Typical response of the differential pressure evolution for successive steps of imposed flow rate through the sample. Not that the range of applied flow rates may vary depending on the direction of injection and is selected to remain below the differential pressure transducer range (0-250 mbar).

P_{eff} (MPa)	k_{ax_FL} (mD)	k_{ax_Int} (mD)	k_{rad} (mD)	G
2	2.44	2.29	10.72	0.23
12	2.01	2.11	9.13	0.22
22	1.98	2.09	8.48	0.23

Table 5 Evolution of the directional permeability and geometrical factor values obtained on the Donnybrook sandstone.

Tested samples

The list of the sample tested using the protocol described above are reported in Table 6. Among the tested samples, 2513 is the only one of the size required for standard geomechanical testing, i.e. with a diameter to length ratio of 1:2. This sample has been tested using a specially moulded Viton core sleeve with provision to insert pore fluid ports. Due to the poorly consolidated nature of the sandstone and the large pore and grain size, this thin membrane indented the sample circumference surface and ruptured at high pressure into the large surface pores. To remediate this and to adapt to the size of the remaining samples, a shorter and thicker sleeve has been machined was for the rest of the testing program.

Borehole	Depth (m)	CSIRO id	Unit	Porosity (%)	PV (cc)	k_{gas} (mD)	CP (MPa)	PP (MPa)	T (°C)
Harvey 3	1417.90	2513	Y	20.6	19.03	23	32.04	14.18	51.94
Harvey 3	1472.10	2514	W	21.0	11.25	615	33.27	14.72	52.97
Harvey 3	1544.05	2708	W	17.4	9.83	3356	36.23	15.44	55.56
Harvey 2	1245.80	2515	W	19.1	9.62	1111	28.16	12.46	48.67
Harvey 2	1247.90	2516	W	17.4	9.39	260	28.20	12.48	48.71

Table 6 Tested samples from Harvey 2 and Harvey 3. Y = Yalgorup; W = Wonnerup. PV = pore volume; k_{gas} = gas permeability; CP = confining pressure; PP = pore pressure; T = temperature.

As shown in Figure 53, the samples present various degree of heterogeneities (i) from sample to sample and (ii) internally for sample 2708 and 2516. 2708 shows strong variation of the granulometry along the sample axis, while 2516 shows evidence for fine layering of dense material along the sample axis, parallel to the sedimentary bedding planes. All samples were placed into the core sleeve, so that the axial permeability was measured across the structural lineation, therefore measuring horizontal permeability. The radial permeability measurement corresponds to vertical permeability.

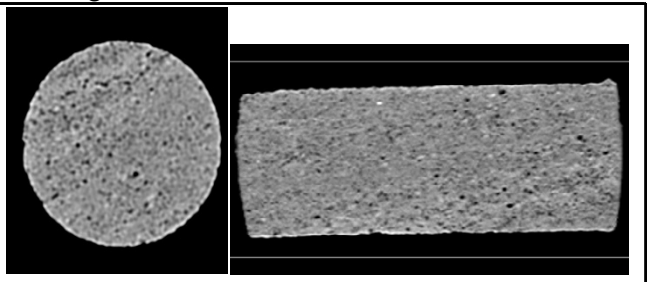
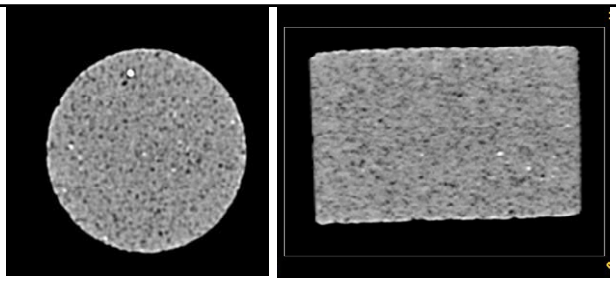
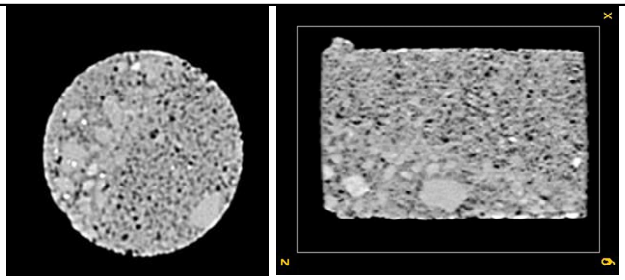
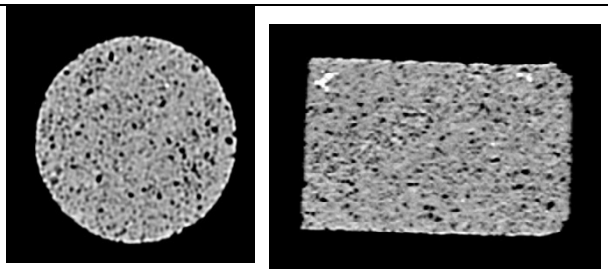
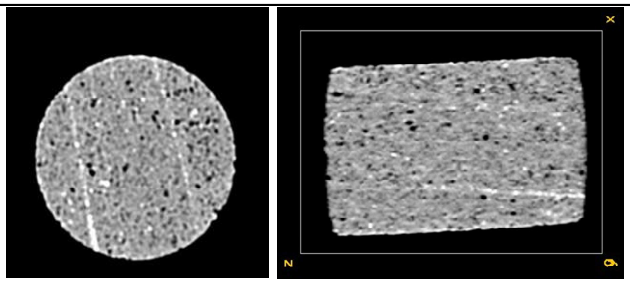
Sample	Photograph	X- Ray CT	
		Longitudinal	Axial
2513			
2514			
2708			
2515			
2516			

Figure 53 Photographs, axial and longitudinal CT-scan slices of the tested samples.

Results

Sample 2513 (Harvey 3 1417.90 m)

As reported in the previous section, sample 2513 presents the optimal 1:2 diameter to length to perform deformation experiments. The sample ends has been flatten prior to the test such as the initial length of the sample is of 79.23 mm.

Figure 54 reports the pressure dependency of the 3 sets of permeability k_{ax_FL}, k_{ax_Int} and k_{rad} up to 30 MPa of effective pressure. The permeability scattering is less than 10% and can be considered as isotropic, which is in agreement with the pre-testing CT-scanner image of the sample. The mean initial permeability is of 13.3 mD. Regardless of the measurement direction, k_{ax_FL} and k_{rad} strongly decrease at the first increment of effective pressure (40 and 50 % of permeability loss respectively). Between 10 and 30 MPa effective pressure, k_{ax_FL}, k_{ax_Int} and k_{rad} follow a near linear decrease to reach 50, 70 and 35 % of their initial values, respectively. The ratio k_{rad}/k_{ax_Int}, i.e. kv/kh reaches 0.54 at the maximum effective pressure.

P_{eff} (MPa)	k_{ax_FL} (mD)	k_{ax_Int} (mD)	k_{rad} (mD)
1	14.3	12.6	13.0
10	8.7	10.0	6.5
20	7.1	8.9	5.7
30	6.9	8.7	4.7

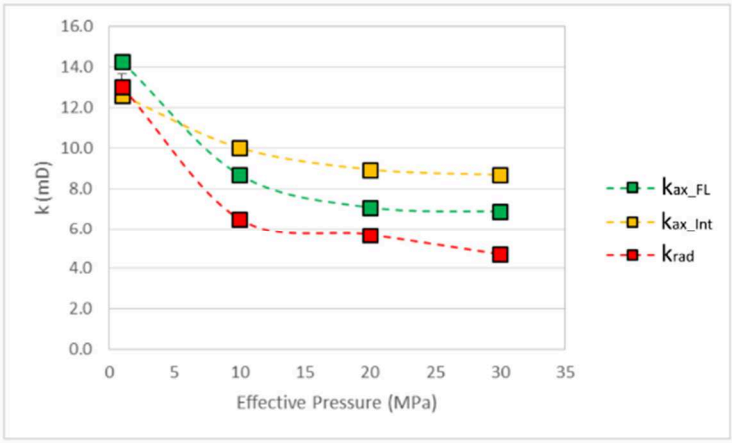


Figure 54 Sample H3-1417.90 (2513) Pressure dependency of the directional permeabilities. No data available above 30MPa effective pressure due to membrane failure.

Sample 2514 (Harvey 3 1472.10 m)

Figure 55 shows the evolution of the directional permeabilities during the brine saturated hydrostatic loading and to in-situ conditions. Despite an apparent homogeneity of sample 2514, a strong discrepancy is observed between the axial (full length) and radial permeability values. This can potentially be induced by end-effects occurring at the interface between the sample and the platens described by Korsnes et al. (2005) and Dautriat et al. (2009). The poor consolidation of the sample precluded an efficient sample preparation due to loosening of the grains at the surface. This probably favoured pervasive damage at the end of the sample during the dry hydrostatic loading and to permeability reduction in this area. As the pressure drop is not affected by such end effects when measured on the intermediate length, it appears more relevant to use this data to quantify the permeability anisotropy. A moderate permeability anisotropy is measured, with an initial ratio between vertical and horizontal permeability of 0.82. The permeability evolves quite linearly with the effective pressure and this initial anisotropy ratio is somehow preserved up to 50 MPa (considering the measurement uncertainty). At in-situ conditions k_{ax_Int} and k_{rad} have been reduced by 64 and 60% of their initial values with the anisotropy remaining almost unchanged. The ratio k_{rad}/k_{ax_Int}, i.e. kv/kh reaches 0.90 at maximum effective pressure and equals 0.88 at in-situ conditions.

P_{eff} (MPa)	k_{ax_FL} (mD)	k_{ax_Int} (mD)	k_{rad} (mD)
2	108.3	339.3	278.6
10	74.9	288.6	182.6
20	76.6	248.0	209.8
30	33.5	207.0	158.3
40	18.6	151.8	111.0
46.5	18.4	121.5	109.7
17.83	11.2	123.6	109.1

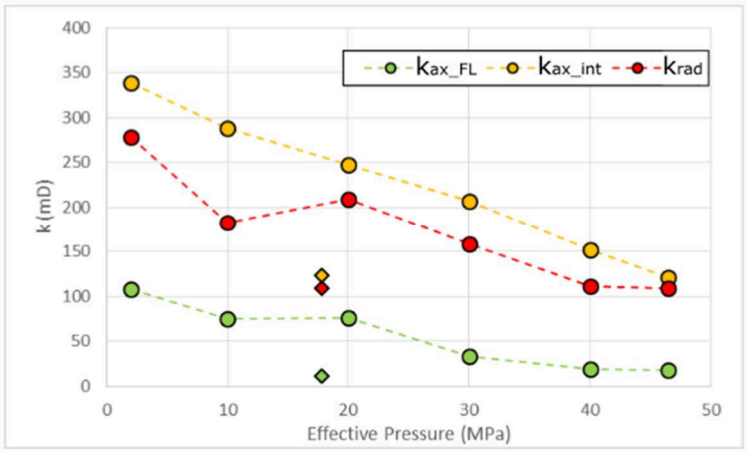


Figure 55 Sample H3-1472.10 (2514) Pressure dependency of the directional permeabilities.

Sample 2708 (Harvey 3 1544.05)

As shown in Figure 53, sample H3-1544.05 is strongly heterogeneous. Figure 56 shows the evolution of directional permeabilities with pressure. As reported in the table, a strong discrepancy is observed between the initial permeability values. The initial permeability in the axial direction is of 613 mD, while the radial one is more than 5 times higher at 3.5 Darcy. This permeability is the highest recorded among the whole set of tested samples. However, it is difficult to relate this apparent anisotropy to the nature of the sample. Based on the location of the pore flow and pressure ports, the discrepancy can mainly be related to a preferential flow path, located between the radial injector and receptor ports (reported schematically in the Figure 57). As shown in Figure 57, a large aggregate of dense grain overlapped with the upper platen flow and/or pressure ports, potentially resulting in a larger pressure drop and an apparent low permeability. Also the upper intermediate pressure port was located in front of the same heterogeneity possibly resulting in abnormal pressure drop sampling. This example illustrates a limitation of our apparatus to derive consistent permeability anisotropy values for sample highly heterogenous.

P_{eff} (MPa)	k_{ax_FL} (mD)	k_{ax_Int} (mD)	k_{rad} (mD)
5	613.3	200.6	3505.9
10	472.2	27.2	2232.1
20	424.4	20.3	1371.1
30	233.4	28.4	1176.8
40	159.4	20.6	1110.9
46.5	98.0	11.3	839.2
20.79	23.9	9.5	388.8

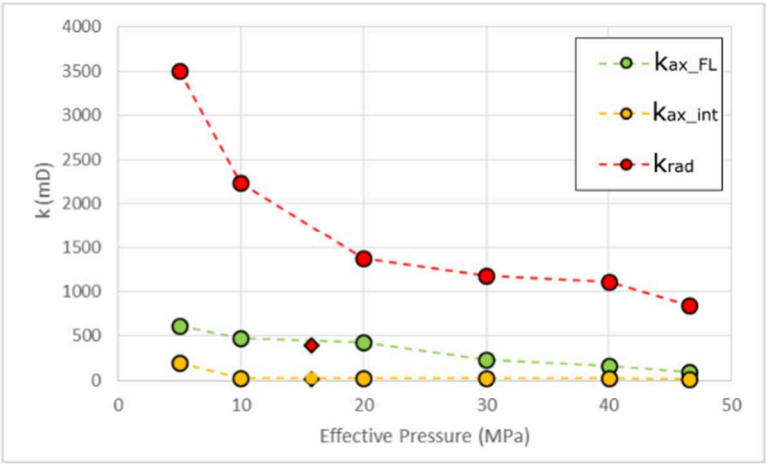


Figure 56 Sample H3-1544.05 (2708) Pressure dependency of the directional permeabilities.

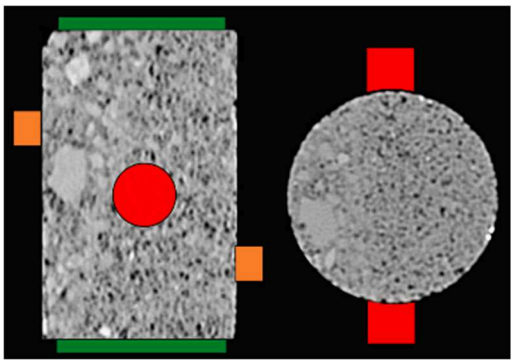


Figure 57 Schematic of the location of the pore flow (axial in green, radial in red) and intermediate pressure ports (orange) with respect to the internal heterogeneities of sample H3-1544.05 (2708).

Sample 2515 (Harvey 2 1245.80 m)

Figure 58 shows the pressure dependency of directional permeabilities measured on sample 2515. No clear evolutions of the permeability can be derived from this test. Compared to the other samples tested, steady state flow regime has been either impossible or difficult to achieve. Several repeat measurements have been attempted at each pressure stage to check for (i) reproducibility of the $\Delta P/Q$ slope at different imposed flow rates and (ii) attempt to reach steady state differential pressure regime. As illustrated in Figure 59, the stability of the differential pressure was not verified at a same confining pressure (example provided for k_{ax_FL} with flow rates ranged between 0.2 and 1 ml/min) leading to a strong uncertainty on the permeability calculation. On the other hand, for some of the measurements, a continuous drift of the differential pressure has been recorded, regardless of the applied flow rates. This behaviour can be associated with fines migration. Indeed, the applied flow rate is prone to mobilize loose grains within the porous network that can potentially clog the pore throats. Both intermediate axial permeability (k_{ax_Int}) and radial (k_{rad}) one have been affected by differential pressure drift, explaining their erratic evolution with pressure. This effects could be minimized by applying lower flow rates at each pressure step, but in that case the induced differential pressure would not be detected by our transducers. Consequently, the permeability results of this test should be disregarded.

P_{eff} (MPa)	k_{ax_FL} (mD)	k_{ax_Int} (mD)	k_{rad} (mD)
5	72.7	468.0	259.8
10	46.1	488.2	210.5
20	41.6	484.9	N/A
30	32.1	481.0	227.0
40	32.5	375.2	217.6
46.5	34.7	391.8	325.7
15.7	32.0	353.6	357.1

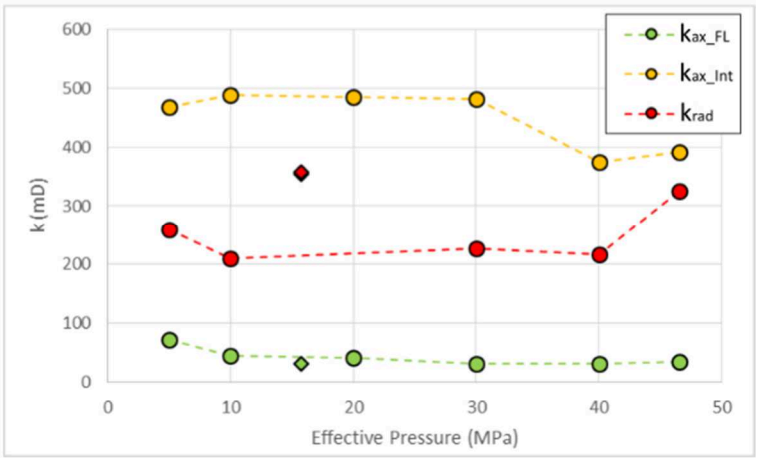


Figure 58 Sample H2-1245.80 (2515) Pressure dependency of directional permeabilities.

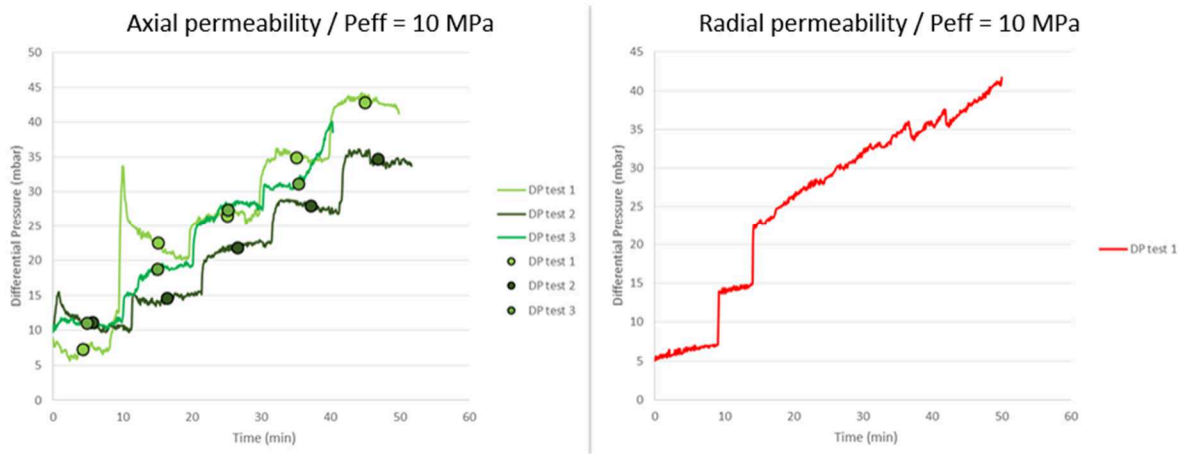


Figure 59 Illustration of unsteady state differential pressure evolution with increasing flow rate due to fine migration within the porous space.

Sample 2516 (Harvey 2 1247.90 m)

Figure 60 presents the evolution of directional permeability with the increasing effective pressure. k_{ax_Int} is missing at 2 and 10MPa effective pressure. Assuming a linear decrease of this permeability with pressure (as observed on previous samples), the initial permeability should be of 105 mD. Again a strong discrepancy is observed between the two horizontal measurements, which can be explained by end-effects at the sample/platen interfaces. Considering k_{ax_Int} and k_{rad} the permeability anisotropy of sample 2516 remains low (8 %), despite the existence of fine layering observed on CT-scan images. The anisotropy increased slightly with the effective pressure, as a potential higher pressure sensitivity in the direction orthogonal to the bedding. The ratio k_{rad}/k_{ax_Int}, i.e. kv/kh reaches 0.57 at maximum effective pressure and equals 0.42 at in-situ conditions.

P_{eff} (MPa)	k_{ax_FL} (mD)	k_{ax_Int} (mD)	k_{rad} (mD)
2	53.9	-	113.5
10	35.7	-	83.5
20	28.1	82.3	75.3
30	20.7	74.7	64.6
40	16.2	57.5	41.6
46.5	12.9	55.8	31.9
15.72	15.1	67.4	28.0

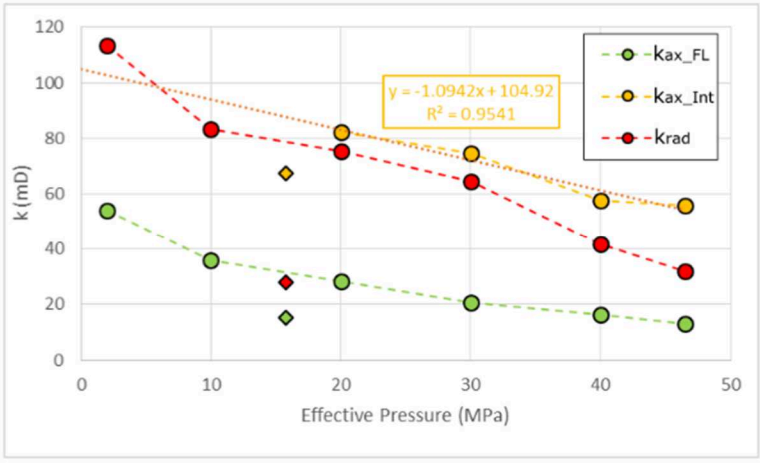


Figure 60 Sample H2-1247.90 (2516) Pressure dependency of directional permeabilities.

Section 3 Discussion and conclusions

Petrophysical characterisation of core plugs from Harvey 2, Harvey 3 and Harvey 4 was obtained by a combination of conventional gas permeametry, laboratory NMR and brine permeability measurements complementing the results of the routine and special core analysis commissioned by DMIRS

Porosity depth trends

The comparison between gas and NMR porosity shown above (Figure 33) indicate that the latter can be used as a reliable petrophysical estimate if NMR logs are available, similar to that which was shown for samples extracted from Harvey 1 (Delle Piane et al., 2013b). Porosity-depth trends derived from laboratory measurements on plugs and from wireline logs are shown in Figure 61A. There is a broad overlap in terms of porosity values and a general trend of decreasing porosity with depth that can be associated with the diagenetic history of the sediments illustrated in Section 2. Normalizing the depth of the specimens and logs by the only correlatable stratigraphic marker of interest (i.e. the Wonnerup to Yalgorup transition) facilitates the interpretation of porosity evolution showing that all the available data recovered from the South West Hub area follows the same trend defined over the thickness of the Wonnerup in Harvey 1. This is qualitatively seen by an overlap of both laboratory and wireline log-derived porosity of the four available boreholes as shown in Figure 61B and in an enlarged section of the 250 m below the Wonnerup to Yalgorup transition (Figure 61C).

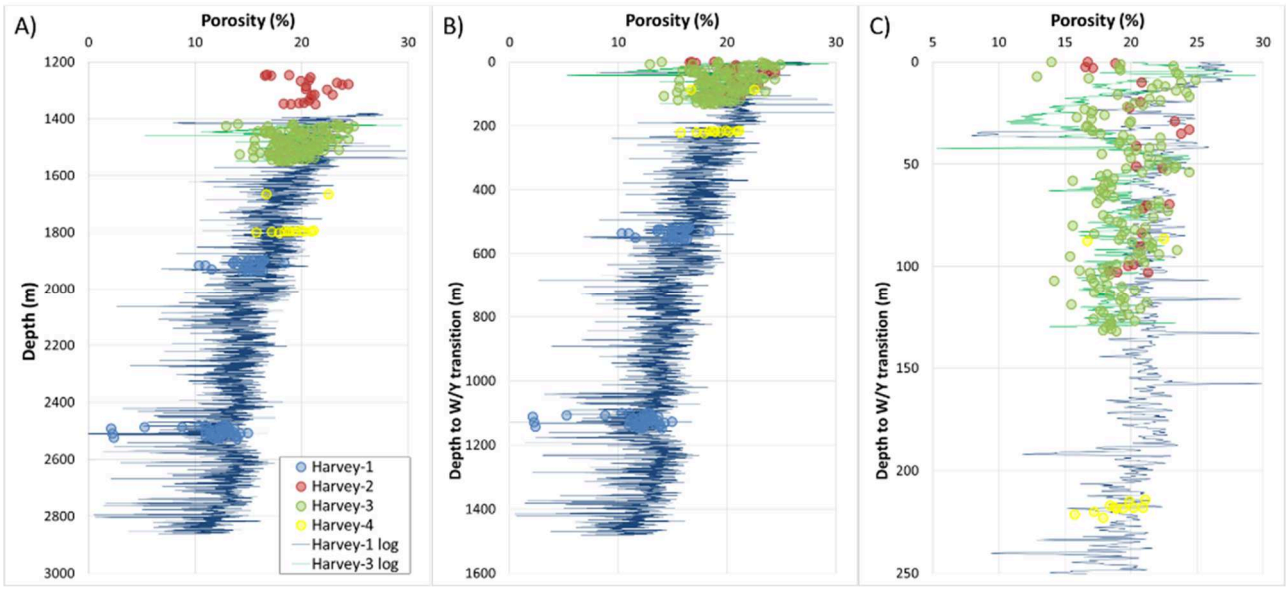


Figure 61 Porosity-depth trends in the South West Hub area. A) Laboratory measured porosity and porosity derived from density logs as function of depth. B) Laboratory measured porosity and porosity derived from density logs as function distance from the Wonnerup to Yalgorup transition. C) Laboratory measured porosity and porosity derived from density logs as function distance from the Wonnerup to Yalgorup transition: showing only the 250 m below the transition.

Comparison between brine and gas permeability

Previous tests on samples from Harvey 1 indicated that the difference between gas and brine permeability can be significant (Delle Piane et al., 2013). The data presented above and that collected as part of the core analysis commissioned by DMIRS and performed by core lab, confirm the observation from the Harvey 1 plugs. Similarly, in rocks from other sedimentary basins brine permeabilities are often found to be significantly lower than gas permeabilities in the same formations (e.g. Villar and Lloret, 2001; Ellis and Singer,

2008). Significant differences between gas and brine permeabilities may occur in reservoirs with concentrations of clays of 5-10 % (Pugh et al., 1991). To overcome this discrepancy authors have proposed empirical correlations to obtain additional permeability values if only one is provided. A review of gas-to-brine correlations for different lithologies can be found in Busch and Amann-Hildenbrand (2013), here we compare our experimental results with the prediction obtained using the correlation of Pugh et al. (1991) based on measurements on 578 sandstone samples:

$$Log(k_{brine}) = 1.047 Log(k_{gas}) - 0.834 \quad \text{Equation 10}$$

Figure 62 shows a comparison of Klinkenberg corrected vs. brine permeability indicating a significant difference of up to one order of magnitude between the two. For gas permeability lower than approximately 400 mD the empirical correlation Pugh et al. (1991) predicts well the experimentally measured brine permeability. For higher gas permeability, the difference between the two methods is less obvious.

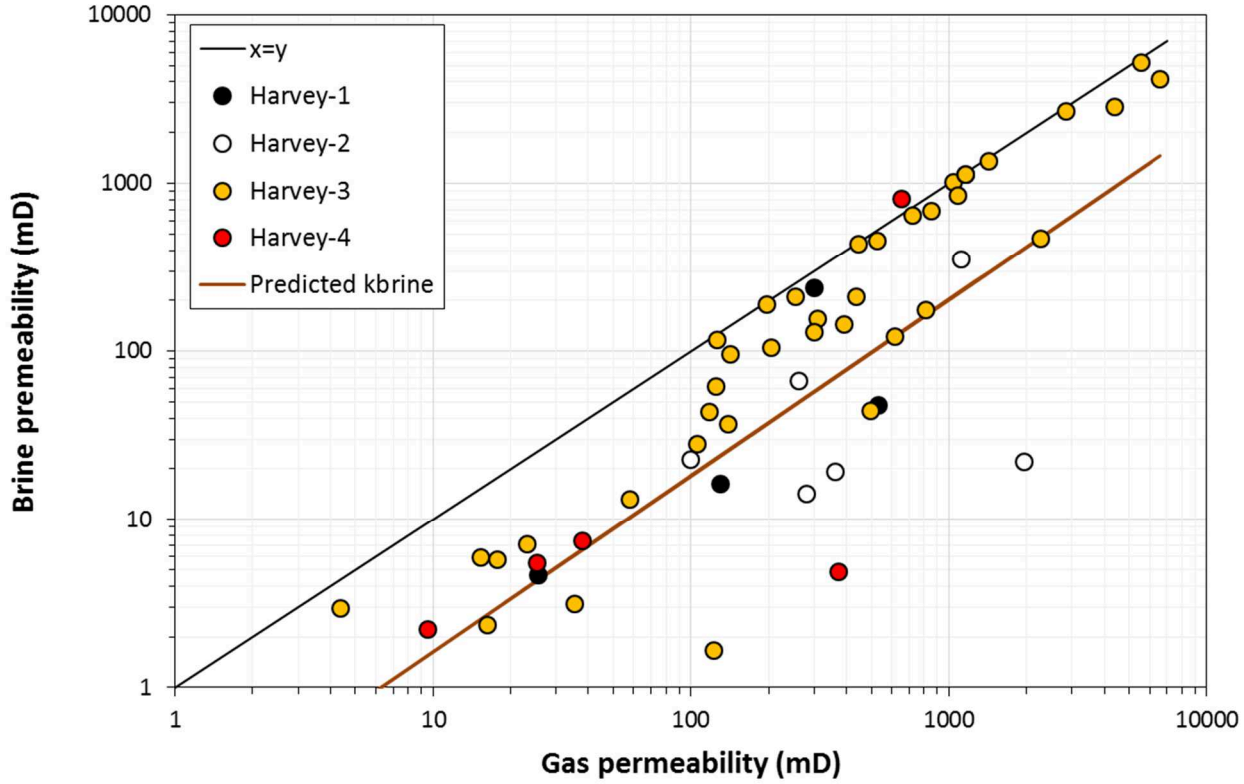


Figure 62 Comparison between Klinkenberg corrected gas permeability and experimentally measured brine permeability. Also shown is the predicted brine permeability from the empirical relationship proposed by Pugh et al. (1991) based on the analysis of 578 sandstone samples (orange line).

It is therefore recommended that Equation 10 is applied to the gas permeability data if these are used to populate the updated geological model of the South West Hub area.

Permeability anisotropy

Fluvial sandstone display stratification and laminations which can affect vertical and horizontal fluid movement at the production time scale. Understanding and quantifying in-situ permeability anisotropy and its distribution in the target reservoir affects the prediction of plume movement as well as decisions on well completion and spacing that will ultimately impact the overall project development. In this project, we developed a new experimental apparatus in the CSIRO Geomechanics and Geophysics laboratory, allowing for the determination of permeability of a single sample in 2 orthogonal directions and the evaluation the

anisotropy of permeability at in situ conditions and as a function of effective pressure. Results indicate that the anisotropy of permeability of the tested samples ranged from low (kv/kh = 0.88, sample 2514) to moderate (kv/kh = 0.41, sample 2516) in samples from the shallow portion of the Wonnerup. These values are in the same order of magnitude as those obtained from simulations of fluid flow through small volumes of samples imaged by X-ray micro tomography. The simulations yielded anisotropic permeability expressed as Kmin/kmax = 0.22 for sample 1924.73m (Harvey 1) and kmin/kmax = 0.17 for sample 1800.42m (Harvey 4) (see Milestone 2 report for the project 7-1215-0263 "Report on insights into pore controls on permeability in Wonnerup").

Absolute values of permeability anisotropy measured on the plugs of the Harvey boreholes are in the same range as those experimentally measured on fluvial sandstones from the Middle Boggy Formation, of Oklahoma (0.23 < kv/kh < 0.80) by laboratory measurements (Yang and Kerr, 2016) and the fluvial Crab Orchard Sandstone (kv/kh = 0.41) from Tennessee (Benson et al., 2003). We note however that previous estimates based on couples of orthogonally oriented plugs extracted from the deeper section of the Wonnerup gave indications of higher permeability anisotropy with kv/kh values as low as 0.01 (Delle Piane et al., 2013b). Such low values have also been reported in Algerian fluvial sandstones by the use of laboratory measurements and confirmed in situ by running vertical interference tests (VITs) with a multiprobe formation tester during openhole (OH) logging (Domzalski et al., 2002). As such these values could be taken as constraints to the range of permeability anisotropy in the Wonnerup to be used in an updated geological model of the South West Hub area.

Fines migration

Measurements with brine show a sensitivity of permeability to the applied flow rate: several example presented in section 3B (most notably in sample H4 1796.8) and 3C (sample 2515 H2-1245.8) show a non-recoverable decrease in permeability with increasing injection rate. This response could be explained by fines migration. Indeed clay mobilization has been reported before to explain the differences in gas permeability before and after multiphase (brine and CO_2) flooding in sample from Harvey 1 (Saeedi et al., 2016a) and after single phase flooding in samples from Harvey 4 (Saeedi et al., 2016a). Xie et al. (2017) used a modelling approach to show that kaolinite particles can indeed be detached during multiphase flow due to induced electrostatic charges at kaolinite to kaolinite interfaces at conditions of pH and brine salinity relevant for the South West Hub. The results presented above further highlight that fluid-rock interactions responsible for clay mobilization are active at the experimental time scale and produce measureable modifications to the permeability of the potential reservoir target. Steady state permeability can be strongly affected by these mechanisms. It should be noted that while fines migration has been investigated in detail for oil and gas production (e.g. Thomas and Crowe, 1981; Tang and Morrow, 1999), current understandings of this process in the context of the geological storage of carbon dioxide are inadequate and this should be given more attention in view of the potential damaging effects to reservoir quality and injectivity.

References section 3

Bai, M., Meng, F., Elsworth, D., & Roegiers, J. C., 1999. Analysis of stress-dependent permeability in non orthogonal flow and deformation fields. Rock Mechanics and Rock Engineering, 32(3), 195-219.

Benson, P.M., Meredith, P.G. and Platzman, E.S., 2003. Relating pore fabric geometry to acoustic and permeability anisotropy in Crab Orchard Sandstone: a laboratory study using magnetic ferrofluid. Geophysical research letters, 30(19).

Bernabé, Y., 1992. On the measurement of permeability in anisotropic rocks. International Geophysics, 51, 147-167.

Busch, A. and Amann-Hildenbrand, A., 2013. Predicting capillarity of mudrocks. Marine and petroleum geology, 45, pp.208-223.

Clennell, M. B., Dewhurst, D. N., Siggins, A. and Raven, M. D., 2006. Shale Petrophysics: Electrical, dielectric and Nuclear Magnetic Resonance studies of shales and clays. Transactions, SPWLA 47th Annual Logging Symposium, June 4-7, paper KK, 13pp.

Coates, G.R., Peveraro, R.C.A., Hardwick, A., Roberts, D., 1991. Magnetic resonance imaging log characterized by comparison with petrophysical properties and laboratory core data. Proceedings – SPE Annual Technical Conference and Exhibition, Vol. Omega, 627-635.

Coates, G. R., Marschall, D., Mardon, D., Galford, J., 1998. A new characterization of bulk-volume irreducible using magnetic resonance. The Log Analyst, 39, 51-63.

Daigle, H. and Dugan, B., 2009. Extending NMR data for permeability estimation in fine-grained sediments. Mar. Petrol. Geol., 26, 1419-1427.

Dautriat, J., Gland, N., Guelard, J., Dimanov, A., & Raphanel, J. L., 2009. Axial and radial permeability evolutions of compressed sandstones: end effects and shear-band induced permeability anisotropy. Pure and Applied Geophysics, 166(5-7), 1037-1061.

Delle Piane, C., Esteban, L., Timms, N.E. and Ramesh Israni, S., 2013a. Physical properties of Mesozoic sedimentary rocks from the Perth Basin, Western Australia.

Delle Piane, C., Olierook, H.K., Timms, N.E., Saeedi, A., Esteban, L., Rezaee, R., Mikhaltsevitch, V., Iglauer, S. and Lebedev, M., 2013b. Facies-based rock properties distribution along the Harvey 1 stratigraphic well. Australian National Low Emissions Coal Research & Development CSIRO Report Number EP133710. Available at: http://anlecrd.com.au/projects/facies-based-rock-properties-distribution-along-the-Harvey-1-stratigraphic-well/

Domzalski, S., Boydell, W.G., Pop, J.J. and Hadbi, A., 2002, January. In-Situ Permeability Anisotropy vs. Depth in a Fluvial Sandstone Reservoir Using a Multiprobe Formation Tester. In SPE Annual Technical Conference and Exhibition. Society of Petroleum Engineers.

Dunn, K.J., Bergman, D.J. and Latorraca, G.A., 2002. Nuclear Magnetic Resonance: Petrophysical and Logging Applications. Pergamon, Amsterdam, 293pp.

Ellis, D. V., Singer, J.M. 2008. Well Logging for Earth Scientists, Second Edition, Springer, The Netherlands.

Evans, B., Saeedi, A., Reza, R., Rasouli, V., Lebedev, M., Iglauer, S., Liu, K., 2014. Predicting CO2 injectivity properties for application at CCS sites. Final Report to ANLECR&D, Project 3-1110-0122.

Gehne, S., & Benson, P. M., 2017. Permeability and permeability anisotropy in Crab Orchard sandstone: experimental insights into spatio-temporal effects. Tectonophysics, 712, 589-599.

Gray, D. H., & Fatt, I., 1963. The effect of stress on permeability of sandstone cores. Society of Petroleum Engineers Journal, 3(02), 95-100.

Grunewald, E., & Knight, R. 2011. A laboratory study of NMR relaxation times in unconsolidated heterogeneous sediments. Geophysics, 76(4), G73-G83.

Hurlimann, M.D., Flaum, M., Venkataramanan, L., Flaum, C., Freedman, R. and Hirasaki, G.J., 2003. Diffusion-relaxation distribution functions of sedimentary rocks in different saturation states. Mag. Res. Imaging, 3-4, 305-10.

Josh, M., Esteban, L., Delle Piane, C., Sarout, J., Dewhurst, D.N. and Clennell, M.B., 2012. Laboratory characterization of shale properties. J. Petrol. Sci. Engin., vol. 88-89, 107-124; doi: 10.1016/j.petrol.2012.01.023.

Jorand, R., Fehr, A., Kock, A., Clauser, C., 2011. Study of the variation of thermal condictivity with water saturation using nuclear magnetic resonance. J. Geophys. Res., 116, B08208.

Kestin, J., Khalifa, H. E., & Correia, R. J., 1981. Tables of the dynamic and kinematic viscosity of aqueous NaCl solutions in the temperature range 20–150 C and the pressure range 0.1–35 MPa. Journal of physical and chemical reference data 10(1), 71-88.

Kleinberg, R. L., C. Flaum, D. D. Griffin, P. G. Brewer, G. E. Malby, E. T. Peltzer, and J. P. Yesinowski, 2003a, Deep sea NMR: Methane hydrate growth habit in porous media and its relationship to hydraulic permeability, deposit accumulation, and submarine slope stability, J. Geophys. Res., 108(B10), 2508, doi:10.1029/2003JB002389.

Kleinberg, R. L., C. Flaum, C. Straley, P. G. Brewer, G. E. Malby, E. T. Peltzer III, G. Friederich, and J. P. Yesinowski. 2003b, Seafloor nuclear magnetic resonance assay of methane hydrate in sediment and rock, J. Geophys. Res., 108(B3), 2137, doi:10.1029/2001JB000919.

Klinkenberg, L.J. 1941. The Permeability of Porous Media to Liquids and Gases. Drill. & Prod. Prac. 200.

Korsnes, R. I., Risnes, R., Faldaas, I., & Norland, T., 2006. End effects on stress dependent permeability measurements. Tectonophysics, 426(1), 239-251.

Olierook, H.K.H., Delle Piane, C., Timms, N.E., Esteban, L., Rezaee, R., Mory, A.J. and Hancock, L., 2014. Facies-based rock properties characterization of CO2 sequestration: GSWA Harvey 1 well, Western Australia. Marine and Petroleum Geology, 50, 83-102.

Olierook, H., Timms, N.E., Rezaee, R. and Delle Piane, C., 2012. Facies-based rock properties distribution along the Harvey-1 stratigraphic well. ANLEC Interim Report project 199.

Pugh, V.J., Thomas, D.C., and Gupta, S.P., 1991. Correlations of liquid and air permeabilities for use in reservoir engineering studies. The Log Analyst, 32(05).

Rezaee, R., 2012. Wireline log analysis of Harvey-1, South Perth Basin. Curtin University – ANLEC report.

Saeedi, A., Delle Piane, C., Esteban, L., & Xie, Q., 2016a. Flood characteristic and fluid rock interactions of a supercritical CO2, brine, rock system: South West Hub, Western Australia. International Journal of Greenhouse Gas Control, 54, 309-321.

Saeedi, A., Delle Piane, C., Esteban, L., Noble, R., Gray, D., Iglauer, S., Lebedev, M., and Stalker, L., 2016b. Understanding Fluid Rock Interactions and Their Impact on Rock Properties as a Result Of CO_2 Injection in the SW Hub. Final Project Report, SCRIPT Project RES-SE-DPE-AS-53419-2, Curtin University.

Schutjens, P. M. T. M., & De Ruig, H., 1997. The influence of stress path on compressibility and permeability of an overpressurised reservoir sandstone: some experimental data. Physics and Chemistry of the Earth, 22(1), 97-103.

Tang, G.Q. and Morrow, N.R., 1999. Influence of brine composition and fines migration on crude oil/brine/rock interactions and oil recovery. Journal of Petroleum Science and Engineering, 24(2), pp.99-111.

Tiab, D. and Donaldson, E.C., 2004. Petrophysics. Gulf Professional Publishing, Elsevier, Burlington, Massachusetts.

Timur, A., 1968. An Investigation of Permeability, Porosity and Residual Water Saturation Relationships, paper presented at SPWLA 9th Annual Logging Symposium, Society of Petrophysicists and Well Log Analysts, 23–26 June.

Thomas, R.L. and Crowe, C.W., 1981. Matrix treatment employs new acid system for stimulation and control of fines migration in sandstone formations. Journal of Petroleum Technology, 33(08), pp.1-491.

Villar, M. V., Lloret, A., 2001. Variation in the intrinsic permeability of expansive clays upon saturation, in Clay science for engineering, edited by M. F. K. Adachi, pp. 259–266, A.A. Balkema, Rotterdam.

Walbrecker, J. O., Hertrich, M., & Green, A. G., 2011. Off-resonance effects in surface nuclear magnetic resonance. Geophysics, 76(2), G1-G12.

Wu Y-S, Pruess K, and Persoff P (1998) Gas flow in porous media with Klinkenberg effects. Transport in Porous Media 32: 117-137.

Xie, Q., Saeedi, A., Delle Piane, C., Esteban, L. and Brady, P.V., 2017. Fines migration during CO 2 injection: Experimental results interpreted using surface forces. International Journal of Greenhouse Gas Control, 65, pp.32-39.

Yang, K. and Kerr, D.R., 2016. Permeability Anisotropy Related to Braided Fluvial Facies Architectural Elements in Middle Boggy Formation, Middle Pennsylvanian, McIntosh County, Oklahoma. Search and Discovery Article #51219 AAPG Mid-Continent Section meeting in Tulsa, Oklahoma, October 4-6, 2015.

Zhu, W., & Wong, T. F., 1997. The transition from brittle faulting to cataclastic flow: Permeability evolution. Journal of Geophysical Research: Solid Earth, 102(B2), 3027-3041.

Zoback, M. D., & Byerlee, J. D., 1975. Permeability and effective stress: Geologic notes. AAPG Bulletin, 59(1), 154-158.

Appendix 3A

Experimentally measured gas porosity and Klinkenberg corrected permeability at different values of confining pressure.

ϕ = porosity

ϕ_0 = porosity extrapolated to room conditions

k = permeability

k_0 = permeability extrapolated to room conditions

Borehole	Depth (m)	ϕ_0 (%)	ϕ (%) 3.45 MPa	ϕ (%) 5.52 MPa	ϕ (%) 6.89 MPa	ϕ (%) 10.34 MPa	k_0 (mD)	k (mD) 5.52 MPa	k (mD) 6.89 MPa	k (mD) 10.34 MPa	k (mD) 3.45 MPa
Harvey 2	1245.15	18.03	17.55	17.18	16.97	16.73	397	382	366	362	355
Harvey 2	1245.8	19.88	19.51	19.25	19.05	18.82	1203	1159	1118	1111	1071
Harvey 2	1247.5	17.5	17.16	16.97	16.8	16.57	128	118	104	99	95
Harvey 2	1247.9	18.06	17.68	17.5	17.4	17.1	296	273	268	260	241
Harvey 2	1344.65	20.99	20.18	20.39	19.92	19.77	2121	1970	2009	1941	1914
Harvey 2	1347.5	19.27	18.94	18.7	18.53	18.32	271	270	289	279	290
Harvey 2	1347.9	19.95	19.64	19.33	19.18	18.97	334	325	315	315	305
Harvey 3	1313	18.6	18.45	18.32	18.25	18.09	414	406	394	391	383
Harvey 3	1417.9	21.29	21.01	20.83	20.62	20.42	30	28	24	23	21
Harvey 3	1470.2	20.62	20.22	19.95	20.16	19.63	166	154	139	126	128
Harvey 3	1470.86	20.89	20.75	20.63	20.53	20.46	95	87	76	72	67
Harvey 3	1470.96	20.98	20.72	20.49	20.36	20.21	114	108	102	96	95
Harvey 3	1472.1	21.64	21.56	22.47	21	20.85	924	759	646	615	581
Harvey 3	1476.3	17.09	16.85	16.63	16.49	16.3	1224	1227	1307	1364	1360
Harvey 3	1476.45	16.42	16.13	15.94	15.76	15.57	1647	1637	1862	1916	1927
Harvey 3	1511.65	21.5	21.15	20.98	20.75	20.5	549	531	505	495	487
Harvey 3	1544.05	18.24	17.86	17.59	17.42	17.19	4105	3770	3450	3356	3121
Harvey 3	1549.6	18.67	18.44	18.2	18.08	17.89	2834	2263	2438	2476	2234
Harvey 4	1716.8	21.87	21.46	21.06	20.75	20.33	847.7	789.6	679.5	622.2	595.6
Harvey 4	1716.8	22.64	22.12	21.64	21.32	20.94	511.7	484.6	458.4	446.1	421.8
Harvey 4	1795	19.45	19.38	19.05	19.03	18.79	32.2	31.6	27.6	26.3	24.6
Harvey 4	1797.5	19.71	19.44	19.27	19.1	18.88	618	570	501	473	443
Harvey 4	1798.3	16.91	16.73	16.53	16.39	16.26	5.2	4.9	4.6	4.5	4.2
Harvey 4	1798.6	19.25	19.08	18.83	18.74	18.58	817	784	669	651	637

Appendix 3B

NMR derived porosity and permeability.

ϕ_{NMR} = porosity derived from NMR measurements on brine saturated plugs

k_{Coates} = permeability calculated from the NMR measurements according to Coates model (see equation 5)

Borehole	Depth (m)	ϕ_{NMR} (%)	k_{Coates} (mD)
Harvey 2	1138.20	26.49	540.02
Harvey 2	1139.25	26.41	76.06
Harvey 2	1140.00	23.09	17.38
Harvey 2	1245.15	17.81	27.58
Harvey 2	1245.80	19.79	81.42
Harvey 2	1247.50	17.91	58.22
Harvey 2	1247.90	17.82	22.25
Harvey 2	1344.65	20.54	151
Harvey 2	1347.50	19.16	19.93
Harvey 2	1347.90	19.11	43.07
Harvey 3	1313.00	18.29	1.32
Harvey 3	1313.60	16.47	0.48
Harvey 3	1314.00	23.11	10.13
Harvey 3	1314.60	16.56	1.05
Harvey 3	1417.90	20.63	331.94
Harvey 3	1470.20	20.24	103.26
Harvey 3	1472.10	21.26	201.42
Harvey 3	1511.65	21.64	56.29
Harvey 3	1544.05	17.86	43.68

Section 4: Geomechanical-acoustic core plug characterisation

Summary

The elasto-mechanical properties of reservoir overlying rock units are important for assessing the performance of a CO_2 storage site. Laboratory measurements on rock samples are one method to assess these properties and such results can be used to populate modelling studies of near well-bore and reservoir scale behaviour in response to fluid injection. This section of the project is motivated by a critical paucity of geomechanical and rock physics data on the Lesueur Sandstone. The only available measurements so far are related to samples extracted from Harvey 1 and mostly related to the potential storage reservoir within the Wonnerup Member. The mechanical behaviour of the clay rich units of Yalgorup Member has not been assessed although the drilling operations conducted so far in the South West Hub area indicate that most of the well bore instability issues encountered in the field are associated with these horizons. Below we summarize the results of laboratory geomechanical and rock physics experiments performed on core plugs from the Yalgorup and Wonnerup Members of the Triassic Lesueur Formation. The specimens were tested at conditions simulating the in situ pressure and fluid content. The tests indicate that the members behave significantly differently from the mechanical and elastic points of view: the Yalgorup is relatively weak while the Wonnerup shows stronger and stiffer responses. Under the testing conditions, the mechanical response of the Wonnerup can be well approximated by a Mohr Coulomb dilatant behaviour. On the other hand, the clay rich units of the Yalgorup display strain hardening and compactant behaviour, typical of the transitional/ductile regime for porous materials and call for a different choice of constitutive behaviour to be used in the geomechanical models of the area.

Rock physics measurements performed on dry, fully saturated and partially saturated samples suggest that the commonly used Gassmann fluid substitution theory adequately describes the experimental results. This indicates that the theoretical framework could be used to extract fluid types or saturations from seismic, cross-well, or borehole sonic data, in a fluid injection monitoring scenario. Furthermore, by the use of an innovative broad frequency experimental set-up, it is demonstrated that there is negligible dispersion in dynamic elastic properties measured at seismic and ultrasonic frequency in samples from the Wonnerup Member. This last observation supports the use of laboratory results to aid the interpretation of seismic and log data collected in the South West Hub area. Moreover, the results of measurements at seismic frequencies (elastic moduli and attenuation, not only Vp/Vs) can be used (and are already being used) in the modelling of plume seismic response without introducing corrections for wave induced flow, such as squirt and/or global flow.

This section is concluded with a preliminary assessment the changes in stress-induced anisotropy occurring during fluid injection. An innovative true triaxial rig equipped with a laser Doppler interferometer was used to test cubic samples of the cored material from the Harvey 4. Although the outcome of the tests performed on two samples show initial indications of changes in anisotropy due to brine injection, the limited data set does not allow further conclusions to be made and the results are reported for the sake of completeness.

4A: Triaxial testing of Yalgorup samples

Claudio Delle Piane[1]

[1]CSIRO Energy

Introduction

Due to current lack of data, there is a critical need to better characterize the geomechanical response of the Yalgorup Member of the Lesueur Sandstone. With the exception of four tests, most of the available geomechanical data is from experiments conducted on the Wonnerup and the limited dataset indicates significant differences in the two Members of the Lesueur Sandstone in terms of elastic moduli and geomechanical properties. In particular, the only available data on the clay-rich portions of the Yalgorup are from a previous ANLEC supported project and indicated a peculiar, pressure insensitive geomechanical behaviour (see results of samples 206628 and 206635 in Delle Piane et al. 2013) that could not be described by the normally assumed Mohr Coulomb behaviour. This response was unexpected and difficult to explain and it was hypothesized that the preservation status of the samples could have affected their experimental response. Based on this experience, in this study care was taken to select clay rich samples of the Yalgorup that were preserved in the best possible way by the drillers and the Geological Survey. These were stored under oil to preserve their natural water content and avoid desiccation and delivered to CSIRO in sealed PVC tubes (Figure 63). To drive the sample selection we used a document circulated by Sandeep Sharma to the South West Hub researchers (SWH Project - Harvey 2, 3, 4 Core Analysis Program - RCA/SCAL - Planning Document with update incorporating lessons "learned" by Tony Kennaird, Core Lab, 11 March 2016) detailing the air exposure time of each section and chose those that were least exposed.



Figure 63 Preserved core sections from Harvey 2, 3 and 4.

The resulting selected sections are as follows:

Harvey 3A: Sample 17: 888.05-888.35

Sample 20: 1226.3-1226.65

Harvey 4: 900.60-901.6 (exposed to air for 2 hours)

907.15-908.05 (exposed to air for 3.75 hours)

The sample preparation procedure was also designed to minimize artefacts and reduce desiccation to the practical minimum. In particular, instead of a traditional core barrel, we used a diamond encrusted wire to cut cylindrical plugs out of the core sections. This is a more gentle procedure that although much slower, resulted in a successful sample preparation whereas previous attempt with the traditional method results in loss of sample material.

Methodology

Multi-stage triaxial tests were performed on naturally brine saturated samples using an Autonomous Triaxial Cell (ATC) similar to that described in section 3. The main reasons for using this type of testing is i) maximise the outcome of a limited number of suitable samples, in our case limited by the preservation state of the received cores; and ii) to avoid heterogeneity in properties between core plugs. The downside of multi-stage testing is potentially fatiguing samples from repeated cycling above the elastic yield point of the material therefore achieving a lower bound of the mechanical properties characteristic of the tested rock.

The equipment comprises a high stiffness load frame, a pressure vessel, and three stepping motor pumps for independent control of cell pressure (overburden), pore pressure and axial load. All experiments were conducted at room temperature; data logging and pump control is based on a LabVIEW program.

Multi-stage triaxial tests were performed at 4 levels of confining pressure (CP) ranging between 5 and 40 MPa using brine preserved, naturally saturated sample listed above. To ensure drained behaviour, axial loading was conducted in axial displacement control at a rate of approximately 0.25mm/hr, and excess pore pressures generated during loading are allowed to drain via fluid ports in the loading platens (i.e. top and bottom pore taps kept open with pore pressure = 0). At each stage of confining pressure the samples were axially loaded up to approximately 90% of peak strength. Subsequent loading stages were carried out after isotropic pressurisation and a suitable stabilisation period; during the final stage at the highest confining pressure the sample was loaded until failure.

During each test compressive stresses and compaction strains are considered positive, axial strain (ε_{ax}) is measured using two diametrically opposed LVDTS mounted parallel to the sample axis, radial strain (ε_{rad}) is measured at mid-height of the rock sample via two cantilevers, and volumetric strain (ε_{vol}) is calculated as:

$$\boldsymbol{\varepsilon_{vol} = \varepsilon_{ax} + 2\varepsilon_{rad}} \qquad \textbf{Equation 11}$$

The static Young's modulus (E_{st}) and Poisson's ratio (ν_{st}) were determined as the tangential slope of the curve of differential stress versus average axial strain and the tangential slope of the curve of average radial strain versus average axial strain at between 40% and 60% of the maximum differential stress. Knowing E_{st} and ν_{st}, the static bulk (K_{st}) and shear (μ_{st}) moduli were calculated as:

$$\boldsymbol{K_{st} = \frac{E_{st}}{3(1-2\nu_{st})}} \qquad \textbf{Equation 12}$$

$$\boldsymbol{\mu_{st} = \frac{E_{st}}{2(1+\nu_{st})}} \qquad \textbf{Equation 13}$$

Results

Sample 2481 (Harvey 4 907.55 m)

Stress strain curves collected at different stages of effective pressure are shown in Figure 64. The yield point, i.e. the departure from linear stress-strain response, occurs at rather low levels (< 10 MPa) of differential stress (σ_1-σ_3) as indicated by the down pointing red arrows in Figure 64. At the highest tested effective confining pressure of 20 MPa, following yielding the sample showed strain hardening evolving to a relatively flat stress-strain curve and continuous compactant response of the volumetric strain up to a gentle stress drop visible at axial strain of approximately 23 millistrain (2.3 % strain). Rather than a typical brittle failure, such a stress-strain curve is indicative of a more ductile/transitional regime. Figure 65 shows pictures of the

sample before and after testing the latter highlighting the presence of a shear band on the surface of the sample

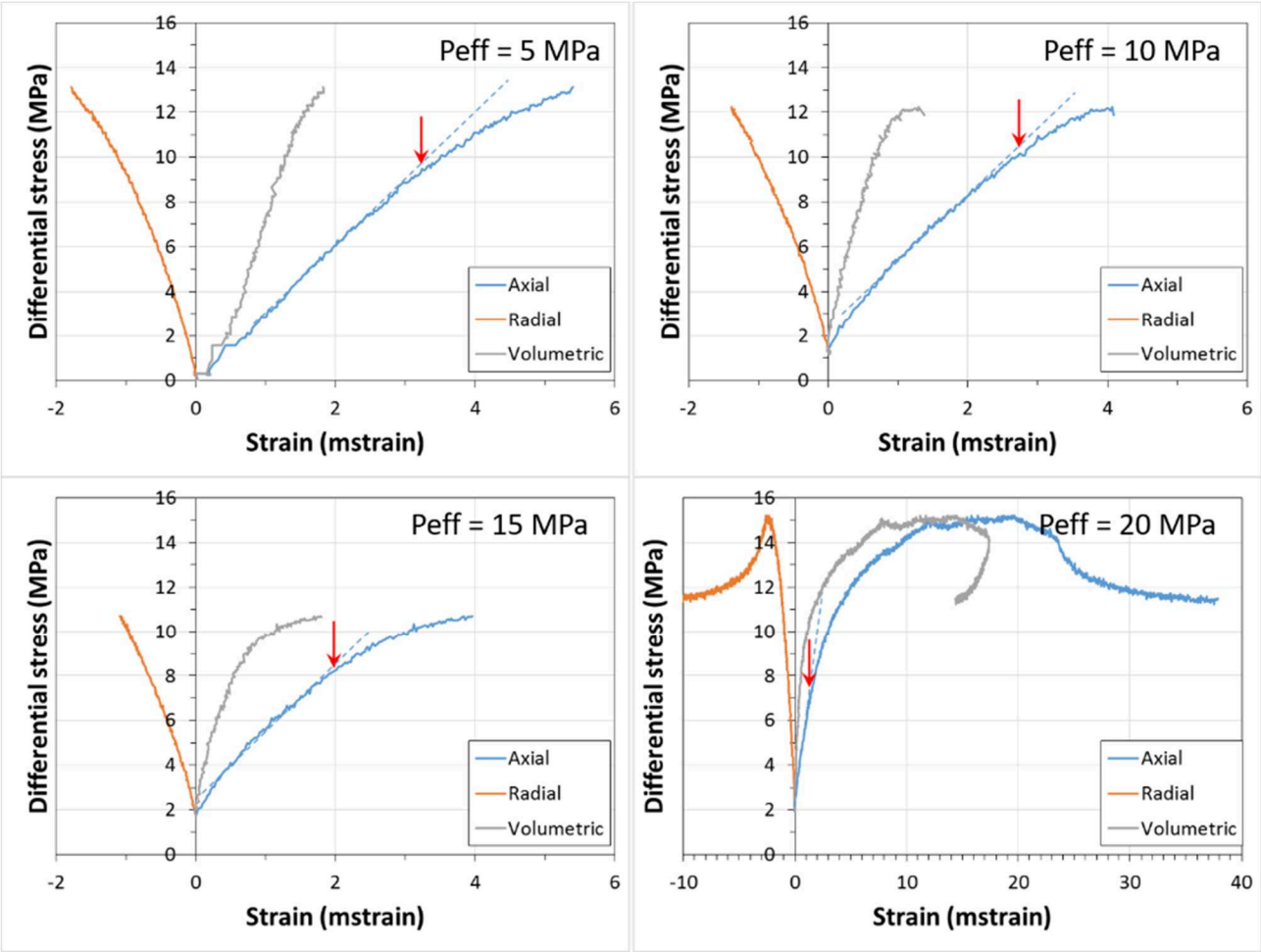


Figure 64 Stress strain curves obtained during multi stage triaxial test on sample 2481. Red arrow in each plot indicates the yield point, i.e. the point of departure from a linear stress-strain curve (traced as a dashed blue line for reference).

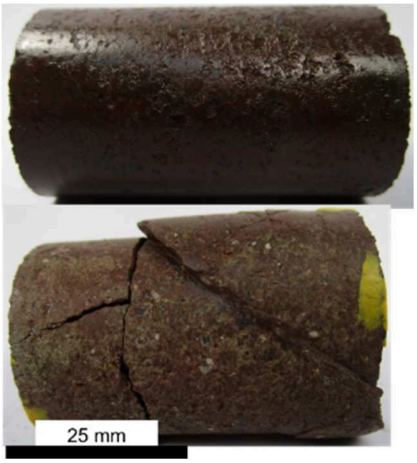


Figure 65 Pictures of sample 2481 before (top) and after testing (bottom).

Sample 2483 (Harvey 4 900.05 m)

Stress strain curves collected at different stages of effective pressure are shown in Figure 66. The yield point, occurs at differential stress in the order of approximately 6 MPa, nearly irrespective of Peff. At the highest tested effective pressure of 20 MPa, following yielding the sample showed strain hardening evolving to a flat stress-strain curve and compactant response of the volumetric strain. No stress drop was recorded in the sample deformed to maximum axial strain of approximately 15 millistrain (1.5 %). Figure 67 shows pictures of the sample before and after testing the latter highlighting the presence of a shear band on the surface of the sample, based on the mechanical data it should be interpreted as compactive shear band.

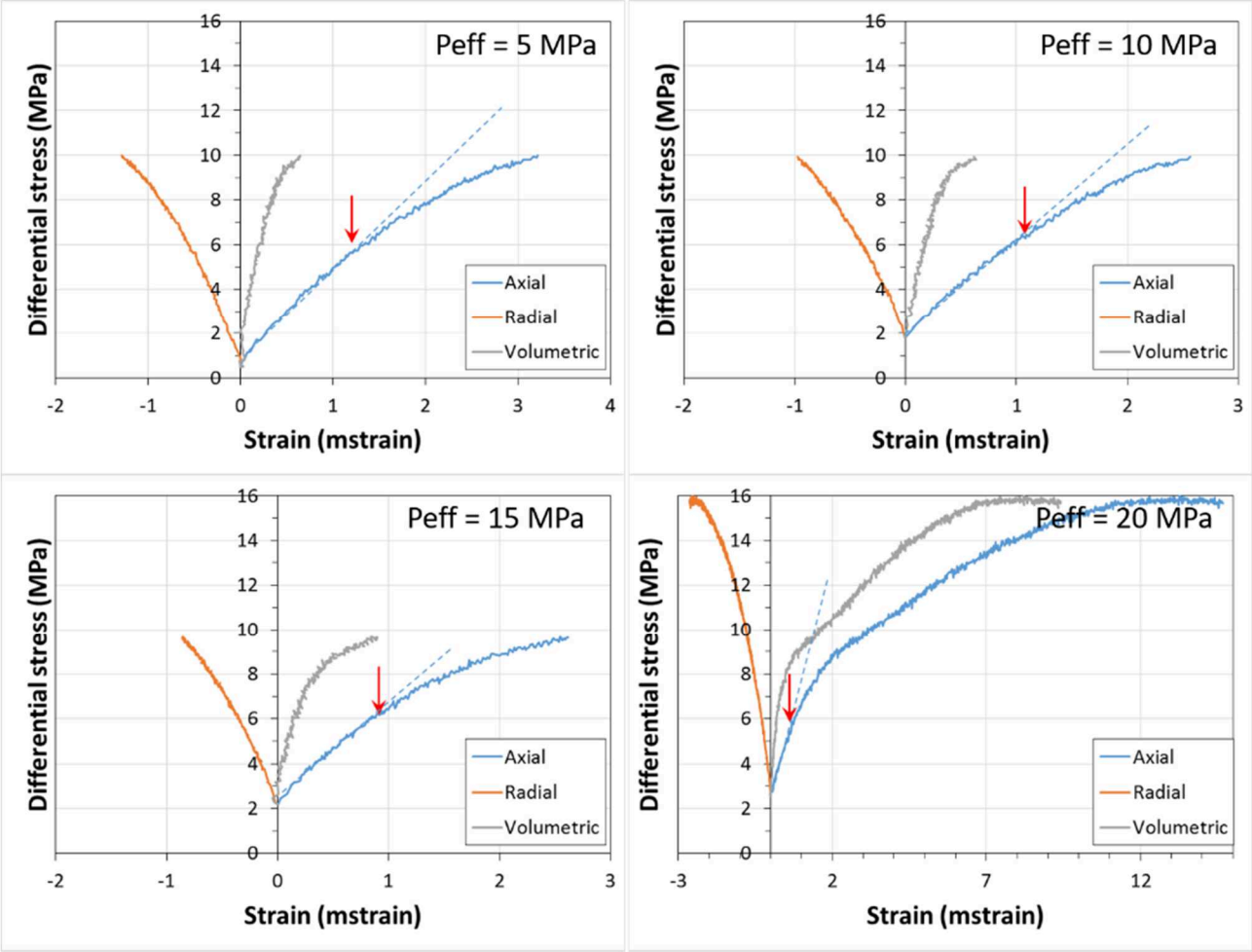


Figure 66 Stress strain curves obtained during multi stage triaxial test on sample 2481. Red arrow in each plot indicates the yield point, i.e. the point of departure from a linear stress-strain curve (traced as a dashed blue line for reference).

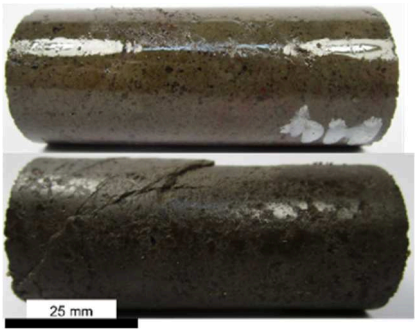


Figure 67 Pictures of sample 2481 before (top) and after testing (bottom).

Sample 2485 (Harvey 3A 888.075 m)

Stress strain curves collected at different stages of effective pressure are shown in Figure 68. The yield point occurs at differential stress in the order of approximately 8 - 9 MPa. This sample could not be brought to failure as it suffered a jacket failure following the third loading stage at 20 MPa of effective confining pressure. In all three successful loading stages the volumetric strain curve is monotonically increasing indicating compactant mechanical response. Figure 69 shows pictures of the sample before and after testing.

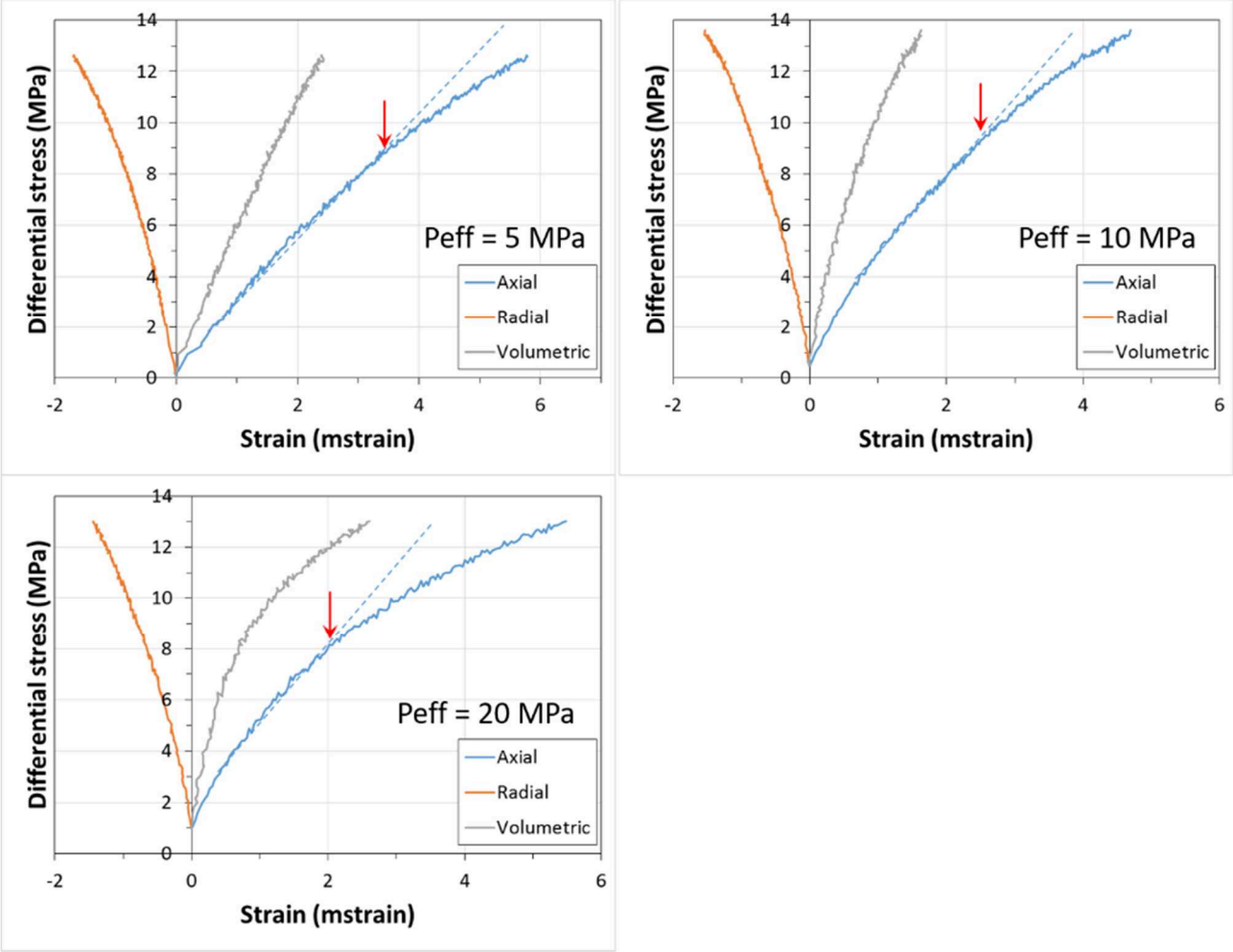


Figure 68 Stress strain curves obtained during multi stage triaxial test on sample 2485. Red arrow in each plot indicates the yield point, i.e. the point of departure from a linear stress-strain curve (traced as a dashed blue line for reference).



Figure 69 Pictures of sample 2485 before (top) and after testing (bottom).

Sample 2490 (Harvey 3A 1226.45 m)

Stress strain curves collected at different stages of effective pressure are shown in Figure 70. The yield point, occurs at differential stress in the order of approximately 15 to 17 MPa depending on the applied effective pressure. At the highest tested effective pressure of 40 MPa, following yielding the sample showed strain hardening evolving to a flat stress-strain curve and compactant response of the volumetric strain. No stress drop was recorded in the sample deformed to maximum axial strain of approximately 25 millistrain (2.5 %). Figure 71 shows pictures of the sample before and after testing the latter highlighting the presence of a shear band on the surface of the sample, based on the mechanical data it should be interpreted as compactive shear band.

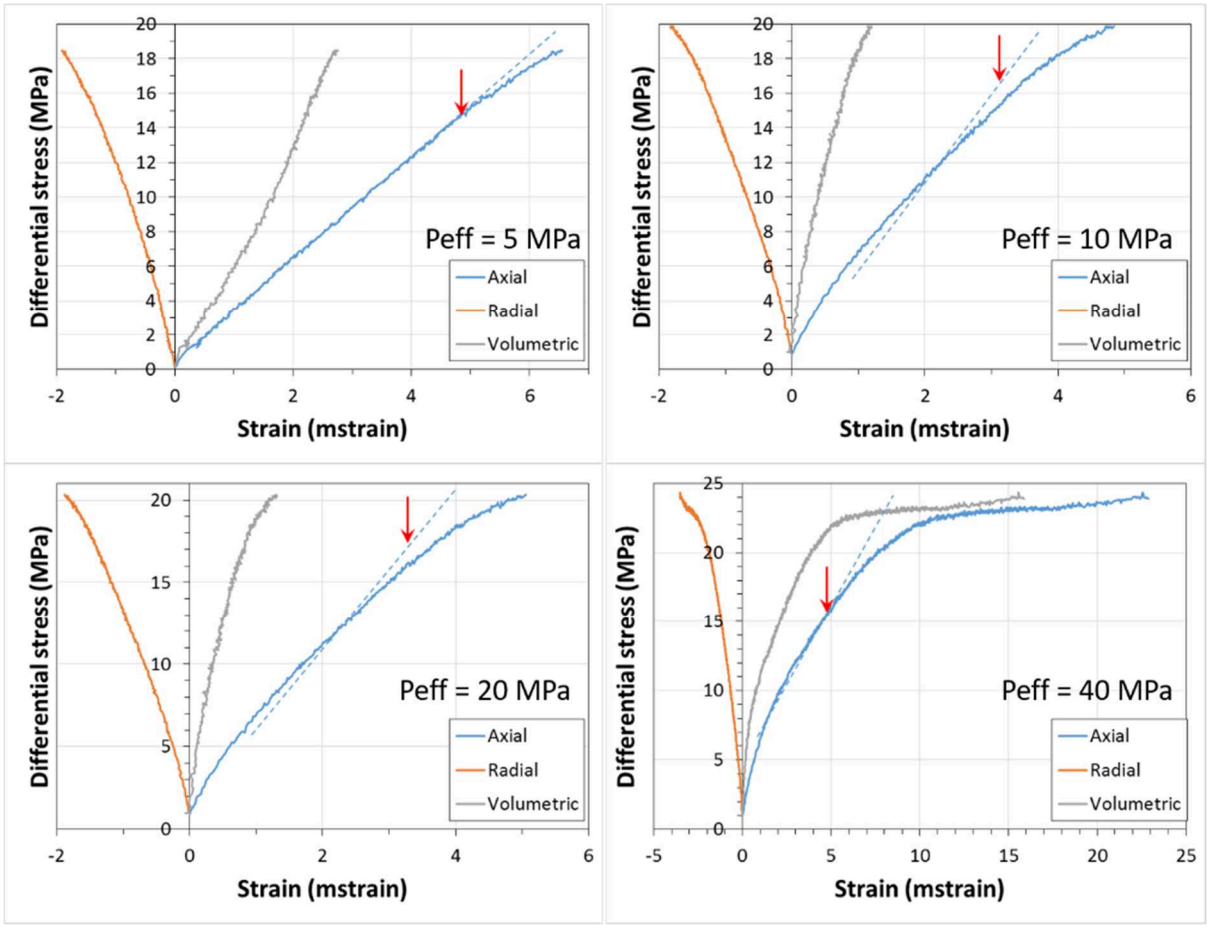


Figure 70 Stress strain curves obtained during multi stage triaxial test on sample 2490. Red arrow in each plot indicates the yield point, i.e. the point of departure from a linear stress-strain curve (traced as a dashed blue line for reference).



Figure 71 Pictures of sample 2490 before (top) and after testing (bottom).

Summary

During triaxial tests on four preserved samples of the Yalgorup, we observed strain hardening, and lack of a well-defined stress drop with increasing strain, typical of the ductile regime for porous materials. Visual inspection of the tested sample indicated that strain localization occurred in the samples in form of compactive shear bands as supported by the mostly compactive strain recorded during the tests.

The triaxial data are summarized in Table 7 and in Figure 72 where the differential stress at yield is plotted against mean effective stress. The four samples produce compactant yield envelopes where the more deeply buried sample is stronger than the other three.

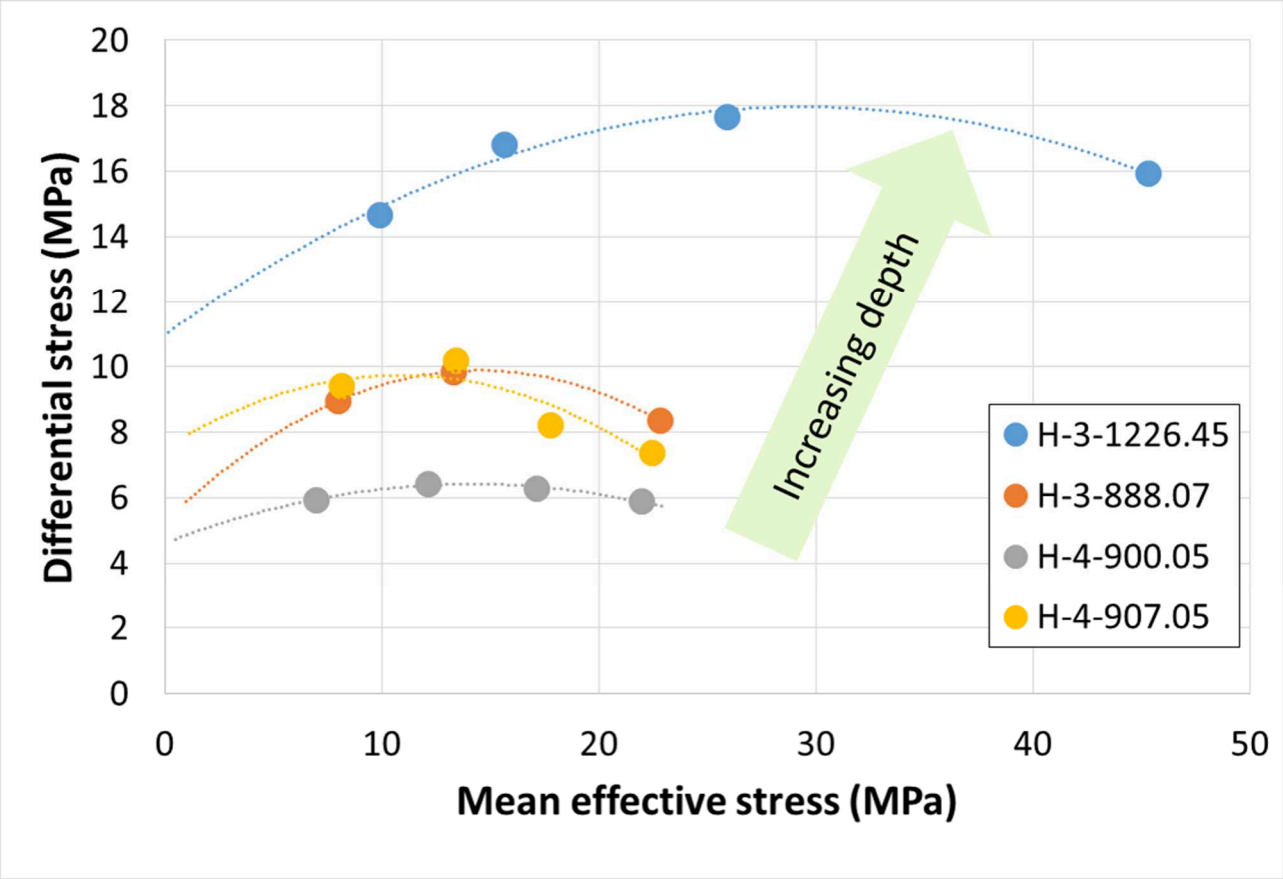


Figure 72 Summary of experimental data plotted in mean effective stress versus differential stress space.

This new data confirms the preliminary observation collected from the Harvey 1 core material indicating a non dilatant, pressure insensitive response in some of the samples from the Yalgorup characterised by high clay content.

The implication of these experimental results is that the geomechanical response of the clay rich horizons in the Yalgorup is more akin to that of an unconsolidated soil than that of a cemented sandstone like the Wonnerup. Therefore, clay-rich intervals of the Yalgorup should not be modelled using the traditional Mohr-Coulomb approach as at the inferred in situ conditions the material behaviour is compactant.

Sample	Peff (MPa)	Peak differential stress (MPa)	Yield stress (MPa)	E_{st} (GPa)	ν_{st}	μ_{st} (GPa)	K_{st} (GPa)
2481	5	13.1	9.44	2.8	0.36	3.33	1.03
	10	12.2	10.2	3.0	0.37	3.85	1.09
	15	10.7	8.23	3.1	0.35	3.44	1.15
	20	15.2	7.38	2.3	0.31	2.02	0.88
2483	5	9.8	5.94	3.2	0.41	1.13	5.93
	10	9.7	6.43	3.6	0.42	1.27	7.50
	15	9.5	6.29	3.7	0.39	1.33	5.61
	20	15.8	5.89	1.2	0.24	0.48	0.77
2485	5	12.4	8.96	2.2	0.27	0.87	1.59
	10	13.4	9.86	2.8	0.33	1.05	2.75
	20	13.7	8.37	2.5	0.31	0.95	2.19
2490	5	18.4	14.69	2.9	0.29	1.12	2.30
	10	19.8	16.82	4.1	0.38	1.49	5.69
	20	20.3	17.66	4.0	0.39	1.44	6.06
	40	24.28	15.96	2.1	0.22	0.86	1.25

Table 7 Summary of geomechanical parameters measured during multi-stage triaxial tests. Peff = effective pressure; E_{st} = static Young Modulus; ν_{st} = static Poisson's ratio; μ_{st} = static shear modulus; K_{st} = stastic bulk modulus.

It is also of interest here to review the available geomechanical data for the Lesueur Sandstone in the South West Hub Area. In previous studies, core plugs have been laboratory tested to provide geomechanical data and to develop a failure criteria of the material. During such tests, static and dynamic elastic properties were also collected and have been subsequently used for correlations with wireline logs data (Rasouli et al. 2013) and as input for large scale geomechanical modelling of injection related fault-reactivation (Zhang et al. 2015). Geomechanical multi-stage triaxial tests on 3 sandstone samples from Harvey 1 were conducted by Evans 2014. These were carried out at 4 different confining pressures of 5, 12.5 and 20 and 30 MPa under not specified saturation conditions. Testing protocols and ultrasonic velocities measurements are reported in Evans (2014), a summary of the geomechanical results is shown in Table 8.

A larger dataset was collected by Delle Piane et al., (2013) in an attempt to better characterize the geomechanical properties of the Yalgorup and Wonnerup Members of the Lesueur Sandstone intersected by Harvey 1. Multi-stage triaxial tests were carried out on 10 samples following saturation with 40,000 and 30,000 ppm sodium chloride brine solution for the Yalgorup and Wonnerup samples, respectively. Results of these geomechanical tests are also summarised in Table 8. Due limitations in the amount of preserved core in the clay rich parts of the Yalgorup, the tests were carried out on sandstone samples. Single stage triaxial compression testing with concurrent ultrasonic velocity measurements were also conducted on three suites

of sandstone samples at room temperature for Mohr-Coulomb failure envelope determination as part of the special core analysis testing programme commissioned by DMIRS. Tests were run on closely spaced plugs selected from the Wonnerup Member in Harvey 3 under unspecified saturation conditions. Summary of these results is again given in Table 8.

Borehole	Depth (m)	E_{st} (GPa)	ν_{st}	K_{st} (GPa)	Cohesion (MPa)	Friction angle (°)	UCS (MPa)	Member	Reference
Harvey 1	915.46	13.73	0.37	17.60	8.33	29.11	28.36	Yalgorup	Evans, 2014
	1935	20.6	0.32	19.07	10.00	36.85	40.01	Wonnerup	
	1935 (?)	21	0.3	17.50	12.35	39.2	52	Wonnerup	
Harvey 1	920.56	10.2	0.17	5.15	7.79	14.36	20.08	Yalgorup	Delle Piane et al., 2013
	1273.89	2.20	N/A	N/A	N/A	N/A	N/A	Yalgorup	
	1323.93	1.8	0.25	1.20	2.48	N/A	N/A	Yalgorup	
	1343.61	7.9	0.23	4.88	5.82	11.25	14.18	Yalgorup	
	1897.66	16.10	0.21	9.25	15.47	26.75	50.25	Wonnerup	
	1897.91	21.60	0.18	11.25	7.93	32.13	28.88	Wonnerup	
	1902.92	19.30	0.21	11.09	20.58	30.88	72.59	Wonnerup	
	1940.58	20.00	0.19	10.75	10.60	31.23	37.63	Wonnerup	
	2496.22	20.30	0.22	12.08	18.84	32.86	69.19	Wonnerup	
	2503.46	23.30	0.17	11.77	14.17	35.72	55.27	Wonnerup	
Harvey 3	1420.65	13.20	0.26	9.34	2.99	41.37	13.22	Wonnerup	DMIRS report
	1420.65	17.75	0.26	12.17				Wonnerup	
	1420.65	19.40	0.24	12.52				Wonnerup	
	1471.45	18.15	0.19	9.76	3.95	37.03	15.86	Wonnerup	
	1471.63	19.59	0.19	10.42				Wonnerup	
	1471.73	20.93	0.1	8.61				Wonnerup	
	1511.71	13.33	0.18	6.92	3.38	42.07	15.23	Wonnerup	
	1511.79	13.61	0.18	7.17				Wonnerup	
	1511.86	19.79	0.18	10.15				Wonnerup	

Table 8 Summary of Multi-Stage Triaxial Compression Tests and derived Mohr Coulomb failure parameters. UCS = unconfined compressive strength.

While the homogeneous, sandstone-rich Wonnerup Member is reasonably well characterised, there is still a paucity of samples to be considered representative of the heterogeneous Yalgorup Member. Additional geomechanical tests have been planned to characterise the different litho-facies of the Yalgorup as part of the currently running ANLEC supported project "Assessment of multi-barrier systems for CO_2 containment in the Yalgorup Member" (ANLEC Project ID 7-1215-0262).

4B: Ultrasonic monitoring of dry and brine saturated Wonnerup samples

Jeremie Dautriat[1], Shane Kager[1]

[1]CSIRO Energy

Introduction

This part of the project aims to complete the extensive ultrasonic measurements obtained on the Harvey 1 core plugs by testing samples from Harvey 2, 3 and 4. Ultrasonic elastic wave velocities are measured as function of effective stress under dry and brine saturated conditions and the results compared to the theoretical predictions based on the commonly used fluid substitution approach. These results provide supporting information for the interpretation of the seismic data from log and surface collected in the South West Hub area.

Methodology

Ultrasonic measurements were conducted on dry and water saturated samples using the same triaxial cell and protocol described in section 3C. Within the cell, the sample is placed between a top and bottom loading platen, each equipped with a piezo-ceramic S-wave crystal to measure ultrasonic velocity following the pulse transmission technique described by Birch (1960). The method consists in measuring the travel time of an elastic pulse through a rock sample of known length. The nominal excitation has a mean frequency of 500 kHz and amplitude of 500 V. Waveforms associated with the arrival of the transmitted pulse at the receiving transducer are recorded at 10 MHz sampling rate. A typical example of a recorded waveform is provided in Figure 73. The raw data recorded in .csv format are converted into .atf, such as the travel times of both S-waves and precursory P-waves are picked semi-automatically using commercial Insite software. After a correction for the travel time into the platens, P- and S-waves velocities, Vp and Vs respectively, are determined based on the deformation corrected sample length.

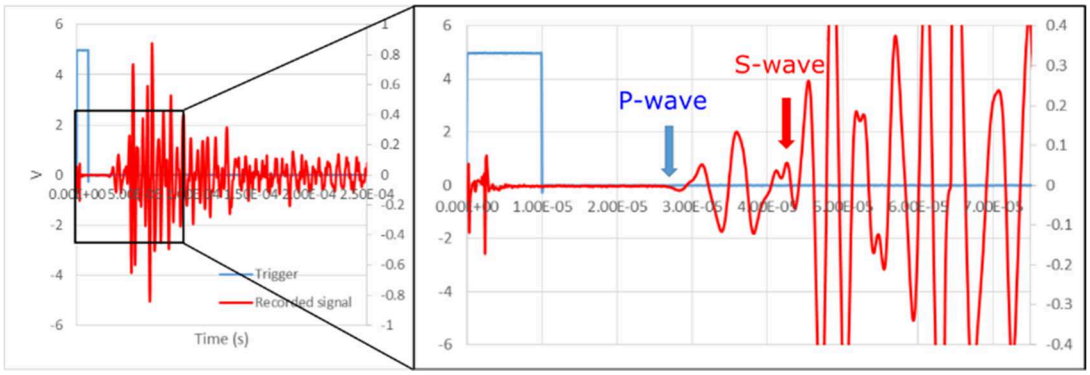


Figure 73 Typical recorded waveform: Arrivals of P and S-waves are clearly observed.

Table 9 provides a list of the tested samples and the in-situ stress and temperature conditions calculated from each samples' depth.

Borehole	Depth (m)	CSIRO id	Unit	Porosity (%)	k_{gas} (mD)	CP (MPa)	PP (MPa)	Peff (MPa)	T (°C)
Harvey 3	1417.9	2513	Y	20.6	23	32.04	14.18	17.86	51.94
Harvey 3	1472.1	2514	W	21	615	33.27	14.72	18.55	52.97
Harvey 3	1544.05	2708	W	17.4	3356	36.23	15.44	20.79	55.56
Harvey 2	1245.8	2515	W	19.1	1111	28.16	12.46	15.7	48.67
Harvey 2	1247.9	2516	W	17.4	260	28.2	12.48	15.72	48.71

Table 9 List of samples used for ultrasonic monitoring of P and S wave velocities and the estimated in situ conditions of confining pressure (CP), pore pressure (PP), effective pressure (Peff) and temperature (T). Y = Yalgorup; W = Wonnerup and k_{gas} = Klinkenberg corrected gas permeability.

Results

For each tested sample, we report the deformation associated with the hydrostatic loading in dry and saturated conditions, the evolution of dry and saturated Vp and Vs velocities and the evolution of the directional permeabilities at the successive effective pressure stage.

The velocity results are compared to those predicted with Gassmann's fluid substitution law (Gassmann, 1951):

$$K_{sat} = K_{dry} + \frac{\left(1-\frac{K_{dry}}{K_0}\right)^2}{\frac{\varphi}{K_{fl}}+\frac{1-\varphi}{K_0}-\frac{K_{dry}}{K_0^2}} \quad \text{Equation 14}$$

where φ is the rock porosity and K_{sat}, K_{dry}, K_0 and K_{fl} are the bulk moduli of the saturated rock, dry rock, the mineral phase and the pore fluid, respectively. K_0 is chosen to be equal to 36.4 GPa, the bulk modulus of quartz mineral. The bulk modulus of the dry sample is calculated from P and S-wave velocities, and sample density ρ:

$$K_{dry} = \rho V_p^2 - \frac{4}{3}\rho V_s^2 \quad \text{Equation 15}$$

Gassmann's fluid substitution laws assume that shear moduli of dry and saturate sample, μ_{dry} and μ_{sat} are identical:

$$\mu_{dry} = \mu_{sat} = \rho V_s^2 \quad \text{Equation 16}$$

Finally, compressional and shear velocities of the saturated samples can be obtained and compared to the experimental results:

$$V_p = \sqrt{\left(K_{sat} + \frac{4}{3}\mu_{dry}\right)\left(\rho + \varphi\rho_{fl}\right)^{-1}} \quad \text{Equation 17}$$

and

$$V_s = \sqrt{\mu_{dry}\left(\rho + \varphi\rho_{fl}\right)^{-1}} \quad \text{Equation 18}$$

Sample 2513 (H3-1417.90 m)

Figure 74 shows the sample strain in response to the confining pressure cycle under dry (Figure 74A) and brine saturated (Figure 74B) conditions at 3 MPa pore pressure. Except at the early stage of loading, axial and radial strains are almost superimposed, as expected for a homogenous, isotropic sample. Strain fluctuation (especially affecting the radial deformation measurements) are due to permeability measurement stages. The static bulk modulus (K) is derived as the slope of the linear part of the volumetric strain curve and shows values of 4.2 and 4.7 GPa under dry and saturated conditions, respectively.

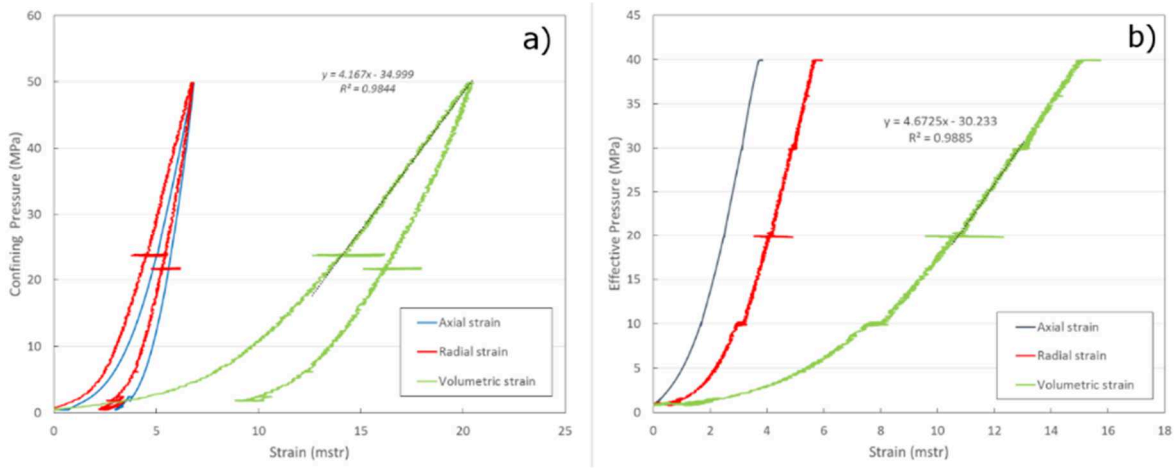


Figure 74 Sample H3-1417.90 (2513) Evolution of axial, radial and calculated volumetric strains with applied hydrostatic pressure in (a) dry and (b) saturated conditions. No data available above 40 MPa effective pressure due to membrane failure.

Figure 75 shows the dependence of P-wave and S-wave velocities to effective pressures for the dry and 100% brine saturated sample. The velocities calculated using Gassmann fluid substitution are also reported. As expected, the initial P-wave velocities are higher in saturated conditions while the S-waves remains almost unchanged. P- and S-wave velocity shows a quick and non-linear increase at low confining pressure. At higher confining pressure, moderate increase is recorded. This behaviour is basically correlated with the micro-crack closure under pressure, inducing a non-linear increase of the elastic moduli (see tabulated values in Appendix 4A). Both saturated P- and S- wave velocity are well predicted by Gassmann fluid substitution.

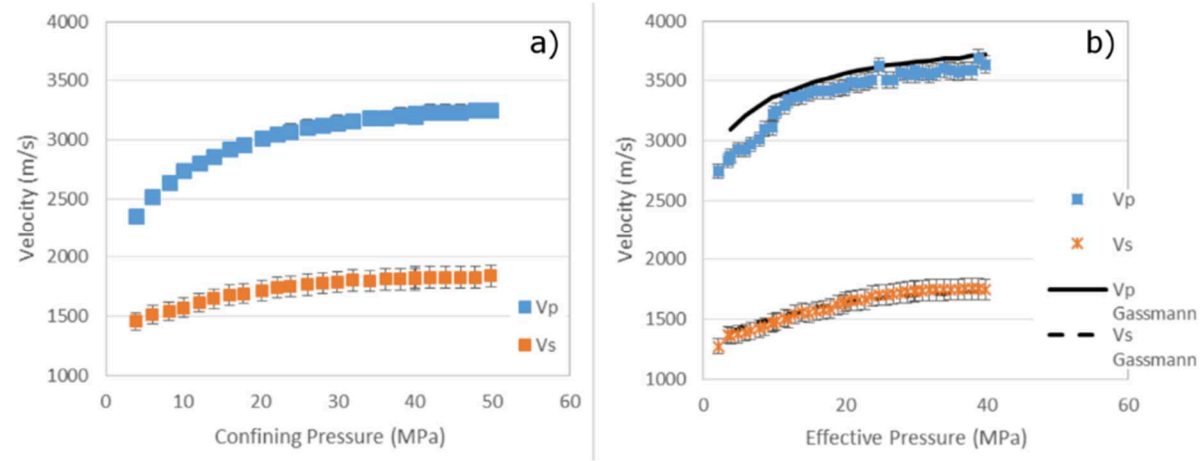


Figure 75 Sample H3-1417.90 (2513) Evolution of P- and S-wave velocities in (a) dry and (b) saturated conditions. Saturated P- and S- wave velocities estimated from Gassmann fluid substitution law are also reported. No data available above 40 MPa effective pressure due to membrane failure.

Sample 2514 (H3-1472.10 m)

Figure 76 shows the sample strain in response to the confining pressure cycle under dry (Figure 76A) and brine saturated (Figure 76B) conditions at 3 MPa pore pressure. Axial and radial deformation appears to diverge slightly during loading. The static bulk modulus (*K*) is derived as the slope of the linear part of the volumetric strain curve and shows values of 5.3 and 4.7 GPa under dry and saturated conditions, respectively.

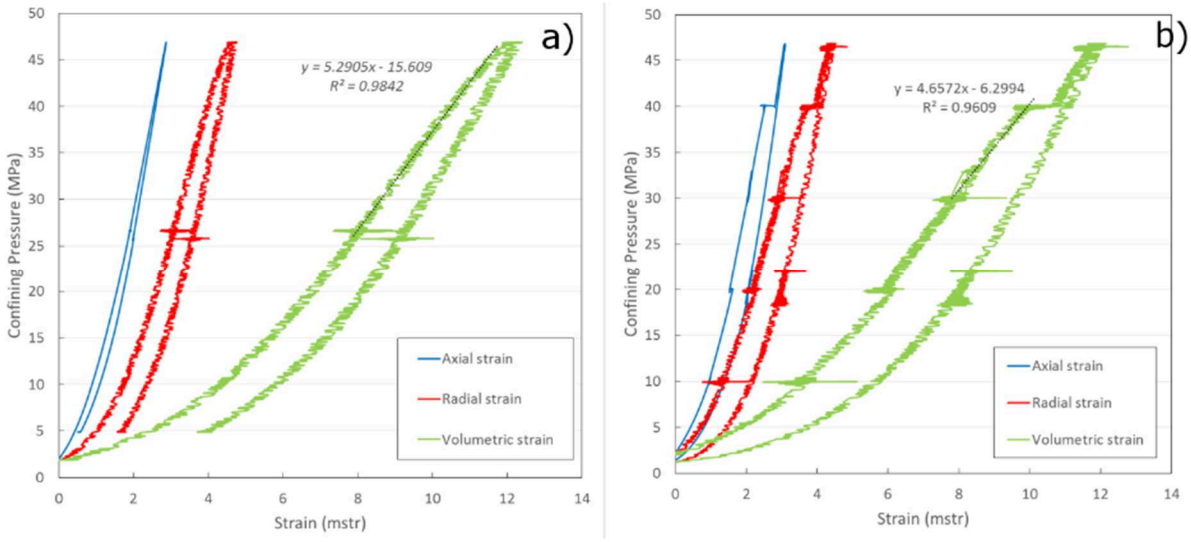


Figure 76 Sample H3-1472.10 (2514) Evolution of axial, radial and calculated volumetric strains with applied hydrostatic pressure under (a) dry and (b) saturated conditions.

Figure 77 shows the dependence of P-wave and S-wave velocities to effective pressures for the dry and 100% brine saturated sample. The velocities calculated using Gassmann fluid substitution are also reported. Values of dynamic shear and bulk moduli calculated from Vp and Vs are tabulated in Appendix 4A. As expected, P-wave velocities are higher under brine saturated conditions while the S-waves remains almost unchanged. Non-linear evolutions of P- and S- wave velocities with effective pressure are related to micro-crack closure. Gassmann theory predictions are less satisfying than for the previous sample. Vs is slightly underestimated at low confining pressure, mainly due to a strong uncertainty on the S-wave first arrival picking in dry conditions. On the other hand, Vp are slightly overestimated at high effective pressure.

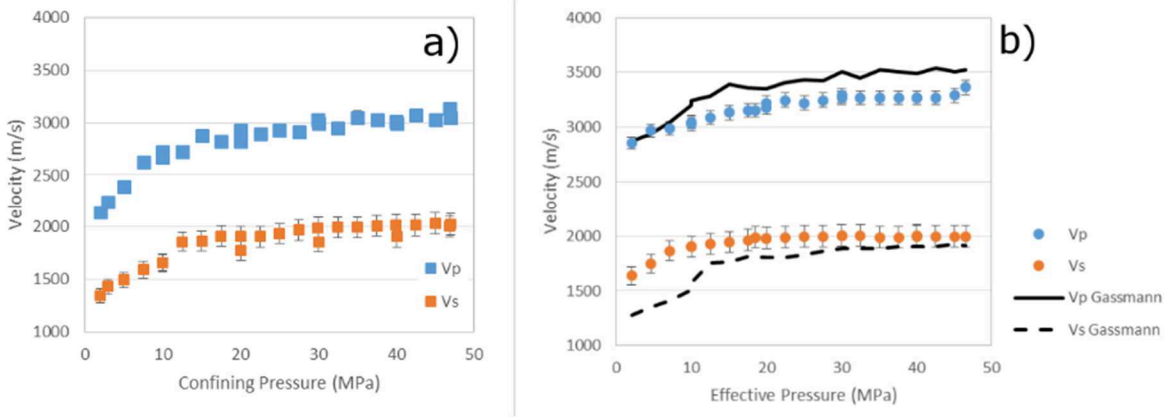


Figure 77 Sample H3-1472.10 (2514) Evolution of P- and S-wave velocities in (a) dry and (b) saturated conditions. Saturated P- and S- wave velocities estimated from Gassmann fluid substitution law are also reported.

Sample 2708 (H3-1544.05 m)

Figure 78 shows the sample strain in response to the confining pressure cycle under dry (Figure 78A) and brine saturated (Figure 78B) conditions at 3 MPa pore pressure. Axial and radial deformation appears to diverge slightly during loading. The static bulk modulus (*K*) is derived as the slope of the linear part of the volumetric strain curve and shows values of 5.1 and 5.9 GPa under dry and saturated conditions, respectively. During the dry hydrostatic loading stage, the axial strain response calculated from the average of 2

diametrically opposed independent displacement transducers, is probably affected by the strong heterogeneity revealed by the CT-scan imaging (see Figure 57 in section 3C). The contrast in density and compressibility at the sample scale due to the presence of a large grain on one side of the sample is responsible for an inhomogeneous deformation.

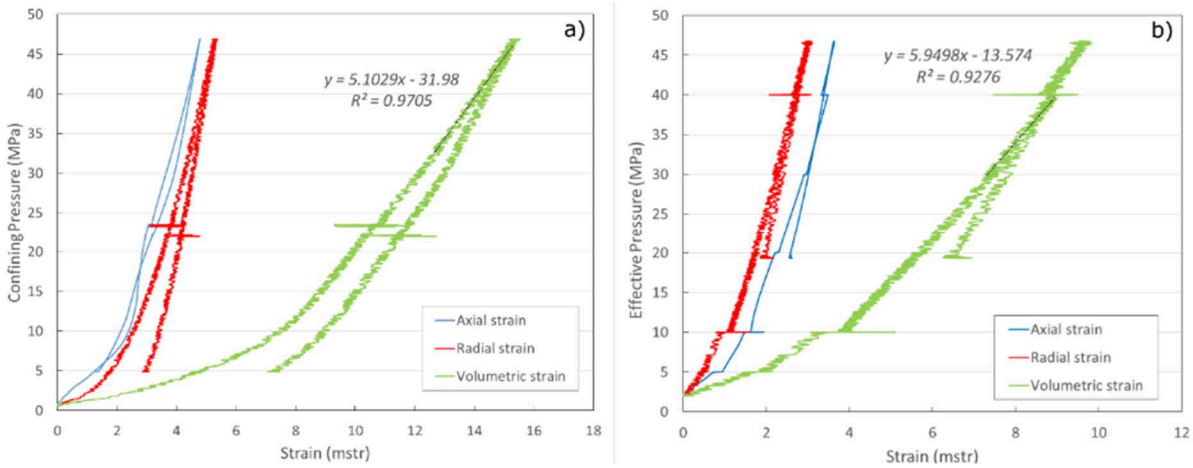


Figure 78 Sample H3-1544.05 (2708) Evolution of axial, radial and calculated volumetric strains with applied hydrostatic pressure in (a) dry and (b) saturated conditions.

Figure 79 shows the dependence of P-wave and S-wave velocities to effective pressures for the dry and 100% brine saturated sample. The velocities calculated using Gassmann fluid substitution are also reported. Values of dynamic shear and bulk moduli calculated from Vp and Vs are tabulated in Appendix 4A. As expected, P-wave velocities are higher under brine saturated than dry conditions while the S- are apparently lower and do not exceed 2000 m/s in this case. Non-linear evolutions of P- and S- wave velocities with effective pressure are related to micro-crack closure. Gassmann theory predicts the saturated P and S wave velocities within the measurement uncertainty.

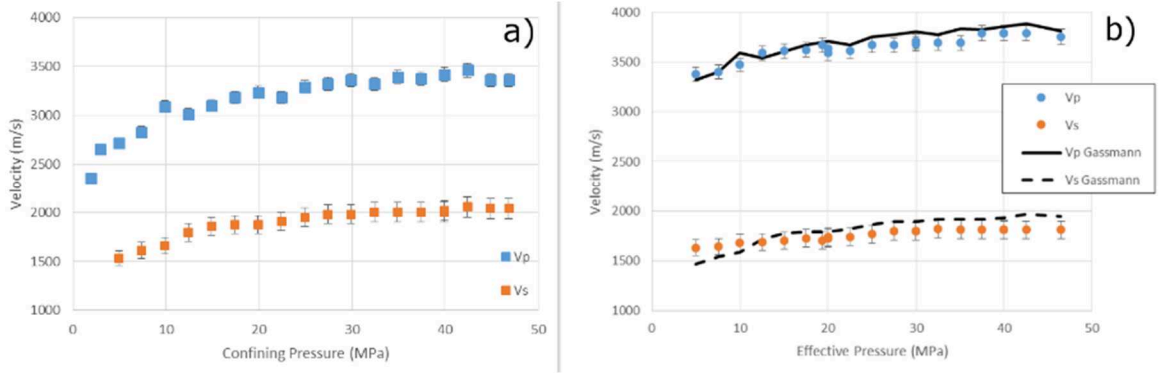


Figure 79 Sample H3-1544.05 (2708) Evolution of P- and S-wave velocities in (a) dry and (b) saturated conditions. Saturated P- and S- wave velocities estimated from Gassmann fluid substitution law are also reported.

Sample 2515 (H2-1245.80 m)

Figure 80 shows the sample strain in response to the confining pressure cycle under dry (Figure 80A) and brine saturated (Figure 80B) conditions at 3 MPa pore pressure. Axial and radial deformation appears to diverge slightly during loading. The static bulk modulus (*K*) is derived as the slope of the linear part of the volumetric strain curve and shows values of 4.7 and 7.1 GPa under dry and saturated conditions, respectively.

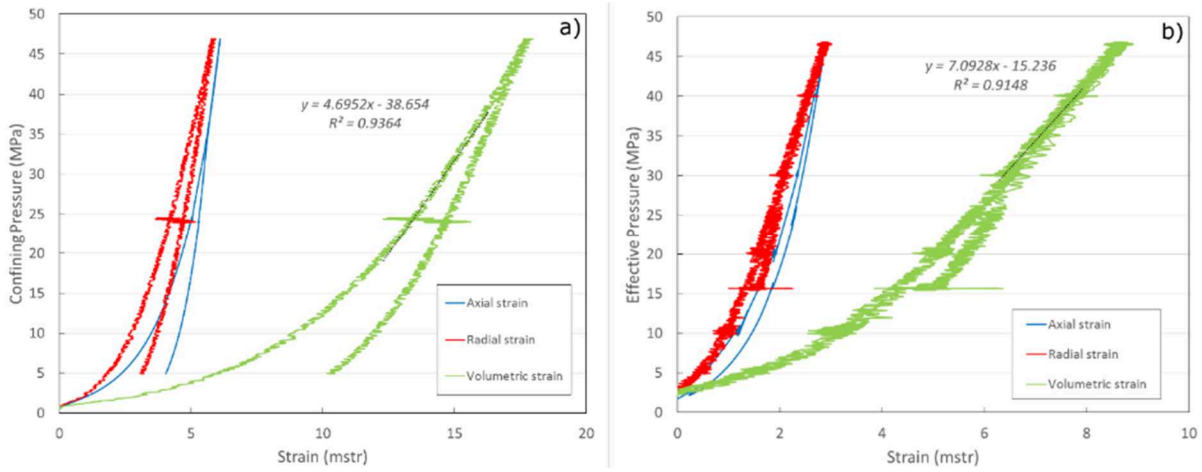


Figure 80 Sample H2-1245.80 (2515) Evolution of axial, radial and calculated volumetric strains with applied hydrostatic pressure in (a) dry and (b) saturated conditions.

Figure 81 shows the dependence of P-wave and S-wave velocities to effective pressures for the dry and 100% brine saturated sample. The velocities calculated using Gassmann fluid substitution are also reported. Values of dynamic shear and bulk moduli calculated from Vp and Vs are tabulated in Appendix 4A. As expected, P-wave velocities are higher under brine saturated than dry conditions while the S- are almost unchanged. Non-linear evolutions of P- and S- wave velocities with effective pressure are related to micro-cracks closure. Gassmann theory slightly overestimates the measured P-wave velocities although the prediction is generally very close to the upper bound of experimental uncertainty.

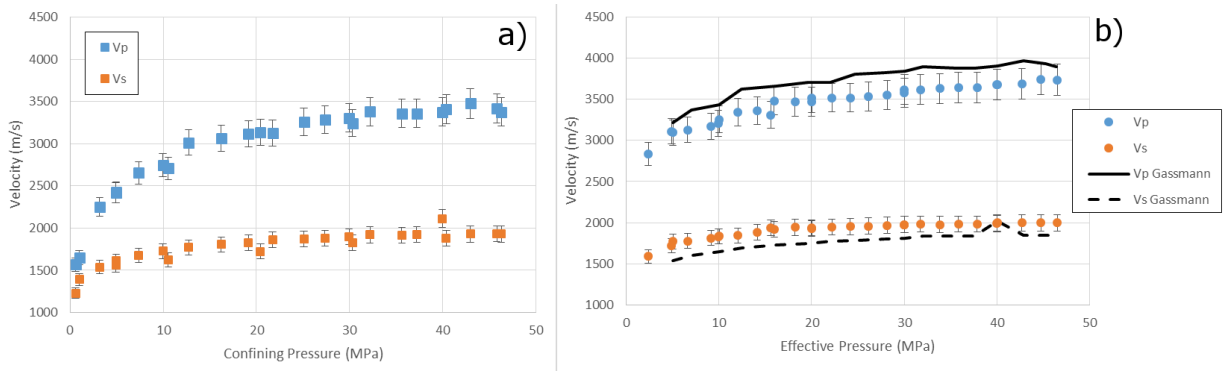


Figure 81 Sample H2-1245.80 (2515) Evolution of P- and S-wave velocities in (a) dry and (b) saturated conditions. Saturated P- and S- wave velocities estimated from Gassmann fluid substitution law are also reported.

Sample 2516 (H2-1247.90 m)

The oscilloscope used to record the ultrasonic waveforms during this test had been malfunctioning, consequently the recorded signals have been affected by a loss of time synchronisation that was not detected during the test. Therefore, the evolution of P- and S-wave velocity with applied effective pressure is not reported for this test. Figure 82 shows the sample strain in response to the confining pressure cycle under dry (Figure 82A) and brine saturated (Figure 82B) conditions at 3 MPa pore pressure. The static bulk modulus (*K*) is derived as the slope of the linear part of the volumetric strain curve and shows values of 4.7 and 6.5 GPa under dry and saturated conditions, respectively in good agreement with the values measured on sample 2515 extracted from the same borehole only 2 m away.

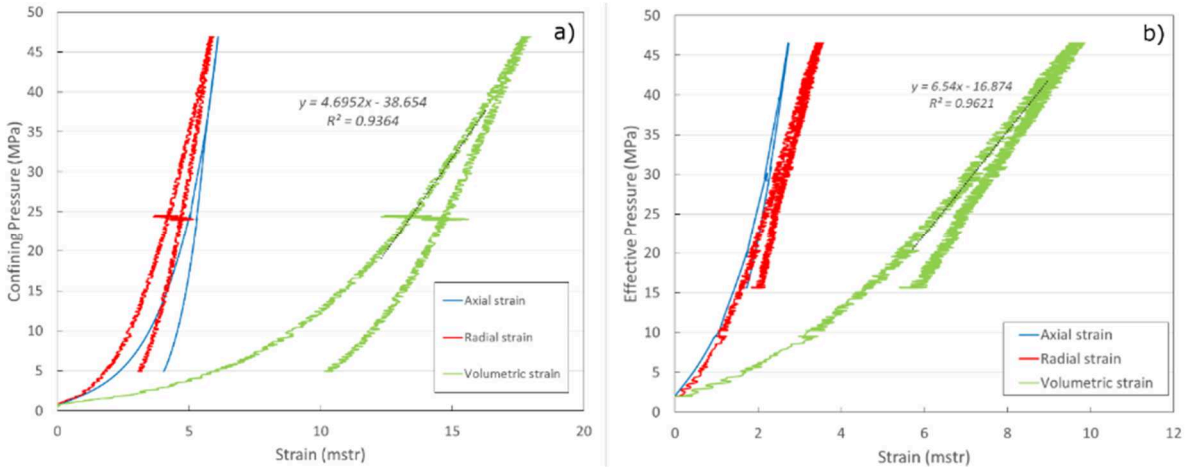


Figure 82 Sample H2-1247.90 (2516) Evolution of axial, radial and calculated volumetric strains with applied hydrostatic pressure in (a) dry and (b) saturated conditions.

Summary

Strain and ultrasonic elastic wave velocity measurements conducted as a function of effective stress under dry and brine saturated conditions lead to the quantification of static and dynamic elastic moduli of 5 sandstone samples from Harvey 2 and Harvey 3. Table 10 lists the static and dynamic elastic moduli derived for each sample under dry and brine saturated conditions.

The experiments also show that the predictions based on Gassmann fluid substitution are generally adequately close to the measured values.

Borehole	Depth (m)	CSIRO id	Unit	Porosity (%)	k_{gas} (mD)	Dry Kst (GPa)	Sat Kst (GPa)	Dry Kdyn (GPa)	Sat K dyn (GPa)
Harvey 3	1417.9	2513	Y	20.6	23	4.2	4.7	9.89	18.40
Harvey 3	1472.1	2514	W	21	615	5.3	4.7	6.17	11.40
Harvey 3	1544.05	2708	W	17.4	3356	5.1	5.9	12.20	18.20
Harvey 2	1245.8	2515	W	19.1	1111	4.7	7.1	10.30	16.10
Harvey 2	1247.9	2516	W	17.4	260	4.7	6.5	N/A	N/A

Table 10 summary of static and dynamic moduli measured on sandstone samples from Harvey 2 and Harvey 3. Kgas = Klinkenberg corrected permeability; Kst = static bulk modulus; Kdyn = dynamic bulk modulus.

4C: Broadband elastic moduli measurements to determine the frequency dependence of the elastic moduli

Alexey Yurikov[2], Maxim Lebedev[2]

[2]Curtin University

Introduction

Surface seismic measurements are performed at seismic frequencies of 20-100 Hz (which correspond to wavelengths of hundreds of meters) because these are the highest frequencies that can penetrate the earth down to typical reservoir depths (2 - 4 km). Borehole logging measurements are performed at frequencies on the order of 10 kHz (so-called sonic frequencies). On the other hand, in laboratory wave propagation experiments, typical wavelength cannot exceed a fraction of a sample size of; say 10-20 cm, corresponding to the frequencies of 100 kHz-1 MHz (ultrasonic frequencies). The frequency difference of three to four orders of magnitude can limit the application of laboratory measurements to seismic prospecting. To overcome these limitations, we tested samples from the Harvey boreholes using a unique low frequency rig (Australia patent AU2011318229) in the frequency range 1 Hz – 100 Hz under in situ conditions. Results of measurements are compared with standard measurements at ultrasonic (1 MHz) frequencies. These results provide supporting information for the interpretation of the seismic data from log and surface collected in the South West Hub area.

Low-frequency measurements

Low-frequency measurements were conducted on five sandstone samples extracted from Harvey 3 and Harvey 4. We present the data obtained with a low-frequency laboratory apparatus designed for measurements of complex Young's moduli and extensional attenuation of rocks at seismic (1-120 Hz) and teleseismic (0.1-1Hz) frequencies and at strain amplitudes of 10^{-8} – 10^{-6}. The experiments include two stages of measurements: on a dry sample and on the same sample saturated with brine. The measurements with brine were performed at pressure and temperature corresponding to the estimated in situ conditions based on the depths of the samples.

Apparatus and method

The experiments in this project were performed using a low-frequency laboratory apparatus (Figure 83) based on the strain-stress technique with longitudinal forced oscillations. The Poisson ratio (ν) and Young modulus (E) of the rock sample are inferred from the known Young modulus of an aluminium standard and strains detected in the standard and sample. The bulk (K) and shear (μ) moduli of a sample are computed according to equations 15 and 16 of section 4B.

The mechanical and electrical parts of the apparatus are presented in Figures 82a and 82b, respectively. The multilayer piezoelectric actuator transforms the periodic voltage, applied by an oscillator, into mechanical stress, which causes displacements in the aluminum standard and the tested sample which are mounted in series. The displacements modulate the conductivity of the strain gauges. A set of electric bridges transforms the modulated conductivity into electric signals, which, after digitizing by an analogue-to-digital converter (model 100, InstruNet, Omega Engineering Ltd), are received by an acquisition computer, where the signals are averaged and processed. The value of extensional attenuation is derived from the phase delay between the stress applied to the sample and the strain in the rock. The extensional attenuation Q_E^{-1} in the rock sample is estimated as the phase shift ($\Delta\varphi$) of the signals obtained from the axial strain gauges coupled with the sample and the aluminium standard:

$$\boldsymbol{Q_E^{-1} = \Delta\varphi} \qquad \textbf{Equation 19}$$

We used the following procedure to estimate $\Delta\varphi$. The signals obtained from two axial strain gauges attached to the sample and standard, are first digitized, averaged and subjected to Fourier transform. The complex Fourier transform amplitudes of those signals are then computed at the frequency of the harmonic stress,

and the target value $\Delta\varphi$ is calculated as the difference between the phases of the computed complex amplitudes. The uncertainty in the phase measurements is about ± 0.003 rad.

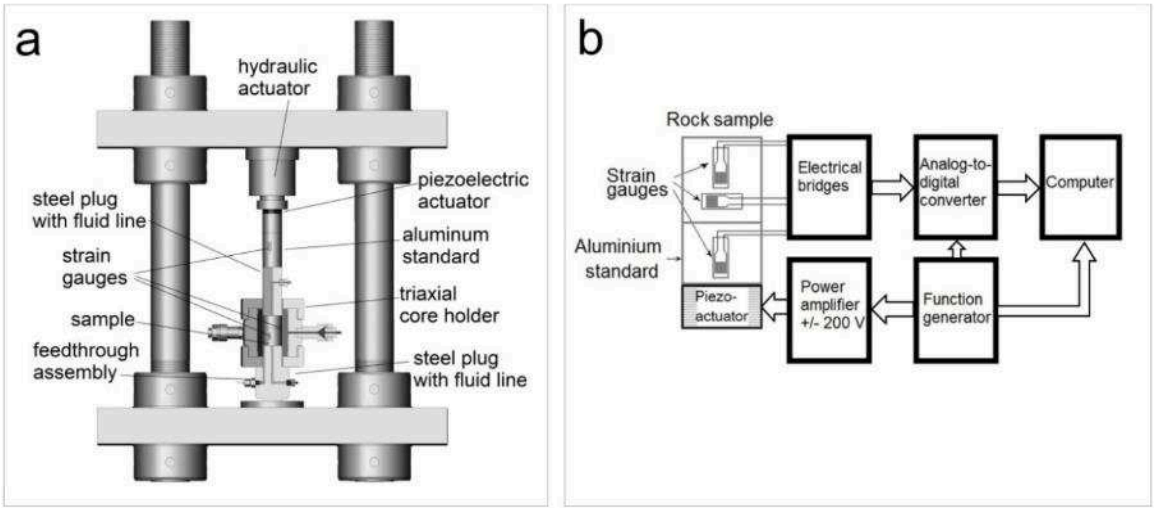


Figure 83 The mechanical assembly (a) and electrical schematics (b) of the low-frequency laboratory apparatus.

Results

Low-frequency measurements were conducted on sandstone samples obtained from Harvey 3 and 4 at environmental conditions replicating those found in-situ. The sample characteristics and experimental conditions of temperature and pressure are presented in Table 11.

Borehole	Sample ID	Depth (m)	Dry Bulk density (kg/m³)	Wet Bulk density (kg/m³)	Porosity (%)	Permeability (mD)	Temperature (°C)	Confining pressure (MPa)	Pore pressure (MPa)
Harvey 4	H4-1	1797.1	1899	2064	17.4	35	44	40.6	18
Harvey 4	H4-2	1797.5	2023	2213	19	550	44	40.6	18
Harvey 3	H3-26	1549.6	2083	2263	18	2200	40	35	15.5
Harvey 4	H4-3	1795.0	2049	2229	18	5.5	44	40.6	18
Harvey 4	H4-4	1800.4	2194	2336	14.2	0.9	44	40.7	18

Table 11 Physical parameters of the samples.

The measurements presented below were conducted using oscillating frequencies ranging between 0.1 and 100 Hz. At each frequency, the stress-strain readings of 100 oscillations were averaged to improve the signal-to-noise ratio of the signals obtained from the strain gauges. The results obtained for the specimens are presented in Figures 83 to 87 and in Appendix 4B in tabulated form. Each sample was first tested dry at a given confining pressure replicating the in-situ lithostatic stress assuming an effective stress gradient of 0.0126 MPa/m. Subsequently the sample was brine saturated and tested again using an effective pressure (Peff = Confining Pressure – Pore pressure) equivalent to the confining pressure of the dry cycle. The samples

were saturated with brine (same as that described in section 3 of this report) at a confining pressure of 40 MPa. To ensure the full saturation of the sample at least 10 pore volumes of brine were injected through the sample with a constant flow rate of 0.5 cm^3/min.

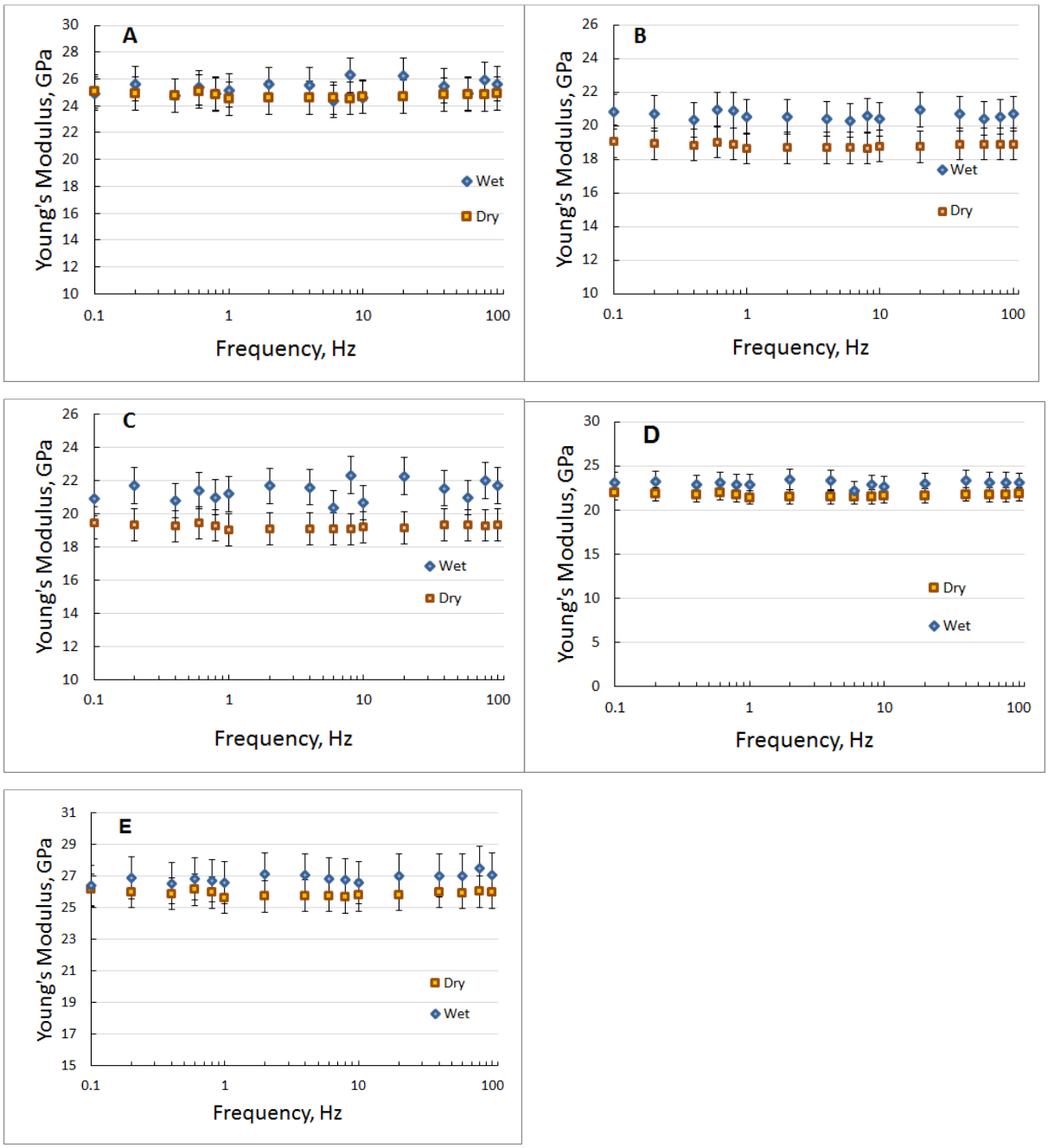


Figure 84 Young's moduli measured on dry and wet Harvey samples (A) H4-1, (B) H4-2 and (C) H3-26; (D) H4-3 and (E) H4-4. The measurements with the dry samples are conducted at confining pressures equal to the difference between confining and pore pressures of the wet cycle.

Theoretical predictions of bulk moduli were obtained using the Gassmann fluid substitution procedure and shown as dashed lines in Figure 85. For our calculations, we used the mineral bulk modulus of quartz equal to 36 GPa. The Poisson's ratio obtained for dry and wet samples are given in Figure 86.

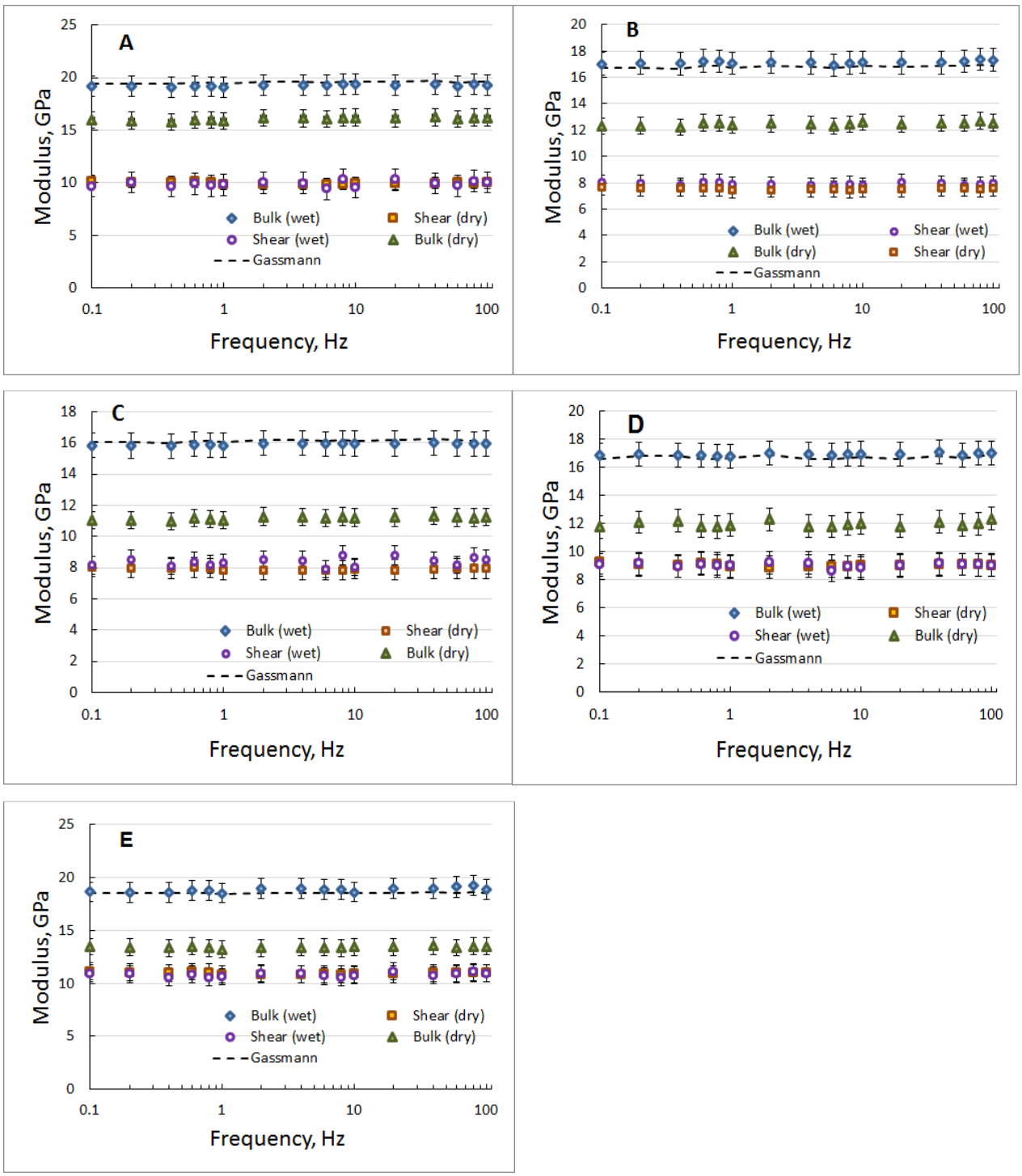


Figure 85 Seismic frequency bulk and shear moduli measured on dry and wet Harvey samples (A) H4-1, (B) H4-2 and (C) H3-26; (D) H4-3 and (E) H4-4.

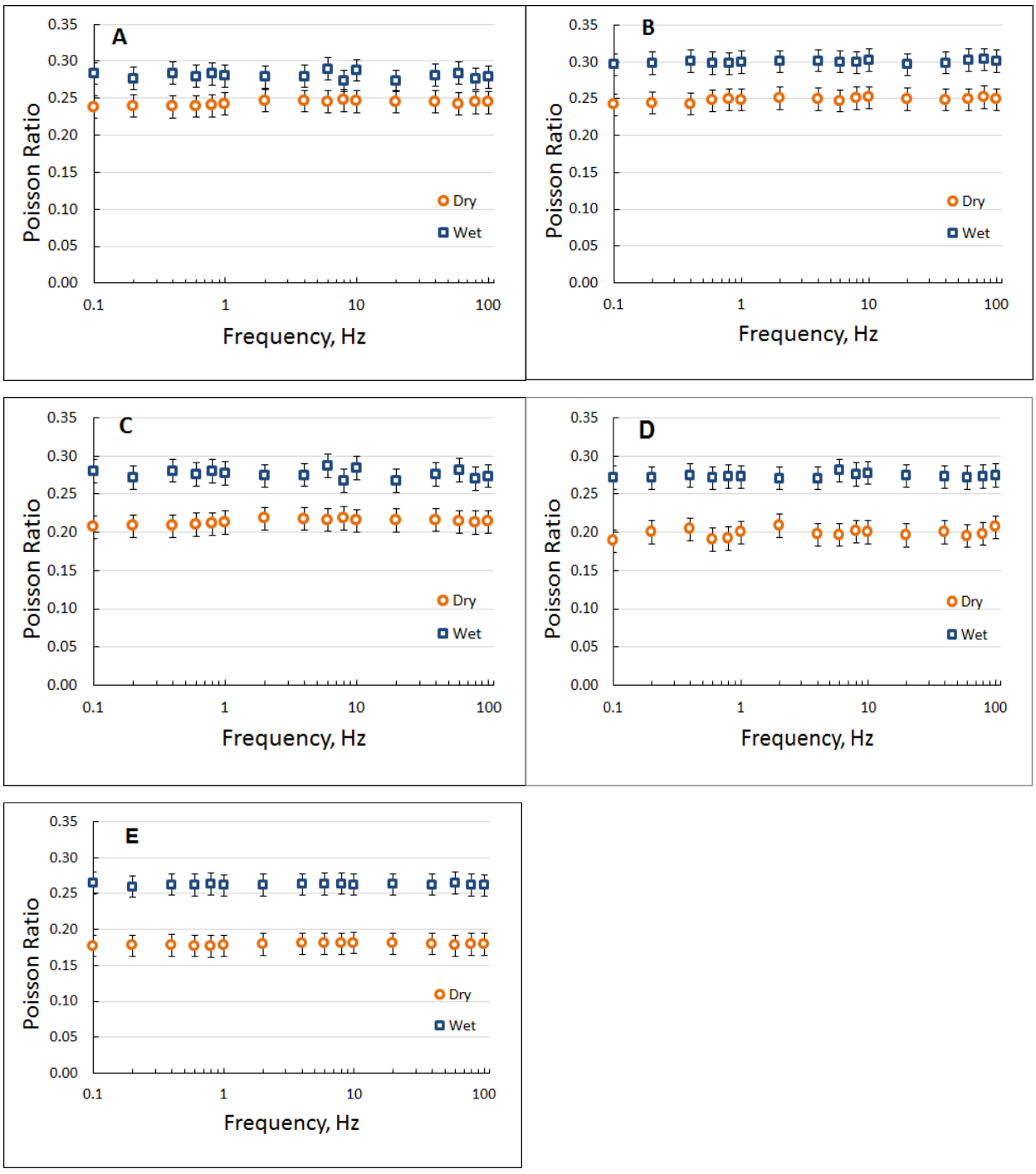


Figure 86 Poisson ratio obtained for dry and wet Harvey samples (A) H4-1, (B) H4-2 and (C) H3-26; (D) H4-3 and (E) H4-4.

P and S wave velocities (Figure 87) were computed from the bulk (K) and shear (μ) moduli using the following equations:

$$V_p = \sqrt{\frac{K+\frac{4}{3}G}{\rho}}$$ Equation 20

$$V_s = \sqrt{\frac{\mu}{\rho}}$$ Equation 21

We found that the extensional attenuation measured for all samples in dry and water saturated states is insignificant, as demonstrated in Figure 88.

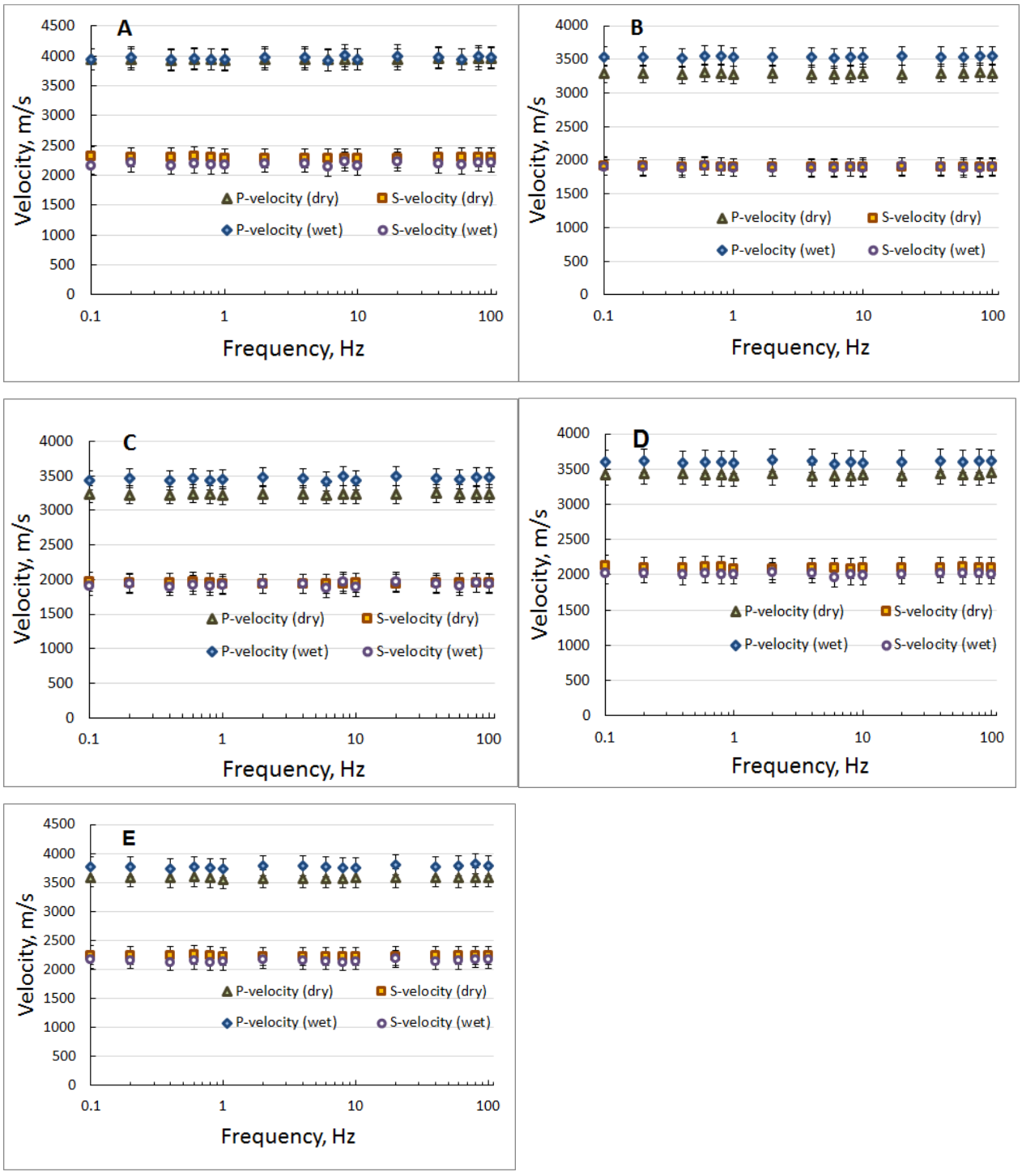


Figure 87 P and S wave velocities obtained for dry and brine saturated samples (A) H4-1, (B) H4-2 and (C) H3-26, (D) H4-3 and (E) H4-4.

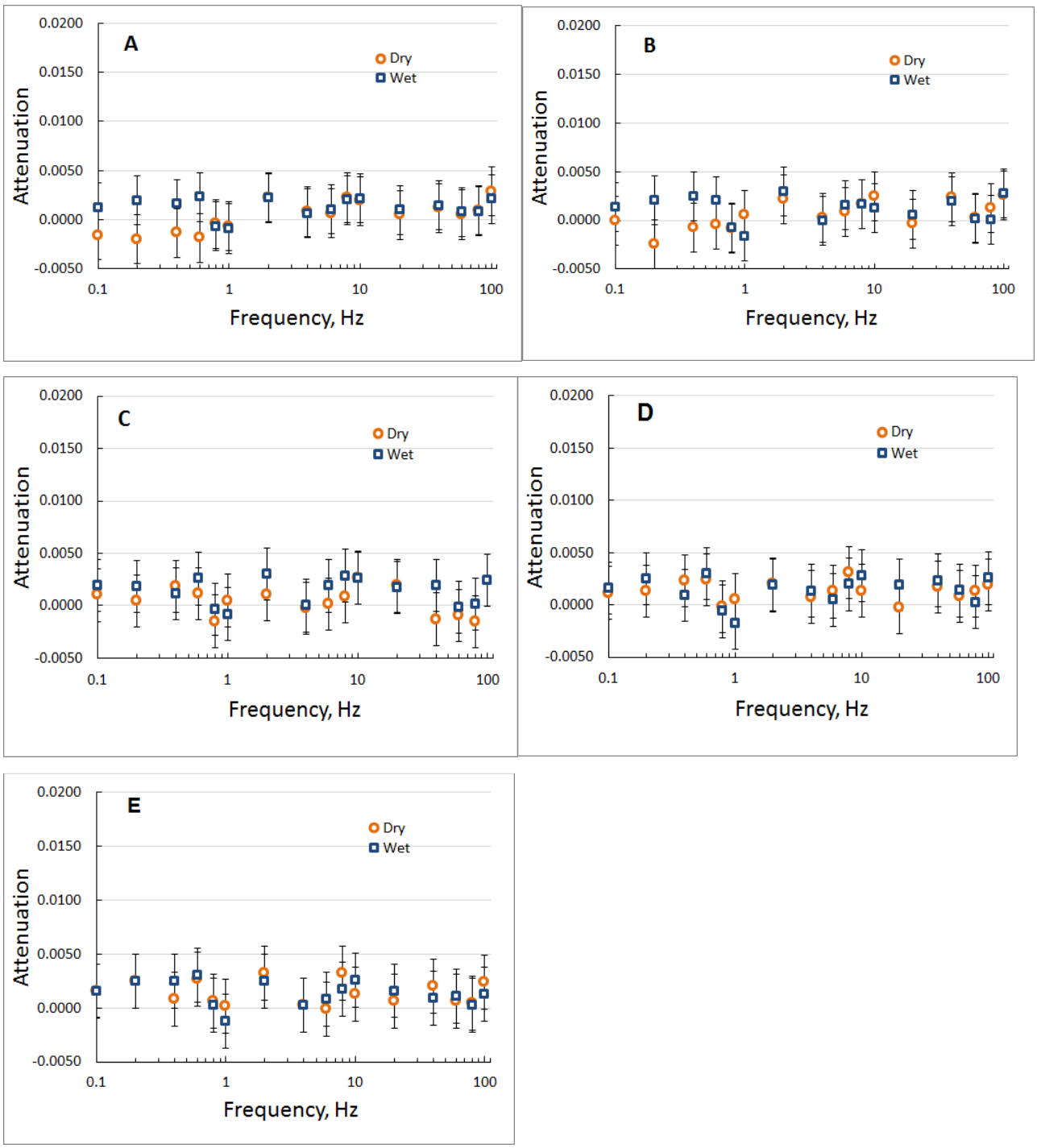


Figure 88 Extensional attenuation measured for the dry and brine saturated Harvey samples (A) H4-1, (B) H4-2 and (C) H3-26, (D) H4-3 and (E) H4-4.

Ultrasonic measurements

To obtain elastic properties and their dependency on effective stress, laboratory measurements are conducted using the equipment shown in Figure 89. A triaxial (Hoek) high pressure cell with a capacity of up to 70 MPa and hydraulic press with capacity for measurements up to 150 MPa are used to apply, respectively, radial and axial stresses to the sample, while measuring P and S wave velocities along the axis of the cylindrical sample. An example of the recorded waveforms is given in Figure 90. All measurements are conducted under room temperature and isotropic pressure (i.e. radial and axial stresses are equal); further details on the experimental set-up are given by Lebedev et al. (2013). Dynamic shear (μ_{dyn}), bulk (K_{dyn}), Young's (E_{dyn}) elastic moduli and Poisson's ratio (υ_{dyn}) are derived from measured velocities and density (ρ) of the sample:

$$Vp = \sqrt{\frac{K_{dyn} + {}^{4}/_{3}\mu_{dyn}}{\rho}} \qquad \text{Equation 22}$$

$$Vs = \sqrt{\frac{\mu_{dyn}}{\rho}} \qquad \text{Equation 23}$$

$$E = \frac{9K_{dyn}\mu_{dyn}}{3K_{dyn} + \mu_{dyn}} \qquad \text{Equation 24}$$

$$\nu = \frac{3K_{dyn} - 2\mu_{dyn}}{2(3K_{dyn} + \mu_{dyn})} \qquad \text{Equation 25}$$

Measurements are done on fully saturated samples by injecting brine into a sample using a fluid pressure of 5 MPa and confining pressure of 10 MPa. Further, to test partially saturated samples, air is injected into the sample under atmospheric pressure. The sample is weighed after injection in order to estimate the saturation. To assess the fluid saturation effect on elastic properties of the sample, Gassmann fluid substitution theory is used (see section 4B above for governing equations). For partially saturated conditions, the effective bulk modulus of the pore fluid (K_{fl}) is estimated using Brie's mixing law as:

$$K_{fl} = (K_{water} - K_{air})s^3 - K_{air} \qquad \text{Equation 26}$$

where K_{water} and K_{air} are bulk moduli of water and air respectively and s is the water saturation.

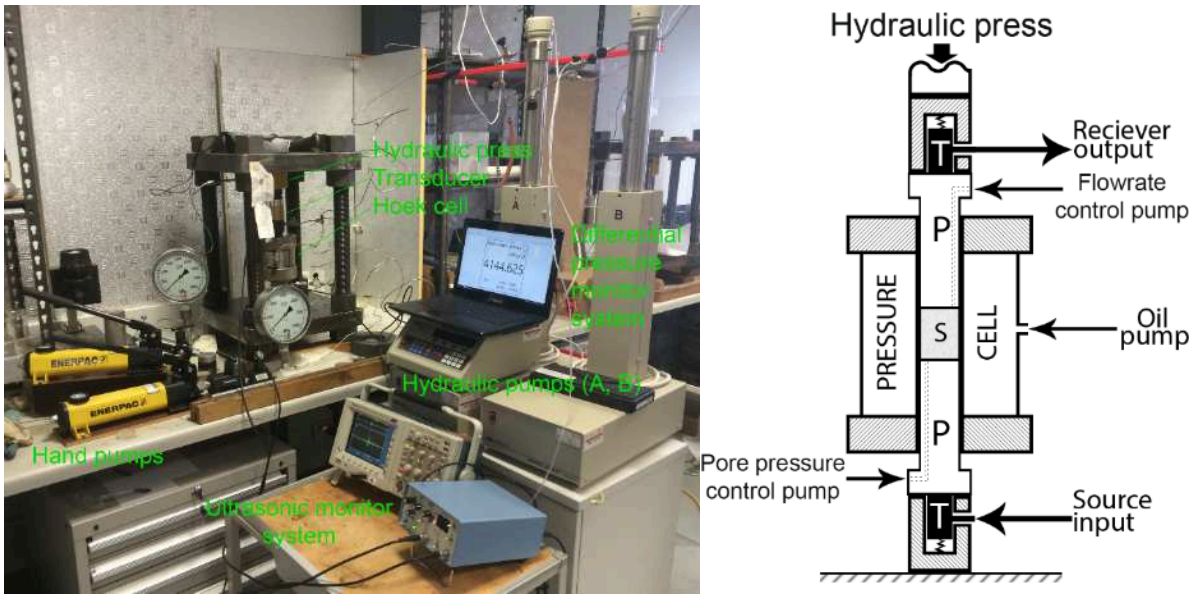


Figure 89 Left: Rock physics testing equipment. Right: schematic drawing of the experimental set-up inside the pressure cell. T – ultrasonic transducers, P – PEEK pistons, , S –sample.

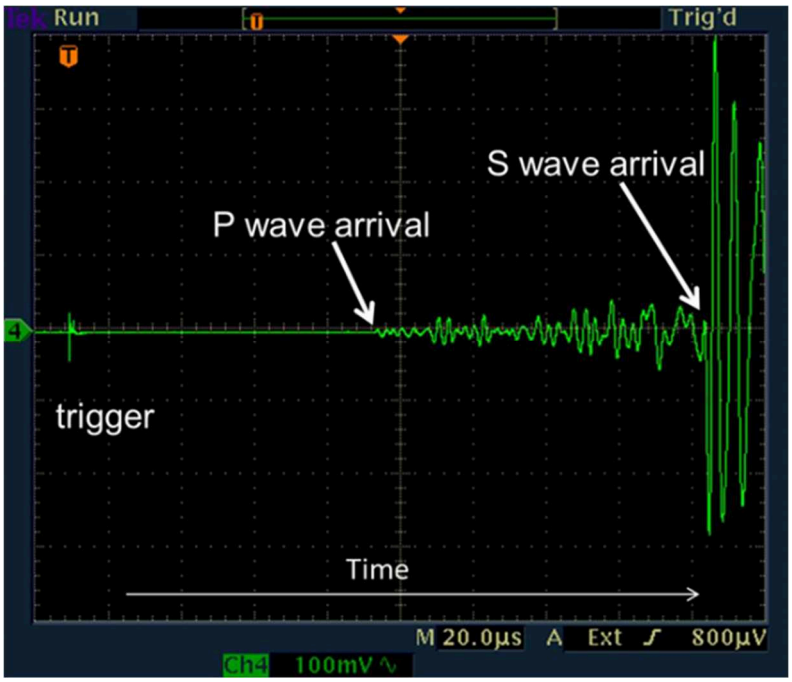


Figure 90 Typical recorded waveform: Arrivals of P and S-waves are clearly observed.

The experimental protocol consisted of the following steps:

- Measurements of velocities versus effective pressure on dry sample;
- Saturation of the sample with brine;
- Measurements of velocities versus effective pressure on fully brine saturated sample;
- Injection of air into the brine saturated sample;
- Measurements of velocities versus effective pressure on partially saturated sample.

Results

Sample: H4-1 (1797.1)

Figures 91, 92 and 93 show the dependence of P-wave and S-wave velocities versus different effective pressures for dry, 100% brine saturated, and ~80% brine saturated sandstone and velocities calculated using Gassmann fluid substitution. Dynamic moduli (bulk, shear, Young's) as well as Poisson's ratio for these series of experiment are tabulated in Appendix 4A.

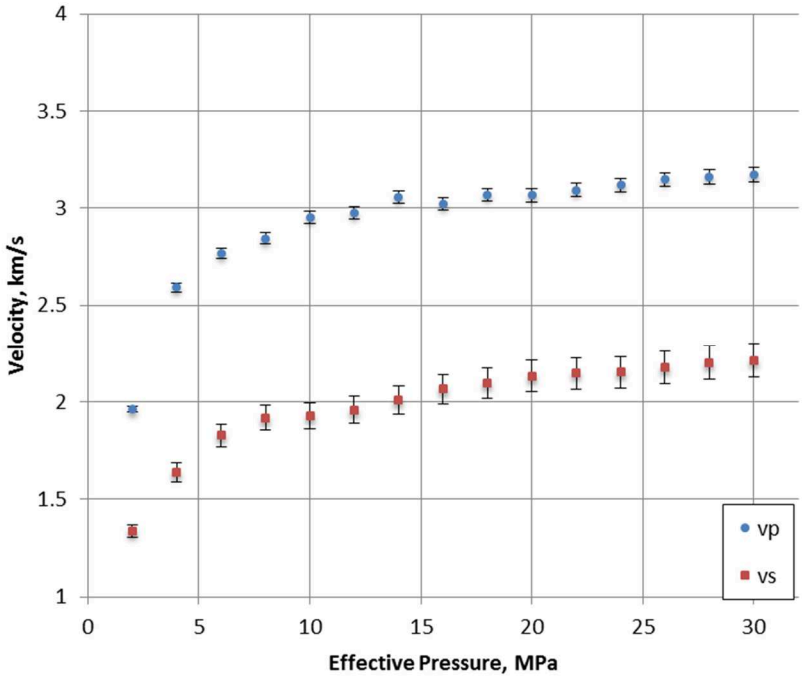


Figure 91 P and S-wave velocities as a function of effective pressure for dry sample at room temperature. Sample H4 (1797.1).

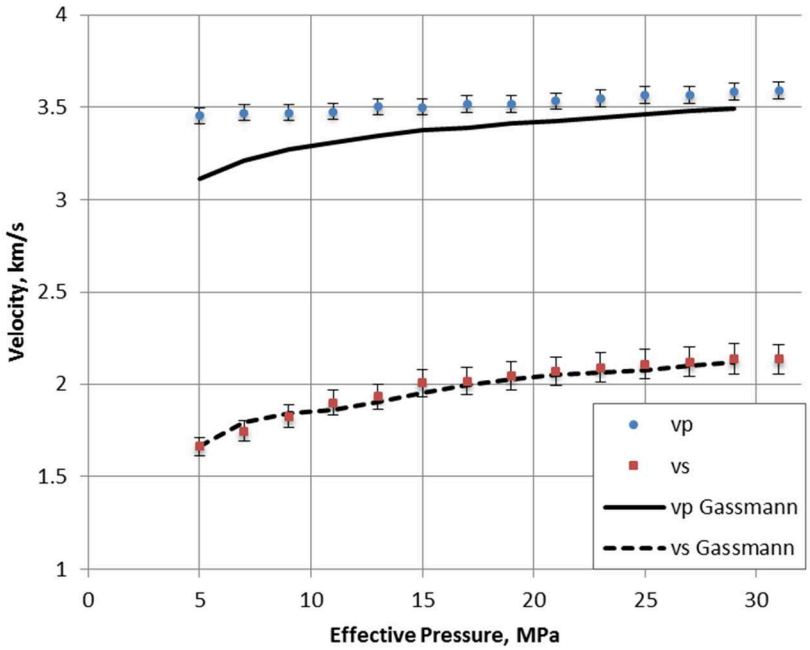


Figure 92 P-wave and S-wave velocities as a function of effective pressure for 100% brine saturated sample at room temperature. Pore pressure is 5 MPa. Theoretical predictions of vp and vs velocities using Gassmann fluid substitution procedure is shown as solid and dashed lines. Sample H4 (1797.1).

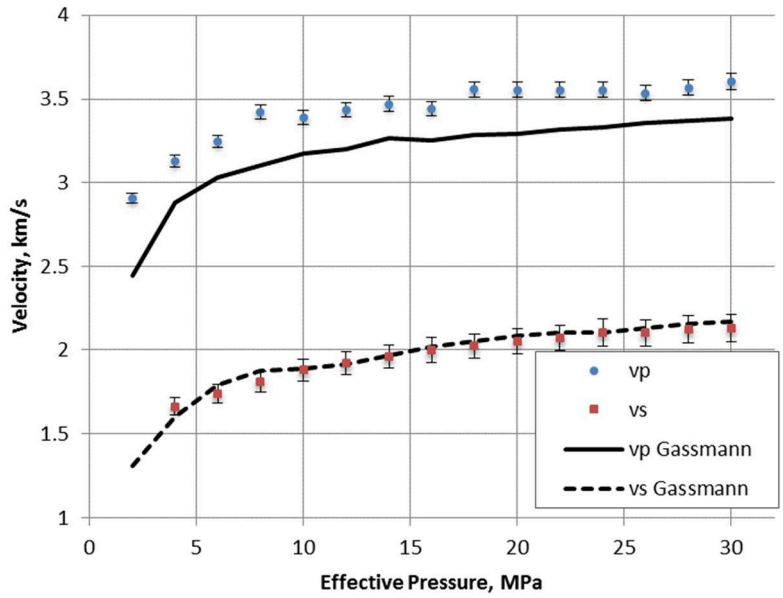


Figure 93 P-wave and S-wave velocities as a function of effective pressure for ~ 80% brine saturated sample at room temperature. Pore pressure is 0.1 MPa. Theoretical predictions of vp and vs velocities using Gassmann fluid substitution procedure is shown as solid and dashed lines. Sample H4 (1797.1)

Sample H4 (1797.5)

Figure 94 shows the dependence of P-wave and S-wave velocities versus different effective pressures for dry sample H4 (1797.5). During the brine saturation stage of the experiment the rubber jacket inside the Hoek cell was damaged and hydraulic oil intruded the sample. Cleaning procedures for removing the oil led to the destruction of the sample such that further testing was not possible impossible. Dynamic moduli (bulk, shear, Young's) as well as Poisson's ratio for these series of experiment are reported in Appendix 4A.

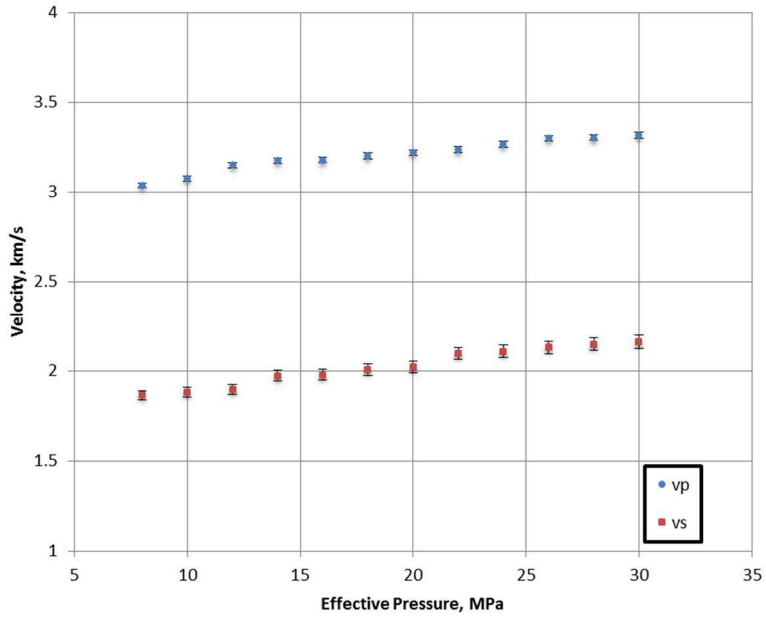


Figure 94 P and S-wave velocities as a function of effective pressure for dry sample at room temperature. Sample H4 (1797.5).

Sample H4 (1800.4)

Figures 95, 96, and 97 show the dependence of P-wave and S-wave velocities versus different effective pressures for dry, 100% brine saturated, and 82% brine saturated sample and velocities calculated using Gassmann fluid substitution. Dynamic moduli (bulk, shear, Young's) as well as Poisson's ratio for these series of experiment are provided in Appendix 4A.

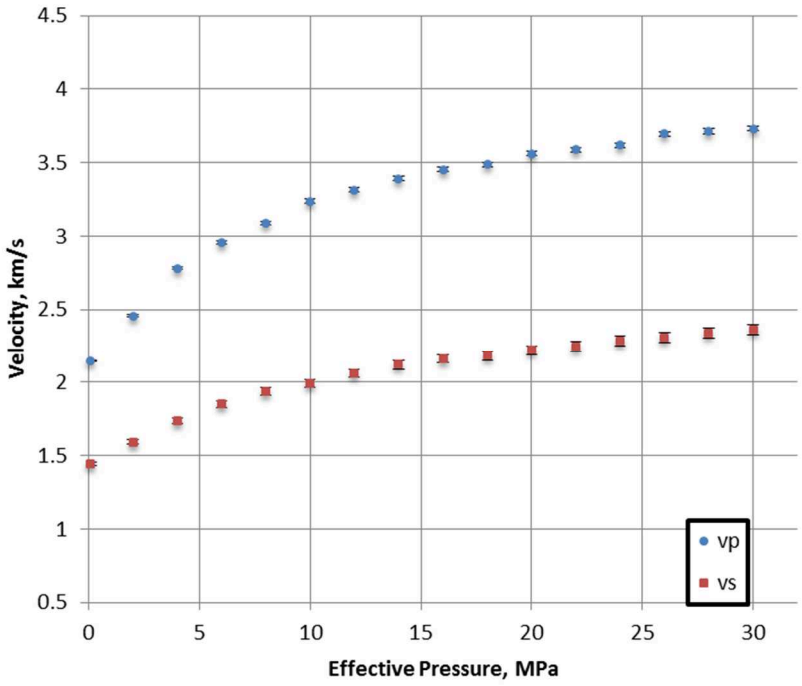


Figure 95 P and S-wave velocities as a function of effective pressure for dry sample at room temperature. Sample H4 (1800.4).

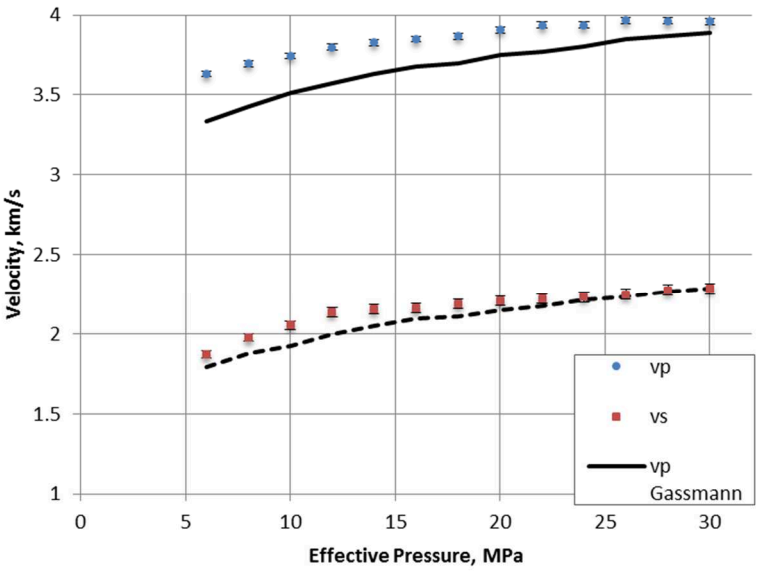


Figure 96 P-wave and S-wave velocities as a function of effective pressure for 100% brine saturated sample at room temperature. Pore pressure is 6 MPa. Theoretical predictions of vp and vs velocities using Gassmann fluid substitution procedure is shown as solid and dashed lines. Sample H4 (1800.4).

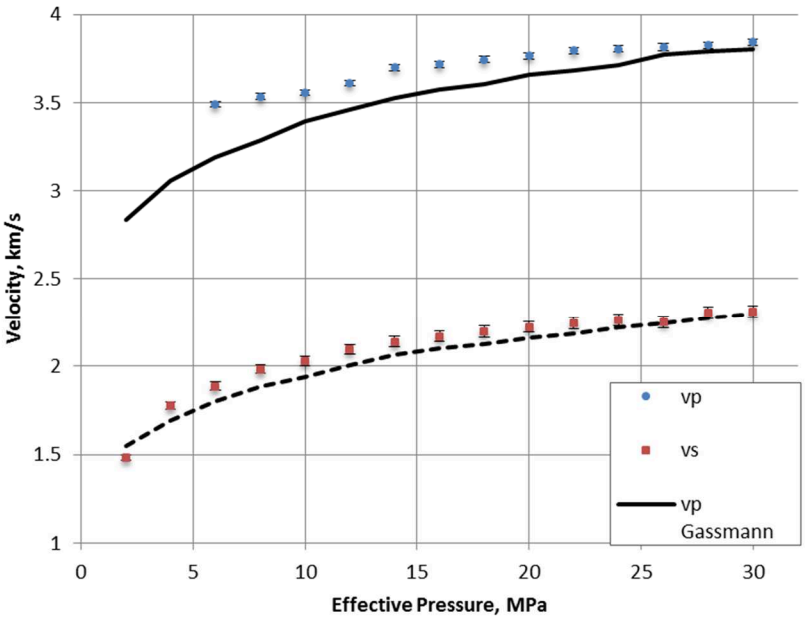


Figure 97 P-wave and S-wave velocities as a function of effective pressure for ~82% brine saturated sample at room temperature. Pore pressure is 0.1 MPa. Theoretical predictions of vp and vs velocities using Gassmann fluid substitution procedure is shown as solid and dashed lines. Sample H4 (1800.4).

Sample H4 (1796.8)

Figures 98, 99, and 100 show the dependence of P-wave and S-wave velocities versus different effective pressures for dry, 100% brine saturated, and 83% brine saturated sample and velocities calculated using Gassmann fluid substitution. Dynamic moduli (bulk, shear, Young's) as well as Poisson's ratio for these series of experiment are provided in Appendix 4A.

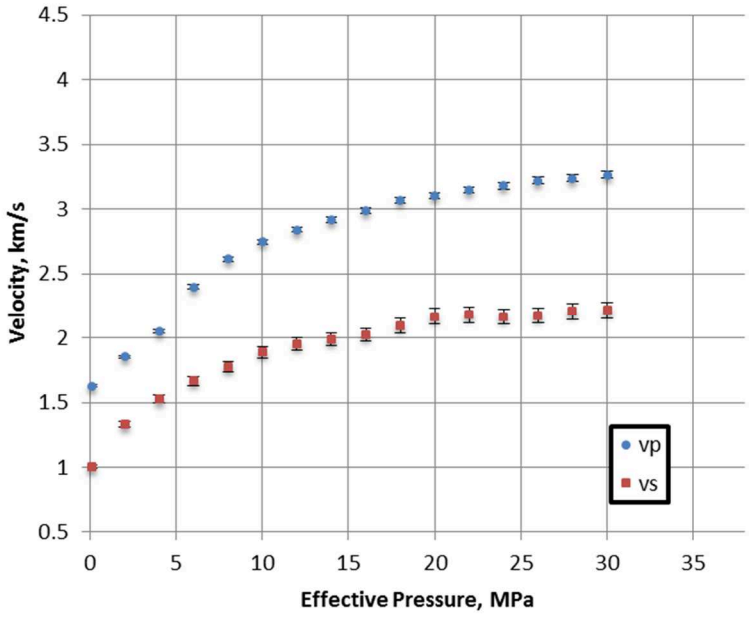


Figure 98 P and S-wave velocities as a function of effective pressure for dry sample at room temperature. Sample H4 (1796.8).

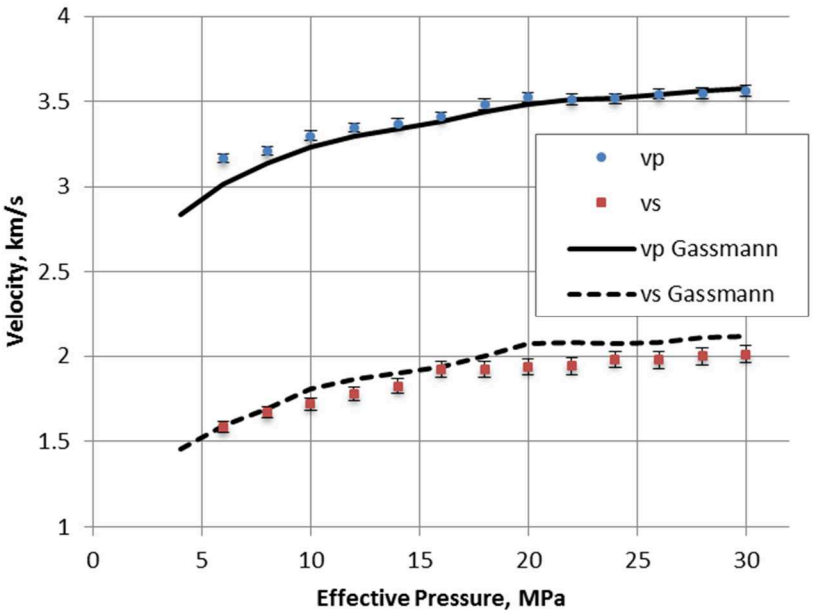


Figure 99 P-wave and S-wave velocities as a function of effective pressure for 100% brine saturated sample at room temperature. Pore pressure is 6 MPa. Theoretical predictions of vp and vs velocities using Gassmann fluid substitution procedure is shown as solid and dashed lines. Sample H4 (1796.8).

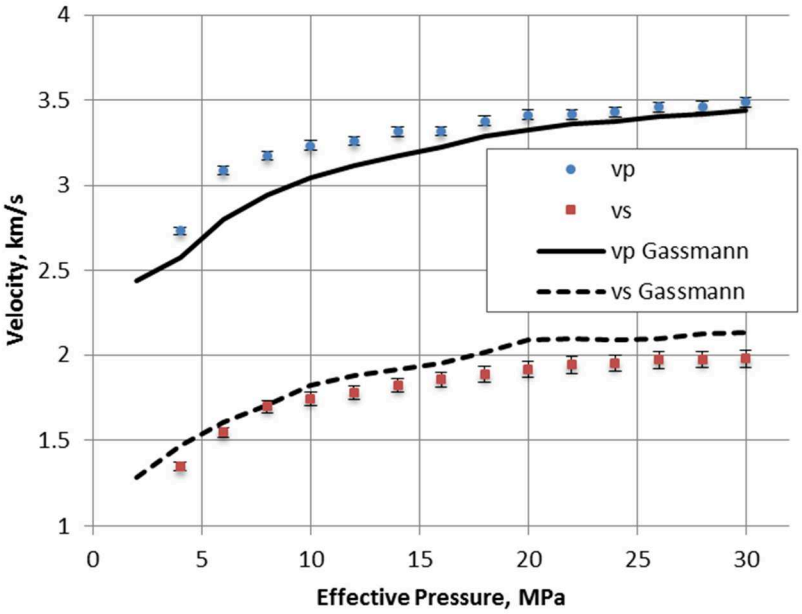


Figure 100 P-wave and S-wave velocities as a function of effective pressure for ~83% brine saturated sample at room temperature. Pore pressure is 0.1 MPa. Theoretical predictions of vp and vs velocities using Gassmann fluid substitution procedure is shown as solid and dashed lines. Sample H4 (1796.8).

Sample H4 (1795)

Figures 101, 102, and 103 show the dependence of P-wave and S-wave velocities versus different effective pressures for dry, 100% brine saturated, and 74% brine saturated sample and velocities calculated using

Gassmann fluid substitution. Dynamic moduli (bulk, shear, Young's) as well as Poisson's ratio for these series of experiment are provided in Appendix 4A.

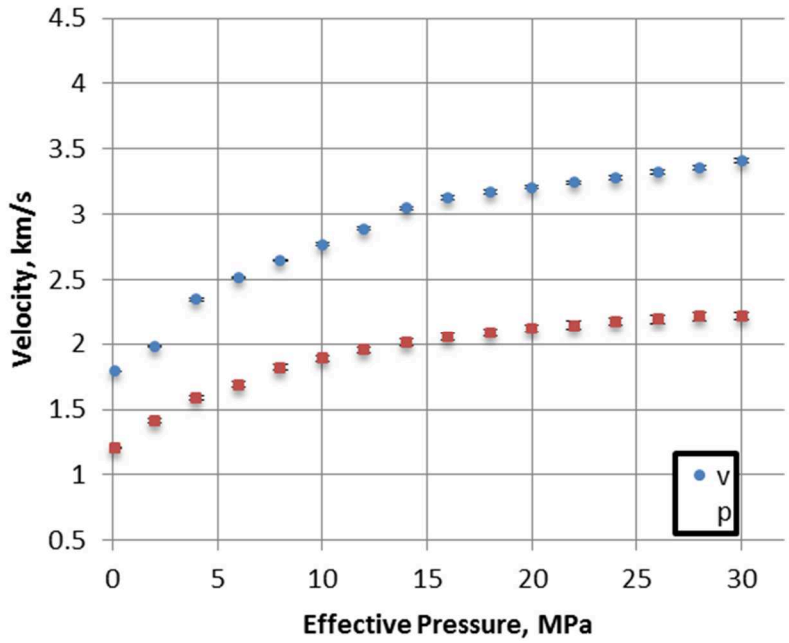


Figure 101 P and S-wave velocities as a function of effective pressure for dry sample at room temperature. Sample H4 (1795).

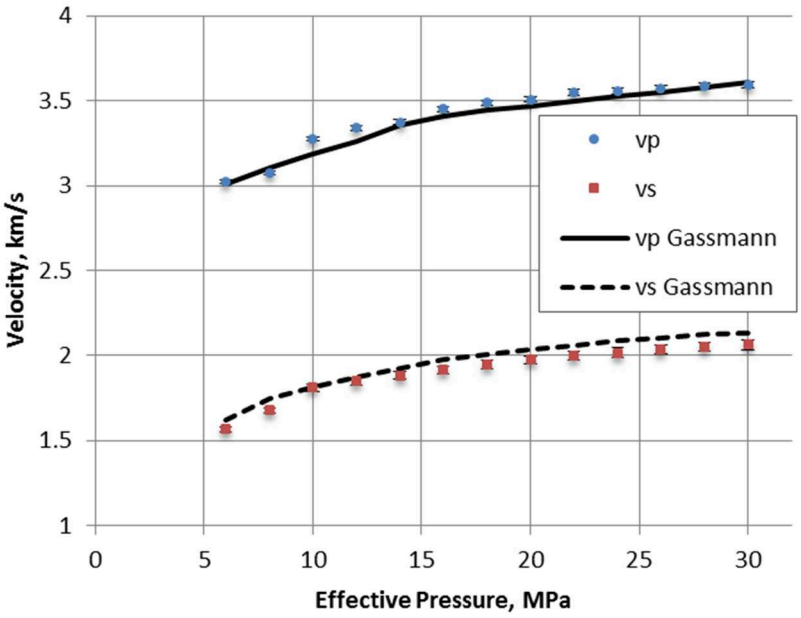


Figure 102 P-wave and S-wave velocities as a function of effective pressure for 100% brine saturated sample at room temperature. Pore pressure is 6 MPa. Theoretical predictions of vp and vs velocities using Gassmann fluid substitution procedure is shown as solid and dashed lines. Sample H4 (1795).

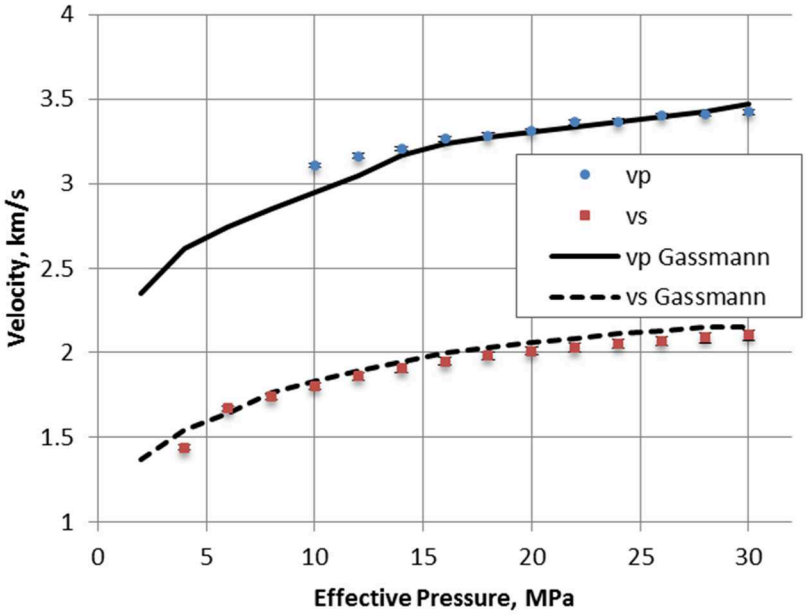


Figure 103 P-wave and S-wave velocities as a function of effective pressure for ~74% brine saturated sample at room temperature. Pore pressure is 0.1 MPa. Theoretical predictions of vp and vs velocities using Gassmann fluid substitution procedure is shown as solid and dashed lines. Sample H4 (1795).

Sample H3 (1549.6)

Figures 104, 105 and 106 show the dependence of P-wave and S-wave velocities versus different effective pressures for dry, 100% brine saturated, and 93% brine saturated sample and velocities calculated using Gassmann fluid substitution. Dynamic moduli (bulk, shear, Young's) as well as Poisson's ratio for these series of experiment are provided in Appendix 4A.

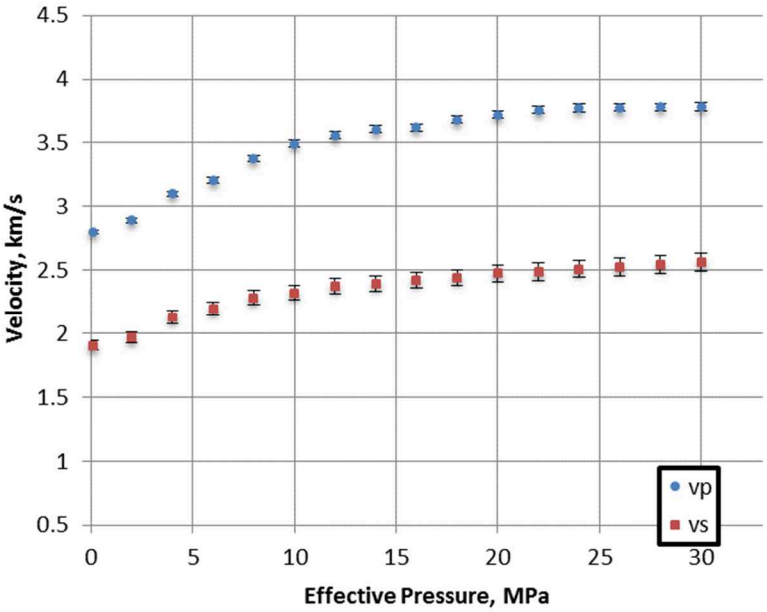


Figure 104 P and S-wave velocities as a function of effective pressure for dry sample at room temperature. Sample H3 (1549.6).

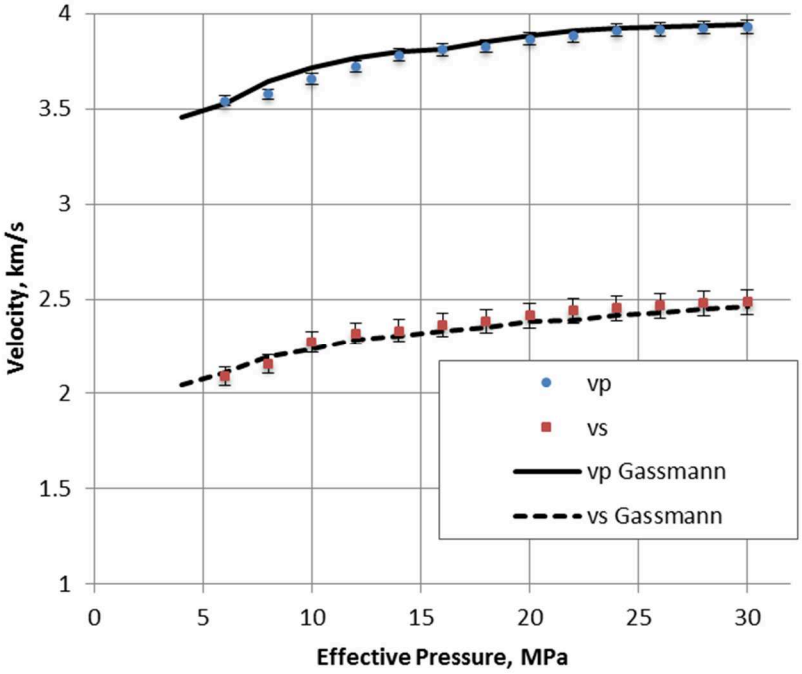


Figure 105 P-wave and S-wave velocities as a function of effective pressure for 100% brine saturated sample at room temperature. Pore pressure is 6 MPa. Theoretical predictions of vp and vs velocities using Gassmann fluid substitution procedure is shown as solid and dashed lines. Sample H3 (1549.6).

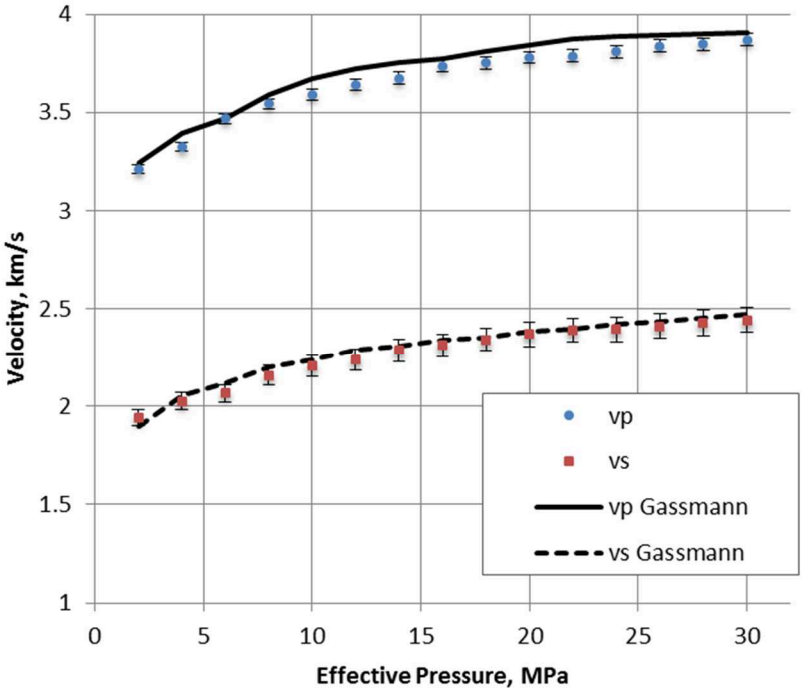


Figure 106 P-wave and S-wave velocities as a function of effective pressure for ~93% brine saturated sample at room temperature. Pore pressure is 0.1 MPa. Theoretical predictions of vp and vs velocities using Gassmann fluid substitution procedure is shown as solid and dashed lines. Sample H3 (1549.6).

Summary

Experimental measurements of the elastic properties of five samples from Harvey 4 and one from Harvey 3 were conducted at frequencies spanning from teleseismic (0.1 Hz) to ultrasonic (500 kHz) under dry, fully brine saturated and partially saturated conditions. The experimental results indicate that:

- No significant difference in elastic moduli between ultrasonic and seismic frequencies was observed;
- No significant attenuation was observed at seismic frequencies under dry and brine saturated conditions;
- Experimental data for fully and partially saturated sample can be adequately predicted using the Gassmann theory of fluid substitution;
- Based on measurement on these six samples it is very likely that Gassmann fluid substitution procedure can be applied for tested samples from Harvey 3 and 4.

4D: Calibration of stress induced anisotropy changes during fluid substitution

Nazanin Nourifard[2], Maxim Lebedev[2]

[2] Curtin University

Introduction

Anisotropy of rocks, i.e. directional dependence of physical properties, strongly effects propagation of seismic waves inside the earth. Detailed knowledge of seismic anisotropy is extremely important for time lapse monitoring of subsurface reservoirs. Fluid injection into the pore space of a reservoir (for example during injection of CO_2 into an aquifer) can change the elastic properties of rocks and thus their anisotropy. Moreover, fluid injection can change the stress regime acting on the reservoir, also leading to change of anisotropy. To assess the potential influence of fluids and stresses on anisotropy, two samples of the Wonnerup Member of the Lesueur Sandstone from Harvey 4 have been tested in the laboratory.

Method

Laboratory studies of anisotropy in rocks provide important input into the understanding of seismic anisotropy in the field. The inclusion of anisotropic models in seismic methods can assist, for example, in fracture detection and subsurface monitoring (Tsvankin et al., 2010). Laboratory techniques usually involve measuring P and S wave velocities with ultrasonic transducers and then inverting these velocities to calculate elastic stiffness coefficients. The rock symmetry is often known in advance (or is assumed) and this enables the inversion. Despite the wide use of ultrasonic transducers, they suffer several disadvantages when applied to the study of anisotropy: their finite size (typically 100 mm^2 contact area) means that only an average velocity of a relatively large area can be measured. Also, transducers can only record the components of particle motion in the planes parallel and perpendicular to the sample surface. Finally, there is an uncertainty in whether phase or group velocities are measured which depends upon the relative sizes of the source, sample and receiver (Dellinger and Vernik, 1994). To overcome these limitations, Lebedev et al. (2011) elaborated a laboratory technique using Laser Doppler Interferometry (LDI) to measure wave polarizations. LDI can measure particle velocity at a point and by recording three independent components can reconstruct the full 3D motion (and hence polarization) of any point on the surface of a sample. Since the spot size of the laser beam is small (1 mm^2) detailed knowledge of the surface motion can be obtained. This is important as errors in the inversion can be reduced by increasing the number of measured raypaths. The ability to detect changes in polarization is important for the understanding of, for example, stress-induced anisotropy where cracks forming as a result of the applied stress field can affect the elastic waves travelling through the rock in different directions (e.g., Nur, 1971; Gurevich et al., 2011).

The experimental set-up used to measure ultrasonic velocities consisted of a cubic sample mounted in a load frame, held in place by four actuators capable of applying pressure up to 70 MPa (see Figure 107). The actuators were housed in steel supports, adjustable in both azimuth and elevation to allow for precise alignment. Each vertical face of the sample was connected to an actuator via a platen fabricated from PEEK material to ensure uniform load distribution over the cubic rock face. An Olympus 5077PR pulser/receiver was used to drive a Panametrics V153 1 MHz S wave transducer (14 mm in diameter) glued to the bottom of the sample. The orientation of the transducer was such that its polarization direction was at 45 ° to the x and y axes (see Figure 108). The LDI measurement system comprised a Polytec OFV-505 sensor head and Polytec OFV-5000 Vibrometer Controller. Surface vibrations were recorded using the LDI with its beam aligned along each of the directions A, B and C as shown in Figure 109. Special reflective tape, manufactured with spherical glass microbeads, was attached to each measurement point on the surface of the sample. This ensured that the Doppler shifted beam was reflected back into the sensor head. The output signal of the LDI was fed to a Tektronix TDS 3034C oscilloscope from which waveforms were recorded by computer for further analysis.

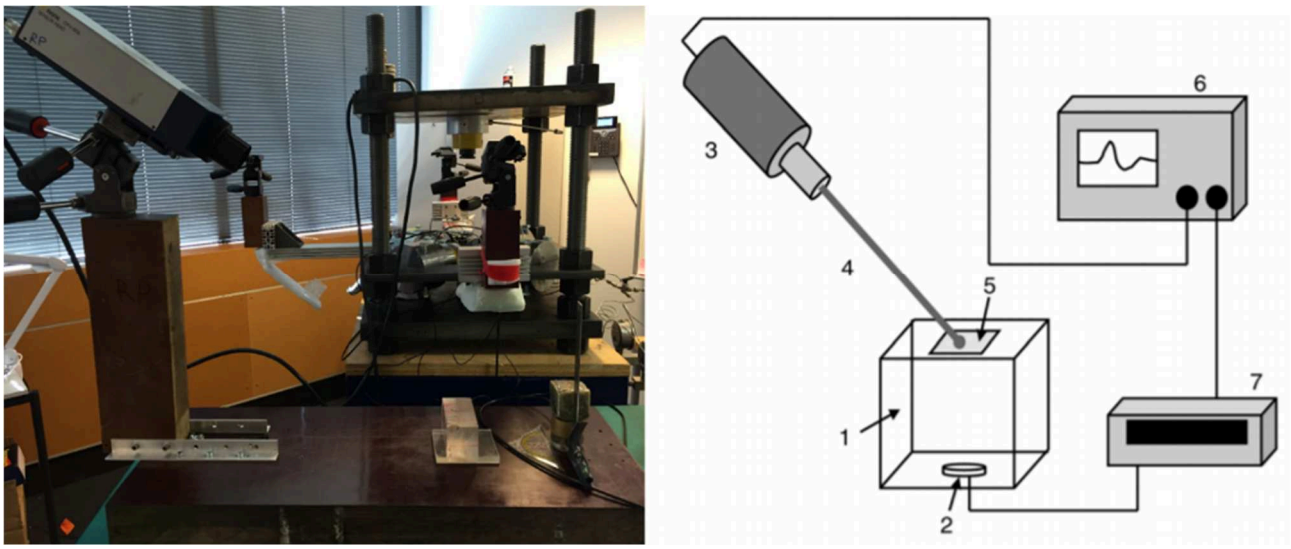


Figure 107 Right: Laser Doppler Interferometry setup. Left: Schematic of the experimental set-up. 1 = sample; 2: source of elastic waves; 3: Laser Doppler Interferometer; 4: laser beams (emitted and backscattered); 5: reflective film; 6: acquisition system device; 7: pulse generator (from Lebedev et al., 2011).

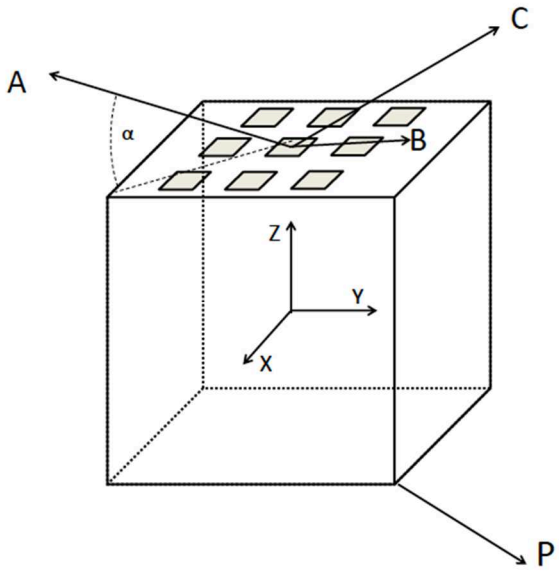


Figure 108 Schematic showing the relevant geometry of the experiment with respect to the cubic sample. A, B, C are directions of the measurement by laser interferometer. P- Direction of the polarization of the source transducer.

Calibration

Initial calibration tests were carried out on a 50 mm cubic sample of Perspex (PMMA). Two S wave transducers were attached to opposite faces of the sample with coupling gel to provide efficient transmission of the shear wave. The transmitted velocities were found to be 1388 m/s and 2777 m/s for shear and compressional elastic waves, respectively (the P wave arises from mode conversion at the interface between the sample and the S wave transducer). The S wave transducer was then attached to the bottom of the sample at an angle of 45° to the x and y axes. The sample was inserted into the load frame and the LDI used

to measure the particle displacement at the centre point on the top surface. Figure 109 shows the displacement waveforms, after transformation to the Cartesian coordinate system. The P and S wave arrival times match the arrivals recorded with the S wave transducer. In-phase components of the S wave can be seen along both the x and y axes. The P wave can be seen only on the z axis, which demonstrates that the plane wave from the source transducer is moving vertically upward. The y component of the S wave has about 70% of the amplitude of the x component. Since the source transducer polarization is at 45° to the x and y axes, we would expect equal amplitude components along both axes. This amplitude asymmetry could be due to inexact placement of the transducer on the bottom of the sample but is more likely due to the imperfect nature of the transducer as a plane polarized source. The hodogram shown in Figure 110 demonstrates this effect more clearly. The figure shows the particle displacement in the xy plane between 36 µs and 41 µs. It can be seen that the displacement is polarized at about 36° to the x axis. The sample was then stressed with stresses of σx = 6 MPa, σy = 24 MPa and σz = 0. The amplitude of the waveform reduces slightly but the arrival time is unchanged (Figure 109). Repeating the measurement with (σx = 6 MPa; σy = 24 MPa; σz = 0 MPa) shows the same effect. The P wave is unchanged throughout.

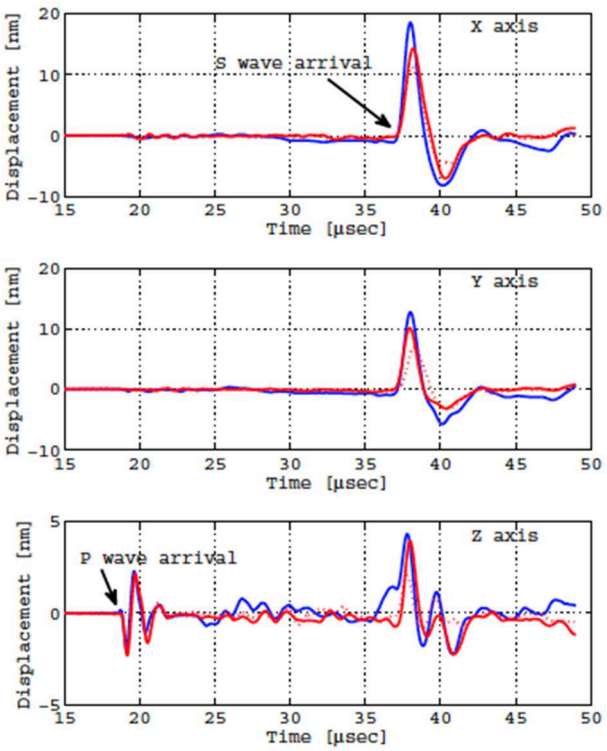


Figure 109 Waveforms along x, y and z axes at the centre of the Perspex sample. Blue waveforms were recorded without applied stress. The waveforms in red were recorded with stresses (σx, σy, σz) = (6, 24, 0 MPa). The dotted red waveforms were recorded with the (σx, σy, σz) = (24, 6, 0 MPa). Note that the scale for the z axis has been increased in order to make the P wave more visible.

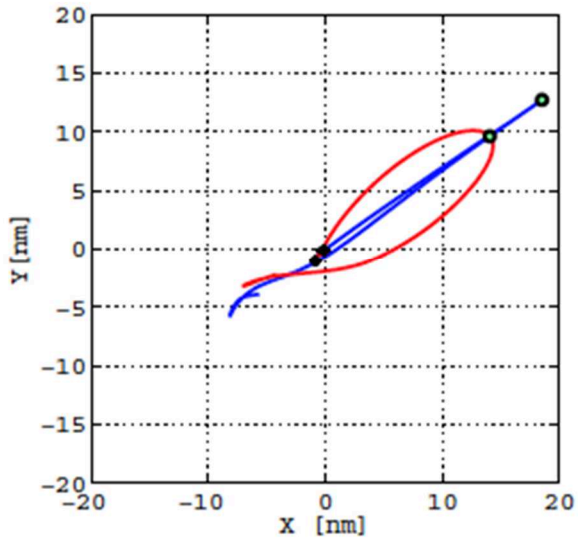


Figure 110 Hodogram of particle displacement for the S wave propagating through a Perspex calibration sample. The blue curve show the displacement without applied stress. The red curve shows the displacement under anisotropic stress conditions (σx = 6 MPa; σy = 24 MPa; σz = 0 MPa).

Sample preparation

Two cubic shape samples 50 mm x 50 mm x 50 mm were cut from cores recovered from Harvey 4 at depth of 1794.4 m and 1797.0 m (Figure 111). Porosity and gas permeability at reservoir pressure of a sister sample to H4 (1794.4m) are 20.2 % and 0.7 D, respectively.

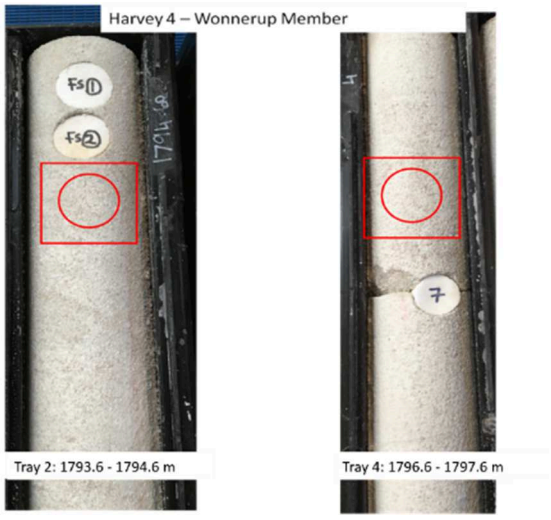


Figure 111 Selection of cubic shape samples from the tray

After extraction from the cores, samples were dried in a vacuum oven at 105 °C for 24h. Samples densities were estimated by measurement of weight and volumes. Ultrasonic P and S wave velocities were measured before and after applying layers of flexible epoxy resin on the surface of the samples. The latter was used to seal the samples and to create smooth surfaces (Figure 112). Two 2-mm-diameter and 2 mm depth holes were drilled on two parallel faces to act as fluid ports for samples saturation. (Figure 112). Flexible plastic

fittings were inserted into the drilled holes and fixed by epoxy resin for later saturation. Samples were vacuumed to verify the absence of any hydraulic leakage (Figure 112). Nine pieces of 2 mm x 2 mm reflective tape were glued on the sample surface as nominated points for the Laser Doppler Interferometry displacement experiment (Figure 113). A 1 MHz -S type-transducer was glued to the bottom of the sample (Figure 113). The polarisation direction of S-wave transduces was chosen to be parallel to diagonal of the square face. Finally, the sample was mounted inside the apparatus between four platens, driven by actuators; each platen has S-wave transducer sealed inside.

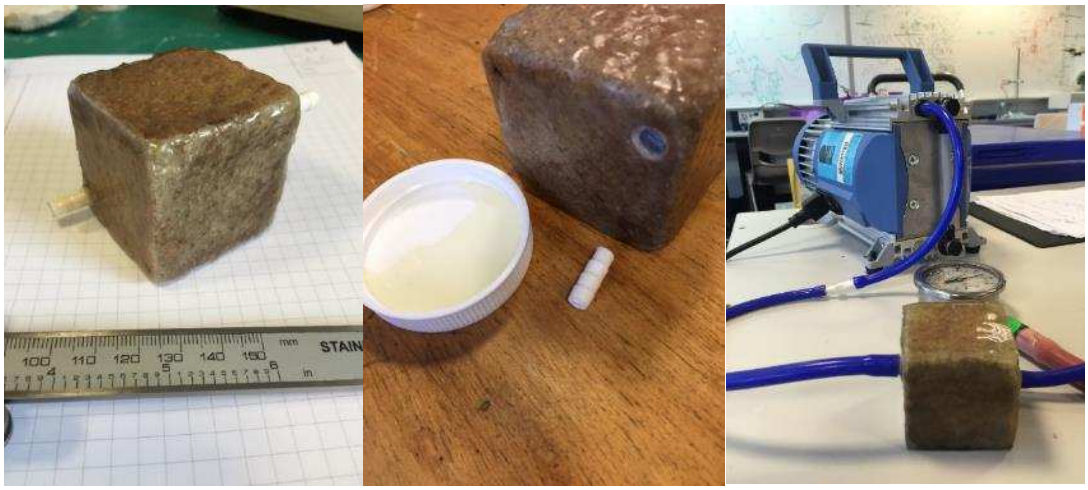


Figure 112 Sample coating with epoxy layer (left); attachment of fluid fittings (middle) and vacuuming of the sample (right).

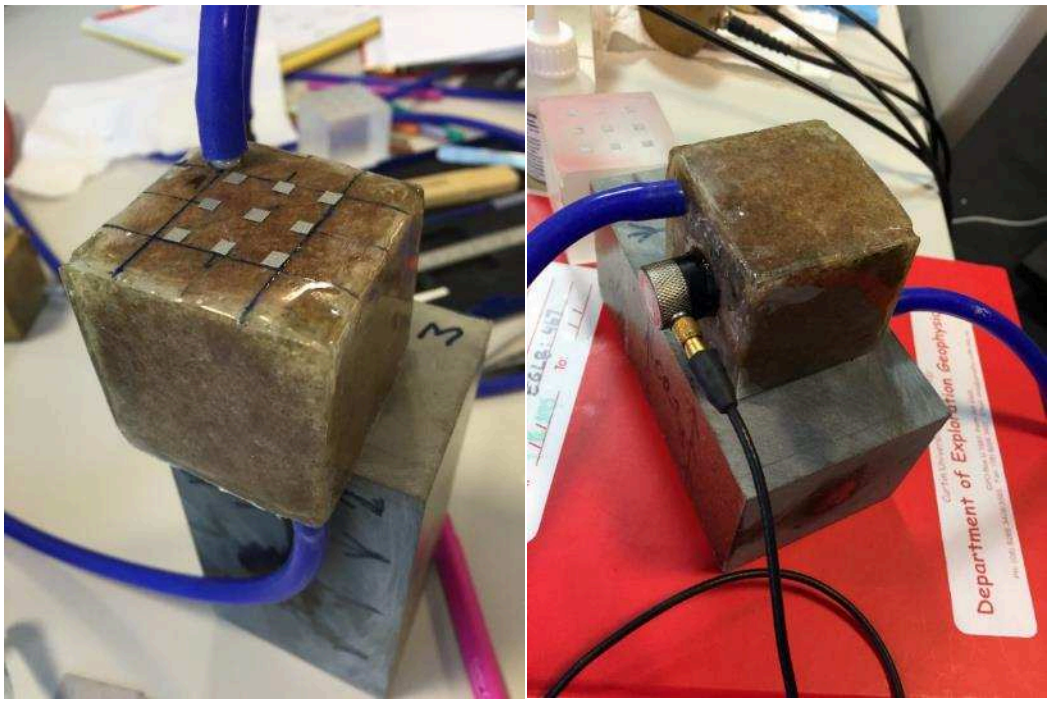


Figure 113 Left: attachment of reflective tape on the top surface for laser measurement. Right: attachment of an ultrasonic S-wave transducer to the bottom left face of the sample.

Results

Sample H4 (1794.4m)

Sample H4 1794.4 failed at a stress of 12 MPa during the dry stress cycle. Figure 114 shows recorded ultrasonic waveforms during sample loading from 0 to 16 MPa. Velocities and amplitudes of both P and S waves are increasing with increasing confining stress (Figure 115).

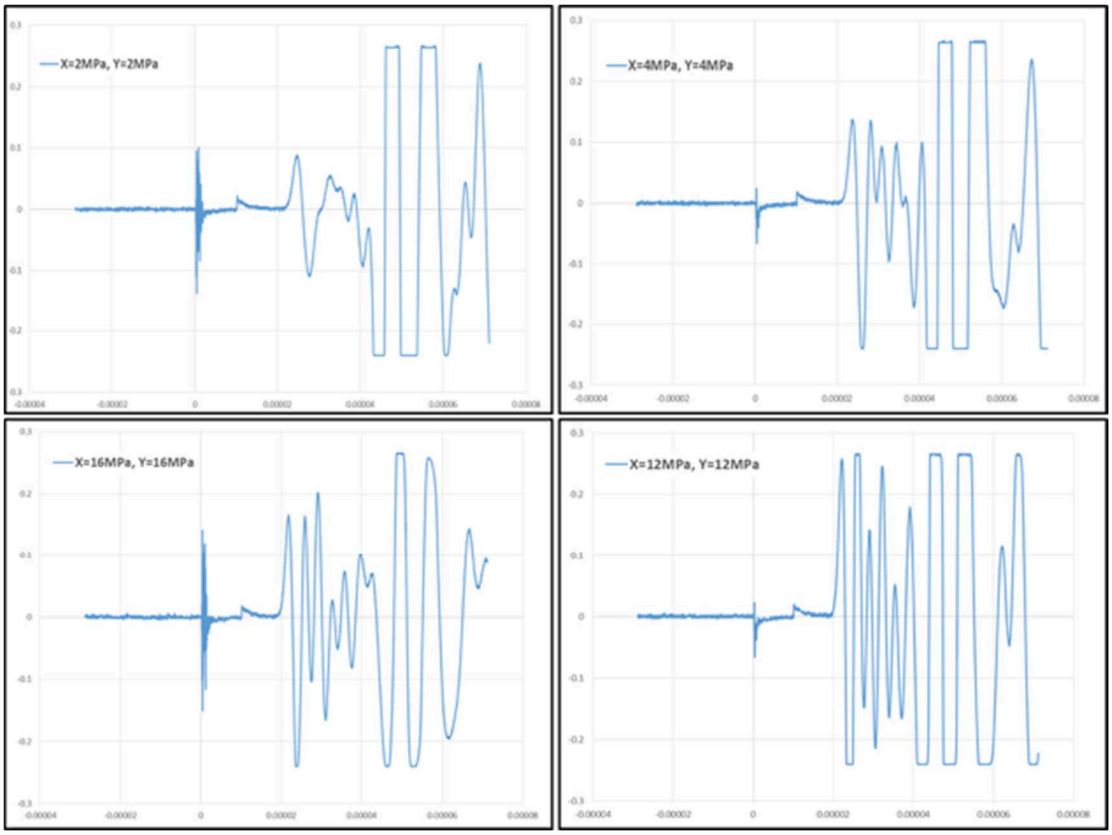


Figure 114 Recorded ultrasonic waveforms at stresses 2, 4, 12 and 16 MPa.

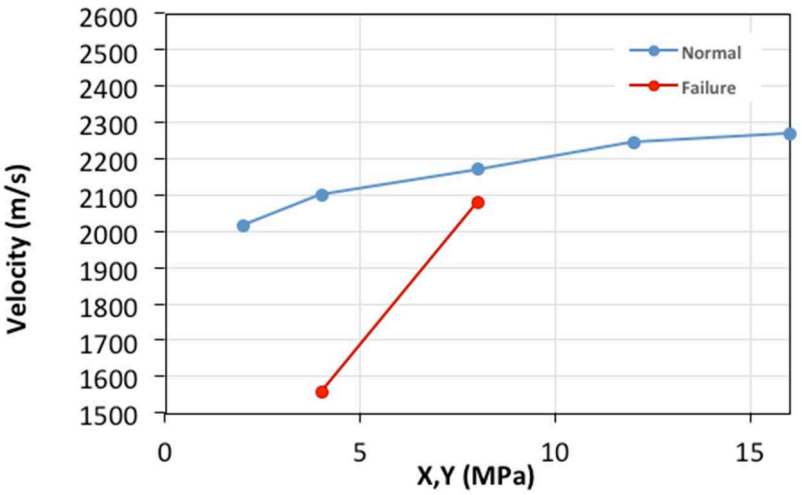


Figure 115 P wave velocity of H4 1794.4 as a function of stress for intact (normal in the figure legend) and damaged sample (failure in the figure legend).

Sample H4 (1797.0)

To assess an intrinsic anisotropy of sample H4 1797.0, both P and S wave ultrasonic velocities are measured across different directions of the cubic sample at room conditions. The sample was initially vacuum dried for 72 hrs and coated with a thin epoxy layer. Opposing faces of the sample were marked as A-A (red mark), B-B (green mark) and C-C (blue mark) (Figure 116).



Figure 116 Sample H4 1797.0 indication of directions by triangle markers. of A-A, B-B, and C-C in Red, Green and Blue respectively.

Registered waveforms for initial test are shown in the Figure 117, the quality of the recorded waveforms is rather poor at room conditions and detection of the S-wave arrival using conventional ultrasonic transducers is challenging. The LDI set-up was then used to improve detection of the S- waves.

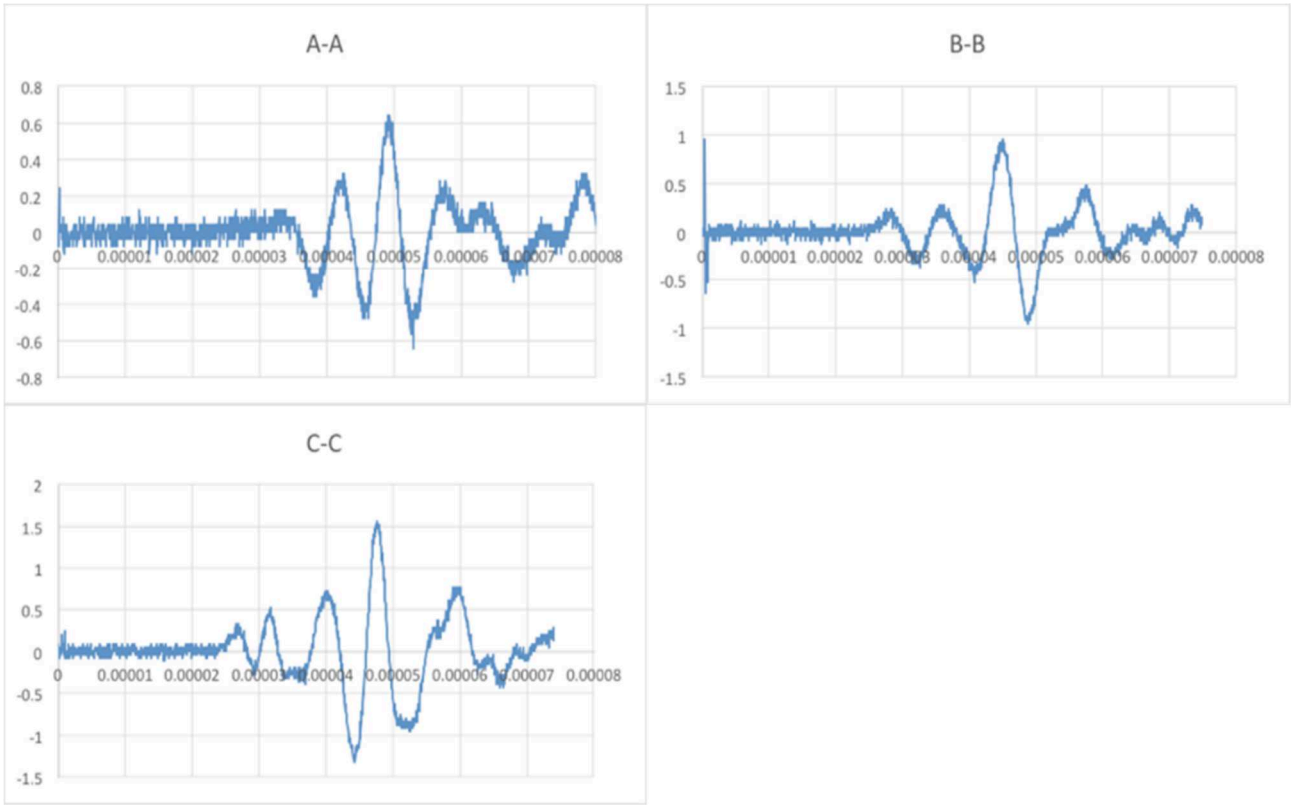


Figure 117 Ultrasonic waveforms recorded through faces A-A, B-B and C-C.

The recorded waveforms were first corrected for dead time of the equipment (3.7 μs) and the baseline shift in order to compensate any DC offset in the signal. The data were then transformed from the measurement coordinate system (ABC) to the Cartesian coordinate system (XYZ) of the experimental setup. After that, the recorded signals were time integrated to determine the displacement of the measurement point upon wave

arrival on the surface. Figure 118 shows the recorded signals (ABC coordinate system), which are proportional to velocity of particle displacement in ultrasonic wave in the direction towards laser interferometer. Displacements transferred to the Cartesian coordinate system (XYZ) and the corresponding hodograms are shown in Figures 119 to 122.

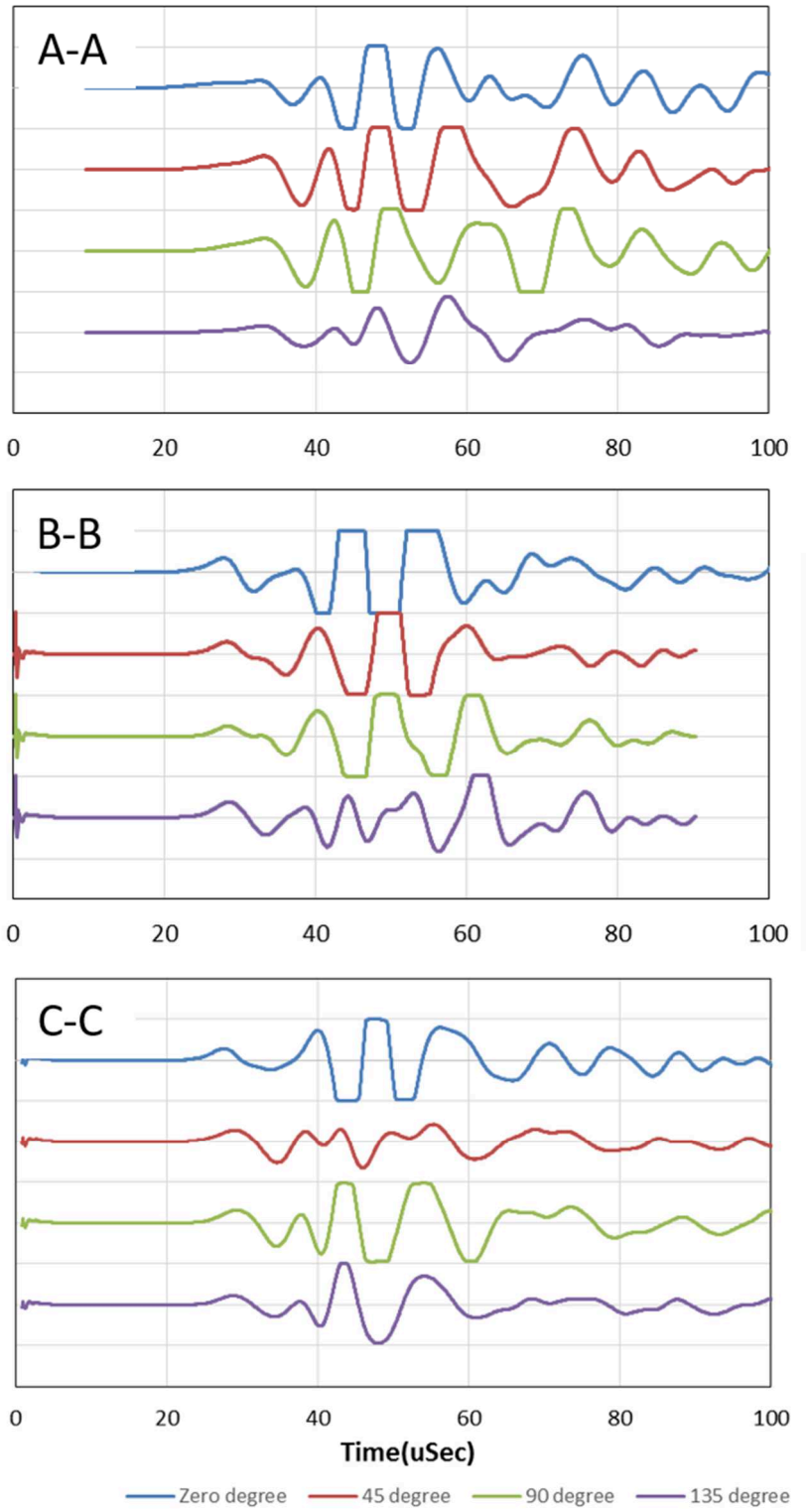


Figure 118 Dry sample. Recorded waveforms (proportional to velocity of the particle displacement in ultrasonic wave) in the direction laser interferometer. Signals are acquired at different directions of the source transducer (from 0 to 135°).

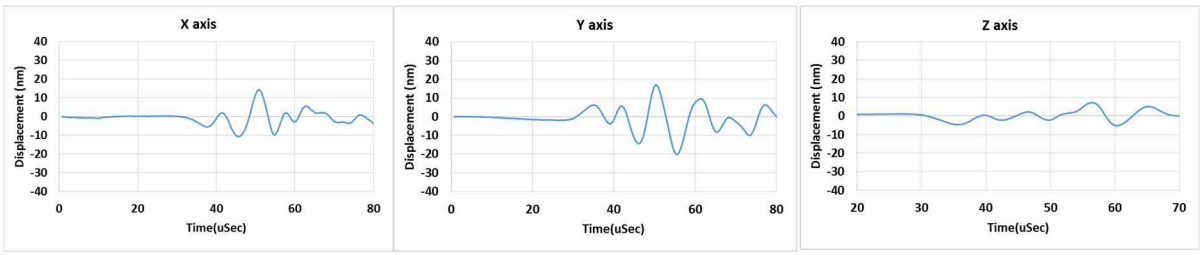


Figure 119 Sample H4 (1794.0), dry conditions. Displacement of the central point in Cartesian coordinate system (XYZ) face B-B.

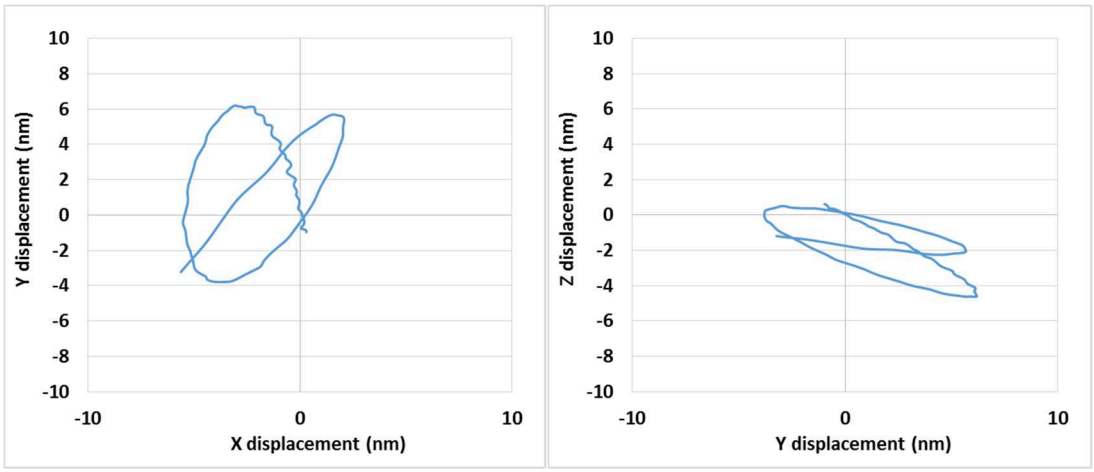


Figure 120 Sample H4 (1794.0), dry conditions. Hodogram of particle displacement face B-B.

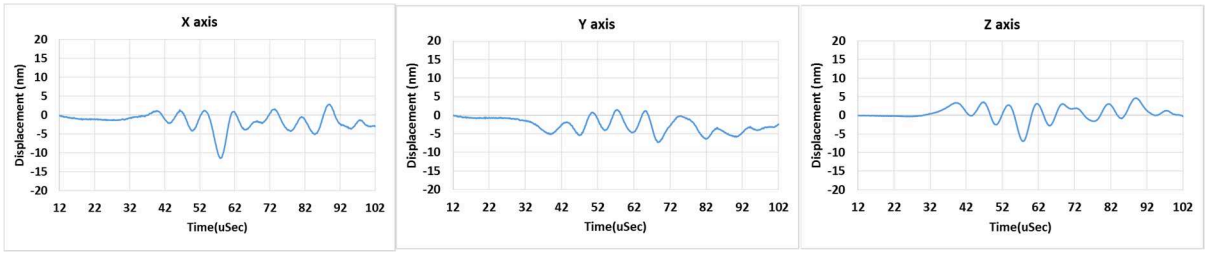


Figure 121 Sample H4 (1794.0), dry conditions. Displacement of the central point in Cartesian coordinate system (XYZ) face A-A.

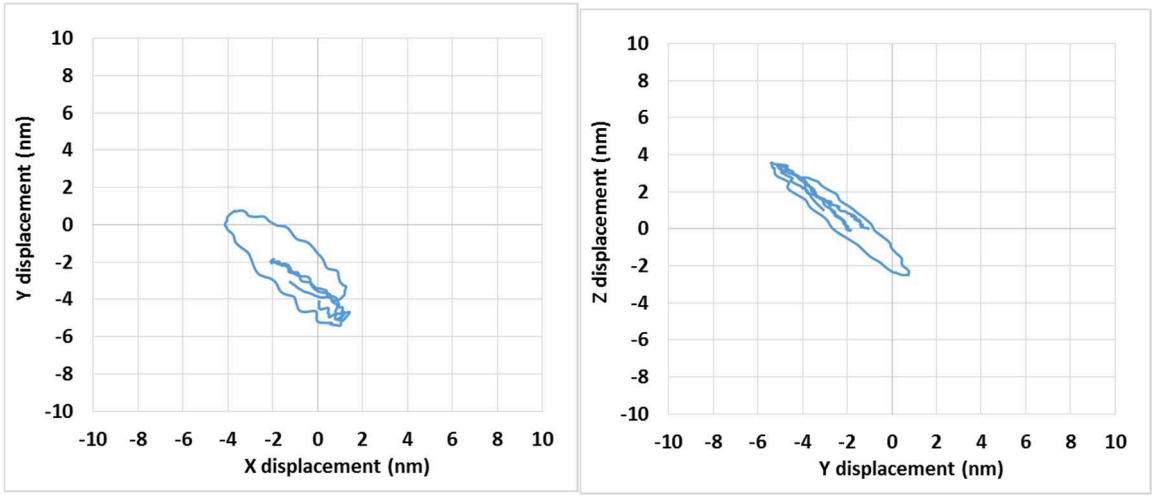


Figure 122 Sample H4 (1794.0), dry conditions. Hodogram of particle displacement face A-A.

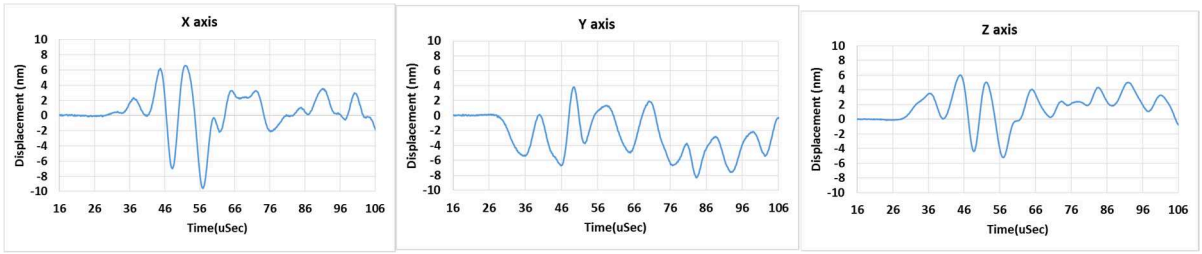


Figure 123 Sample H4 (1794.0), dry conditions. Displacement of the central point in Cartesian coordinate system (XYZ) face C-C.

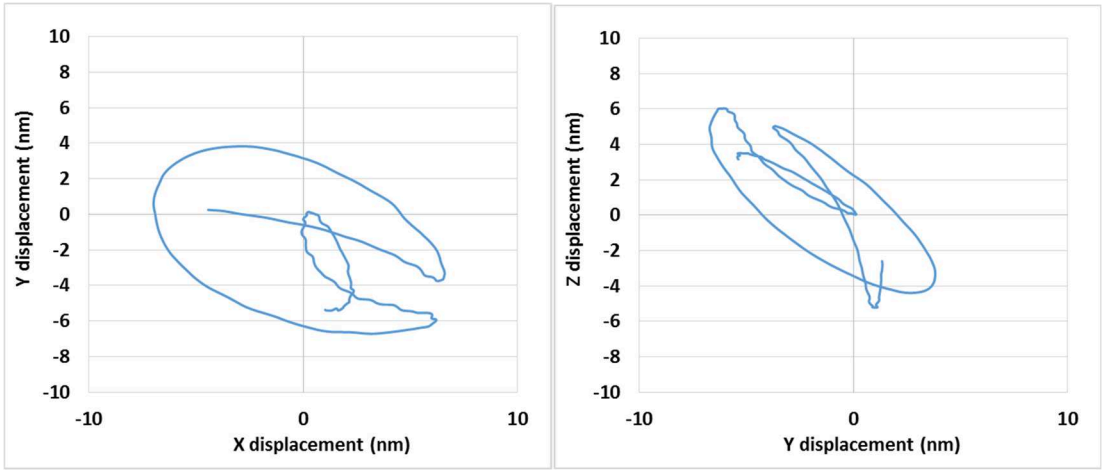


Figure 124 Sample H4 (1794.0), dry conditions. Hodogram of particle displacement face C-C.

After measurement in dry conditions, the sample was saturated with brine in a vacuum chamber for 100 hours. The measurements were then repeated on the brine saturated sample, Figure 125 shows the recorded signals (in ABC coordinate system), which are proportional to velocity of particle displacement in an ultrasonic wave in the direction towards the laser interferometer. Significant decrease in the signal amplitude was observed upon saturation that prevented the measurement of the trajectory of the particle and thus the plotting of the hodograms.

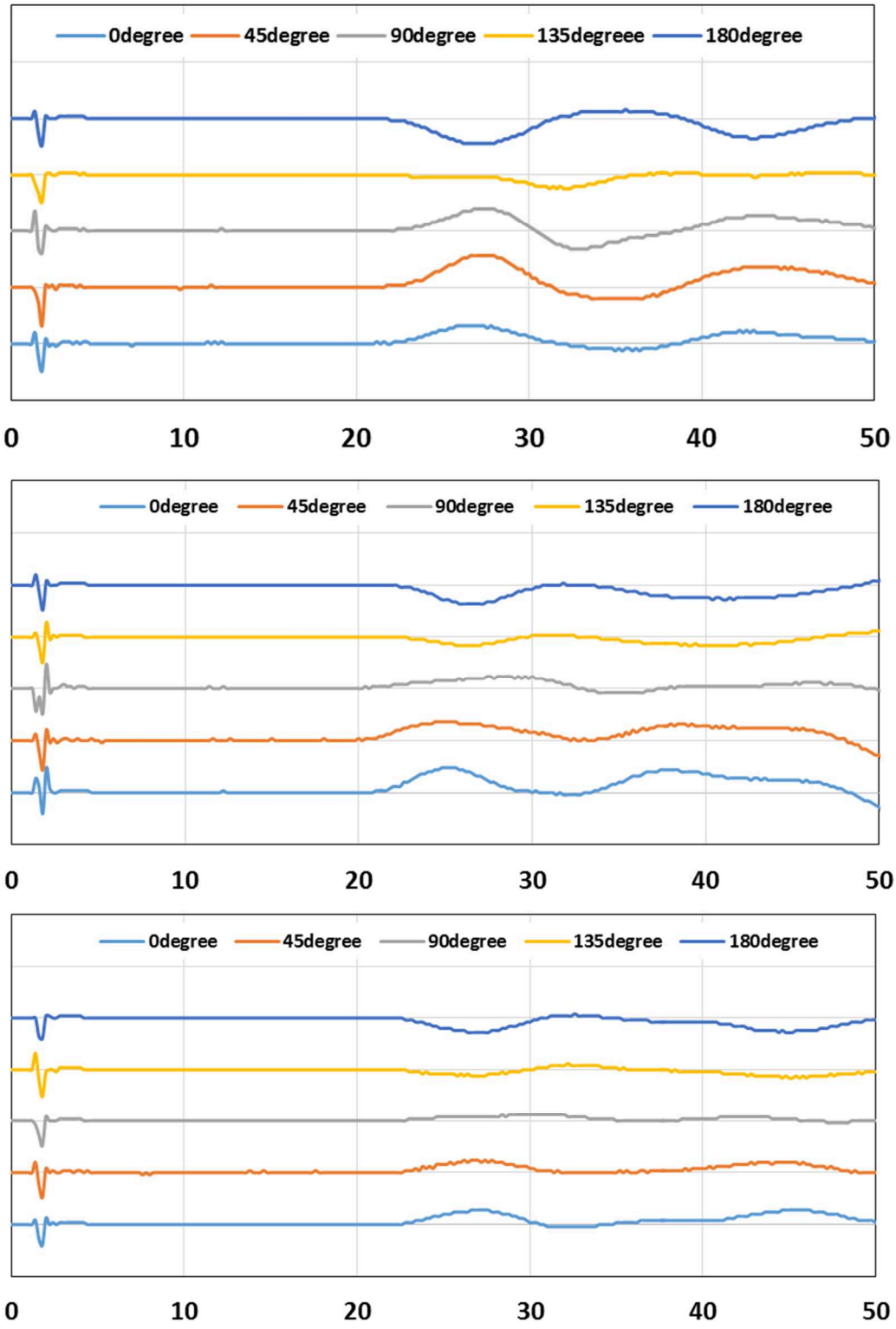


Figure 125 Sample H4 (1794.0) brine saturated conditions. Recorded waveforms (proportional to velocity of the particle displacement in ultrasonic wave) in the direction laser interferometer. Signals are acquired at different directions of the source transduces (from 0° to 135°).

Appendix 4A: Ultrasonic frequency measurements: tabulated results

Sample 2513 (H3-1417.90 m) Dry and saturated dynamic elastic moduli computed from P- and S- wave velocities in dry and saturated conditions. Pc = confining pressure; μ = shear modulus; K = bulk modulus; Peff = effective pressure.

Pc (MPa)	μdry (Pa)	Kdry (Pa)	Peff (MPa)	μsat (Pa)	Ksat (Pa)
4	4.24E+09	5.43E+09	4	4.10E+09	1.28E+10
6	4.61E+09	6.55E+09	6	4.25E+09	1.33E+10
8	4.79E+09	7.61E+09	8	4.45E+09	1.42E+10
10	4.96E+09	8.46E+09	10	4.77E+09	1.50E+10
12	5.23E+09	8.75E+09	12	4.97E+09	1.81E+10
14	5.45E+09	9.15E+09	14	5.37E+09	1.80E+10
16	5.66E+09	9.60E+09	16	5.41E+09	1.86E+10
18	5.73E+09	9.89E+09	18	5.56E+09	1.84E+10
20	5.91E+09	1.03E+10	20	5.84E+09	1.85E+10
22	6.06E+09	1.05E+10	22	6.06E+09	1.86E+10
24	6.15E+09	1.07E+10	24	6.32E+09	1.88E+10
26	6.26E+09	1.10E+10	26	6.40E+09	1.87E+10
28	6.34E+09	1.11E+10	28	6.52E+09	1.95E+10
30	6.43E+09	1.13E+10	30	6.66E+09	1.91E+10
32	6.51E+09	1.13E+10	32	6.72E+09	1.90E+10
34	6.48E+09	1.17E+10	34	6.72E+09	1.97E+10
36	6.60E+09	1.15E+10	36	6.75E+09	1.92E+10
38	6.60E+09	1.18E+10	38	6.78E+09	1.94E+10
40	6.70E+09	1.19E+10	40	6.75E+09	2.02E+10
42	6.70E+09	1.21E+10			
44	6.70E+09	1.21E+10			
46	6.70E+09	1.21E+10			
48	6.70E+09	1.22E+10			
50	6.79E+09	1.21E+10			
40	6.60E+09	1.17E+10			

Pc (MPa)	µdry (Pa)	Kdry (Pa)	Peff (MPa)	µsat (Pa)	Ksat (Pa)
30	6.26E+09	1.10E+10			
22	5.83E+09	9.89E+09			
20	5.76E+09	9.60E+09			
10	4.91E+09	7.64E+09			

Sample 2514 (H3-1472.10 m) Dry and saturated dynamic elastic moduli computed from P- and S- wave velocities in dry and saturated conditions. Pc = confining pressure; μ = shear modulus; K = bulk modulus; Peff = effective pressure.

Pc (MPa)	μdry (Pa)	Kdry (Pa)	Peff (MPa)	μsat (Pa)	Ksat (Pa)
2.01	3.57E+09	4.30E+09	2.03	5.90E+09	1.01E+10
3.00	4.03E+09	4.50E+09	4.61	6.69E+09	1.05E+10
5.01	4.39E+09	5.43E+09	7.11	7.66E+09	9.46E+09
7.52	4.99E+09	6.95E+09	10.04	7.98E+09	9.56E+09
10.03	5.44E+09	6.84E+09	10.02	7.98E+09	9.83E+09
12.54	6.80E+09	5.53E+09	12.58	8.18E+09	1.01E+10
15.03	6.86E+09	7.16E+09	15.08	8.32E+09	1.05E+10
17.54	7.21E+09	6.09E+09	17.58	8.47E+09	1.06E+10
20.04	7.15E+09	6.17E+09	20.01	8.62E+09	1.14E+10
22.55	7.15E+09	6.98E+09	22.55	8.69E+09	1.16E+10
25.05	7.39E+09	7.08E+09	25.09	8.77E+09	1.12E+10
27.51	7.65E+09	6.52E+09	27.55	8.77E+09	1.15E+10
30.01	7.82E+09	7.66E+09	30.03	8.85E+09	1.17E+10
32.51	7.85E+09	6.69E+09	32.52	8.85E+09	1.17E+10
35.01	7.85E+09	7.86E+09	35.10	8.69E+09	1.19E+10
37.51	7.96E+09	7.48E+09	37.61	8.69E+09	1.19E+10
40.03	7.99E+09	7.19E+09	40.05	8.85E+09	1.17E+10
42.52	7.99E+09	7.92E+09	42.56	8.77E+09	1.18E+10
45.03	8.17E+09	7.19E+09	45.06	8.77E+09	1.22E+10
46.97	8.06E+09	7.58E+09	46.54	8.77E+09	1.32E+10
40.09	7.15E+09	8.09E+09	18.54	8.69E+09	1.03E+10
30.03	6.74E+09	8.62E+09			
20.08	6.18E+09	8.70E+09			
10.03	5.40E+09	7.40E+09			

Sample 2708 (H3-1544.05 m) Dry and saturated dynamic elastic moduli computed from P- and S- wave velocities in dry and saturated conditions. Pc = confining pressure; μ = shear modulus; K = bulk modulus; Peff = effective pressure.

Pc (MPa)	μdry (Pa)	Kdry (Pa)	Peff (MPa)	μsat (Pa)	Ksat (Pa)
5	4.93E+09	8.92E+09	5.00	5.86E+09	1.58E+10
8	5.45E+09	9.55E+09	7.59	5.95E+09	1.59E+10
10	5.79E+09	1.23E+10	10.00	6.21E+09	1.65E+10
13	6.76E+09	9.97E+09	12.55	6.30E+09	1.81E+10
15	7.25E+09	1.05E+10	15.05	6.39E+09	1.83E+10
18	7.37E+09	1.14E+10	17.52	6.59E+09	1.82E+10
20	7.37E+09	1.22E+10	20.02	6.68E+09	1.82E+10
23	7.61E+09	1.11E+10	22.51	6.68E+09	1.79E+10
25	7.95E+09	1.21E+10	25.02	6.89E+09	1.85E+10
28	8.23E+09	1.22E+10	27.51	7.13E+09	1.81E+10
30	8.23E+09	1.27E+10	29.98	7.11E+09	1.83E+10
33	8.40E+09	1.19E+10	32.50	7.31E+09	1.82E+10
35	8.40E+09	1.29E+10	35.09	7.27E+09	1.83E+10
38	8.40E+09	1.28E+10	37.50	7.27E+09	1.97E+10
40	8.55E+09	1.31E+10	40.00	7.22E+09	1.98E+10
43	8.86E+09	1.33E+10	42.51	7.22E+09	1.98E+10
45	8.70E+09	1.21E+10	46.48	7.22E+09	1.92E+10
47	8.70E+09	1.21E+10	19.39	6.41E+09	1.91E+10
40	8.40E+09	1.19E+10			
30	8.23E+09	1.09E+10			
20	6.93E+09	8.70E+09			
10	5.99E+09	6.73E+09			
5	5.80E+09	1.38E+10			

Sample 2515 (H2-1245.80 m) Dry and saturated dynamic elastic moduli computed from P- and S- wave velocities in dry and saturated conditions. Pc = confining pressure; μ = shear modulus; K = bulk modulus; Peff = effective pressure.

Pc (MPa)	μdry (Pa)	Kdry (Pa)	Peff (MPa)	μsat (Pa)	Ksat (Pa)
1.1	3.96E+09	3.04E+08	2.4	5.66E+09	1.04E+10
3.3	4.85E+09	3.90E+09	4.9	6.60E+09	1.29E+10
5.0	5.32E+09	4.96E+09	5.0	7.03E+09	1.20E+10
7.5	5.73E+09	6.83E+09	6.6	7.08E+09	1.25E+10
10.1	6.10E+09	7.30E+09	10.0	7.54E+09	1.36E+10
12.8	6.43E+09	1.00E+10	12.1	7.62E+09	1.48E+10
16.3	6.68E+09	1.03E+10	16.0	8.25E+09	1.61E+10
19.2	6.84E+09	1.08E+10	20.0	8.32E+09	1.58E+10
21.8	7.07E+09	1.06E+10	22.2	8.46E+09	1.64E+10
25.2	7.15E+09	1.22E+10	24.2	8.53E+09	1.63E+10
27.4	7.24E+09	1.25E+10	28.1	8.66E+09	1.66E+10
30.0	7.37E+09	1.26E+10	30.0	8.74E+09	1.76E+10
32.3	7.56E+09	1.33E+10	31.7	8.80E+09	1.75E+10
35.7	7.53E+09	1.31E+10	35.8	8.80E+09	1.79E+10
37.3	7.58E+09	1.30E+10	37.9	8.80E+09	1.79E+10
40.0	9.15E+09	1.12E+10	40.0	8.94E+09	1.83E+10
43.0	7.63E+09	1.46E+10	42.7	8.94E+09	1.85E+10
45.9	7.66E+09	1.38E+10	44.7	8.94E+09	1.94E+10
46.4	7.63E+09	1.32E+10	46.5	8.94E+09	1.93E+10
40.5	7.23E+09	1.42E+10	15.6	8.40E+09	1.33E+10
30.4	6.85E+09	1.25E+10			
20.5	6.08E+09	1.20E+10			
10.6	5.39E+09	7.83E+09			
5.0	4.98E+09	5.37E+09			

H4-1 (1797.1) results. P_{eff} = effective pressure; μ = shear modulus; K = bulk modulus; E = Young modulus; ν = Poisson ratio.

	Dry				
Borehole: Harvey 4	**P_{eff} (MPa)**	**μ (GPa)**	**K (GPa)**	**E (GPa)**	**ν**
Depth: 1797.1 m	**2**	3.69	3.00	7.84	0.06
Type: Sandstone	**4**	5.52	6.46	12.90	0.17
Length: 27.65 mm	**6**	6.87	6.60	15.30	0.11
Diameter: 36.65 mm	**8**	7.57	6.58	16.41	0.08
Mass of dry sample: 60.04 g	**10**	7.65	7.77	17.27	0.13
Measured porosity: 17.4 %	**12**	7.89	7.74	17.67	0.12
Estimated pore volume: 5.08 mL	**14**	8.32	8.14	18.62	0.12
	16	8.78	7.10	18.65	0.06
	18	9.06	7.31	19.22	0.06
	20	9.35	6.90	19.32	0.03
	22	9.48	7.06	19.65	0.04
	24	9.52	7.35	19.95	0.05
	26	9.75	7.40	20.32	0.04
	28	9.98	7.27	20.54	0.03
	30	10.09	7.29	20.72	0.03

*sample for this measurement was cut from the longer sample, as the full length sample was damaged during seismic frequencies experiments.

100% brine saturation					*~80% brine saturation*				
P_{eff} (MPa)	**μ (GPa)**	**K (GPa)**	**E (GPa)**	**ν**	**P_{eff} (MPa)**	**μ (GPa)**	**K (GPa)**	**E (GPa)**	**ν**
5	6.19	18.50	16.71	0.35	**4**	5.94	13.15	15.49	0.30
7	6.83	17.89	18.18	0.33	**6**	6.49	14.01	16.87	0.30
9	7.46	17.04	19.52	0.31	**8**	7.05	15.79	18.40	0.31
11	8.08	16.32	20.81	0.29	**10**	7.59	14.55	19.40	0.28
13	8.35	16.35	21.42	0.28	**12**	7.93	14.82	20.19	0.27
15	8.99	15.47	22.60	0.26	**14**	8.25	14.89	20.89	0.27
17	9.10	15.60	22.85	0.26	**16**	8.58	14.04	21.39	0.25
19	9.37	15.21	23.32	0.25	**18**	8.79	15.49	22.16	0.26
21	9.59	15.18	23.77	0.24	**20**	9.05	15.12	22.63	0.25
23	9.77	15.21	24.13	0.24	**22**	9.21	14.88	22.90	0.24
25	9.94	15.25	24.50	0.23	**24**	9.49	14.49	23.36	0.23
27	10.06	15.06	24.69	0.23	**26**	9.49	14.19	23.27	0.23
29	10.19	15.17	24.97	0.23	**28**	9.66	14.49	23.71	0.23
31	10.19	15.30	25.01	0.23	**30**	9.72	14.97	23.97	0.23

H4-2 (1797.5) results. P_{eff} = effective pressure; μ = shear modulus; K = bulk modulus; E = Young modulus; ν = Poisson ratio.

	Dry sample				
Borehole: Harvey 4	**Peff (MPa)**	**μ (GPa)**	**K (GPa)**	**E (GPa)**	**ν**
Depth 1797.5 m	8	7.65	10.10	18.31	0.20
Type: Sandstone	10	7.79	10.43	18.70	0.20
Length: 64.93 mm	12	7.89	11.33	19.22	0.22
Diameter: 38.85 mm	14	8.56	10.76	20.29	0.19
Mass of dry sample: 166.43 g	16	8.60	10.77	20.38	0.19
Type: Sandstone	18	8.86	10.75	20.85	0.18
	20	9.00	10.81	21.13	0.17
	22	9.66	10.17	22.02	0.14
	24	9.77	10.47	22.36	0.14
	26	9.99	10.63	22.82	0.14
	28	10.16	10.48	23.03	0.13
	30	10.28	10.49	23.24	0.13

H4 (1800.4) Results. P_{eff} = effective pressure; μ = shear modulus; K = bulk modulus; E = Young modulus; ν = Poisson ratio.

	Dry sample				
Borehole: Harvey 4	**P_{eff} (MPa)**	**μ (GPa)**	**K (GPa)**	**E (GPa)**	**ν**
Depth: 1800.4 m	0.10	4.56	3.99	9.91	0.09
Type: Sandstone	2.00	5.54	5.83	12.63	0.14
Length: 78.22 mm	4.00	6.61	8.13	15.60	0.18
Diameter: 38.45 mm	6.00	7.49	9.14	17.64	0.18
Mass of dry sample: 198.75 g	8.00	8.22	9.88	19.30	0.17
Measured porosity: 14.2 %	10.00	8.67	11.38	20.74	0.20
Estimated pore volume: 12.9 mL	12.00	9.32	11.60	22.05	0.18
	14.00	9.83	12.08	23.20	0.18
	16.00	10.23	12.47	24.10	0.18
	18.00	10.42	12.72	24.55	0.18
	20.00	10.80	13.36	25.53	0.18
	22.00	11.04	13.43	26.00	0.18
	24.00	11.43	13.42	26.70	0.17
	26.00	11.66	14.34	27.52	0.18
	28.00	11.99	14.23	28.08	0.17
	30.00	12.23	14.17	28.49	0.17

100% brine saturation					*~82% brine saturation*				
P_{eff} (MPa)	**μ (GPa)**	**K (GPa)**	**E (GPa)**	**ν**	**P_{eff} (MPa)**	**μ (GPa)**	**K (GPa)**	**E (GPa)**	**ν**
6	8.19	19.93	21.62	0.32	6.00	8.23	17.19	21.28	0.29
8	9.13	19.72	23.73	0.30	8.00	9.08	16.74	23.08	0.27
10	9.86	19.58	25.32	0.28	10.00	9.51	16.53	23.93	0.26
12	10.68	19.49	27.08	0.27	12.00	10.15	16.57	25.29	0.25
14	10.84	19.77	27.50	0.27	14.00	10.58	17.47	26.41	0.25
16	10.92	20.05	27.73	0.27	16.00	10.87	17.42	26.99	0.24
18	11.17	20.03	28.26	0.27	18.00	11.17	17.49	27.63	0.24
20	11.38	20.49	28.80	0.27	20.00	11.43	17.49	28.15	0.23
22	11.54	20.83	29.22	0.27	22.00	11.64	17.75	28.66	0.23
24	11.65	20.65	29.41	0.26	24.00	11.85	17.64	29.05	0.23
26	11.81	20.99	29.84	0.26	26.00	11.73	17.97	28.91	0.23
28	12.09	20.59	30.34	0.25	28.00	12.27	17.43	29.81	0.22
30	12.21	20.32	30.52	0.25	30.00	12.33	17.65	30.01	0.22

H4 (1796.8) Results. P_{eff} = effective pressure; μ = shear modulus; ; E = Young modulus; ν = Poisson ratio.

	Dry sample				
Borehole: Harvey 4	**P_{eff} (MPa)**	**μ (GPa)**	**K (GPa)**	**E (GPa)**	**ν**
Depth: 1796.8 m	2	3.41	2.02	6.55	0.04
Type: Sandstone	4	4.46	2.10	7.83	0.12
Length: 39.9 mm	6	5.32	3.94	11.01	0.04
Diameter: 37.9 mm	8	6.03	5.07	12.95	0.07
Mass of dry sample: 86.3 g	10	6.84	5.33	14.38	0.05
Measured porosity: 17.4 %	12	7.30	5.75	15.39	0.05
Estimated pore volume: 7.8 mL	14	7.60	6.21	16.18	0.07
	16	7.86	6.68	16.93	0.08
	18	8.41	6.82	17.88	0.06
	20	9.02	6.43	18.43	0.02
	22	9.11	6.86	18.94	0.04
	24	9.01	7.39	19.22	0.07
	26	9.06	7.79	19.59	0.08
	28	9.32	7.67	19.90	0.07
	30	9.42	7.90	20.22	0.07

100% brine saturation					*~80% brine saturation*				
P_{eff} (MPa)	**μ (GPa)**	**K (GPa)**	**E (GPa)**	**ν**	**P_{eff} (MPa)**	**μ (GPa)**	**K (GPa)**	**E (GPa)**	**ν**
6	5.28	14.04	14.07	0.33	**2**	0.14	0.52	0.38	0.38
8	5.87	13.83	15.42	0.31	**4**	3.76	10.42	10.07	0.34
10	6.20	14.58	16.30	0.31	**6**	4.95	13.15	13.18	0.33
12	6.66	14.62	17.36	0.30	**8**	5.96	12.85	15.48	0.30
14	7.00	14.53	18.09	0.29	**10**	6.28	13.26	16.28	0.30
16	7.75	14.05	19.65	0.27	**12**	6.57	13.21	16.90	0.29
18	7.77	15.11	19.89	0.28	**14**	6.87	13.58	17.63	0.28
20	7.90	15.52	20.26	0.28	**16**	7.14	13.25	18.15	0.27
22	7.91	15.36	20.26	0.28	**18**	7.36	13.76	18.75	0.27
24	8.24	14.97	20.89	0.27	**20**	7.60	13.97	19.31	0.27
26	8.22	15.41	20.94	0.27	**22**	7.79	13.75	19.67	0.26
28	8.40	15.21	21.29	0.27	**24**	7.87	13.86	19.85	0.26
30	8.48	15.34	21.49	0.27	**26**	8.04	14.02	20.24	0.26
					28	8.05	14.04	20.27	0.26
					30	8.09	14.37	20.44	0.26

H4 (1795) Results. P_{eff} = effective pressure; μ = shear modulus; K = bulk modulus; ; E = Young modulus; ν = Poisson ratio.

	Dry sample				
Borehole: Harvey 4	**P_{eff} (MPa)**	**μ (GPa)**	**K (GPa)**	**E (GPa)**	**ν**
Depth: 1795.0 m	0.1	3.00	2.60	6.50	0.08
Type: Sandstone	2	4.12	2.58	8.07	0.02
Length: 77.2 mm	4	5.23	4.39	11.22	0.07
Diameter: 37.9 mm	6	5.90	5.17	12.82	0.09
Mass of dry sample: 179.38 g	8	6.81	5.34	14.34	0.05
Measured porosity: 18.0 %	10	7.37	5.98	15.68	0.06
Estimated pore volume: 15.7 mL	12	7.88	6.70	16.98	0.08
	14	8.33	8.04	18.57	0.12
	16	8.75	8.48	19.52	0.12
	18	9.04	8.68	20.12	0.11
	20	9.30	8.80	20.63	0.11
	22	9.51	9.00	21.10	0.11
	24	9.77	9.16	21.63	0.11
	26	9.93	9.47	22.08	0.11
	28	10.14	9.67	22.54	0.11
	30	10.17	10.42	23.02	0.13

100% brine saturation					*~74% brine saturation*				
P_{eff} (MPa)	**μ (GPa)**	**K (GPa)**	**E (GPa)**	**ν**	**P_{eff} (MPa)**	**μ (GPa)**	**K (GPa)**	**E (GPa)**	**ν**
6	5.51	13.20	14.51	0.32	**6**				
8	6.30	12.86	16.25	0.29	**8**				
10	7.35	14.32	18.82	0.28	**10**	7.11	11.78	17.75	0.25
12	7.65	14.87	19.59	0.28	**12**	7.58	11.90	18.77	0.24
14	7.95	14.97	20.27	0.27	**14**	7.98	11.95	19.58	0.23
16	8.23	15.79	21.03	0.28	**16**	8.33	12.32	20.38	0.22
18	8.48	16.02	21.62	0.28	**18**	8.60	12.26	20.91	0.22
20	8.73	16.02	22.15	0.27	**20**	8.86	12.31	21.43	0.21
22	8.93	16.39	22.67	0.27	**22**	9.05	12.80	21.97	0.21
24	9.12	16.28	23.05	0.26	**24**	9.23	12.63	22.26	0.21
26	9.28	16.31	23.39	0.26	**26**	9.39	12.93	22.67	0.21
28	9.44	16.34	23.74	0.26	**28**	9.55	12.87	22.98	0.20
30	9.54	16.34	23.96	0.26	**30**	9.68	12.86	23.22	0.20

H3 (1549.6) Results. P_{eff} = effective pressure; μ = shear modulus; K = bulk modulus; ; E = Young modulus; ν = Poisson ratio.

	Dry sample				
Borehole: Harvey 3	**P_{eff} (MPa)**	**μ (GPa)**	**K (GPa)**	**E (GPa)**	**ν**
Depth: 1549.6 m	2	8.11	6.70	17.34	0.07
Type: Sandstone	4	9.49	7.46	19.99	0.05
Length: 46.4 mm	6	10.08	8.10	21.38	0.06
Diameter: 38.6 mm	8	10.91	9.35	23.56	0.08
Mass of dry sample: 113.67 g	10	11.28	10.50	24.92	0.11
Measured porosity: 16.3%	12	11.81	10.78	25.95	0.10
Estimated pore volume: 8.85 mL	14	12.03	11.20	26.57	0.11
	16	12.30	11.04	26.91	0.09
	18	12.48	11.73	27.63	0.11
	20	12.82	11.86	28.27	0.10
	22	12.95	12.30	28.75	0.11
	24	13.20	12.20	29.10	0.10
	26	13.34	12.07	29.24	0.10
	28	13.53	11.85	29.40	0.09
	30	13.74	11.62	29.56	0.08

100% brine saturation					***~93% brine saturation***				
P_{eff} (MPa)	**μ (GPa)**	**K (GPa)**	**E (GPa)**	**ν**	**P_{eff} (MPa)**	**μ (GPa)**	**K (GPa)**	**E (GPa)**	**ν**
6	9.90	15.18	24.40	0.23	**2**	8.49	11.92	20.58	0.21
8	10.51	14.93	25.55	0.22	**4**	9.23	12.60	22.25	0.21
10	11.67	14.72	27.70	0.19	**6**	9.61	14.26	23.53	0.23
12	12.16	15.09	28.76	0.18	**8**	10.50	14.28	25.30	0.21
14	12.33	15.95	29.41	0.19	**10**	10.96	14.41	26.23	0.20
16	12.65	16.00	30.04	0.19	**12**	11.27	14.86	27.00	0.20
18	12.88	15.96	30.45	0.18	**14**	11.79	14.70	27.90	0.18
20	13.17	16.29	31.13	0.18	**16**	12.04	15.39	28.65	0.19
22	13.47	16.17	31.63	0.17	**18**	12.36	15.22	29.17	0.18
24	13.61	16.50	32.03	0.18	**20**	12.63	15.32	29.72	0.18
26	13.75	16.37	32.23	0.17	**22**	12.86	15.17	30.08	0.17
28	13.89	16.36	32.48	0.17	**24**	12.91	15.48	30.30	0.17
30	13.97	16.30	32.61	0.17	**26**	13.09	15.72	30.73	0.17
					28	13.28	15.63	31.04	0.17
					30	13.44	15.80	31.41	0.17

Appendix 4B: Low frequency measurements: tabulated results

Results of low-frequency measurements on sample H4-1 (1797.1m) under dry conditions

Frequency (Hz)	Extensional attenuation	Poisson ratio	Young's modulus (GPa)	Bulk modulus (GPa)	Shear modulus (GPa)	Vp (m/s)	Vs (m/s)
0.1	-0.0016	0.238	25.07	15.95	10.13	3947	2315
0.2	-0.0020	0.239	24.89	15.92	10.04	3937	2305
0.4	-0.0014	0.239	24.78	15.81	10	3927	2300
0.6	-0.0019	0.239	25.04	15.99	10.11	3948	2312
0.8	-0.0005	0.240	24.86	15.95	10.02	3938	2303
1	-0.0007	0.242	24.51	15.86	9.866	3918	2285
2	0.0022	0.246	24.59	16.16	9.867	3938	2285
4	0.0008	0.246	24.59	16.14	9.867	3937	2285
6	0.0006	0.245	24.58	16.08	9.869	3933	2285
8	0.0022	0.247	24.56	16.19	9.847	3939	2283
10	0.0019	0.246	24.7	16.2	9.914	3946	2290
20	0.0005	0.245	24.66	16.13	9.901	3939	2289
40	0.0012	0.245	24.87	16.25	9.988	3955	2299
60	0.0005	0.242	24.86	16.07	10.01	3945	2301
80	0.0009	0.244	24.85	16.19	9.987	3951	2299
100	0.0028	0.244	24.88	16.21	9.998	3954	2300

Results of low-frequency measurements on sample H4-1(1797.1m) under brine-saturated conditions.

Frequency (Hz)	Extensional attenuation	Poisson ratio	Young's modulus (GPa)	Bulk modulus (GPa)	Shear modulus (GPa)	Vp (m/s)	Vs (m/s)
0.1	0.0012	0.238	24.89	19.16	9.695	3944	2168
0.2	0.0019	0.239	25.65	19.15	10.04	3972	2206
0.4	0.0016	0.239	24.78	19.09	9.655	3936	2163
0.6	0.0023	0.239	25.36	19.15	9.914	3961	2192
0.8	-0.0007	0.240	24.91	19.14	9.706	3943	2169
1	-0.0009	0.242	25.12	19.07	9.81	3948	2181
2	0.0022	0.246	25.61	19.27	10.02	3977	2203
4	0.0006	0.246	25.55	19.3	9.984	3976	2200
6	0.0010	0.245	24.33	19.25	9.436	3928	2139
8	0.0020	0.247	26.28	19.33	10.32	4005	2237
10	0.0021	0.246	24.63	19.34	9.563	3944	2153
20	0.0009	0.245	26.24	19.3	10.3	4002	2235
40	0.0014	0.245	25.49	19.38	9.95	3978	2196
60	0.0007	0.242	24.92	19.21	9.706	3948	2169
80	0.0008	0.244	25.96	19.34	10.17	3993	2220
100	0.0021	0.244	25.65	19.31	10.03	3980	2205

Results of low-frequency measurements on sample H4-2 (1797.5) under dry conditions

Frequency (Hz)	Extensional attenuation	Poisson ratio	Young's modulus (GPa)	Bulk modulus (GPa)	Shear modulus (GPa)	Vp (m/s)	Vs (m/s)
0.1	-0.0001	0.242	19.05	12.29	7.67	3288	1919
0.2	-0.0024	0.244	18.91	12.32	7.60	3283	1910
0.4	-0.0008	0.243	18.83	12.20	7.58	3272	1907
0.6	-0.0004	0.247	19.03	12.55	7.63	3303	1914
0.8	-0.0008	0.249	18.89	12.52	7.56	3295	1906
1	0.0006	0.248	18.63	12.34	7.46	3271	1893
2	0.0021	0.251	18.69	12.49	7.47	3283	1894
4	0.0002	0.249	18.69	12.41	7.48	3278	1895
6	0.0009	0.247	18.68	12.29	7.49	3270	1896
8	0.0017	0.250	18.67	12.46	7.47	3280	1893
10	0.0024	0.251	18.78	12.58	7.50	3293	1898
20	-0.0004	0.249	18.74	12.45	7.50	3283	1898
40	0.0023	0.248	18.90	12.51	7.57	3294	1906
60	0.0002	0.249	18.89	12.53	7.57	3295	1906
80	0.0013	0.252	18.89	12.68	7.54	3304	1903
100	0.0025	0.249	18.91	12.54	7.57	3296	1907

Results of low-frequency measurements on sample H4-2 (1797.5) under brine-saturated conditions.

Frequency (Hz)	Extensional attenuation	Poisson ratio	Young's modulus (GPa)	Bulk modulus (GPa)	Shear modulus (GPa)	Vp (m/s)	Vs (m/s)
0.1	0.0013	0.238	21.18	17.01	8.19	3553	1924
0.2	0.0021	0.239	20.63	17.10	7.94	3537	1894
0.4	0.0025	0.239	20.65	17.04	7.95	3534	1896
0.6	0.0020	0.239	20.75	17.25	7.98	3550	1899
0.8	-0.0007	0.240	20.82	17.21	8.02	3550	1904
1	-0.0016	0.242	20.37	17.06	7.83	3525	1881
2	0.0029	0.246	20.39	17.14	7.83	3530	1881
4	0.0000	0.246	20.46	17.11	7.87	3531	1885
6	0.0016	0.245	20.53	16.90	7.91	3522	1891
8	0.0016	0.247	20.22	17.09	7.76	3521	1872
10	0.0013	0.246	20.43	17.15	7.85	3532	1883
20	0.0006	0.245	20.64	17.12	7.95	3539	1895
40	0.0019	0.245	20.31	17.12	7.80	3526	1877
60	0.0001	0.242	20.82	17.22	8.02	3551	1904
80	0.0001	0.244	20.63	17.37	7.92	3553	1892
100	0.0027	0.244	20.59	17.30	7.91	3547	1891

Results of low-frequency measurements on sample H3-26 (1549.6) under dry conditions.

Frequency (Hz)	Extensional attenuation	Poisson ratio	Young's modulus (GPa)	Bulk modulus (GPa)	Shear modulus (GPa)	Vp (m/s)	Vs (m/s)
0.1	0.0010	0.206	19.46	11.05	8.06	3235	1967
0.2	0.0004	0.208	19.31	11.03	7.99	3227	1959
0.4	0.0019	0.208	19.23	10.98	7.96	3220	1955
0.6	0.0011	0.210	19.43	11.16	8.03	3240	1964
0.8	-0.0015	0.211	19.29	11.12	7.96	3230	1955
1	0.0005	0.213	19.02	11.05	7.84	3213	1940
2	0.0010	0.218	19.09	11.27	7.84	3229	1940
4	-0.0003	0.217	19.08	11.25	7.84	3228	1940
6	0.0002	0.216	19.07	11.19	7.84	3224	1940
8	0.0008	0.218	19.06	11.28	7.82	3228	1938
10	0.0026	0.215	19.17	11.21	7.89	3230	1946
20	0.0019	0.216	19.13	11.22	7.87	3229	1944
40	-0.0013	0.216	19.30	11.33	7.93	3243	1952
60	-0.0010	0.214	19.29	11.22	7.95	3237	1953
80	-0.0015	0.213	19.28	11.20	7.95	3235	1954
100	-0.0022	0.214	19.31	11.24	7.95	3238	1954

Results of low-frequency measurements on sample H3-26 (1549.6) under brine-saturated conditions.

Frequency (Hz)	Extensional attenuation	Poisson ratio	Young's modulus (GPa)	Bulk modulus (GPa)	Shear modulus (GPa)	Vp (m/s)	Vs (m/s)
0.1	0.0019	0.280	20.91	15.83	8.17	3436	1900
0.2	0.0018	0.272	21.67	15.81	8.52	3465	1940
0.4	0.0011	0.281	20.79	15.79	8.12	3430	1894
0.6	0.0026	0.276	21.38	15.91	8.38	3459	1924
0.8	-0.0004	0.280	20.97	15.87	8.19	3441	1903
1	-0.0008	0.277	21.17	15.82	8.29	3446	1914
2	0.0030	0.274	21.66	15.98	8.50	3474	1938
4	0.0000	0.275	21.58	15.97	8.47	3471	1934
6	0.0019	0.287	20.36	15.93	7.91	3420	1870
8	0.0029	0.267	22.31	15.97	8.81	3499	1973
10	0.0027	0.284	20.65	15.93	8.04	3432	1885
20	0.0017	0.267	22.25	15.94	8.78	3495	1970
40	0.0020	0.276	21.52	16.01	8.43	3471	1931
60	-0.0002	0.281	20.95	15.95	8.18	3445	1901
80	0.0001	0.270	21.97	15.93	8.65	3484	1955
100	0.0024	0.273	21.68	15.95	8.51	3473	1939

Results of low-frequency measurements on sample H4-3 (1795.0) under dry conditions.

Frequency (Hz)	Extensional attenuation	Poisson ratio	Young's modulus (GPa)	Bulk modulus (GPa)	Shear modulus (GPa)	Vp (m/s)	Vs (m/s)
0.1	0.0011	0.188	21.95	11.74	9.24	3426	2123
0.2	0.0013	0.200	21.77	12.09	9.07	3436	2104
0.4	0.0023	0.204	21.66	12.19	9.00	3436	2095
0.6	0.0024	0.191	21.92	11.80	9.21	3428	2120
0.8	-0.0002	0.192	21.74	11.76	9.12	3416	2110
1	0.0005	0.200	21.39	11.87	8.92	3405	2086
2	0.0020	0.209	21.47	12.29	8.88	3432	2082
4	0.0007	0.197	21.47	11.80	8.97	3405	2092
6	0.0013	0.196	21.46	11.78	8.97	3404	2092
8	0.0031	0.201	21.44	11.95	8.93	3412	2087
10	0.0013	0.200	21.58	12.01	8.99	3422	2095
20	-0.0003	0.196	21.54	11.81	9.00	3409	2096
40	0.0017	0.200	21.75	12.09	9.06	3435	2103
60	0.0008	0.195	21.74	11.88	9.10	3423	2107
80	0.0013	0.198	21.73	11.98	9.07	3428	2104
100	0.0019	0.206	21.76	12.36	9.02	3449	2098

Results of low-frequency measurements on sample H4-3 (1795.0) under brine-saturated conditions.

Frequency (Hz)	Extensional attenuation	Poisson ratio	Young's modulus (GPa)	Bulk modulus (GPa)	Shear modulus (GPa)	Vp (m/s)	Vs (m/s)
0.1	0.0016	0.272	23.08	16.84	9.08	3603	2018
0.2	0.0025	0.271	23.24	16.91	9.14	3613	2025
0.4	0.0009	0.275	22.80	16.86	8.94	3594	2003
0.6	0.0030	0.271	23.15	16.84	9.11	3606	2022
0.8	-0.0006	0.273	22.90	16.81	8.99	3595	2009
1	-0.0018	0.272	22.92	16.78	9.01	3594	2010
2	0.0019	0.271	23.40	17.01	9.21	3625	2033
4	0.0014	0.271	23.32	16.95	9.18	3618	2029
6	0.0005	0.281	22.13	16.84	8.64	3567	1969
8	0.0019	0.276	22.81	16.96	8.94	3599	2002
10	0.0028	0.278	22.63	16.96	8.86	3593	1993
20	0.0019	0.274	22.99	16.93	9.03	3605	2012
40	0.0023	0.273	23.28	17.05	9.15	3622	2026
60	0.0014	0.272	23.12	16.88	9.09	3607	2019
80	0.0002	0.273	23.13	16.99	9.08	3613	2019
100	0.0025	0.275	23.04	17.03	9.04	3612	2014

Results of low-frequency measurements on sample H4-4 (1800.4) under dry conditions.

Frequency (Hz)	Extensional attenuation	Poisson ratio	Young's modulus (GPa)	Bulk modulus (GPa)	Shear modulus (GPa)	Vp (m/s)	Vs (m/s)
0.1	0.0015	0.177	26.12	13.48	11.12	3590	2249
0.2	0.0024	0.177	25.99	13.42	11.03	3581	2243
0.4	0.0008	0.178	25.86	13.37	10.98	3573	2237
0.6	0.0026	0.177	26.15	13.49	11.11	3592	2250
0.8	0.0006	0.176	25.95	13.36	11.03	3577	2242
1	0.0002	0.177	25.61	13.23	10.85	3555	2226
2	0.0032	0.179	25.72	13.37	10.85	3567	2230
4	0.0003	0.180	25.74	13.41	10.85	3569	2229
6	-0.0001	0.180	25.73	13.41	10.88	3569	2229
8	0.0032	0.180	25.64	13.36	10.83	3563	2225
10	0.0013	0.181	25.79	13.47	10.89	3574	2231
20	0.0006	0.180	25.80	13.44	10.90	3574	2232
40	0.0020	0.180	25.99	13.53	11.00	3586	2241
60	0.0007	0.177	25.92	13.38	10.99	3576	2240
80	0.0004	0.179	26.02	13.52	11.00	3587	2243
100	0.0024	0.179	25.95	13.48	11.00	3582	2240

Results of low-frequency measurements on sample H4-4 (1800.4) under brine-saturated conditions.

Frequency (Hz)	Extensional attenuation	Poisson ratio	Young's modulus (GPa)	Bulk modulus (GPa)	Shear modulus (GPa)	Vp (m/s)	Vs (m/s)
0.1	0.0016	0.264	26.37	18.64	10.94	3772	2164
0.2	0.0025	0.259	26.86	18.61	10.90	3767	2161
0.4	0.0025	0.262	26.54	18.61	10.56	3741	2127
0.6	0.0030	0.262	26.81	18.77	10.85	3771	2155
0.8	0.0002	0.263	26.68	18.75	10.54	3747	2124
1	-0.0012	0.261	26.57	18.53	10.63	3742	2134
2	0.0025	0.262	27.10	18.97	10.96	3792	2166
4	0.0003	0.263	27.04	19.00	10.87	3787	2158
6	0.0008	0.263	26.83	18.87	10.72	3768	2142
8	0.0018	0.264	26.73	18.85	10.54	3754	2125
10	0.0025	0.262	26.57	18.63	10.74	3755	2144
20	0.0016	0.263	27.02	18.99	11.12	3805	2182
40	0.0009	0.262	27.02	18.94	10.76	3775	2146
60	0.0010	0.264	27.02	19.11	10.89	3794	2159
80	0.0002	0.262	27.48	19.22	11.10	3816	2179
100	0.0013	0.261	27.08	18.89	10.96	3787	2166

References section 4

Australia patent AU2011318229. An Apparatus For And A Method Of Characterising Mechanical Properties Of A Sample. Inventors: Gurevich, B., Lebedev, M., Lwin, M., Mikhaltsevitch, V. 2011.

Birch, F., 1960. The velocity of compressional waves in rocks to 10 kilobars: 1. Journal of Geophysical Research, 65(4), pp.1083-1102.

Dellinger, J., and L. Vernik, 1994, Do traveltimes in pulse-transmission experiments yield anisotropic group or phase velocities?: Geophysics, 59, 1774–1779, http://dx.doi.org/10.1190/1.1443564.

Delle Piane, C., Olierook, H.K., Timms, N.E., Saeedi, A., Esteban, L., Rezaee, R., Mikhaltsevitch, V., Iglauer, S. and Lebedev, M., 2013. Facies-based rock properties distribution along the Harvey 1 stratigraphic well. Australian National Low Emissions Coal Research & Development CSIRO Report Number EP133710. Available at: http://anlecrd.com.au/projects/facies-based-rock-properties-distribution-along-the-harvey-1-stratigraphic-well/

Dewangan, P., and V. Grechka, 2003, Inversion of multicomponent, multiazimuth, walkaway VSP data for the stiffness tensor: Geophysics, 68, 1022–1031, http://dx.doi.org/10.1190/1.1581073.

Evans, B., Rezaee, M.R., Rasouli, V., Lebedev, M., Saeedi, A., Liu, K. and Iglauer, S., 2014. Predicting CO2 injectivity properties for application at CCS sites. Available at http://anlecrd.com.au/wp-content/uploads/2016/08/ANLEC-final-Aug22-clean-copy.pdf

Gassmann, F., 1951, Über die elastizität poröser medien: Vierteljahrss-chrift der Naturforschenden Gesellschaft in Zurich, 96, 1-23. The English translation of this paper is available at http://sepwww.stanford.edu/sep/berryman/ PS/gassmann.pdf.

Gurevich, B., M. Pervukhina , and D. Makarynska, 2011, An analytic model for the stress-induced anisotropy of dry rocks : Geophysics, 76, no. 3, WA125–WA133, http://dx.doi.org/10.1190/1.3567950.

Lebedev, M., A. Bóna, R. Pevzner, and B. Gurevich, 2011, Elastic anisotropy estimation from laboratory measurements of velocity and polarization of quasi-P-waves using laser interferometry: Geophysics, 76, no. 3, WA83–WA89, http://dx.doi.org/10.1190/1.3569110.

Lebedev, M., Pervukhina, M., Mikhaltsevitch, V., Dance, T., Bilenko, O., & Gurevich, B. (2013). An experimental study of acoustic responses on the injection of supercritical CO2 into sandstones from the Otway Basin. Geophysics, 78, no. 4, D293–D306.

Mavko, G., Mukerji, T., Dvorkin, J., 2009. The rock physics handbook. Cambridge University Press.

Nur A., 1971. Effects of stress on velocity anisotropy in rocks with cracks: Journal of Geophysical Research, 76, no. 8, 2022–2034.

Rasouli, V., Pervukhina, M., Müller, T.M. and Pevzner, R., 2013. In-situ stresses in the Southern Perth Basin at the GSWA Harvey-1 well site. Exploration Geophysics, 44(4), pp.289-298.

Tsvankin, I., J. Gaiser, V. Grechka, M. van der Baan, and L. Thomsen, 2010, Seismic anisotropy in exploration and reservoir characterization: An overview: Geophysics, 75, no. 5, 75A15–75A29, http://dx.doi.org/10.1190/1.3481775

Zhang, Y., Langhi, L., Schaubs, P.M., Delle Piane, C., Dewhurst, D.N., Stalker, L. and Michael, K., 2015. Geomechanical stability of CO 2 containment at the South West Hub Western Australia: a coupled geomechanical–fluid flow modelling approach. International Journal of Greenhouse Gas Control, 37, pp.12-23.

Section 5: Evaluation of SC-CO_2 containment capacity of shale: Testing recommendations and results on the Yalgorup

Joel Sarout[1], Bruce Maney[1], Jeremie Dautriat[1]

[1]CSIRO Energy

Scope and objectives

The aim of this work package is to develop a laboratory testing method to assess the ability of a cap rock (e.g., shale) to contain supercritical CO_2 (SC-CO_2) after injection for geosequestration purposes. There is no standard protocol in the industry for conducting this evaluation for tight and clay-rich rocks in the laboratory. Such testing is neither part of routine nor special core analysis studies. There are a number of reasons for this, which may be classed as either experimental or conceptual. Experimental data on CO_2 transmission through a brine-saturated shale are scarce in the scientific literature to effectively support industry requirements. Even the testing protocols and the data interpretation vary widely, making them debatable. On the other hand, this gap has been identified as a potential area of growth.

The scarcity of experimental data is related to: (i) the difficulty in preserving, handling and testing shales; (ii) the need to conduct the testing at realistic reservoir stress, pressure and temperature conditions; (iii) the inherent difficulty in controlling a changing-phase CO_2 during an experiment at reservoir conditions, i.e., gas, liquid, super-critical, depending on temperature and pressure; (iv) the long-term nature of the test (several weeks), associated with the extremely low permeability of shales, requiring the long-term stability of the experimental equipment; and (v) the challengingly low fluid volumes to be measured during the test.

In addition, the physical mechanisms at play during the interaction between the brine-saturated shale (natural conditions, in situ) and the injected CO_2 are not fully understood. This gap in understanding is exacerbated by the fact that at the reservoir target depths, CO_2 is in a super-critical state, a hybrid state between gas and liquid, i.e., super-critical CO_2 has a density close to that of a liquid and a compressibility close to that of a gas (Span and Wagner, 1996). In the literature, suggested physical mechanisms at play in this situation include: (i) a capillary pressure barrier to the CO_2 entering the pore network of the brine-saturated shale; (ii) dissolution/miscibility between brine and CO_2 in its relevant physical state (super-critical); and (iii) phase diffusion, e.g., CO_2 in the brine.

Often in the literature, the time dependency of the latter mechanism and its impact on the tests/data are neglected. CO_2 and brine are often assumed to be immiscible, which is a reasonable assumption at short interaction time typically expected in conventional reservoir rocks. However, it is well known that CO_2 is soluble and diffuses in brine, given sufficient time. The immiscibility assumption has been used for testing the capillary entry pressure of CO_2 in brine-saturated reservoir rocks such as sandstones and carbonates. For permeable rocks, the breakthrough of CO_2 occurs at relatively small times, making the dissolution and diffusion of CO_2 into the brine an irrelevant mechanism. Unfortunately, this assumption has also been applied to tight rocks such as cap shales, with extremely low permeability. Due to the long-term interaction between CO_2, brine and the cap rock during experimental evaluation, dissolution, diffusion and miscibility of CO_2 and brine have time to occur and influence the measurements being conducted, making the interpretation of the results debatable.

We propose here to conduct a theoretical and experimental study on the feasibility and interpretation of CO_2 transmission/breakthrough tests in tight shales. For the experimental study, we used a clay-rich sample of the Yalgorup Member of the Lesueur Sandstone, i.e. a potential barrier to vertical upflow of CO_2 in the South West Hub project.

SC-CO_2 containment capacity of shales: How?

At the typical depths of CO_2 geosequestration, in a normally pressurised subsurface environment, CO_2 is in its supercritical phase ($P > 7.4$ MPa, $T > 31.1$°C). The containment capacity of a shale to SC-SCO_2, can be either evaluated directly in the laboratory on a shale specimen, or estimated indirectly from Washburn-Laplace equation and the mercury entry pressure usually obtained from a mercury injection porosimetry tests on *dry* shale samples.

In view of the extremely low permeability/diffusivity in shales, three mechanisms have been recognised as operative at the contact between a SC-CO_2 phase and a naturally brine-saturated shale (Figure 126):

- Capillary effect: threshold entry pressure associated with (i) interfacial pressure between the saturating brine and the SC-CO_2 on one hand; and (ii) wettability of minerals (clays in particular) by the brine and SC-CO_2;
- Solubility of SC-CO_2 into brine described by Henry's law or modified versions;
- Diffusivity of (i) brine in the saturated shale and of (ii) CO_2 in the brine-saturated shale described by Fick's law.

The indirect method relies exclusively on the capillary barrier concept, and ignores time-dependent solubility and diffusion processes. It therefore focuses only on the determination of the so-called capillary entry pressure of SC-CO_2 in the naturally brine-saturated shale. The direct method on the other hand is driven by laboratory observation as it aims at estimating experimentally how fast and how much SC-CO_2 passes through a naturally brine-saturated shale specimen.

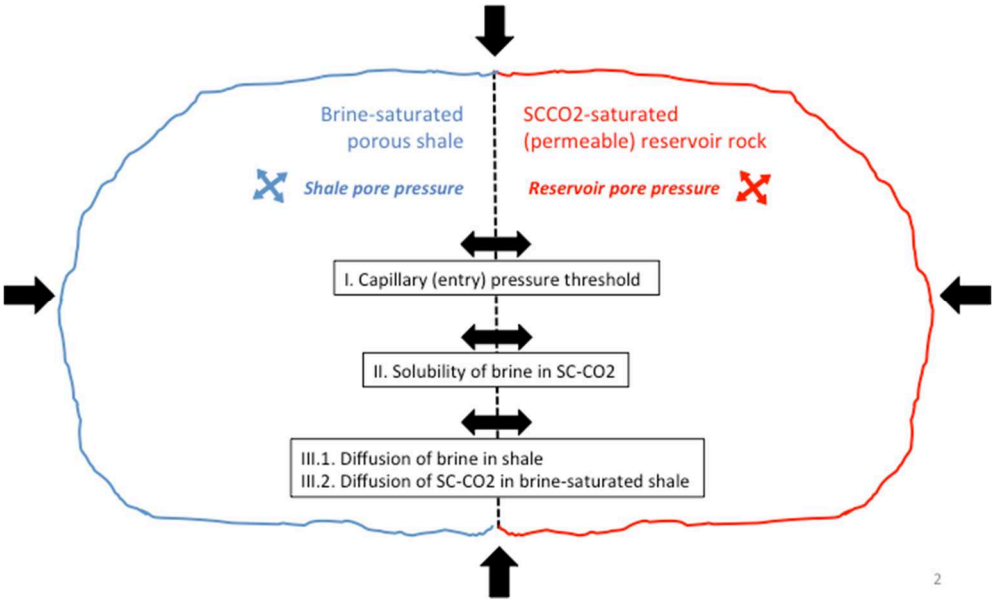


Figure 126 Physico-chemical interactions expected at the interface between a reservoir saturated with supercritical CO_2 and a naturally brine-saturated cap shale.

Indirect estimation of P_{cap}

It is possible to estimate the SC-CO_2 entry pressure of a shale using the Washburn-Laplace equation and the mercury entry pressure usually obtained from a mercury injection porosimetry tests on *dry* shale samples. This approach is valid provided that:

- The brine and SC-CO_2 are effectively immiscible;
- The interfacial tension between SC-CO_2 and brine is known at the relevant PT conditions;
- The contact angles between SC-CO_2, brine and mineral is known at the relevant PT conditions.

Interfacial tension and contact angle data for the SC-CO_2, brine and shale system have been published in the literature. For instance, Bachu et al. (2009) published an extensive dataset of interfacial tension between CO_2 and CO_2-presaturated brine with various salinities and at various pressures and temperatures, including

supercritical CO_2 conditions. For supercritical CO_2 pressure and temperature conditions in the range 10 MPa-50°C, they report an interfacial tension of $\gamma^{SC\text{-}CO_2/w}$ = 20 to 28 mN/m. For CO_2-brine-mineral contact angles, one difficulty lies in the selection and preparation of the mineral samples, especially clay minerals. Most published work refers to (muscovite) mica as a structural analogue for clays (Chiquet et al., 2007; Mills et al., 2011; Farokhpoor et al., 2013). To our knowledge, only Wang et al. (2012) published results for kaolinite, illite and phlogopite (white mica). The contact angles they find for these minerals (18°-26°) differ significantly from those published for (muscovite) mica (34° to 40°). However, they also tested quartz and calcite for which they find contact angles that do match other published data. Note that Farokhpoor et al. (2013) show a time dependency of the contact angle for (muscovite) mica, i.e., variation from 35° to 60° in 50 days. These values of contact angles are obtained at pressure/temperature conditions close or within the supercritical domain of CO_2.

Although there is a large variability (and time dependency) in the published contact angles for the CO_2-brine-mineral system, the impact on the value of entry pressure is minimal. Using Washburn-Laplace equation and a range of contact angles 20° to 60°, and interfacial tensions 20 to 28 mN/m, we find that the capillary entry pressure (P_{cap}) of SC-CO_2 in *CO_2-presaturated brine* ranges from 0.2 to 0.53 MPa for a typical mercury entry pressure in a dry shale of 7.6 MPa for instance. This means that as soon as its pressure increases above P_{cap}, SC-CO_2 should start invading the pore space of this shale, the so-called breakthrough.

Direct laboratory evaluation

On the other hand, CO_2 transmission or breakthrough tests have been developed to evaluate directly shales containment capacity. They involve various testing protocols for controlling and monitoring the upstream and downstream fluid types (brine or CO_2), pressures and volumes. A preliminary baseline brine permeability test is often conducted before the CO_2 transmission itself to constrain the shale's natural hydraulic conductivity (Figure 127). The essential stages of the successful testing protocols include:

- Subjecting the shale sample to the in situ temperature, confining pressure, and pore pressure using a pore fluid simulating the natural formation brine.
- Conducting a preliminary brine permeability test to constrain shale hydraulic transmissivity.
- Conducting the SC-CO_2 transmission/breakthrough test per se.

CO_2 breakthrough occurs when SC-CO_2 invades the shale's pore space, introducing a first SC-CO_2 path percolating through the entire shale sample. This is achieved when the differential fluid pressure between the top and bottom ends of the shale specimen overcomes the SC-CO_2 capillary entry pressure P_{cap}. This type of test has been applied to permeable reservoir rocks and led to successful estimates of P_{cap} in sandstone and carbonate reservoirs.

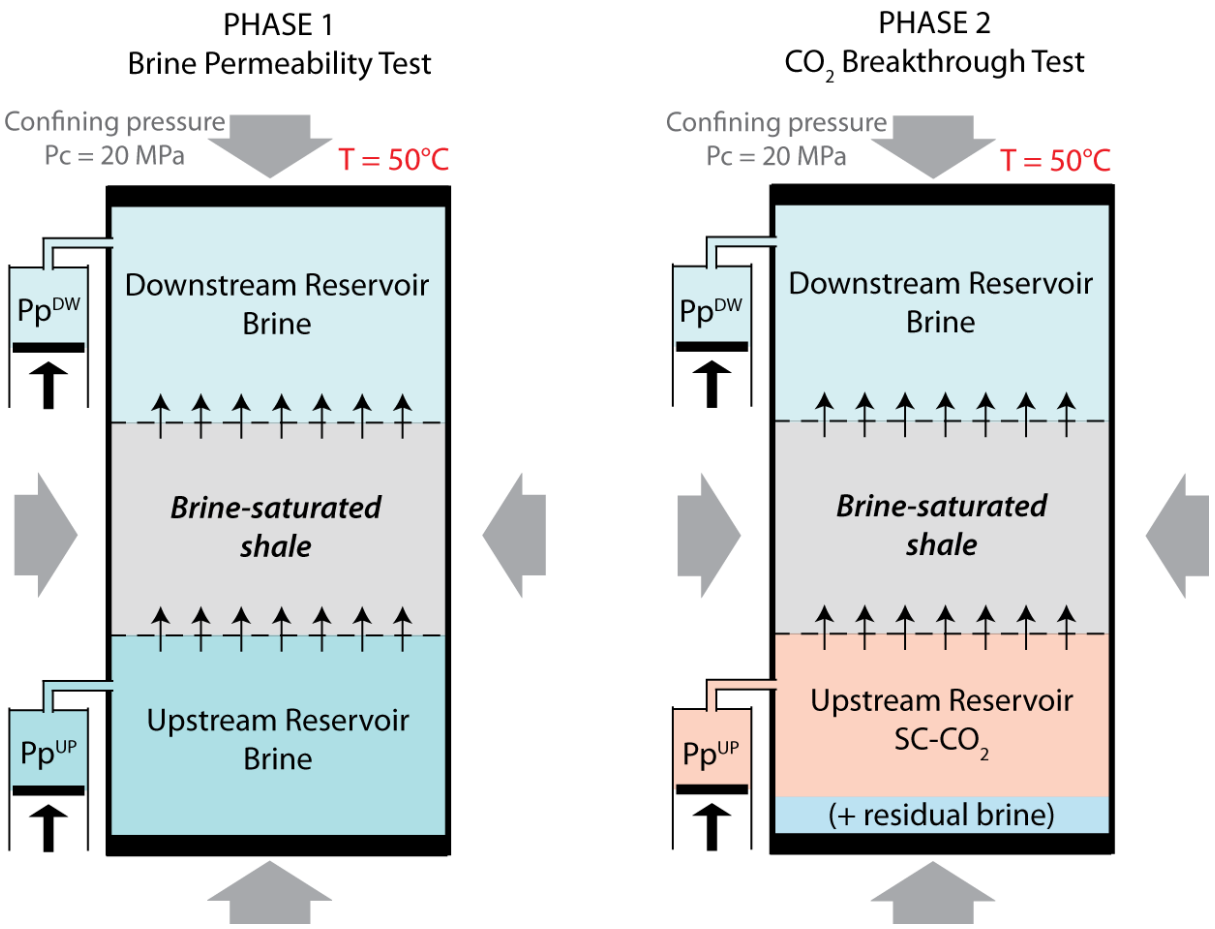


Figure 127 Principle of the brine permeability (PHASE 1) and a CO_2 transmission (PHASE 2) tests conducted in this study

Discussion

It has been shown in the literature that CO_2 (either gas or supercritical) and brine are not "immiscible" fluids as CO_2 coefficient of solubility is known and not negligible. They can be miscible if dissolution is given sufficient time to operate, which is typically the case in shale transmission experiments (e.g. Sarout and Detournay, 2011; Josh et al., 2012). It has also been noted that CO_2 is quantitatively more soluble in water (in terms of mol or g per kg of water) when in supercritical state than when in a gaseous phase (e.g. Tables 3 to 6 in Zhenhao and Sun, 2003, for water NaCl brines with different molarity). In addition, diffusivity (D) of CO_2 in water is of the order of magnitude of self-diffusivity of water molecules, which is in turn of the order of magnitude of brine diffusivity in a brine-saturated shale, that is D = 1 to $10 \cdot 10^{-9}$ m^2/s (e.g. Sarout and Detournay, 2011; Josh et al., 2012). A diffusion length (e.g. sample length in Figure 127) of L = 10 mm yields a characteristic diffusion time of $\tau \sim$ 0.1 to 1 days. For L = 20 mm, this characteristic diffusion time reaches $\tau \sim$ 0.4 to 4 days. Based on these observations and on the typical time scales required for transmission-testing a tight cap shale (days to weeks), dissolution and diffusion mechanisms are more likely to be operative than percolation and breakthrough between immiscible fluids at the interface between SC-CO_2 and the brine-saturated shale.

Note though that the immiscibility hypothesis is more likely to be valid in SC-CO_2 breakthrough tests conducted on permeable reservoir rocks as reported extensively in the literature. In this case, the SC-CO_2 pressure transmission through the permeable rock is much faster than dissolution and diffusion of SC-CO_2 in the brine. For the short durations required to conduct a transmission test in a permeable reservoir rock, SC-

CO_2 and brine could coexist and remain immiscible until the breakthrough threshold occurs, i.e. if the differential fluid pressure across the sample overcomes the SC-CO_2 capillary entry pressure.

In light of the preceding observations, one expects that this capillary entry pressure barrier remains effective until significant amounts of SC-CO_2 dissolve and diffuse in the pore brine, through the rock.

Although similar physical mechanisms are operative in shales and in a permeable reservoir rocks, one expects a significant contrast in behaviour between them during a CO_2 transmission test:

- In a reservoir rock, fluid pressure transmission through the rock frame (relatively fast process), and diffusion of CO_2 in the brine-saturated rock (slower process) occur with very different characteristic times.
- In a shale, both processes are slow and display comparable characteristic times.

Impact of laboratory testing on the project

This suggests that for tight shales, SC-CO_2 dissolution/diffusion mechanisms are essential for the reliable evaluation of the containment capacity of a cap shale layer. Whether the driving pressure gradient overcomes the SC-CO_2 capillary entry pressure in that shale or not should be a secondary concern. More importantly, this outlines the fact that CO_2 dissolution and diffusion rates in the formation brine will control the overall CO_2 migration toward the surface, rather than the capillary pressure barrier. If significant amounts of CO_2 are transported by diffusion through a shale thickness of 1 cm in say 1 week, a similar amount will be transported over 1 m in 200 years, or 10 m in 20,000 years…

In addition, in the literature *CO_2-presaturated* brine is often used for testing with CO_2 to minimise CO_2 dissolution in the brine during the CO_2 test. Although this methodology is valid for maintaining artificially the immiscibility between the in situ brine and the injected CO_2, it is not a realistic scenario in the field where the natural pore fluid in the shale is most likely to be free of CO_2. In light of the above discussion, using a CO_2-presaturated brine becomes unnecessary since dissolution and diffusion are in effect the controlling mechanisms for evaluating the overall upward migration of CO_2 through the shale. The essential parameter to be evaluated is the characteristic time of SC-CO_2 diffusion in the pore brine of the shale formation of interest. In the following section, the experimental protocol developed to carry out this evaluation is described along with the results obtained on a preserved sample of the Yalgorup Member of the Lesueur Sandstone from Harvey 3.

Recommended evaluation method

Recommended testing procedure

The aim is to robustly evaluate the effective SC-CO_2 containment capacity of a shale formation through direct testing under realistic subsurface stress and temperature conditions in the laboratory. This entails evaluating the effective CO_2 transmissivity of the shale, essentially driven by diffusion processes. A pilot experimental evaluation is conducted on a sample of the Yalgorup Member of the Lesueur Sandstone (depth 888.07 m) from Harvey 3 in the South West Hub area.

Building on existing testing procedures reported in the literature, and minimising lab equipment sophistication (e.g. no requirement for an in-line mass spectrometer to detect CO_2 transmission in a pressure vessel in the laboratory), we recommend that the following requirements at least are met for a reliable transmissivity evaluation in the laboratory configuration depicted in Figure 127:

1. **PHASE 0: Preconditioning**. Subject the shale sample to simulated in situ temperature, confining pressure, and pore pressure using a simulated pore fluid.
2. **PHASE 1: Brine Permeability Test (QC)**. Conduct a brine permeability test by applying a constant differential fluid pressure between the top and bottom ends of the shale specimen. Monitor the upstream and downstream volumetric flows using high accuracy volumetric pumps.
3. **PHASE 2: SC-CO_2 Transmission Test**. Conduct the SC-CO_2 transmission/breakthrough test by applying a constant differential fluid pressure between the top and bottom ends of the shale specimen after replacing the upstream brine with SC-CO_2. Monitor the upstream and downstream volumetric flows using high accuracy volumetric pumps.

Thanks to the simple boundary conditions imposed on the specimen in the recommended testing protocol above, the recorded pressure variation curves can be interpreted robustly, provided that:

1. The resolution of the volumetric pumps used is in the order of ~ 0.1 mL/week;
2. The overall temperature stability of the experimental setup is within $\pm$ 1°C over several days/weeks;
3. The overall stability of the experimental setup (fluid lines micro-leaks, software crash) can be maintained over several days/weeks.

Recommended testing procedure

The above constitutes the recommended standard operating procedure (SOP) for evaluating the effectiveness of the SC-CO_2 containment capacity of a shale formation in the laboratory.

This SOP is designed to ensure that the SC-CO_2 transmissivity in tight shales is evaluated in a relevant and robust way, calibrated against brine conductivity, and using only conventional (although high quality) laboratory equipment (no costly in-line mass spectrometer required to detect CO_2 transmission through the shale).

Experimental validation

A long-term experimental testing program has been carried out on a sample from one of the clay-rich intervals of the Yalgorup Member of the Lesueur Sandstone, considered as possible baffles to the upward migration of the CO_2 in South West Hub area.

A preserved cylindrical sample of 25 mm in diameter and 10 to 20 mm long is consolidated at a temperature T = 50°C, a confining pressure Pc = 20 MPa, and a pore pressure Pp = 9 MPa, using the reconstituted brine illustrated in section 3 of this report. The sample preliminary consolidation and subsequent testing are carried out in NGL's Autonomous Triaxle Cell (ATC) hosted and managed by CSIRO's Geomechanics and Geophysics Laboratory (Figure 128).

The sample was subjected to the testing protocol reported in the previous section. The total duration of this multi-stage evaluation experiment was 140 days. Several testing conditions in terms of differential pressure applied and fluid type (brine and/or SC-CO_2) have been investigated. Brine permeability and CO_2 transmissivity have been estimated from the upstream and downstream volumetric flows recorded during PHASE 1: Brine permeability, and PHASE 2: SC-CO_2 transmissivity.

A typical permeability test data set includes recording the upstream and downstream brine volume variations while the high accuracy volumetric pumps maintain a constant differential pore pressure between the two ends of the shale plug (Figure 129). Similarly, a typical SC-CO_2 transmissivity tests data set includes recording the upstream (SC-CO_2) and downstream volume variations while the high accuracy volumetric pumps

maintain a constant differential pore pressure between the two ends of the shale plug (Figure 130). Despite the tight temperature regulation of the laboratory (± 1°C) and the temperature insulation of the ATC heated to 50°C, near-diurnal pressure oscillations are clearly visible on these curves, reflecting room temperature variations. Despite these oscillations, and thanks to their systematic nature, long-term testing under the recommended conditions allows us to reliably estimate the trends in which fluid volumes change upstream and downstream, and therefore how much and how fast CO_2 invades the naturally brine-saturated shale.

Table 12 summarises the range of essential testing parameters investigated in this study and the key results of this laboratory testing program. The most important parameter to monitor in this table is the transmissivity parameter, or apparent permeability. It is defined through Darcy's law, a valid formalism for the steady-state fluid transmission protocol implemented during the testing. Similarly to permeability, the unit for this transmissivity are m^2 or Darcy. Alternatively, an apparent diffusivity could be defined, the units of which would be m^2/s. This parameter reflects the volume of fluid diffused through the shale per unit time as recorded during the experiments.

	Regression Slope (mL / day)	Flow Rate Volume (x 10^{-13} m^3 / s)	Fluid Pressure (MPa)	Delta Fluid Pressure (MPa)	Avg. Fluid Pressure (MPa)	Avg. Effective Pressure (MPa)	Density (kg/m^3)		Viscosity (x 10^{-3} Pa.s)		Apparent Permeability* (x10^{-21} m^2)	Flow Rate Mass (x 10^{-10} kg / s)
							Brine	*CO2*	*Brine*	*CO2*		
PHASE 2: BRINE PERMEABILITY				2.2	9.9	10.1					**2.0 ± 0.1**	
Downstream	0.016899	1.96	8.8				991.8	N/A	0.55	N/A	1.90	1.94
Upstream	-0.018611	-2.15	11				992.73	N/A	0.55	N/A	2.08	-2.13
PHASE 3: BRINE PERMEABILITY				5.2	11.4	8.6					**2.3 ± 0.1**	
Downstream	0.052053	6.02	8.8				991.8	N/A	0.55	N/A	2.46	5.97
Upstream	-0.047174	-5.46	14				994.01	N/A	0.55	N/A	2.23	-5.42
PHASE 4: CO2 TRANSMISSION				7.2	5.8	14.2					**1.0**	
Downstream	0.03492	4.05	2.2				988.96	39.69	0.55	0.016	N/A	N/A
Upstream	-0.64254	-74.4	9.4				N/A	324.76	N/A	0.025	1.00	-24.16
PHASE 5: CO2 TRANSMISSION				10.2	7.3	12.7					**0.4**	
Downstream	0.0823	9.53	2.2				988.96	39.69	0.55	0.016	N/A	N/A
Upstream	-0.2359	-27.3	12.4				N/A	535.79	N/A	0.042	0.43	-14.63
PHASE 6: CO2 TRANSMISSION				13.2	8.8	11.2					**1.1**	
Downstream	0.020328	2.35	2.2				988.96	39.69	0.55	0.016	N/A	N/A
Upstream	-0.58323	-67.5	15.4				N/A	706.57	N/A	0.058	1.15	-47.69
PHASE 7: CO2 TRANSMISSION				16.2	10.3	9.7					**0.24**	
Downstream	0.1523	17.6	2.2				988.96	39.69	0.55	0.016	N/A	N/A
Upstream	-0.13589	-15.7	18.4				N/A	757.33	N/A	0.065	0.24	-11.89

Table 12 Testing conditions and results. Conditions common to all tests are: temperature T = 50°C, confining pressure Pc = 20 MPa, sample length L = 19.46 mm and diameter D = 25.31 mm. * Darcy's law in steady-state flow regime is used to define the apparent permeability or transmissivity: $k = Q \mu L / A \Delta P$, where the sample cross section $A = \pi (D/2)^2$.

In addition, the mass transport rate can be estimated from this volumetric flow rate using the density of the fluid at the relevant PT conditions where they are known (right-most column of Table 12). For the brine permeability test, only brine is involved in the testing so that the nature of the fluid and its thermodynamic properties are unambiguously known at all times during the test. For the CO_2 transmission test, with the basic laboratory equipment purposely involved in this test (no in-line mass spectrometer involved to detect CO_2 transmission downstream), the fluid type and thermodynamic conditions are known reliably only on the injection side of the shale sample (upstream). At the downstream end of the shale sample, a mixture of brine and CO_2 in multi-phasic conditions should flow out (gas/liquid/supercritical CO_2, brine and CO_2 dissolved in the brine depending on the local PT conditions within the specimen), and the fractions of fluid types and phases should vary with time during a CO_2 transmission test.

The main outcomes the testing program are:

1. The simple testing protocol recommended allows for a reliable and reproducible estimation of the brine permeability and CO_2 transmissivity in the Eneabba shale.
2. The brine permeability of the clay-rich Yalgorup sample is of the order of 2.10^{-21} m^2 at the reservoir conditions simulated in the laboratory.

3. The equivalent CO_2 transmissivity in the Yalgorup sample is 2 to 10 times slower than that of the brine.

Application of laboratory results to the project

Under simulated reservoir temperature and pressure conditions (T = 50°C, Pc = 20 MPa, Pp = 6 to 11 MPa), CO_2 diffuses through the naturally brine-saturated clay-rich Yalgorup sample at a rate 2 to 10 times slower than the natural brine. Shales with a permeability in the order of $k = 10^{-21}$ m^2 $= 10^{-6}$ mD (corresponding to a hydraulic diffusivity in the order of $D_H \sim 10^{-9}$ m^2/s) are usually considered efficient cap rocks for hydrocarbon reservoirs over geological time scales. With a CO_2 diffusion rate through a brine-saturated shale 2 to 10 times slower ($DCO_2 \sim 1$ to $5\ 10^{-10}$ m^2/s), and assuming lateral continuity and structural integrity, the clay-rich intervals of the Yalgorup Member of the Lesueur Sandstone could act as effective baffles for CO_2 migration at supercritical PT conditions. Under these conditions and according to the experimental data obtained, CO_2 should diffuse through a 1 m-thick layer of Yalgorup rock in about 63 to 317 years; or a 10 m-thick layer in about 6300 to 31700 years.

Based on these estimates, the most critical aspects constraining the efficiency of the Yalgorup formation in acting as a CO_2 buffer/barrier is the continuity and structural integrity of the formation itself. The accurate estimation of the effectiveness of the Yalgorup buffer/barrier requires (i) the knowledge of the detailed geological structure of the formation; and (ii) and a predictive hydro-geomechanical model accounting for the migration of CO_2. The laboratory data obtained here can be used as an input in such models for the Yalgorup formation.

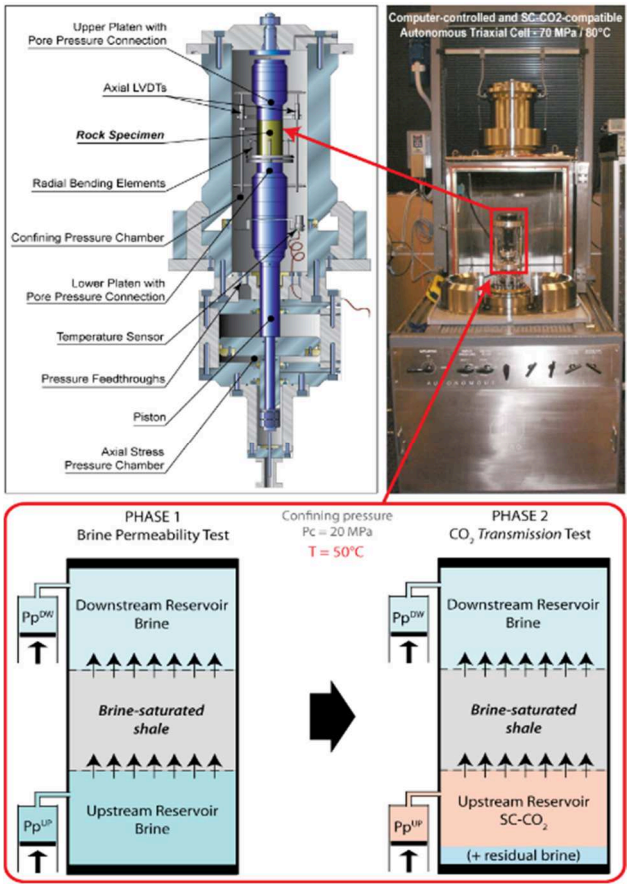


Figure 128 The autonomous Triaxial Cell used to conduct the brine permeability and (PHASE 1) and the CO_2 transmission (PHASE 2) tests.

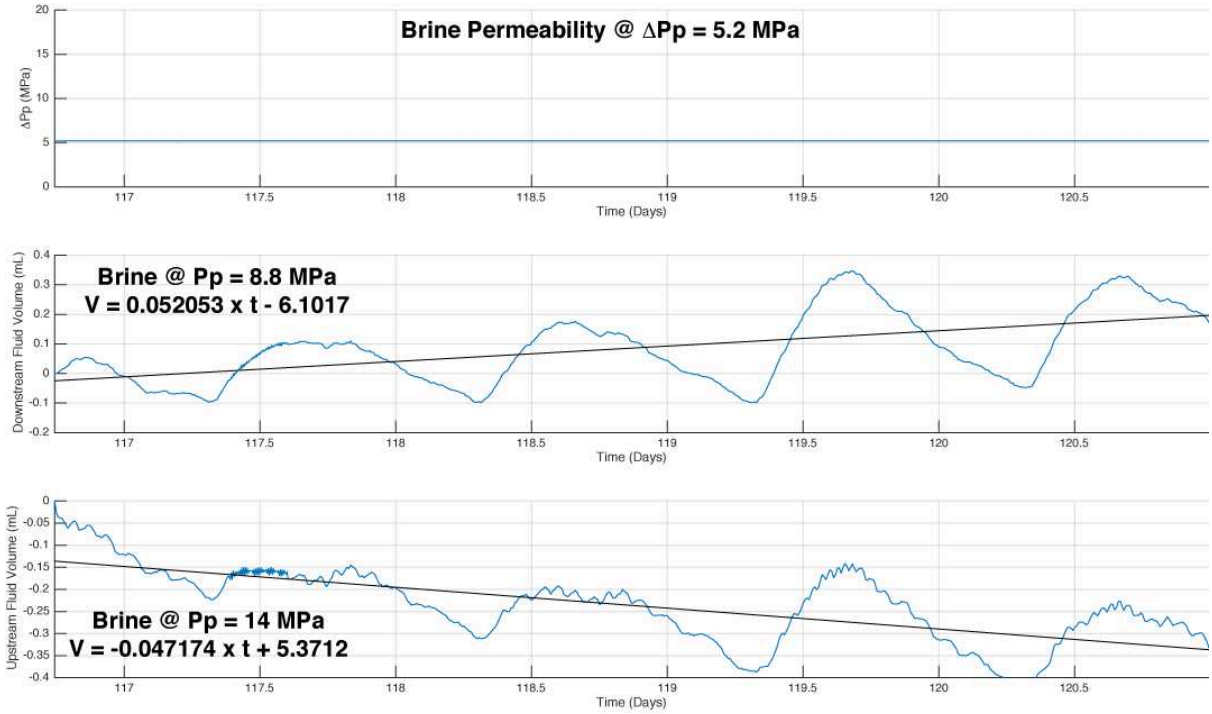


Figure 129 Pressure and volume curves recorded during the steady-state hydraulic transmission regime of the brine permeability test carried out on the Yalgorup sample.

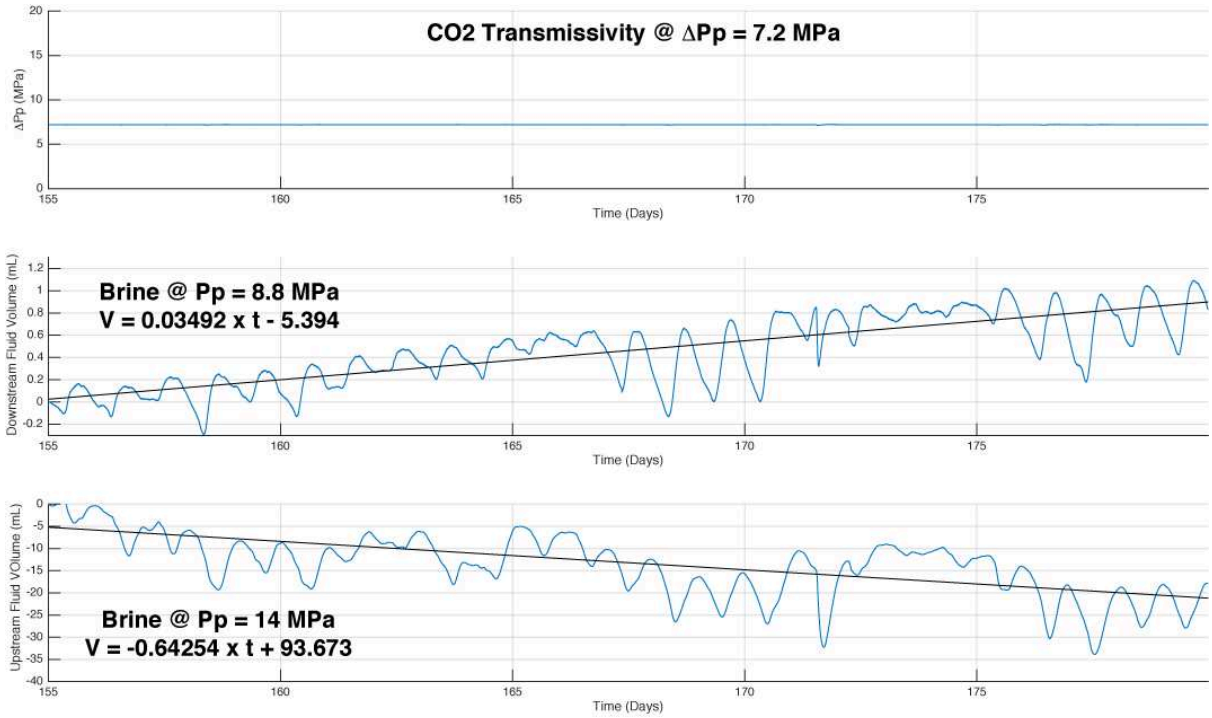


Figure 130 Pressure and volume curves recorded during the steady-state regime of the CO_2 transmissivity test carried out on the Yalgorup sample.

Recommendations and conclusions

1. **Driving mechanisms.** For tight shales, SC-CO_2 dissolution/diffusion mechanisms are essential for the reliable evaluation of the containment capacity of a cap shale layer in a CCS project. Whether the driving pressure gradient overcomes the SC-CO_2 capillary entry pressure in that shale or not should be a secondary concern. More importantly, this underlines the fact that CO_2 dissolution and diffusion rates in the formation brine will control the overall CO_2 migration toward the surface, rather than the capillary pressure barrier. If significant amounts of CO_2 are transported by diffusion through a shale thickness of 1 cm in say 1 week, a similar amount will be transported over 1 m in 200 years, or 10 m in 2 million years…
2. **Recommended testing procedure.** The recommended laboratory assessment protocol builds on existing testing procedures reported in the literature, and minimises lab equipment sophistication (e.g., no requirement for an in-line mass spectrometer to detect CO_2 transmission in a pressure vessel in the laboratory), we recommend that the following requirements at least are met for a reliable transmissivity evaluation in the laboratory configuration depicted in Figure 127:
    a. **PHASE 0: Preconditioning**. Subject the shale sample to simulated in situ temperature, confining pressure, and pore pressure using a simulated pore fluid;
    b. **PHASE 1: Brine Permeability Test (QC)**. Conduct a brine permeability test by applying a constant differential fluid pressure between the top and bottom ends of the shale specimen. Monitor the upstream and downstream volumetric flows using high accuracy volumetric pumps;
    c. **PHASE 2: SC-CO_2 Transmission Test**. Conduct the SC-CO_2 transmission/breakthrough test by applying a constant differential fluid pressure between the top and bottom ends of the shale specimen after replacing the upstream brine with SC-CO_2. Monitor the upstream and downstream volumetric flows using high accuracy volumetric pumps.
3. **Minimal laboratory equipment requirements.** Thanks to the simple boundary conditions imposed on the specimen in the above testing protocol above, the recorded pressure variation curves can be interpreted robustly, provided that:
    a. The resolution of the volumetric pumps used is sufficient, i.e., ~ 0.1 mL/week;
    b. The overall temperature stability of the experimental setup is reasonable, i.e., $\pm$ 1°C over several days/weeks;
    c. The overall stability of the experimental setup (fluid lines micro-leaks, software crash) can be maintained over several days/weeks.
4. **CO_2 containment capacity of the Yalgorup.** Under simulated reservoir temperature and pressure conditions (T = 50°C, Pc = 20 MPa, Pp = 6 to 11 MPa), CO_2 diffuses through the naturally brine-saturated Yalgorup sample at a rate 2 to 10 times slower than the natural brine. Shales with permeability in the order of 10^{-21} m^2 are usually considered competent cap rocks for O&G gas reservoirs over geological time scales. Therefore, assuming lateral continuity and structural integrity the clay-rich portion of the bottom part of the Yalgorup could act as a good retardant for CO_2 migration at supercritical PT conditions. For instance, if brine diffuses through a 10 m thick layer with characteristics similar to those measured in the experiments above in say 2 million years, CO_2 will diffuse through the same layer in 8 to 200 million years.

References section 5

Bachu S. and Bennion D.B. (2009). Interfacial tension between CO_2, freshwater and brine in the range of pressure from 2 to 27 MPa, temperature from 20 to 125°C, and water salinity from 0 to 334000 mg/L. *J. Chem. Eng. Data*, 54:765-775.

Chiquet P., Broseta D. and Thibeau S. (2007). Wettability of caprock minerals by carbon dioxide. *Geofluids*, 7:112-122.

Farokhpoor R., Bjorkvik B.J.A., Lindeberg E. and Torsaeter O. (2013). Wettability behaviour of CO_2 at storage conditions. *Int. J. Greenhouse Gas Control*, 12:18-25.

Josh, M., Esteban, L., Delle Piane, C., Sarout, J., Dewhurst, D.N. and Clennell, M.B. (2012). Laboratory characterization of shale properties: J. Petrol. Sci. Engin., 88-89, 107-124; doi: 10.1016/j.petrol.2012.01.023.

Mills J., Riazi M. and Sohrabi M. (2011). Wettability of common rock-forming minerals in a CO_2-brine system at reservoir conditions. International Symposium of the Society of Core Analysts, Austin, Texas, USA, 18-21 September, 2011 (paper # SCA2011-06).

Sarout J., Detournay E. (2011). Chemoporoelastic analysis and experimental validation of the pore pressure transmission test for reactive shales. International Journal of Rock Mechanics and Mining Sciences, 48, 759-772.

Span R., and Wagner W. (1996). A new equation of state for Carbon Dioxide covering the fluid region from the triple-point temperature to 1100K at pressures up to 800 MPa. *Journal of physical and Chemical Reference Data*, 25:1509.

Wang S., Edwards I.M. and Clarens A.F. (2012). Wettability phenomena at the CO_2-brine-mineral interface: Implications for geologic carbon sequestration. *Environ. Sci. Technol.*, 47:234-241.

Zhenhao D. and Sun R. (2003). An improved model calculating CO_2 solubility in pure water and aqueous NaCl solutions from 273 to 533 K and from 0 to 2000 bar. Chemical Geology, 193: 260–271.

Section 6: Image analysis evaluation of Harvey 1 rock cuttings for wellbore instability

Ali Rezagholilou[2], Christopher Skea[2], Mohammad Sarmadivaleh[2]

[2]Curtin University

Introduction

Harvey 1 was drilled into the S150 5814 block in the Southern Perth Basin Western Australia to examine its potential for CO_2 storage (Stalker et al., 2014). It was drilled to a depth of 2913.8m TVDSS and cuttings were collected at various depths. The borehole intersected mainly sandstone, with subordinate claystone and siltstone and traces of coal. Long open-hole sections during drilling put the wellbore at risk of instability. Detailed evaluation of the ditch-cutting samples is undertaken here to assess the relations between cavings and wellbore instability. It is inclusive of shape, size and type distribution of cavings in available samples. Accordingly, an image processing technique using the ImageJ software is utilised to determine the particle's shape after the visual examination of samples. This allows for the characterisation of the dominant failure types in the Harvey 1 borehole according to depth.

Particle Descriptions

Cuttings

Drill cuttings are important as they provide a real-time description of the rock lithology being drilled. By monitoring the cuttings, the mud engineer is able to detect the likely location and type of wellbore collapses due to the irregularity in size and type of particles present. These irregular fragments can be used to determine the location of breakouts in the wellbore by looking at other logs and matching them with fragment types. However, in order to determine whether a cutting is irregular, it is important to have an understanding of cutting sizes, shapes and colours. These parameters can vary whilst using specific types of drill bits and RPMs when drilling certain types of formations.

Drill bit cuttings

Drill bit selection depends on the formation type, the required rate of penetration (ROP) and service-life of bit. However, these bits all are made from two main types according to their cutting mechanism. Roller cone bits have two or more (usually three) cone shaped elements with teeth to fracture or crush the formation as it is rotated (Figure 131) and are mainly used in hard formations. Weight on bit (WOB) is transferred to the rock by its teeth where crushing of the rock causes micro-fractures and makes it easier to gouge out the rock using lateral motions, induced by the rotation of the cone and drill bit.

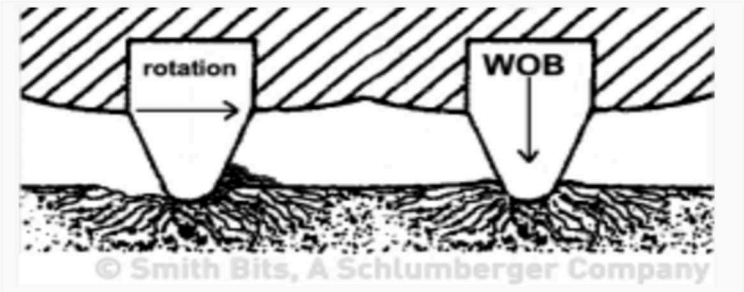


Figure 131 Cutting action of roller cone bits (Wamsley Jr & Pgs, 2015)

Hayatdavoudi et al. (1987) suggested some correlations for predicting of cutting size for tri-cone roller type bits. Equations are linear relationships developed based on work done by bit on rock grain (W),

power input (P_{in}) and power output (P_{out}) against average cuttings size (d) in a firm shale for 8 1/2" and 6 5/8" drill bits. The expressions below show the relations for 8 ½" drill bit:

$$W = 1.07 \times 10^5 + (7.49 \times 10^7)d \quad \text{Equation 27}$$

$$P_{in} = 77.1 + 2702d \quad \text{Equation 28}$$

$$P_{out} = 1.264 \times 10^4 + (8.95 \times 10^8)d \quad \text{Equation 29}$$

These expressions become more complex by increasing size of the drill bit. In Harvey 1, a 12 ¾" a roller cone bit was used in the initial hole section consisting mainly of sandstone. This makes it relatively difficult to develop a precise relationship between power and average cutting size other than saying that increase in power results in a reduction of average cutting size.

Fixed cutter bits employ sharp fixed surfaces to scrape or grind the surface (Figure 132). The most common type is the Polycrystalline Diamond Cutter (PDC), which uses synthetic diamond material to cover the cutting surface. A PDC cuts rock by causing a shear failure along the shear planes of the rock face and are most suitable for soft to medium strength rocks (Bar-Cohen and Zacny, 2009). However, diamond-impregnated bits are the best for ultra-hard abrasive rock formations due to their exceptional durability. This ability keeps them sharp even as they wear down since new impregnated diamonds are exposed (Mostofi and Franca, 2014). Diamond impregnated bits are often used when stringers of ultra-hard rock are expected in soft rock. This eradicates the need to pull back the drill string to replace the bit by a more suitable one, making it more expensive and time consuming.

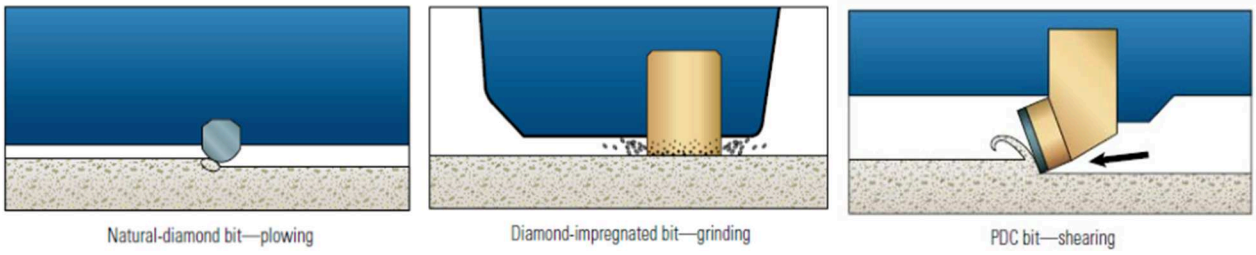


Figure 132 Different cutting mechanisms for fixed cutter bits (Karimi, 2013).

Figure 133 shows the differences in the size of cutting produced by a PDC bit and a tri-cone bit when drilled in the same formation. The size differences occur as the PDC bit shears the formation at a set angle (Figure 132) causing ductile failures of rock mass so cuttings are relatively constant in size. Whereas the tri-cone bits cause brittle failure of the rock mass which leads to a variety of large cutting sizes.



Figure 133 Polycrystalline diamond compact (PDC) vs. Tri-cone bit cuttings from same lithology (Karimi, 2013).

The type of formation being drilled can also have a large impact on the size of cuttings received at the surface. Cuttings produced by hard formations are usually large. However, cuttings from soft formations typically have a more rounded shape and may not reach the surface in the original condition. They have a tendency to grind against the annulus walls and may completely dissolve (Egenti, 2014). The characteristics of cuttings in relation to formation types are as shown in Table 13 below. The small cuttings size of sandstone is due to the low depth of cut by the PDC bit, which is around same depth as grain size. Therefore, the bit grinds the sandstone by breaking up the cement material holding individual grains (Bourgoyne et al. Young, 1986).

Cutting Size (inch)	Rock Type	Shape	Grain Density (gm/cc)	Bed Porosity (%)
Large (0.275)	Limestone	Angular	2.57	41
Medium (0.175)	Limestone	Angular	2.57	36
Small (0.009)	Sand	Round	2.6	39

Table 13 Cutting characteristics in regards to formation type (Egenti, 2014).

The drilling report from Harvey 1 indicates that a tri-cone bit was used up to a depth of 845.6m before switching to a Baker-Hughes 8 ½ inch PDC bit for the rest of the borehole. From literature, it is assumed that the cutting size for PDC bits within sandstone should be less than 1 mm, therefore all the collected samples are considered to be cavings, after 2.6 mm sieving. While cuttings for tri-cone bits, can range up to 2-3 cm making it difficult to distinguish between cavings and cuttings. Size of cuttings depend on various parameters such as cutting speed, depth of cut, number of teeth, material removal rate, hardness of rock, etc. Thus, making a distinction between cavings and cuttings is difficult. However, particles larger than 2-3 mm are often called cavings (Ellis & Stoker, 2014).

Cavings

Cavings occur because of wellbore instability. They appear in shale shakers, which allow for a quick interpretation of the down-hole environment including the nature of the instability and their locations. Cavings can be produced by several mechanisms, such as underbalanced drilling, stress relief, pre-existing planes of weakness, or by the mechanical action of the drilling process and tools (Kumar, 2012). Following Edwards et al. (2004), these mechanisms of wellbore instability can be grouped into two main classes: i) instability of intact rock and ii) instability of rock having pre-existing planes of weakness such as fractures, cleavage or bedding planes. Rock containing pre-existing planes of weakness can be further broken down into two sub categories: a) impermeable, and b) preferentially permeable planes of weakness. An impermeable plane of weakness means that an increase in mud weight will help support wellbore wall helping alleviate breakouts. A permeable plane of weakness will allow drilling fluid to enter the formation, so increase in mud weight may increase the wellbore instability, as it does not add support to wellbore wall (Edwards et al., 2004).

The cutting analysis focuses mainly on the size, shape, appearance, and percentage of particles in order to determine how, when and where the caving occurred. Size describes length, width, thickness of the largest and the average cutting. Shape is a descriptive terms that can be used to classify particles as angular, blocky, oblate, tabular, platy, elongate, and splintery. Appearance of the particles includes descriptors such as lithology, color or any other visible/structural features such as bedding, laminations, and fracture. Percentage relates to the quantity of cutting with respect to depth or drilling parameter change (i.e. change in mud weight).

The three main shapes of cavings often used for identifications are tabular (or blocky), angular and splintered. Osisanya (2011) and Bradford et al. (2000) described these shapes as follows:

Tabular/Blocky

These cavings may originate from two sources, namely natural fractures and weak planes. Natural-fracture cavings are flat with parallel faces and bedding planes not parallel to the faces shown as on the left side of Figure 134. These cavings are caused by the invasion of drilling fluids into the fractures. Weak-plane cavings have flat faces parallel to bedding planes and are often induced because of a low mud weight selection and drilling a borehole with 15 to 20 degrees deviation from the direction of bedding (Bradford et al., 2000); (BP, 2008). The combination of these two factors induces massive failure along planes of weakness on the high side of the wellbore. In vertical wells, however, tabular/blocky cavings are mainly produced through destabilisation of wellbore wall by the fluid invasion into natural fractures rather than a plane of weakness. Figure 134 shows naturally fractured blocky (left) and weak plane tabular cavings (right).

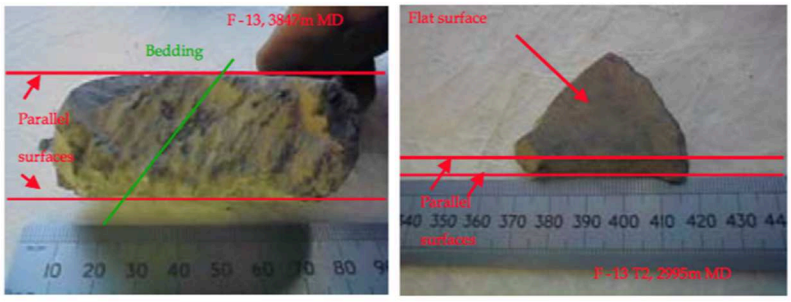


Figure 134 Naturally fractured (Blocky) and weak plane (Tabular) Cavings (Kristiansen, 2004).

Angular

These cavings are produced due to shear failures of the wellbore from excessive horizontal stress. They occur when mud weight is too low to reduce the wellbore stresses to a safe level leading to shear failure of the intact rock. If the surface of the caving appears old they may have come from rubble zones. They can be described as having an arrowhead or triangular shape with curved faces and a rough surface structure as displayed in Figure 135. One side of the cutting may be curved corresponding to the part of the cut borehole circumference (BP, 2008). To restrict this type of breakout, it is recommended that the mud weight is raised if the pore/fracture window allows. If it is not possible to the raise mud weight, then careful drilling practices are advised with improved hole cleaning and reduced ROP.



Figure 135 Angular Caving (Bradford et al., 2000)

Splintered

These cavings are produced from over-pressured zones where induced tensile failures result in flat, thin and planar structures as shown in Figure 136. The size of splintery cavings can range from very tiny splintery fragments to long slivers, several centimeters or inches in length. Splintered cavings can also be produced when a well is drilled through an area of high tectonic stress and wellbore wall collapses (Pasic et al., 2007), when low mud weight is used or when ROP is too high in a low permeability rock. Wellbore enlargement will occur through the circumference of the wellbore rather than only in a specific direction like angular cavings. This type of failure is treated by increasing the weight of the drilling fluid or by reducing ROP, if suspected to be too high (Skalle, 2010).



Figure 136 Splintery Caving from underbalanced drilling (Kumar, 2012)

The summary of explanations above can be used to generate a list of features for cavings. These features may partially coincide with shapes observed in some depths, which highlights the importance

of the other signs. However, the likely features of cavings are listed in Table 14. The size of cavings can range from just a few millimetres to tenths of centimetres or greater, usually prevalent in weak formations (i.e. shales) compared to stronger formations i.e. dolomites (Willson, 2012). It should be noted that the sizes at the ground surface might not be a true representation of the cavings due to fragments and/or cuttings possibly breaking up because of different settling velocities.

Shape	Description	Cause	Remedy
Angular	Triangular /arrow head shape with a rough surface structure	Low mud weight leading shear failure of the wellbore.	Increase Mud weight. Increase flow to ensure good hole cleaning.
Tabular	Flat parallel faces	Combination of wellbore within 15˚ of bedding planes and low mud weight result in bedding failure.	Gentle drilling advised with small adjustments in mud weight. Minimize surge and swap pressures
Splintery	Flat, thin and planar structures	High tectonic stresses with low mud weight.	Stop drilling and increase mud weight, set casing if it cannot be controlled to avoid influx and/or stuck pipe.
Blocky	Cubic in structure	Invasion of drilling fluid into pre-existing fractures within rubble zones destabilising formation.	Gentle drilling advised with small adjustments in mud weight. Change mud type. Minimize surge and swap pressures

Table 14 Summary of caving descriptors, their likely causes and recommended remediate actions.

Figure 137 shows how reducing bottom-hole pressure may change the type of failure on wellbore wall in strong and weak rocks. In weak formations, the breakout will produce a mixture of splintery and angular cavings. The stronger the rock, the further shift to the left of the Mohr circles during failure. This will result in tensile failure of the strong formations. The pressure gradients between high formation pore pressures and low drilling-fluid pressures result in splintery cavings that pop out of the wellbore wall (Halliburton, 2014).

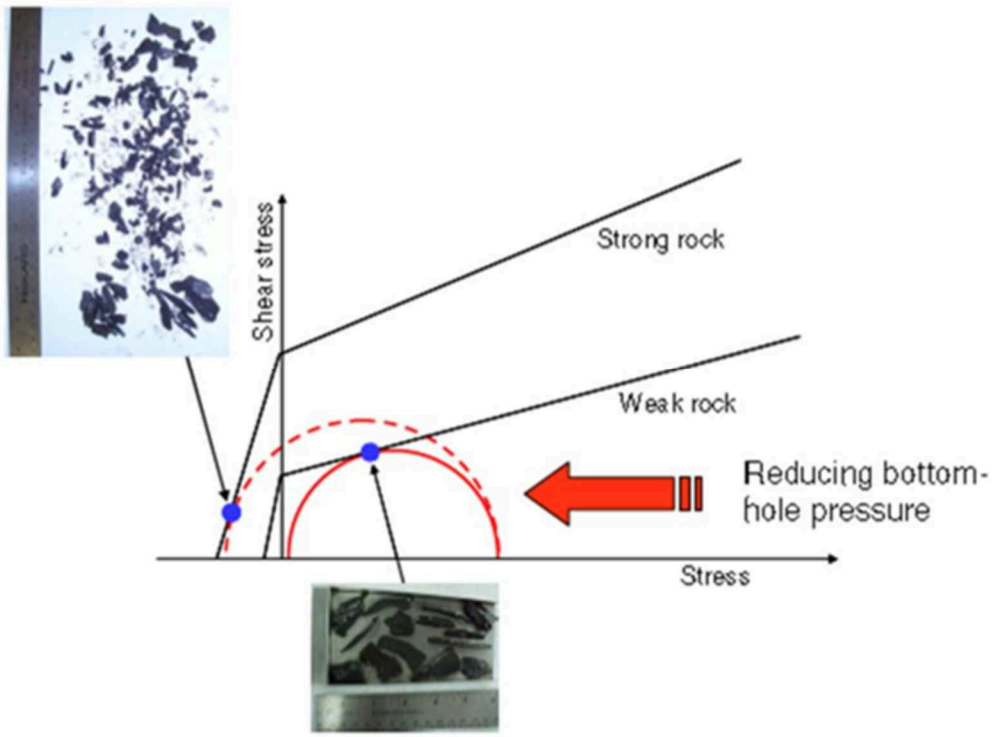


Figure 137 Mohr's circle illustration of borehole tensile and shear failures for strong and weak formations (BP, 2008).

In a well such as Harvey 1, where the formation mostly consists of sandstone, when breakouts occur, the drill string reworks the cavings as they are transported up the borehole. The cavings become rounded by the time they reach the surface making it difficult to identify the original shape. This mostly occurs with angular cavings as they already start out with a more rounded nature (BP, 2008).

Once cavings have appeared at the surface, it is important to be able to quickly identify them and prescribe how and where they were produced. Once this is understood, the required action can be taken in order to fix the problem or at least minimise further damage to wellbore. Figure 138 below shows a decision tree to determine corrective measures to be taken when cavings appear at the surface.

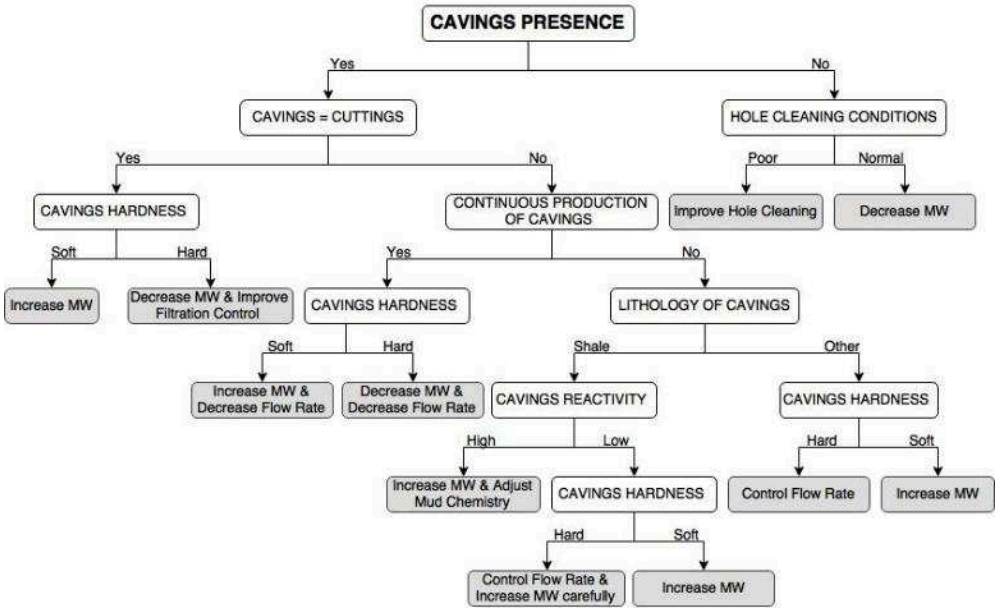


Figure 138 Action flowchart when cavings present at surface (Zausa et al., 1997).

Initial evaluations

The ditch cuttings of different depths from Harvey 1 available at the WA-core library are considered in this study. Samples were examined to see whether they could easily be broken down by hand pressure. This ensured that particles are solid and related to real cavings. They then were sieved using a 2.36 mm sieve and the coarse portions weighted as displayed in Table 15.

Depth (m)		Sample No.	Total weight (g)	Weight(g) of retained on 2.36 mm	Coarse (%)	Comment
From	To					
60	65	1	227.7	199	87.4	
105	110	2	297.7	97.5	32.8	
405	410	3	273.7	148.7	54.3	
420	425	4	261.4	243.3	93.1	
1130	1135	5	307.4	168.8	54.9	
1140	1145	6	264.6	165.7	62.6	
1145	1150	7	264.3	93.3	35.3	
1150	1155	8	292.2	144.5	49.5	
1170	1175	9	278.8	158.1	56.7	
1240	1245	10	286.9	108.3	37.7	
1245	1250	11	271	154.6	57.0	
1265	1270	12	264.8	172.9	65.3	
1275	1280	13	280.3	172.4	61.5	
1280	1285	14	286.8	164.3	57.3	
1285	1290	15	268.5	129.1	48.1	

Depth (m)		Sample No.	Total weight (g)	Weight(g) of retained on 2.36 mm	Coarse (%)	Comment
From	To					
1320	1325	16	311.5			Clods
1330	1335	17	272.3	182.2	66.9	
1350	1355	18	245.2			Clods
1365	1370	19	257.4	153.2	59.5	
1370	1375	20	265.6	196.3	73.9	
1390	1395	21	257.7	158.3	61.4	
1395	1400	22	275.3	138.4	50.3	
1410	1415	23	260.5	162.8	62.5	
1420	1425	24	251	169	67.3	
1465	1470	25	266	152.1	57.2	
1470	1475	26	262.7	159.4	60.7	
1480	1485	27	268.5	179.7	66.9	
1485	1490	28	274.3	154.2	56.2	
1490	1495	29	284	173	60.9	
1495	1500	30	266.4	147.8	55.5	
1500	1505	31	261.6	159.1	60.8	
1505	1510	32	285.3	190	66.6	
1510	1515	33	268.3	169.7	63.3	
1515	1520	34	280.3	173.5	61.9	
1520	1525	35	279.3	173.2	62.0	
1825	1875	36				Clods
1830	1835	37	266.5	141	52.9	
2835	2825	38				Clods
2840	2845	39	295.4	106.3	36.0	Clods
2845	2850	40	307.5	93.8	30.5	Clods
2850	2855	41	303.9	93.6	30.8	
2855	2860	42	306.7	84	27.4	
2860	2865	43	296.3	93.2	31.5	
2865	2870	44	299.4	92.8	31.0	
2870	2875	45	303.6	108.4	35.7	

Table 15 Summary of initial ditch cutting assessments.

Particle size analysis

Images of the coarse portion of samples (cavings) are used for image processing by utilising the ImageJ software. This was done to obtain quantitative data including the area, circularity, roundness, perimeter, minimum and major axis lengths of particles.

The image of samples and their characteristics are shown in Appendix 5A. The images are first cropped, processed to eliminate the background and transformed to an 8-Bit grey scale image prior to manual thresholding to. The thresholded image produces a black and white image with ditch particles in black and background in. To allow the program identify the individual particles the image is processed with watershed algorithm. However due to the complex nature of the image and the high tolerance used when applying the threshold, some particles become clumped together and counted as one. To overcome this issue some manual editing is required using drawing tools to define each ditch particle by comparing it to the original image. Once complete, the image is automatically analysed by the software so that descriptors can be associated to each particle.

This data is used directly to assess the shape, percentage and source of the cavings. Determination of caving type is attained by using the relationship between roundness and circularity of the caving particles which are overlayed on top of the table presented in the Shell Sample Examination Manual for describing grain shape (Swanson, 1981) shown in Figure 139. Having defined the shape, size and distribution of the cavings, it is possible to distinguish the likely cause of the failures, such as tensile (splintery), shear (angular) or bedding failures (tabular/blocky). Summary of ImageJ processing works and descriptions of cuttings are presented in the Appendix 5A.

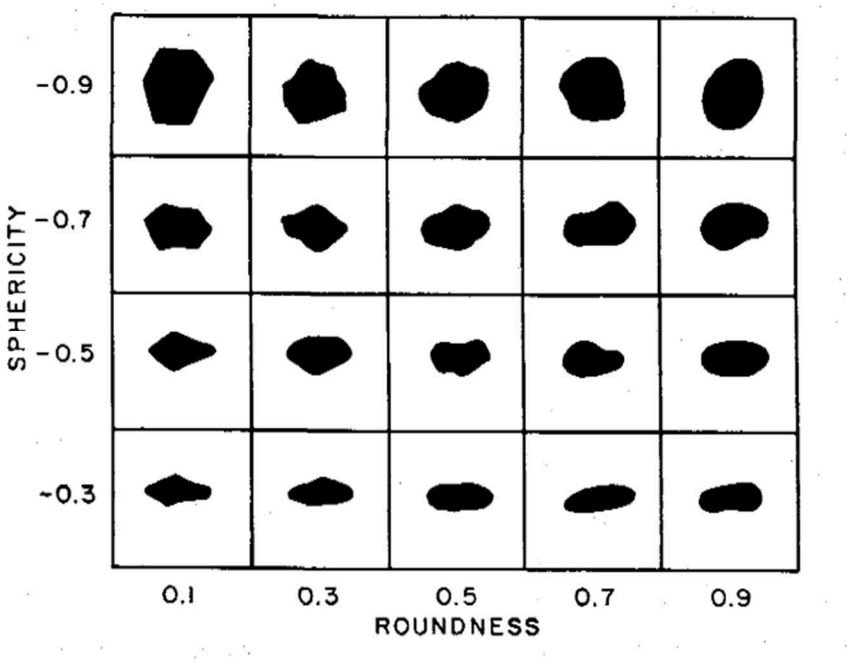


Figure 139 Illustration describing grain shape by roundness and sphericity (Swanson, 1981).

Conclusions and recommendations

This study employed an image-processing technique to examine ditch cuttings and to identify the wellbore failure types in Harvey 1. This method utilises the quantitative data derived from size and shape analysis of particles. A new classification of cavings suggested here is based on the frequency of different particles matching with descriptive definitions available in the literature. In a typical case study, angular cuttings produced from shear failure make up roughly 70-90% with blocky particles from pre-existing fractures and weak planes accounting for the other 10-45%. Small traces of splintery particles are present which indicate tensile failure occurring. However, due to the small amount, these

can be ignored as it is important to remedy the larger wellbore problems as soon as possible to reduce costs. These findings match with the calliper and Star image logs. The image analysis is supported by the stress failure calculations indicating shear failure as the main cause of breakout within the borehole. The method has been used for just one borehole (Harvey 1) and its validity range needs to be further assessed. It is recommended to implement a similar technique for Harvey 4, the nearest borehole with a complete data set.

References section 6

Bar-Cohen, Y., & Zacny, K. (2009). Drilling in extreme environments: penetration and sampling on earth and other planets: John Wiley & Sons.

Bourgoyne, A. T., Millheim, K. K., Chenevert, M. E., & Young, F. S. (1986). Applied drilling engineering.

BP. (2008). Cavings Field Guide An Aid to Mananging Wellbore Stability in Real Time. https://www.scribd.com/doc/262071010/Cavings-Field-Guide: BP America.

Bradford, I., Aldred, W., Cook, J., Elewaut, E., Fuller, J., Kristiansen, T., & Walsgrove, T. (2000). When rock mechanics met drilling: Effective implementation of real-time wellbore stability control. Paper presented at the IADC/SPE Drilling Conference.

Edwards, S., Matsutsuyu, B., & Willson, S. (2004). Imaging unstable wellbores while drilling. SPE Drilling & Completion, 19(04), 236-243.

Egenti, N. B. (2014). Understanding Drill-cuttings Transportation in Deviated and Horizontal Wells. Paper presented at the SPE Nigeria Annual International Conference and Exhibition.

Ellis, D., & Stoker, M. (2014). Hydrocarbon Exploration to Exploitation West of Shetlands.

Halliburton. (2014). Diagnosing Wellbore Failure (pp. 1). http://www.halliburton.com/public/consulting/contents/Posters/Wellbore-Failure-Portrait.pdf: Halliburton

Hayatdavoudi, A., Durugbor, N., Ghalambor, A., & Okoye, C. (1987). Prediction of average cutting size while drilling shales. Paper presented at the SPE/IADC Drilling Conference.

Karimi, M. (2013). Drill-Cuttings Analysis for Real-Time Problem Diagnosis and Drilling Performance Optimization. Paper presented at the SPE Asia Pacific Oil and Gas Conference and Exhibition.

Kristiansen, T. G. (2004). Drilling wellbore stability in the compacting and subsiding Valhall field. Paper presented at the IADC/SPE Drilling Conference.

Kumar, D. A., S; Wang, S; YiMing, J; Ahmed, S; Povstyanova, M and B. Tichelaar. (2012). Real-time Wellbore Stability Analysis: An Observation from Cavings at Shale Shakers. Search and Discovery.

Mostofi, M., & Franca, L. (2014). The wear mechanisms of impregnated diamond bits. Paper presented at the 48th US Rock Mechanics/Geomechanics Symposium.

Osisanya, S. O. (2011). Practical approach to solving wellbore instability problems. SPE Distinguished Lecturer Program.

Pasic, B., Gaurina-Međimurec, N., & Matanovic, D. (2007). Wellbore Instability: Causes And Consequences/Nestabilnost Kanala Busotine: Uzroci I Posljedice. Rudarsko-geolosko-naftni zbornik, 19(1), 87.

Skalle, P. (2010). Drilling fluid engineering: Bookboon.

Stalker, L., Van Gent, D. and Team, N.P., 2014. South West Hub CCS Project in Western Australia–Characterisation of a Greenfield Site. Energy Procedia, 63, pp.5041-5050.

Swanson, R. G. (1981). Sample examination manual.

Wamsley Jr, W., & Pgs, R. F. S. I. I. (2015). PEH: Introduction to Roller-Cone and Polycrystalline Diamond Drill Bits. PetroWiki, from SPE International

Willson, S. M. (2012). A Wellbore Stability Approach For Self-Killing Blowout Assessment. Paper presented at the SPE Deepwater Drilling and Completions Conference.

Zausa, F., Civolani, L., Brignoli, M., & Santarelli, F. (1997). Real-time wellbore stability analysis at the rig-site. Paper presented at the SPE/IADC drilling conference.

Appendix 5A: Image analysis results

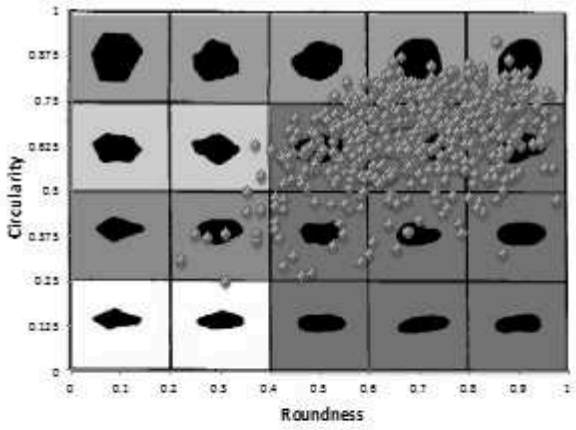
Depth (m)	Shape %		Diameter		Failure type	
405-420	Blocky	17.55%	1-20mm		Tensile Failure	0.18%
	Tabular	0.35%	2-4mm		Shear Failure	81.91%
	Angular	81.91%	1-25mm		Bedding Failure	17.91%
	Splintery	0.18%	4-6mm			

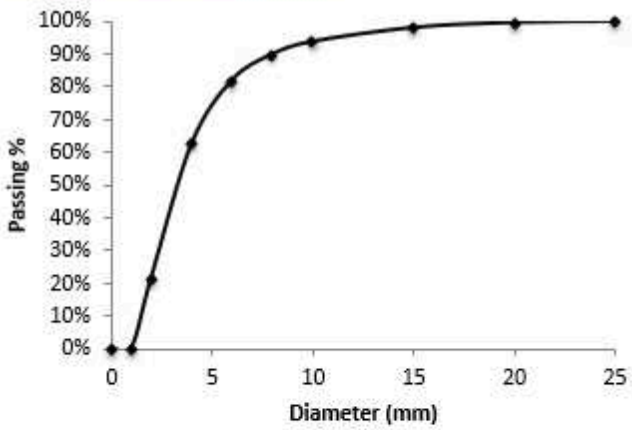
Analysis:

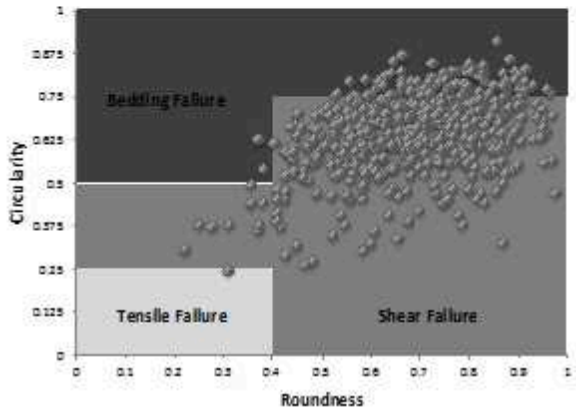
Formation drilled with Tri-cone bit and the large particles are expected from drill bit action rather than breakout. Therefore, the particles in the image are cuttings.

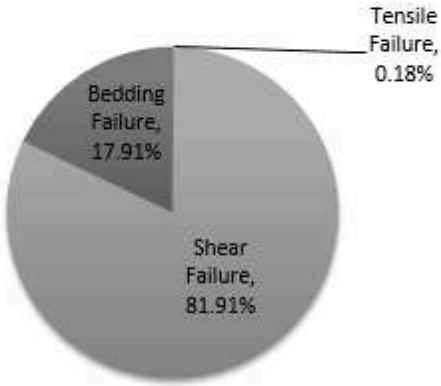


N/A







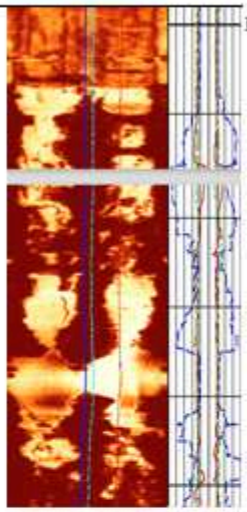


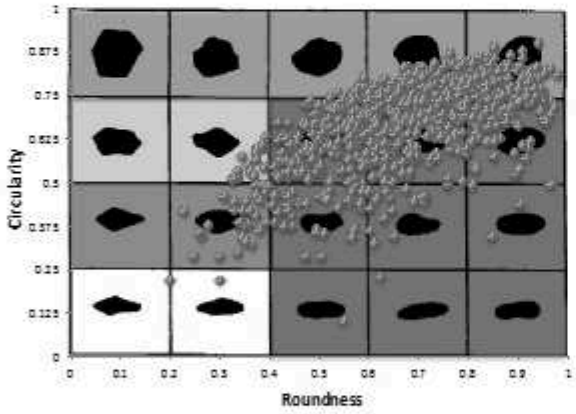
Depth (m)	Shape %		Diameter		Failure type	
1130-1135	Blocky	27.98%	1-20mm		Tensile Failure	0.24%
	Tabular	1.77%	2-4mm		Shear Failure	70.01%
	Angular	70.01%	1-25mm		Bedding Failure	29.75%
	Splintery	0.24%	4-6mm			

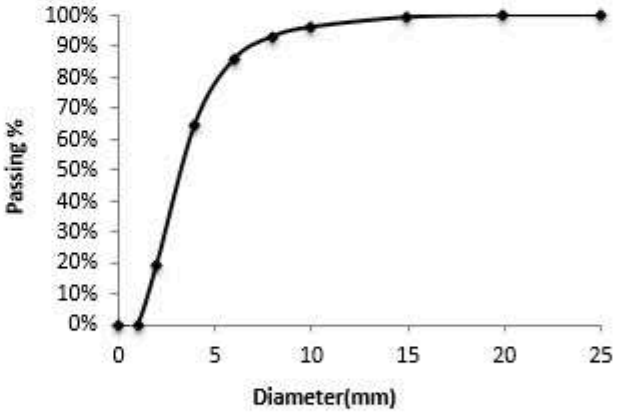
Analysis:

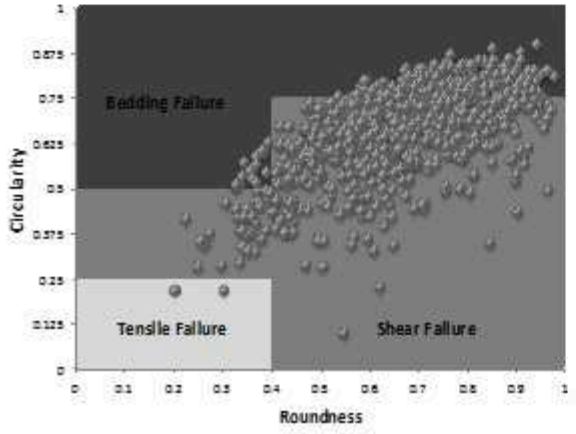
Shear failure of wellbore has occurred, evidenced by the large amount of angular cavings. This is also confirmed by the STAR log showing breakouts 180 degrees apart. The blocky cavings are due to bedding failure of wellbore shown in the middle section of the STAR log.

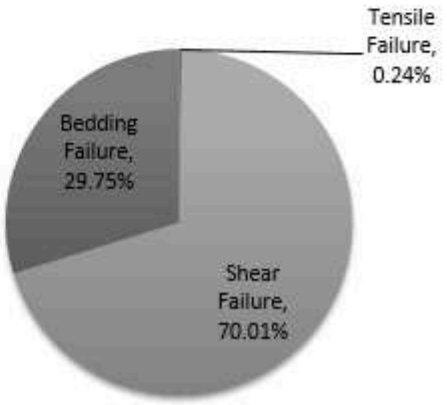










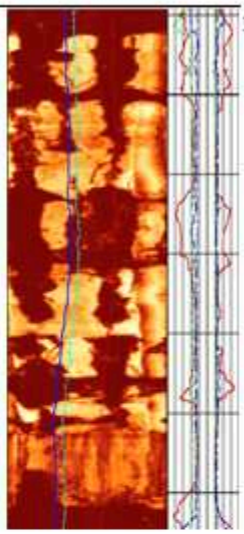


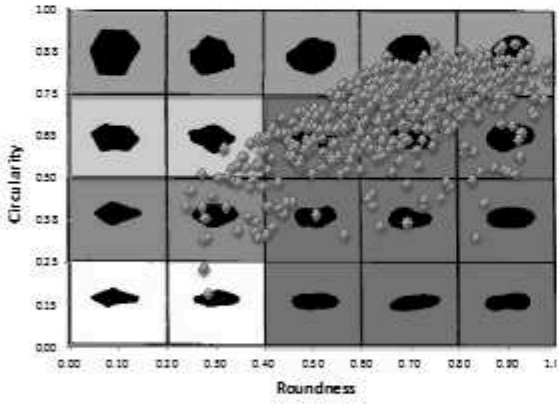
Depth (m)	Shape %		Diameter		Failure type	
1240-1245	Blocky	44.29%	1-15mm		Tensile failure	0.47%
	Tabular	2.03%	0-4mm		Shear Failure	53.21%
	Angular	53.21%	0-15mm		Bedding Failure	46.32%
	Splintery	0.47%	0-4mm			

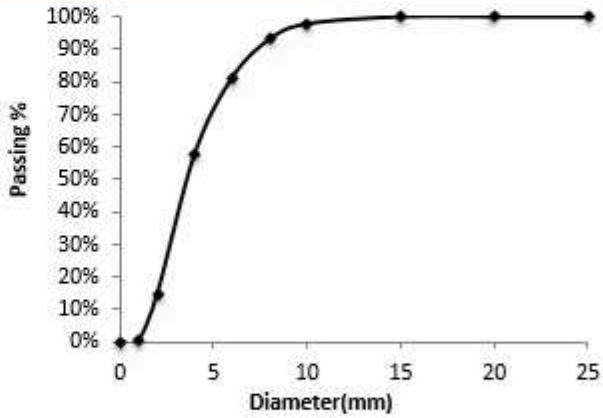
Analysis:

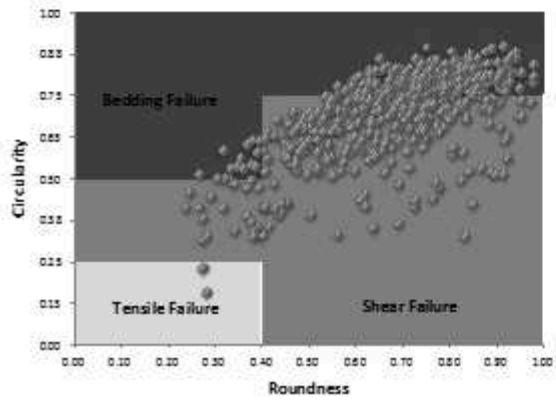
Shear failure of formation is major cause of wellbore breakout with 53% of cavings being angular. Over 44% of cuttings came from bedding. The large increase in blocky cavings can be explained by the large bedding failure shown in STAR logs at depth of 1234-1236m.

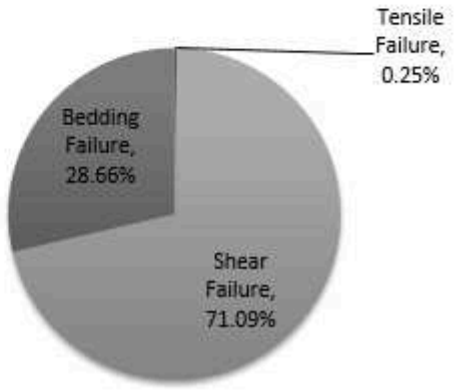








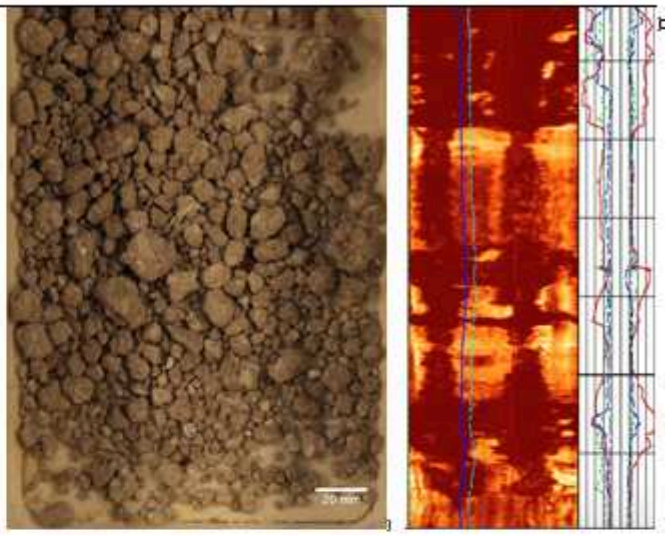


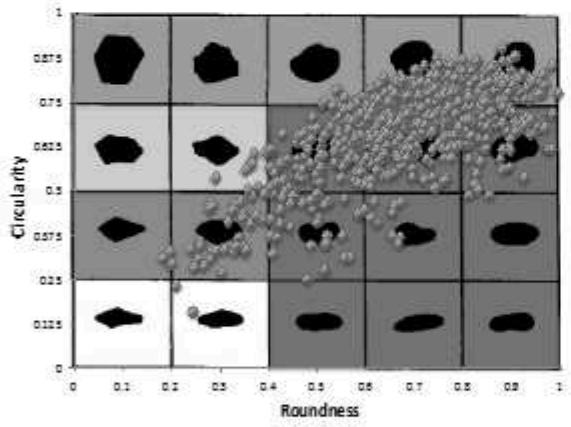


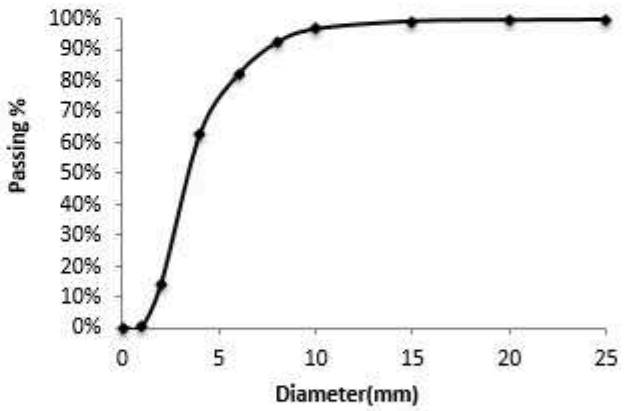
Depth (m)	Shape %		Diameter		Failure type		
1245-1250	Blocky	27.65%	1-15mm		Tensile failure	0.25%	
	Tabular	1.01%	1-4mm		Shear Failure	71.09%	
	Angular	71.09%	0-25mm		Bedding Failure	28.66%	
	Splintery	0.25%	1-4mm				

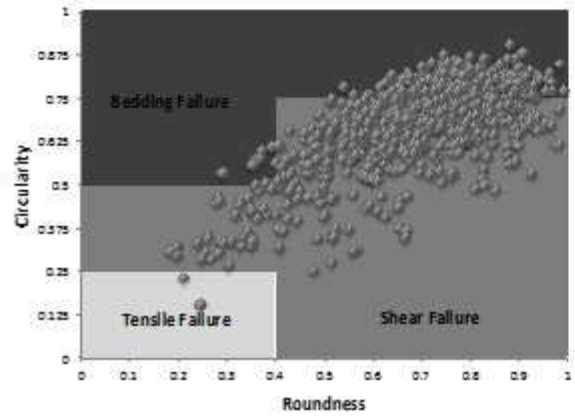
Analysis:

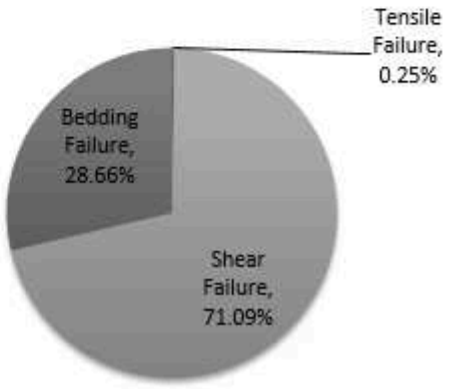
Considerable amount of angular cavings recommends the shear failure. This is in good agreement with the STAR log around the depth of 1247-1450m (dark regions). The top 2 meters of STAR log shows a complete 360° failure of wellbore wall. This indicates either tensile or bedding failure. The cuttings analysis supports bedding failure in the form of blocky cavings.









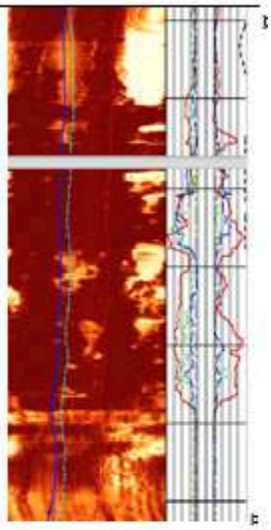


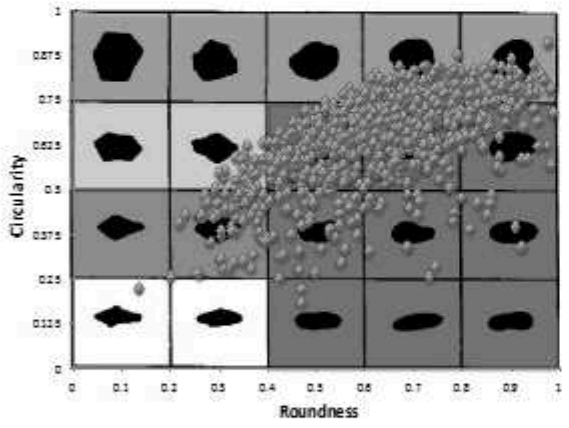
Depth (m)	Shape %		Diameter		Failure type	
1265-1270	Blocky	19.88%	1-25mm		Tensile failure	0.12%
	Tabular	2.87%	1-6mm		Shear Failure	77.13%
	Angular	77.13%	0-30mm		Bedding Failure	22.75%
	Splintery	0.12%	0-1mm			

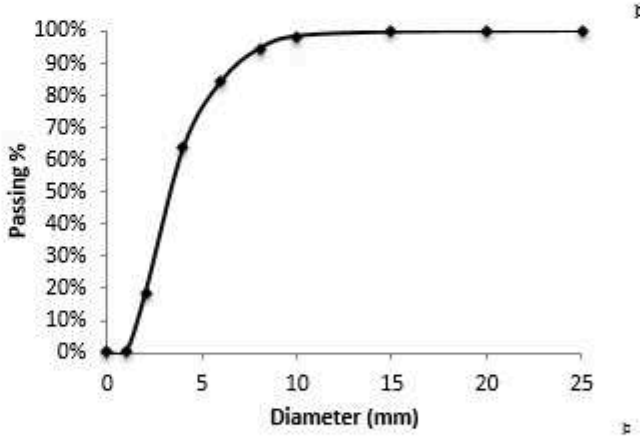
Analysis:

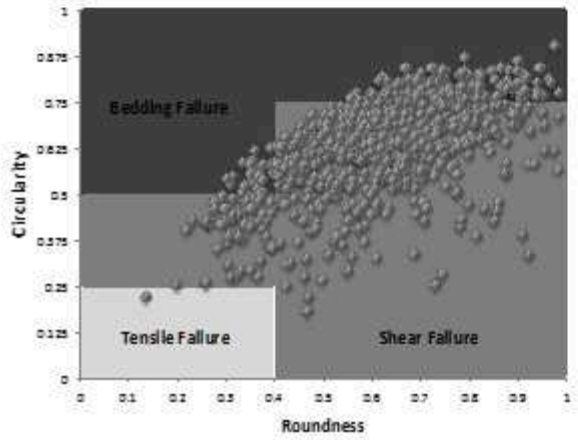
Extensive shear failure has occurred in the wellbore resulting a large amounts of angular cavings. This is clear in the STAR log as well. However this occurred in a depth interval with natural fractures Having 20% blocky cavings in cutting analysis supports bedding failure to be the second failure mechanism of the rock.

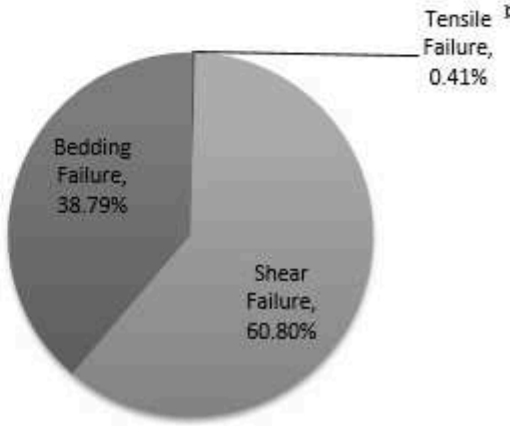










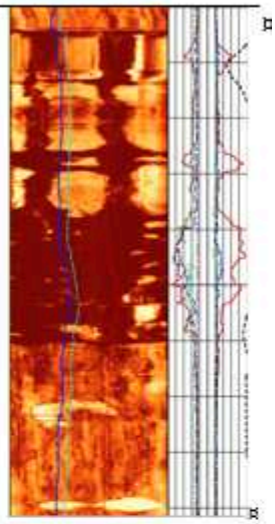


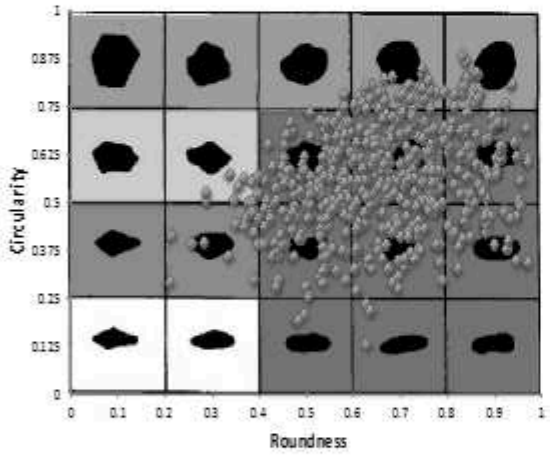
Depth (m)	Shape (%)		Diameter		Failure type		
1275-1280	Blocky	8.22%	1-8mm		Tensile Failure	0.47%	
	Tabular	1.68%	1-4mm		Shear Failure	53.36%	
	Angular	90.09%	0-25mm		Bedding Failure	46.17%	
	Splintery	0.00%	-				

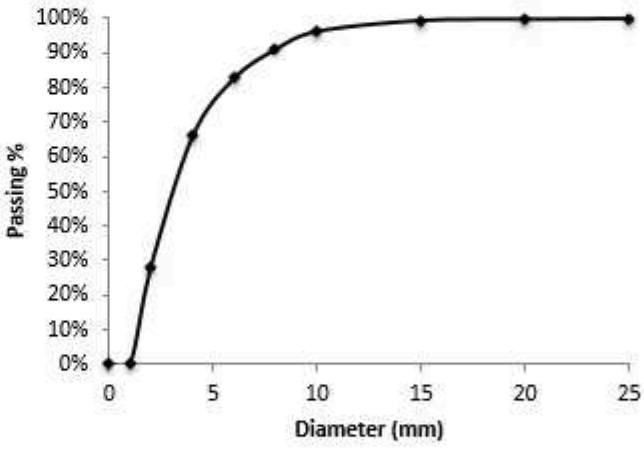
Analysis:

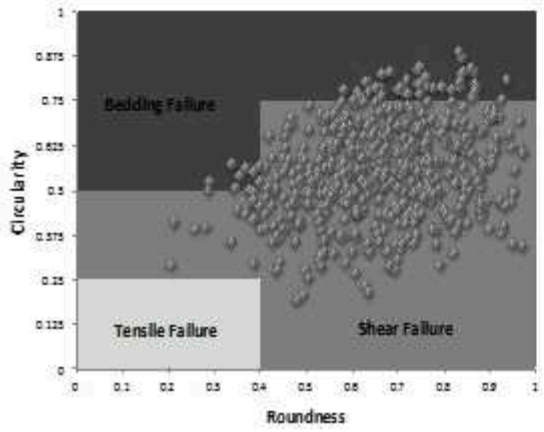
The distinct angular shape of the cavings indicates shear failure of wellbore wall (cavings with sharp edges). The dark region within the middle of the STAR log (with large amounts of angular cavings) suggests abnormal stresses within that region leading to massive shear failure.

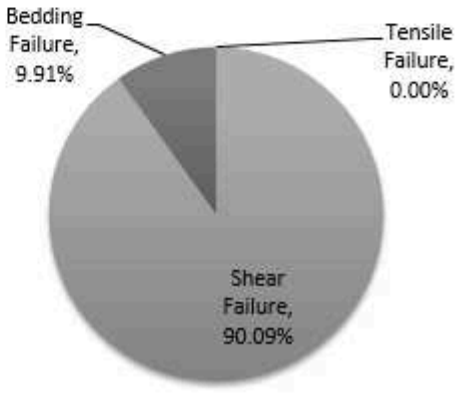








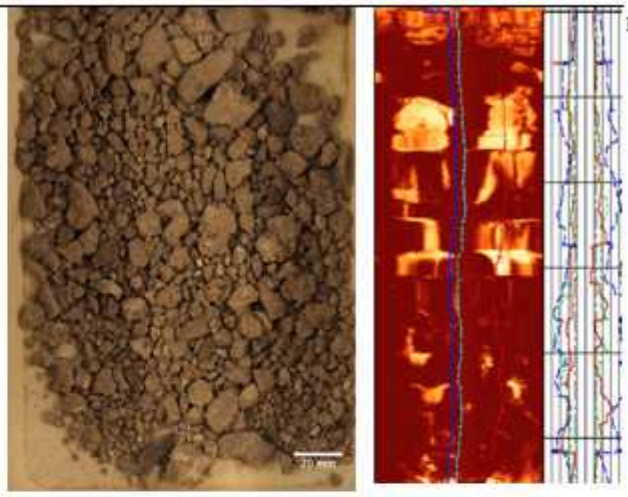


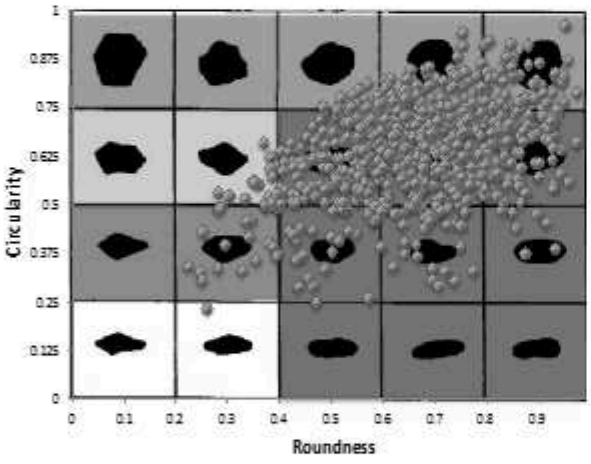


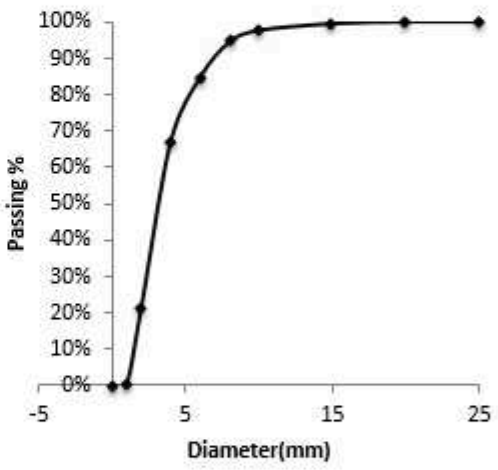
Depth (m)	Shape (%)		Diameter		Failure type	
1280-1285	Blocky	17.48%	1-10mm		Tensile Failure	0.13%
	Tabular	1.99%	0-8mm		Shear Failure	80.40%
	Angular	80.40%	1-20mm		Bedding Failure	19.47%
	Splintery	0.13%	2-4mm			

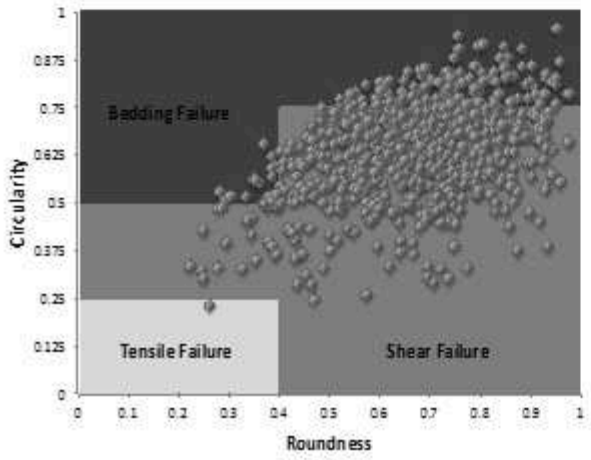
Analysis:

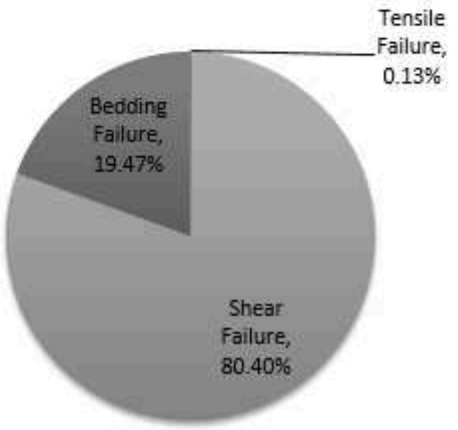
The high volume of angular cavings agrees the shear failures to be main failure mechanism. Likewise, the presence of blocky and tabular cavings implies that there are pre-existing planes of weakness in the formation. Drilling fluid's invasion distress fractures and cause breakouts. Image logs also highlight the damaged zones. The increase in mud weight is recommended.







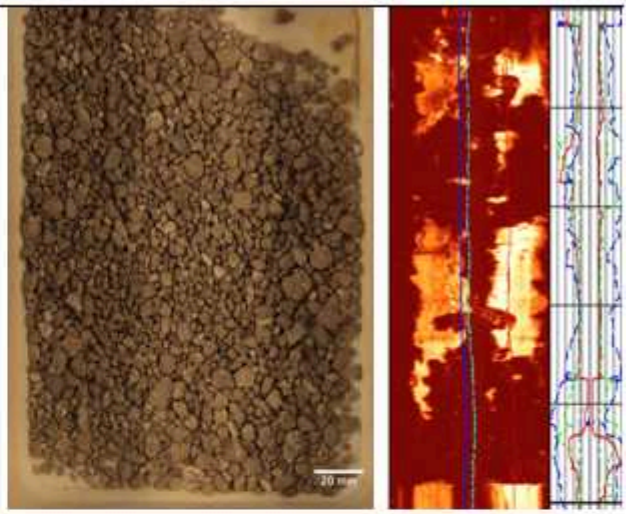


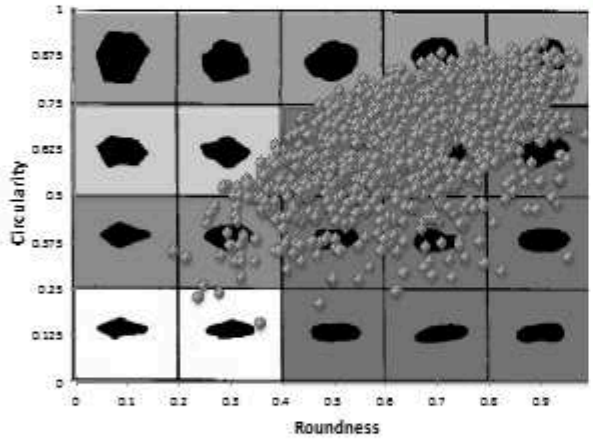


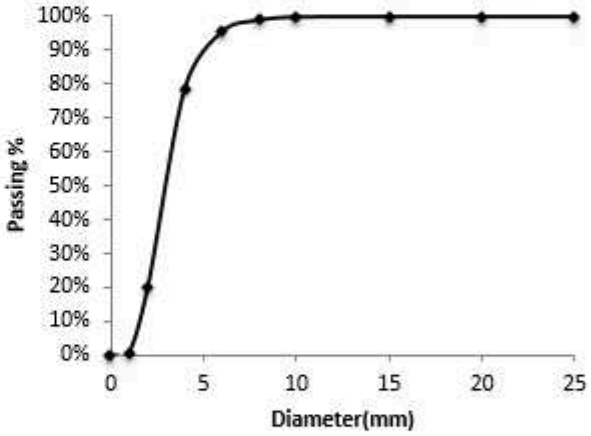
Depth (m)	Shape %		Diameter		Failure type	
1285-1290	Blocky	26.97%	1-15mm		Tensile Failure	0.21%
	Tabular	2.13%	0-6mm		Shear Failure	70.69%
	Angular	70.69%	0-10mm		Bedding Failure	29.10%
	Splintery	0.21%	1-6mm			

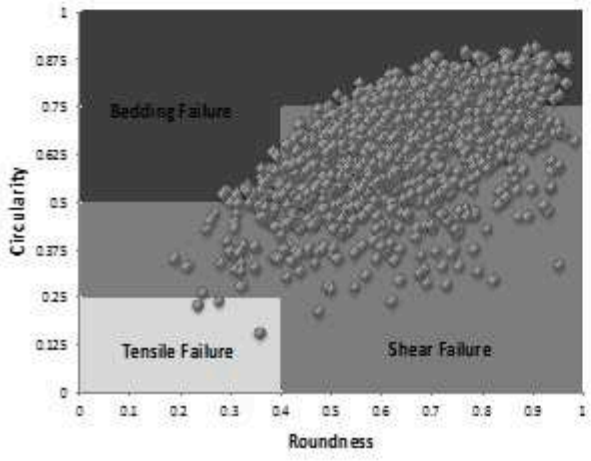
Analysis:

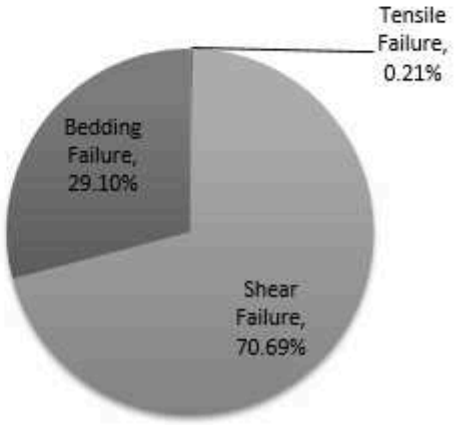
The image analysis shows that there is a high percentage of angular cavings within the sample. These cavings are from shear failure of wellbore wall parallel to minimum horizontal stress. This is shown in the STAR log. There are also a relatively large amount of blocky cavings, which would have been produced in areas where formation had natural pre-existing fractures. This leads to bedding failure around the depth intervals of 1286-1287m and 1289-1290m shown in STAR log.









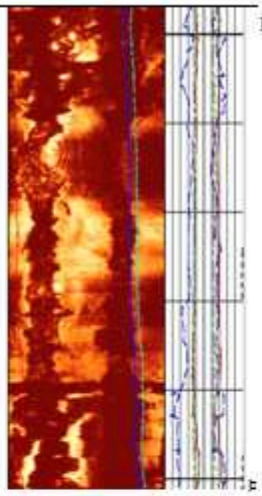


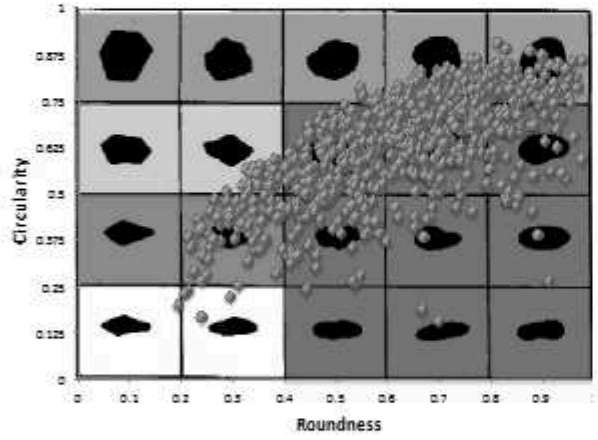
Depth (m)	Shape (%)		Diameter		Failure type		
1320-1325	Blocky	22.72%	1-20mm		Tensile failure	0.59%	
	Tabular	3.16%	1-6mm		Shear Failure	73.54%	
	Angular	73.54%	0-20mm		Bedding Failure	25.88%	
	Splintery	0.59%	0-2mm				

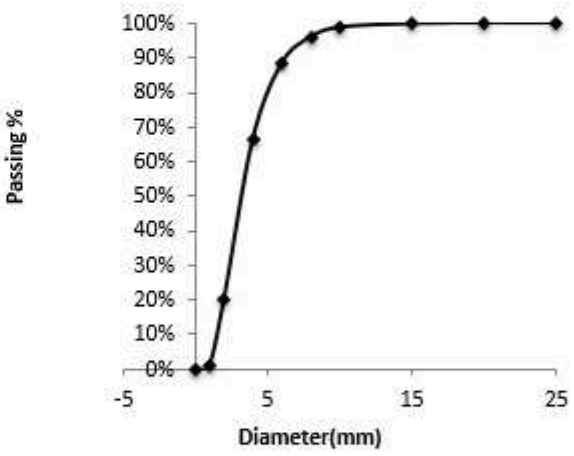
Analysis:

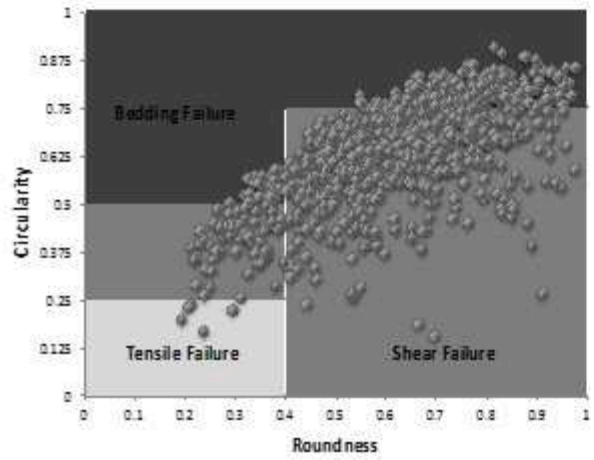
Shear failure has occurred as evidenced by the large amount of angular cavings. STAR log also shows breakouts with 180° apart. 25% of cavings comes from bedding failures There is a bedding failure at 1317-1320m just above the described zone and this is most likely the source of blocky and tabular cavings.

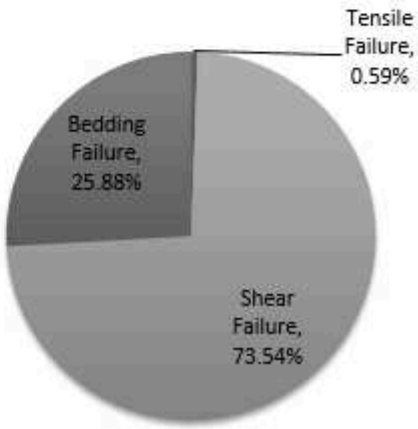










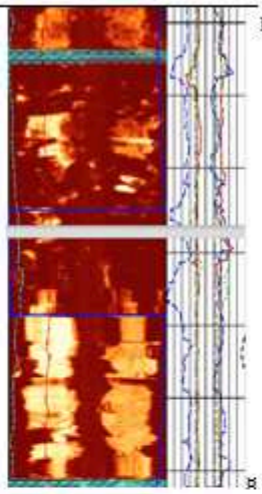


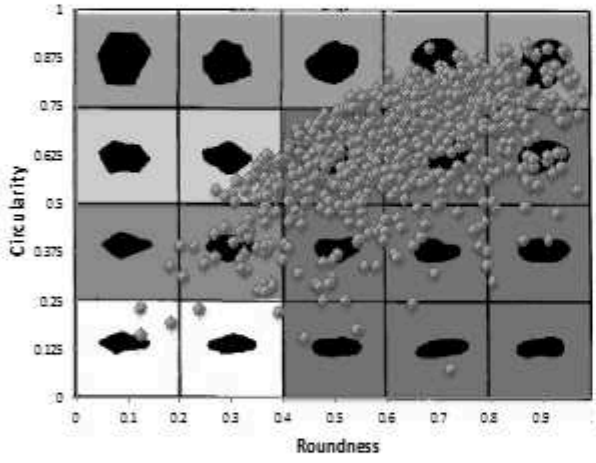
Depth (m)	Shape %		Diameter	Failure type	
1330-1335	Blocky	28.04%	1-20mm	Tensile Failure	0.62%
	Tabular	3.97%	1-6mm	Shear Failure	67.37%
	Angular	67.37%	0-20mm	Bedding Failure	32.01%
	Splintery	0.62%	0-2mm		

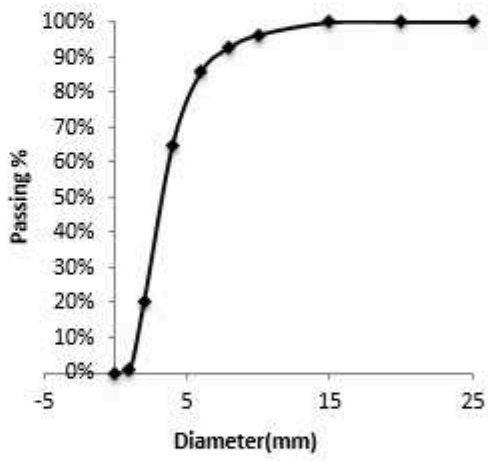
Analysis:

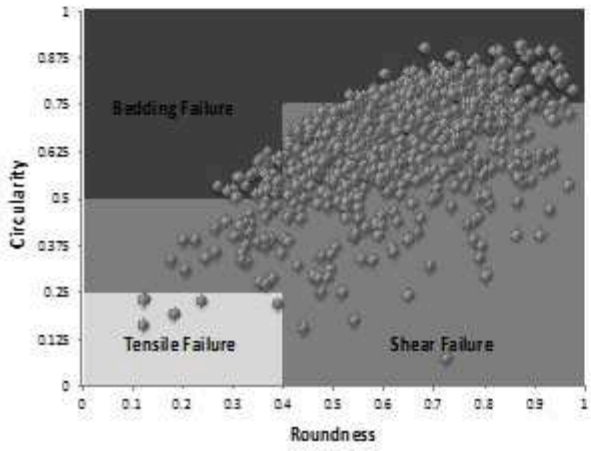
Upper sections of log shows failure of the complete circumference of wellbore and with high presence of blocky and tabular cavings (bedding failure). The high amount of angular cavings shows that the shear failure has occurred (see lower half of the STAR image with breakouts 180° apart).

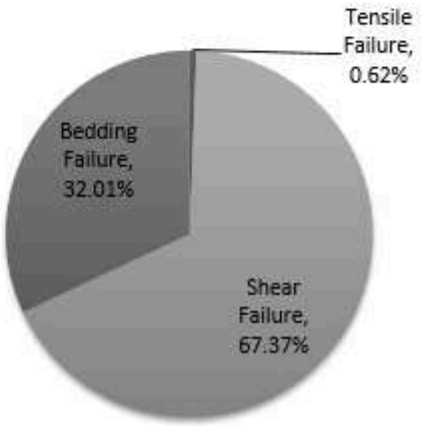










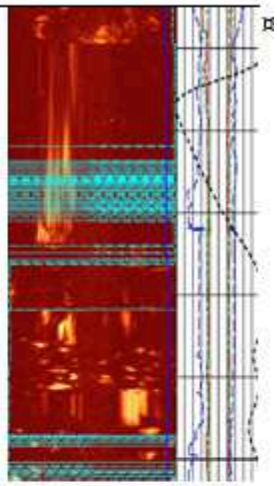


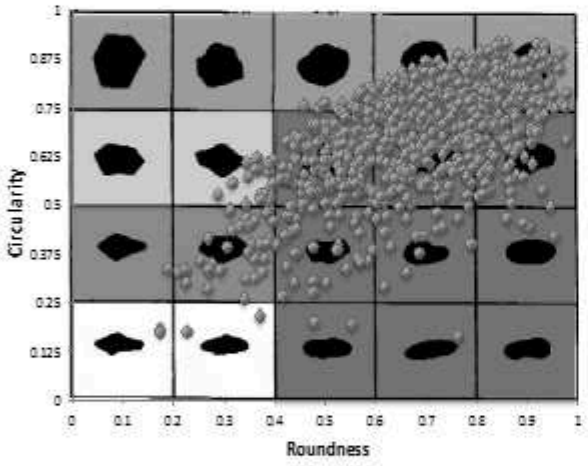
Depth (m)	Shape %		Diameter		Failure type
1365-1370	Blocky	37.04%	1-20mm		Tensile Failure
	Tabular	1.75%	0-4mm		Shear Failure
	Angular	60.80%	0-20mm		Bedding Failure
	Splintery	0.41%	1-4mm		

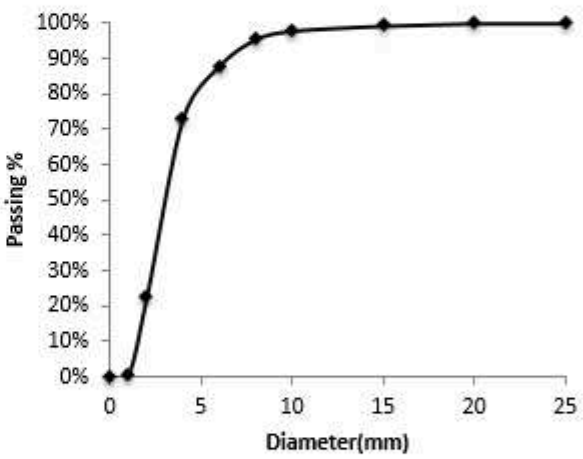
Analysis:

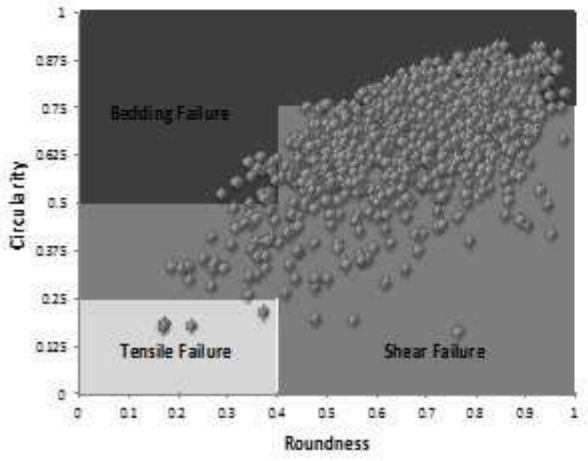
The data show that the primary cause of breakouts has been shear failure according to images and shape type distributions. Breakouts seem to be deep. They possibly have occurred in a naturally fractured zone leading to further blocky cavings.

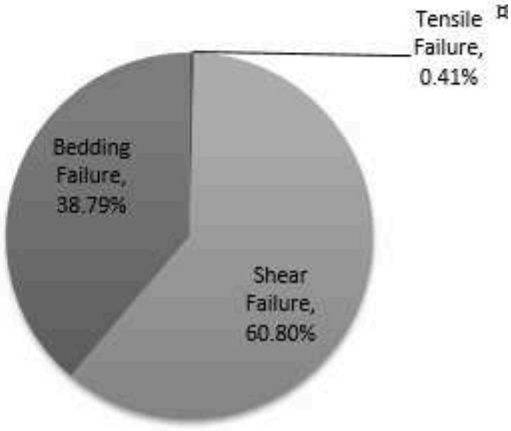










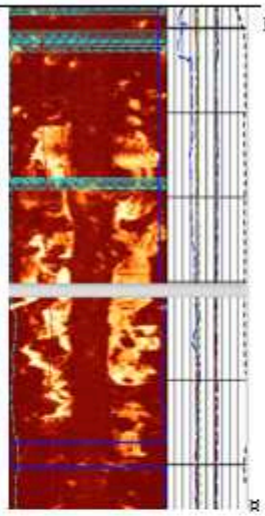


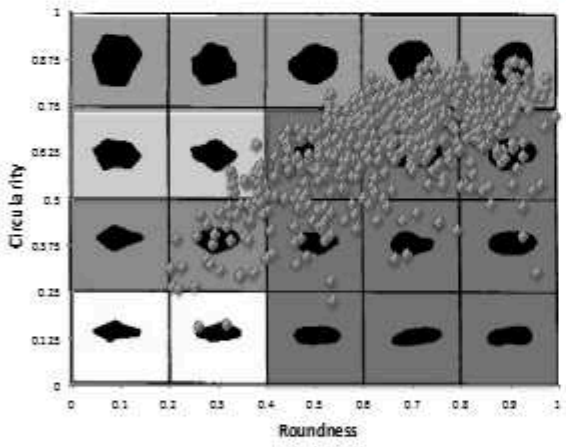
Depth (m)	Shape %		Diameter		Failure type	
1370-1375	Blocky	26.93%	1-25mm		Tensile Failure	0.29%
	Tabular	2.58%	0-6mm		Shear Failure	70.20%
	Angular	70.20%	0-20mm		Bedding Failure	29.51%
	Splintery	0.29%	0-4mm			

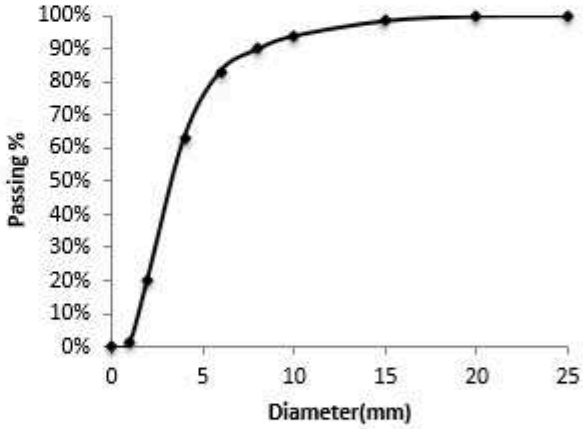
Analysis:

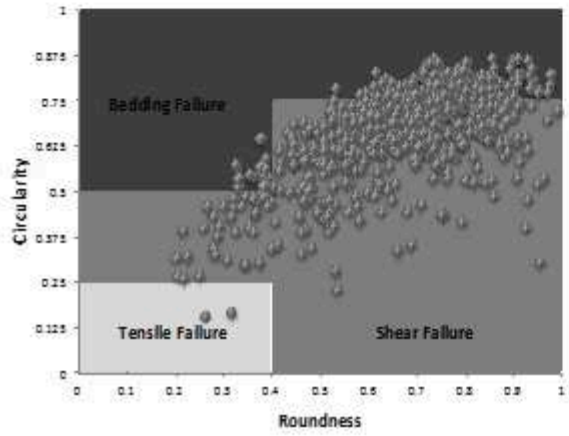
Large blocky cavings with lots of smaller angular cavings suggests that shear failure of wellbore occurred within an area with pre-existing planes of weakness.

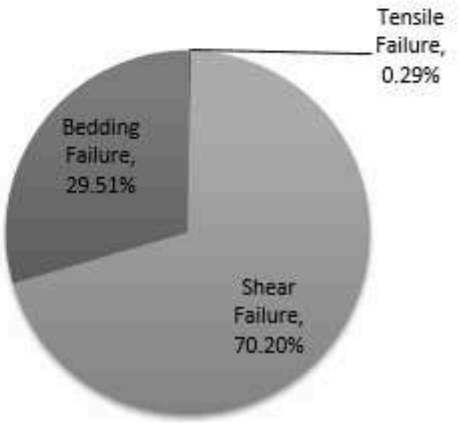










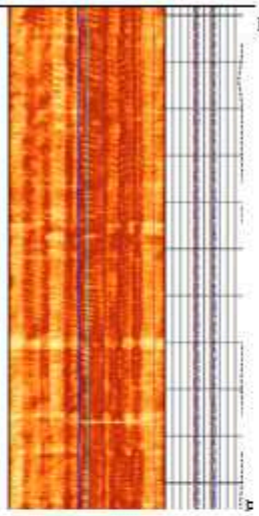


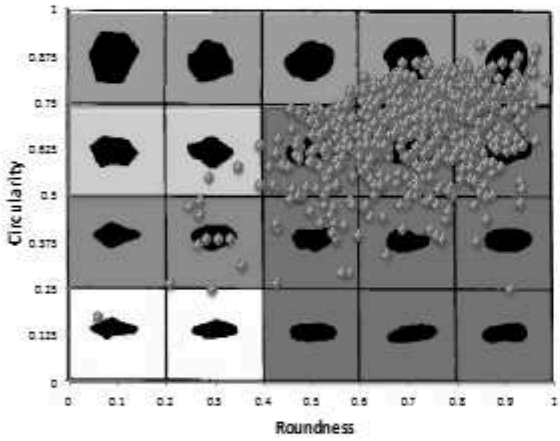
Depth (m)	Shape (%)		Diameter	Failure type	
1835-1840	Blocky	28.57%	1-15mm	Tensile Failure	28.57%
	Tabular	0.61%	1-4mm	Shear Failure	0.61%
	Angular	70.51%	0-20mm	Bedding Failure	70.51%
	Splintery	0.31%	0-4mm		

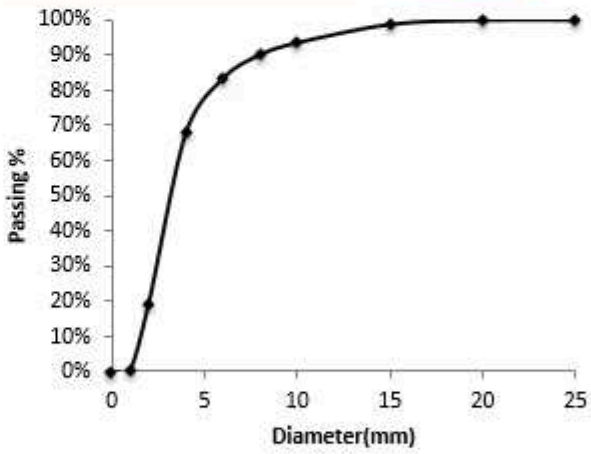
Analysis:

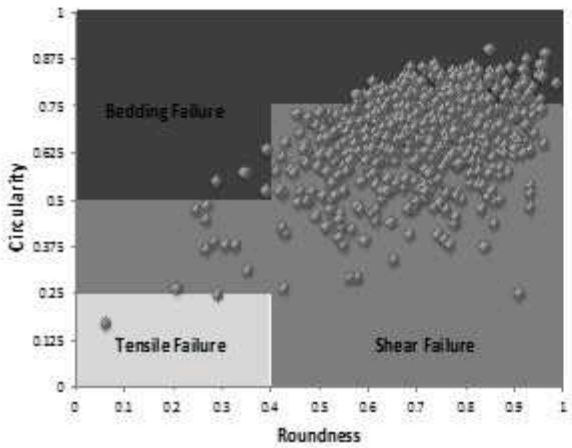
Running the pill increased the cavings over shakers. This along with STAR wire line logging report suggests that the pill destabilised some section further up the wellbore. Therefore, the angular fragments in this depth interval might come from higher depth Image log doesn't support to have any failure in this depth interval.

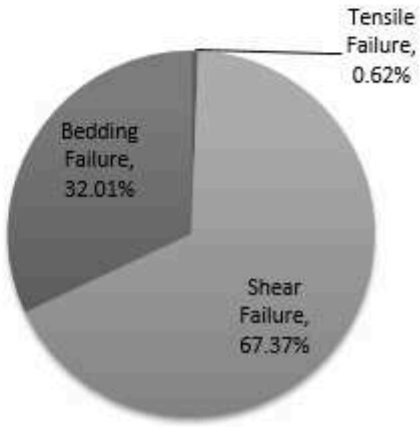










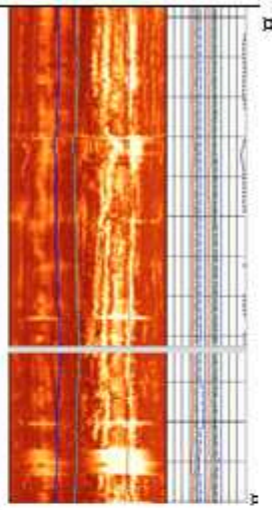


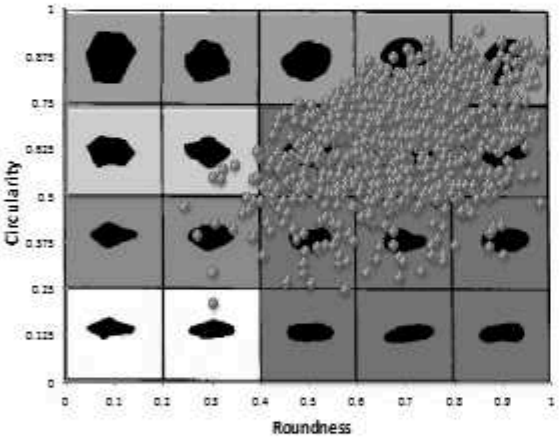
Depth (m)	Shape %		Diameter		Failure type	
2845-2850	Blocky	23.62%	1-8mm		Tensile Failure	0.10%
	Tabular	0.70%	1-4mm		Shear Failure	75.58%
	Angular	75.58%	0-20mm		Bedding Failure	24.32%
	Splintery	0.10%	2-4mm			

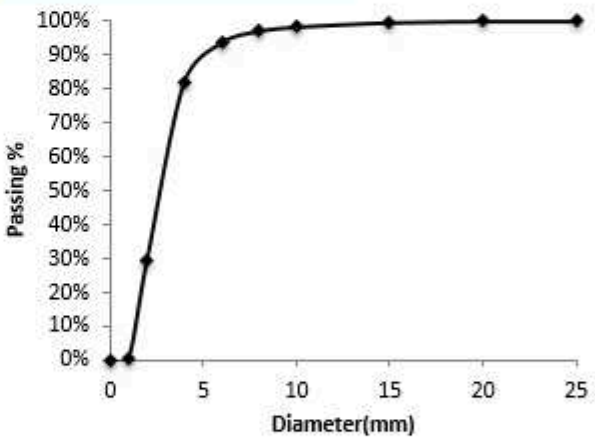
Analysis:

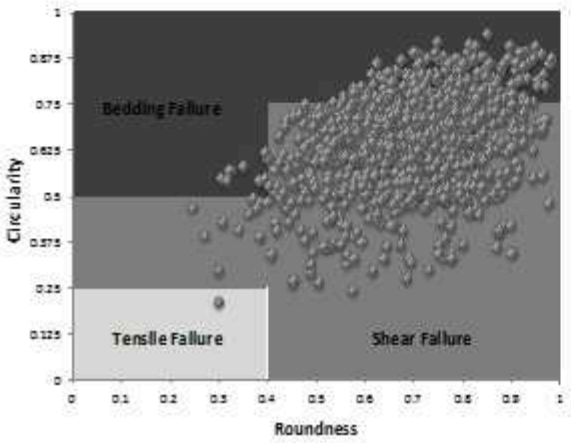
Shape distribution graph shows that the cavings are rounded compared to other samples.

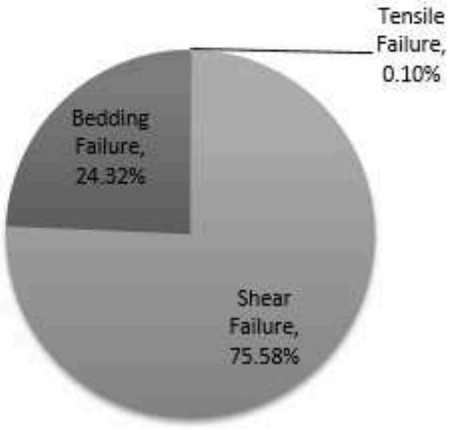












Section 7: Summary and recommendations

Claudio Delle Piane[1]

[1]CSIRO Energy

The goal of the multidisciplinary work presented here is to help enable and further understand the geological and geophysical parameters that will affect the safe and efficient storage of CO_2 at the proposed South West Hub site in the Southern Perth Basin. In particular the study aimed at providing an enhanced understanding of the geological, petrophysical and geomechanical characteristic of the Lesueur Sandstone intersected by Harvey 2, 3 and 4 drilled in the potential storage area. The project aimed at providing data to be used in modelling scenarios of the South West Hub subsurface to reduce the critical uncertainties around injectivity and containment identified by the South West Hub project Sub-surface Uncertainty Management Plan (UMP) compiled by DMIRS in 2017. To this end a multidisciplinary workflow was adopted that led to the outcomes listed in Table 16 below in relationship to the uncertainty domains identified by the UMP.

Uncertainty domain	Analytical / experimental techniques adopted	Outcomes
Sedimentary facies	Sedimentological core evaluation	Lithofacies scheme used for Harvey 1 is broadly applicable to the other boreholes in the South West Hub area indicating a uniformity in the sedimentological characteristics of the Lesueur Sandstone in the subsurface
Reservoir diagenesis	Petrographic analysis via optical and electron microscopy on samples from the new boreholes and review of available data from Harvey 1	The upper section (100 - 220 m) of the Wonnerup Member intersected by the three new boreholes is dominated by quartzo-feldspathic sandstones. Petrographic analysis indicate a detrimental effect of diagenesis on reservoir quality via diagenetic precipitation of pore occluding clay minerals, deposition of quartz overgrowth and chemical compaction. Nevertheless, uplift of the sediments in the South West Hub area helped preserve a porosity of approximately 10 % in the deeper part of the Wonnerup (intersected in Harvey 1)
Formation salinity	Fluid inclusion analysis	Measured palaeo-salinity values constraint the CO_2 solubility in the Lesueur Sandstone. Values > 35,000 ppm were found in samples from the Yalgorup or the top the Wonnerup. Salinities < 35,000 ppm in samples from within the Wonnerup
Fault compartmentalisation	Fluid inclusion analysis	Geochemical analyses of fluid inclusions indicate a consistent range of palaeo-salinities in the different boreholes and give no indication of compartmentalization across different borehole locations

Uncertainty domain	Analytical / experimental techniques adopted	Outcomes
Presence of faults and fractures	Meso and micro scale analysis of core material. Image analysis of electron microscopy images	Sub-seismic scale faults are identified and described within the three new boreholes via core observations and microstructural analysis. These structures could act as local baffles to subsurface fluid flow and potentially reduce injectivity in the targeted reservoir. An estimated density of these structures is provided that can be implemented in geological reservoir models
Porosity-permeability relationships	Laboratory measurements of porosity and permeability. Permeability measurements to gas and to reconstituted brine	Laboratory tests conducted at in situ conditions and with a realistic pore water chemistry show that permeability to brine is systematically lower than the Klinkenberg corrected gas permeability measured on the same samples. The former should be used for populating the flow properties of the reservoir in dynamic reservoir models
Porosity depth trend	Comparison between laboratory and wireline log derived porosity as a function of depth	Porosity reduces with increasing depth in the Wonnerup. Using the Yalgorup-Wonnerup transition as "normalised" depth, it is shown that porosity-depth trends of the four boreholes overlap with each other and with the trend derived from wireline logs. Average laboratory porosity is 19.58 ± 2.3 % in the upper 200 m of the Wonnerup decreasing to 10.93 ± 3.2 % in the bottom part of the section
Heterogeneity of permeability	Laboratory measurements of permeability anisotropy	A novel experimental set up was used to estimate directional permeability on single core plugs from the Lesueur Sandstone at in situ conditions. Permeability is moderately anisotropic with ratios of vertical to horizontal permeability ranging between 0.88 and 0.41 consistent with those from other fluvial sandstone reported in the literature and can be added to realistically model fluid movement in the South West Hub area

Uncertainty domain	Analytical / experimental techniques adopted	Outcomes
Rock compressibility	Laboratory measurements at in-situ pressure and temperature	The elastic properties of the Lesueur Sandstone estimated from laboratory experiments are sensitive to fluid saturation state, and the experimental results can be well predicted via the use of Gassmann fluid substitution theory supporting its use for CO_2 saturation monitoring via seismic methods
Seal capacity	Theoretical and experimental study on the feasibility and interpretation of CO_2 breakthrough tests clay-rich sample of the Yalgorup Member of the Lesueur Sandstone. Analysis of relative importance of capillary versus diffusive processess	Under simulated reservoir temperature and pressure conditions permeability to brine in a clay-rich Yalgorup sample is of the order of 2 nD (2×10^{-21} m^2), CO_2 diffuses through the sample at a rate 2 to 10 times slower than the natural brine. The clay-rich intervals of the Yalgorup Member of the Lesueur Sandstone could act as effective baffles for CO_2 migration

Table 16 Summary of the uncertainties identified by the UMP compiled by DMIRS and the relevant approaches and outcomes resulting from this project.

In addition to what is summarised in Table 16, the project produced new data that can help decipher the geological history of the Perth Basin: temperatures recorded in fluid inclusions provide information on the burial history of the sediments in the South West Hub area which can be reconciled with a local uplift of approximately 1.5 km. This data set is particularly valuable considering the paucity of conventional geothermal constraints like vitrinite reflectance in the area.

The geomechanical properties of the Lesueur Sandstone have been experimentally evaluated and show that the potential reservoir (i.e. the Wonnerup Member of the Lesueur Sandstone) follows a dilational Mohr Coulomb behaviour characterised by a friction coefficient of 0.71 ± 0.13 and cohesion of 10.93 ± 6.06 MPa. On the other hand, the experimental data collected on the clay rich samples of the Yalgorup Member are best described by a compactant yield envelope suggesting that the mechanical response of the formation is sensitive to its lithological characteristics and different constitutive behaviours should be used to appropriately model different facies.
The analysis of cuttings also provided additional elements to better understand the dominant wellbore failure types in Harvey 1 highlighting the relatively small influence of tectonic stresses on the stability of the well.

Finally, no issues were identified that might suggest postponing or cancelling further investigations around the feasibility of the South West Hub geosequestration site.

The data acquired within this project should be used in the new generation of models of the South West Hub subsurface to honour the local geology and distribution of petrophysical properties within the Lesueur Sandstone
In light of the above statements it should be noted that to date Harvey 1 is the only borehole in the South West Hub area penetrating the entire potential reservoir (i.e. the Wonnerup) and as such the project still

lacks actual verification of the reservoir properties of the deeper section of the Lesueur Sandstone. A new deep borehole or the deepening of one of the existing boreholes could supply additional core material to further confirm the diagenetic trends and their influence on reservoir quality inferred above.

Reliable measurements of formation brine salinities are still not available and it is recommended that further studies accessing the existing boreholes are performed to compensate for this lack of information.

The large volume of experimental data collected so far within the programs supported by DMIRS and the various project supported by ANLEC needs to be corroborated via in situ production/injection tests. These should be designed to verify the magnitude of permeability anisotropy in the reservoir and the role of deformation bands in controlling injectivity and fluid movements around the borehole.

CONTACT US

t 1300 363 400
+61 3 9545 2176
e enquiries@csiro.au
w www.csiro.au

AT CSIRO WE SHAPE THE FUTURE

We do this by using science to solve real issues. Our research makes a difference to industry, people and the planet.

As Australia's national science agency we've been pushing the edge of what's possible for over 85 years. Today we have more than 5,000 talented people working out of 50-plus centres in Australia and internationally. Our people work closely with industry and communities to leave a lasting legacy. Collectively, our innovation and excellence places us in the top ten applied research agencies in the world.

WE ASK, WE SEEK AND WE SOLVE

FOR FURTHER INFORMATION

ENERGY
Claudio Delle Piane
t +61 8 6436 8716
e claudio.dellepiane@csiro.au
w www.csiro.au/flagship-businessunit

Insert Flagship/Business Unit name
Insert contact name
t +61 0 0000 0000
e first.last@csiro.au
w www.csiro.au/flagship-businessunit

Insert Flagship/Business Unit name
Insert contact name
t +61 0 0000 0000
e first.last@csiro.au
w www.csiro.au/flagship-businessunit